

**LIFE ASSESSMENT OF
WELDED INCONEL 718 AT HIGH TEMPERATURE**

DAVID W. J. TANNER, BSc

**Thesis submitted to the University of Nottingham for
the degree of Doctor of Philosophy**

June 2009

Abstract

The overall aim behind this work was to gain and apply an understanding of the mechanical effects of welding, in order to mitigate distortions that had previously hampered uniaxial testing of tungsten inert gas (TIG) butt-welded, thin rectangular section, nickel-base superalloy INCONEL 718 (IN718). With this aim achieved, better test data could be obtained, leading to more reliable material data for IN718 welds, which can be used for more accurate life assessments for shell structures and components, with a particular emphasis on those operating at high temperature.

ABAQUS finite element (FE) simulations of the arc welding process were used to understand the development of welding-induced distortions and reduce their prevalence. The sequentially-coupled nonlinear thermal and elastic-plastic models employed were capable of calculating the evolution of stress and deformation, and predicting the residual stresses and distortions that occur as a result of the welding process. An efficient, distortion-mitigating welding procedure, devised using the numerical simulations, was used to manufacture TIG butt-welded specimens that were free of distortion.

Uniaxial tensile, creep and high temperature (620°C) fatigue tests were performed on both welded and non-welded IN718 specimens. It was found that IN718 welds are significantly less ductile than the parent material, and although welded IN718 exhibits comparatively little loss of tensile strength, its creep and high temperature fatigue properties are severely compromised. The lower performance of the welded specimens was attributed to the microstructural differences when compared with the non-welded material.

The stress-strain relationships and mechanical properties of the IN718 weld material were calculated and verified using FE analyses, based on the test data obtained. A continuum damage mechanics approach was employed for creep modelling and the necessary material constants required for the damage equations were determined. A Smith, Watson and Topper (SWT) strain range parameter was proposed for fatigue life assessment, based on validation obtained using the test data.

The material properties and lifing methods were subsequently used with three-dimensional, quasi-static elastic-plastic and creep FE analyses, for a life assessment case study of a welded feature in an IN718 generic spoke structure. The effect of including a weld in a critical region was investigated for both constant (creep) and cyclic loading conditions at 620°C. The depleted high temperature fatigue properties of the welded IN718 material had a negative effect on the high temperature fatigue life of the structure (reducing the life by two orders of magnitude). The effect of welding on the life of the structure under constant loading at high temperature was found to be difficult to evaluate due to significant stress relaxation.

Acknowledgements

I am extremely grateful to the following people who have made the work in this thesis possible:

My supervisors Professor Adib Becker and Professor Tom Hyde for their guidance and support.

Dr Yongle Song for the work that preceded this. Dr Paul Andrews and Dr Yannis Kyriakoglou of Rolls-Royce plc. for their help. Haynes International Ltd. for provision of the sheet material.

Dr Anas Yaghi, Dr Wei Sun and Professor Graham McCartney for their input during technical discussions. Andrew Short for helping with the design of the welding jig, Dr Joel Segal for use of the welding robot and Stuart Branston for operating it. Brian Webster for his indispensable contribution to the experimental work, and Tom Buss and Keith Dinsdale for their expertise.

David Oakland, Ray Pickard and the technical staff of the central engineering workshop, in particular Brian Vincent for machining the specimens. Barry Holdsworth and Graham Malkinson for their contribution to the manufacture of the specimens.

The EU for funding under project VITAL. Rolls-Royce plc. and the Department of Mechanical, Materials and Manufacturing Engineering at the University of Nottingham for the UTC facilities. The University of Nottingham support staff.

Finally, I wish to thank my friends and colleagues in the UTC, and most importantly my parents, Alan and Daphne, the rest of my family, and Babita for looking after me.

Contents

Chapter 1 – Introduction.....	1
1.1 Summary	1
1.2 Background.....	1
1.3 Thesis outline	3
Chapter 2 – Literature review.....	6
2.1 Introduction.....	6
2.2 Welding: residual stresses and distortions	7
2.3 The prediction of weld residual stresses and distortions: A brief history of published research.....	10
2.4 Residual stress and distortion mitigation	20
2.5 Numerically modelling the welding process	22
2.5.1 <i>Simplified welding heat source models</i>	26
2.5.2 <i>Welding filler addition -element activation</i>	31
2.5.3 <i>Equivalent plastic strain as an indicator of damage</i>	32
2.6 Welding distortion	33
2.6.1 <i>Distortion mechanism</i>	34
2.6.2 <i>In-plane shrinkage</i>	35
2.6.3 <i>Angular distortion</i>	38
2.6.4 <i>Buckling distortion</i>	39
2.6.5 <i>Rotational distortion</i>	40
2.6.6 <i>Distortion control</i>	40
2.7 Welding processes.....	41
2.8 Tungsten inert gas (TIG) welding.....	42
2.9 Weld material properties	46
2.10 Metallurgical effects of welding.....	47
2.10.1 <i>Weld pool solidification</i>	47
2.10.2 <i>The heat-affected zone (HAZ)</i>	51

2.10.3	<i>Solid-state phase transformation</i>	52
2.10.4	<i>Weld cracking</i>	53
2.11	INCONEL 718	53
2.11.1	<i>Introduction</i>	53
2.11.2	<i>Background</i>	54
2.11.3	<i>INCONEL 718 welds</i>	55
2.11.4	<i>INCONEL 718 weld mechanical properties</i>	58
2.11.5	<i>Life assessment of welded INCONEL 718 at high temperature</i>	60
Chapter 3 – Finite element welding simulation		62
3.1	Summary	62
3.2	Introduction.....	62
3.3	Modelling approach.....	64
3.4	Model definition.....	65
3.5	Thermal analysis.....	68
3.6	The need for a three-dimensional model	75
3.7	Finite element mesh.....	76
3.8	Material properties.....	80
3.9	Mechanical analysis	84
3.10	Effects of annealing/plastic strain relaxation.....	91
3.11	Effect of using different weld mechanical properties.....	95
3.12	Presetting for distortion mitigation.....	97
3.13	Effects of restraint (clamping).....	98
3.13.1	<i>G-type clamped model</i>	98
3.13.2	<i>Flat clamped model</i>	103
3.14	Modelling filler addition and underbead formation.....	109
3.15	Welding model including jig	118
3.16	Welding model with a ceramic backing plate.....	125
3.17	Discussion and conclusions.....	127

Chapter 4 – Test specimen manufacture	129
4.1 Introduction.....	129
4.2 Material procurement.....	129
4.3 Postweld heat treatment (PWHT).....	130
4.4 Weld material property testing	131
4.5 Thermomechanical material property testing.....	133
4.6 Thermophysical material property testing	134
4.7 Tensile, creep and high temperature fatigue testing	136
4.8 Welding	136
4.9 Tensile, creep and fatigue specimen manufacture	143
4.10 Summary	144
Chapter 5 – Tensile, creep and high temperature fatigue testing.....	145
5.1 Summary	145
5.2 Welded specimen results classification	146
5.3 Extensometer	146
5.4 Temperature measurement	149
5.5 Tensile testing.....	149
5.5.1 <i>Tensile testing setup and procedure</i>	149
5.5.2 <i>Tensile test results</i>	151
5.6 Creep testing.....	157
5.6.1 <i>Creep testing setup and procedure</i>	158
5.6.2 <i>Creep test results</i>	162
5.7 High temperature fatigue testing.....	167
5.7.1 <i>High temperature fatigue testing setup and procedure</i>	168
5.7.2 <i>High temperature fatigue test results</i>	171
5.8 Optical microscopy/fractography	177
5.8.1 <i>Procedure</i>	177
5.8.2 <i>Tensile tests</i>	178

5.8.3	<i>Creep tests</i>	179
5.8.4	<i>High temperature fatigue tests</i>	183
5.9	Discussion and conclusions.....	188
Chapter 6 – Material property determination –weld, creep and fatigue modelling		191
6.1	Summary	191
6.2	Introduction.....	192
6.3	Weld material property determination	194
6.4	Finite element verification of material properties and validation of modelling.....	199
6.5	Finite element modelling of the creep tests	203
6.6	Finite element modelling of the high temperature fatigue tests	211
6.7	Conclusion	222
Chapter 7 – Creep and high temperature fatigue life assessment case study		223
7.1	Summary	223
7.2	Introduction.....	224
7.3	Model definition.....	227
7.4	Finite element model setup.....	227
7.5	Finite element creep analysis.....	231
7.6	Finite element fatigue analysis	241
7.7	Conclusion	246
Chapter 8 – Conclusions and future work		248
8.1	Conclusions.....	248
8.2	Future work	253
References		255

Nomenclature

EB	electron beam
FE	finite element
FZ	fusion zone
HAZ	heat-affected zone
HT	heat-treated
LB	laser beam
NW	non-welded
PMZ	partially melted zone
PWHT	postweld heat treatment
SHT	solution heat treatment
S-N	stress against number of fatigue cycles to failure
SWT	Smith, Watson and Topper (parameter)
TIG	tungsten inert gas
UTS	ultimate tensile strength
W	welded
YS	yield (0.2% proof) stress
C_p	specific heat capacity
E	Young's modulus
h	combined convective and radiative cooling coefficient
q	heat flux
\dot{Q}	rate of internal heat generation
Q_p	energy/power input
T	temperature

t	time
v	welding speed
x,y,z	Cartesian coordinates
α	coefficient of thermal expansion
α_r	multiaxial rupture parameter
ε	strain
$\dot{\varepsilon}^c$	creep strain rate
η	thermal efficiency
k	thermal conductivity
ν	Poisson's ratio
ρ	density
σ	stress
ω	damage parameter

Chapter 1

Introduction

1.1 Summary

The overall aim behind the work presented in this thesis is to gain and apply an understanding of the mechanical effects of welding, in order to mitigate distortions that have previously hampered uniaxial testing of tungsten inert gas (TIG) butt-welded, thin rectangular section, nickel-base superalloy INCONEL 718 (IN718). With this aim achieved, better test data can be obtained, leading to more reliable material data for IN718 welds, which can be used for more accurate life assessments for shell structures and components, with a particular emphasis on those operating at high temperature. It should be noted that much of the work presented generalises to other welding processes and materials.

1.2 Background

The material used throughout this study is wrought sheet INCONEL®¹ 718 (IN718), a precipitation-hardenable, niobium-modified, nickel-base superalloy used extensively in the aerospace, petrochemical and nuclear industries since it exhibits good strength, excellent resistance to oxidation at high temperatures and favourable weldability. IN718 is often used in critical high temperature creep resistant applications up to 650°C [1].

One example of application within the aerospace industry is the gas turbine engine, where IN718 is used for turbine disc forgings and shell structures such as the combustor [2]. Aero engine components are typically demanding

¹INCONEL is a registered trademark of Special Metals Corporation, New York, U.S.A.

with regards to design and manufacturing since they are subject to rigorous structural, thermal and aeronautical requirements. The materials used have to resist tremendous loads under high operating temperatures and dimensional precision is highly important to allow for the required flow through the engine and correct alignment.

The intensely competitive nature of the aero engine market has forced manufacturers to re-evaluate their manufacturing processes and as a result, large components that have traditionally been cast and machined, are being redesigned so that the costly casting process and subsequent transportation from supplier to manufacturer are avoided. One such change in the design and manufacture of aero engine structural components is the fabrication of substructures and small features using advanced material processing technologies with efficient tooling and fixturing provisions. The substructures are then welded together to create the full structure. Hence, it is essential to develop techniques to predict the mechanical effects of the welding process such as residual stress and distortion and to compute new life assessments for the redesigned structures.

Welded IN718 features on components that are subjected to high service temperatures where creep (and possibly high temperature fatigue and creep-fatigue interaction) is significant require well-defined material behaviour, and for all integral structural components, the lifetime requires assessment. Aero engine structures need to be particularly well designed due to safety considerations and the important strength-weight ratio from a commercial and environmental perspective.

Life assessment covering creep and high temperature fatigue has been reported for non-welded IN718 (e.g. [3]), but assessment for welded thin-

section structures is more complex due to the residual stresses, deformations and material microstructural changes caused by the welding process. The residual stresses affect the creep and fatigue life by altering the total stress state, and interact with the deformations to produce distortions in the welded part. These distortions may lead to misalignment of structural members and can significantly alter the behaviour of the structures when loaded, thus compromising their structural integrity and invalidating any lifetime predictions deduced from undistorted components. The weld bead geometry must also be considered since sharp fillet radii result in high stress concentrations at the weld bead and parent interface. Due to these factors, the weld has a direct effect on the creep and fatigue life [4].

Although it has disadvantages such as those mentioned here, welding (as opposed to casting) reduces the cost of large structures and can eliminate the need to transport full size cast components from the supplier to the manufacturer, which is also more cost efficient and better for the environment. As such, welding is an integral manufacturing procedure for many components, some of which could not be produced without its application.

1.3 Thesis outline

The literature review (Chapter 2) that follows this introduction (Chapter 1), is mainly concerned with welding, in terms of residual stress, weld distortions and their mitigation, process modelling of welding (with a focus on computational application) for the prediction of residual stress and distortion, and concludes with a section on INCONEL 718, the material used exclusively throughout this thesis.

The finite element (FE) numerical method is particularly suited to modelling the welding process since it is readily adapted to include both geometric and material nonlinearities [5]. Numerical simulations of the arc welding process are presented in Chapter 3 that use user subroutines with the purpose of trying to understand the development of welding-induced distortions and reduce their prevalence. Sequentially-coupled nonlinear thermal and elastic-plastic three-dimensional (3D) ABAQUS analyses are employed and successfully validated using experimental and numerical results from published literature. The simulations have added complexity, particularly since the effects of restraint are considered, and the addition of filler is included, along with the formation of the typical weld underbead that forms during the welding of thin plates. The importance of including the effects of plastic strain relaxation is also highlighted in terms of residual stress and distortion. The complications of presetting, clamping, and the possible heat loss to a welding jig or backing plate are analysed.

An efficient, distortion-mitigating welding procedure, devised using the FE welding simulations from Chapter 3, is put into practice during the test specimen manufacture covered in Chapter 4.

In Chapter 5, the results of uniaxial tensile, creep and high temperature (620°C) fatigue tests on both welded and non-welded IN718 specimens are presented. The main objectives of the testing is to determine the effect the welds have on life, analyse any differences in their failure behaviour, and obtain material properties for input into FE analyses for welding simulation (Chapter 3) and life prediction purposes (Chapters 6 and 7).

In Chapter 6, calculation of the stress-strain relationships and mechanical properties of the IN718 weld material is presented. Test measurements are

used to determine what the behaviour of the weld must have been in order to give the measured test results. FE verification of the material properties is conducted by modelling the uniaxial tensile and creep tests to check the accuracy of the material properties assigned to the weld region. A creep continuum damage mechanics approach is introduced and the determination of the necessary material constants required for the damage equations is discussed. The high temperature uniaxial fatigue tests documented in Chapter 5 are also accurately modelled using FE analysis, for all the load cases used during the testing, for both the butt-welded and non-welded specimens. The modelling technique is validated by comparing the FE-calculated strain results with the measured test results. A Smith, Watson and Topper (SWT) strain range parameter is introduced for fatigue life assessment.

In Chapter 7, a life assessment case study of a welded feature in a generic spoke structure, using 3D quasi-static elastic-plastic and creep FE analyses, is presented. The effect of including a weld (i.e. welded material) in a critical region is investigated for both constant (creep) and cyclic (fatigue) loading conditions at 620°C. Creep damage and SWT strain range parameter lifing methods are used, based upon the material properties and lifing validation discussed in Chapter 6.

The conclusions drawn from this work, along with suggestions for possible further work, are presented in Chapter 8.

Chapter 2

Literature review

2.1 Introduction

This literature review is mainly concerned with welding, the residual stresses and distortions it produces and their mitigation, process modelling of welding (with a focus on computational application) for the prediction of residual stress and distortion, and it concludes with a section on INCONEL 718 (IN718), the material used exclusively throughout this thesis. Welding and the understanding that can be attained by modelling the process are very important fields in engineering. In particular, the history of published research on the prediction of weld residual stresses and distortions is a very interesting topic since it covers early analytical models right through to present day numerical models that make use of advanced finite element (FE) techniques. In fact, two of the most common commercial general-purpose FE software packages (MARC and ABAQUS) have origins in work on the modelling of welding by Marcal and Hibbitt [5] (respective founding developer of MARC and co-developer of ABAQUS).

A vast amount of work is still ongoing around this topic, and the new knowledge gained and the techniques developed are providing a great benefit to the engineering community. The overall aim behind the work presented in this thesis was to gain and apply an understanding of the mechanical effects of welding, in order to mitigate distortions that had previously hampered uniaxial testing of tungsten inert gas (TIG) butt-welded, thin rectangular section IN718. Once this aim was achieved, better test data could be obtained, leading to more reliable material data for IN718 welds, which could be used for more accurate lifing predictions, at high

temperature in particular. Therefore, it is also appropriate that this literature review should also cover previous research around IN718. Any other background or theory is introduced during the thesis where necessary.

2.2 Welding: residual stresses and distortions

Welding is a well-known fabrication process that joins materials, usually metals or thermoplastics, by causing coalescence. Welding is defined by the American Welding Society (AWS) as a localized coalescence of metals or non-metals produced by either heating of the materials to a suitable temperature with or without the application of pressure, or by the application of pressure alone, with or without the use of filler metal [6].

During the first half of the 20th century, welding began to replace bolting and riveting in the construction of many types of structures, including bridges, buildings, and ships. This change came mainly to meet the urgent demand for steel ship production during World War II [7]. Welding has now become a standard process in the construction, automotive and aircraft industries, and in the manufacture of machinery. Along with soldering and brazing, it is essential in the production of virtually every manufactured product involving metals.

Essentially, welding is a fabrication technique that bridges the divide between materials production and component assembly. Unfortunately, this means that the process can have an adverse effect on material properties and often the careful optimisation of base metal properties and processing are wasted due to failures initiated from welded joints. Poor welding practice can lead to the production of notches and other stress concentrators that increase the likelihood of failure in and around a joint. Once solidified, the weld metal grain structure usually consists of a grain size and class different

to that of the base material, and grain growth occurs in the heat-affected zone (HAZ). Consequently, the yield strength may be significantly different in the weld from that of the base metal.

Since welding is an integral manufacturing procedure for many engineering and structural components, its effects have a direct influence on the integrity of such components and their thermal and mechanical behaviour during service. Due to the high temperatures introduced and the subsequent cooling of the welded metal, welding can produce undesirable residual stresses and deformations. The process-generated residual stresses significantly affect stress corrosion cracking and hydrogen-induced cold cracking in welded steel structures, and can also promote brittle fracture and reduce the fatigue life [8, 9]. In some cases, the welding residual stresses may give a larger contribution to the total stress field than the stresses caused by the service loads themselves [10]. Furthermore, the residual stresses interact with the weld-induced deformations and this can produce large distortions in thin-section structures. These distortions may lead to misalignment of structural members and can significantly alter the behaviour of the structures when loaded, thus compromising their structural integrity and invalidating any lifetime predictions deduced from undistorted components. The welding process itself can even cause buckling, which is a common problem experienced when welding stiffeners to thin section panels used in the ship building industry [11]. Postweld reduction and rectification of weld-induced residual stresses and distortions can require time consuming and expensive procedures such as flame straightening, and in some cases, attempts at these may fail and the component may not be fit for service and have to be scrapped. It is for reasons such as those mentioned here, that it is an engineering obligation to obtain a good understanding of

weld-induced residual stresses and distortions present in structural components, and how best to reduce their prevalence.

Information about the residual stresses in a component after welding is of great interest in order to improve quality and to prevent failures during manufacturing or in service. Residual stresses can also be used as input for lifetime prediction. In principle, there are three types of investigation that can be applied to determine the residual stresses present in a component: Firstly, experimental procedures such as hole drilling or X-ray diffraction can be employed; secondly, analytical descriptions of residual stress development can be used to produce a quantitative estimate; and finally, numerical methods can be used. Hereby, welding process parameters and different fixture set-ups can be evaluated without performing a large number of experiments by the use of a virtual model or simulation.

Various measurement techniques have been developed for measuring residual stress; these techniques are either non-destructive or locally destructive. The former include X-ray diffraction, neutron diffraction and magnetic or ultrasonic methods; the latter include mechanical means such as hole drilling and layer removal methods. However, since in all cases experimental errors are inevitable, there will exist always an uncertainty associated with the measurement results [12].

Numerical methods are becoming increasingly popular for residual stress determination and are advantageous since complex phenomena such as metallurgical effects (e.g. phase transformation) can be included and the results obtained directly compared to the results of experimental residual stress measurements [13].

For many cases, the residual stresses produced during welding can be measured experimentally with fair accuracy, but is not possible to alter the conditions and determine the resulting change in the internal stresses without repeating the entire procedure [14]. In addition, the complexity involved in the measurement of residual stresses and difficulty in obtaining detailed three-dimensional stress maps, have led to an increasing use of numerical simulation for the estimation of the residual stresses that result from welding. Through numerical parametric studies, it is also possible to identify optimal process variables, thereby minimising the use of postweld stress relieving procedures [15]. In addition, it is worth noting that numerical simulations can be used to evaluate the 'weldability' of an alloy [16]. This includes the requirements placed upon the fabricated weld during service, the deformation and residual stresses produced by welding and the occurrence of defects resulting from the welding process. Historically, the evaluation of weldability has mainly been through the manufacture of test welds, this is a time consuming and expensive process. By using numerical welding models, the amount of such experimentation can be minimised. Although numerical modelling eliminates some of the errors and uncertainties associated with experimental measurements, it may introduce other errors due to limitations in the input data or modelling assumptions. The best approach for reliable determination of residual stresses is by a combination of measurements and modelling [17].

2.3 The prediction of weld residual stresses and distortions: A brief history of published research

Deng *et al.* [18] explain that several factors may contribute to the formation of residual stress and distortion: The plastic deformation generated by welding is a function of structural, material and fabrication parameters. The structural parameters include the joint type and the dimensions of the

welded material. The material parameters reflect the metallurgical condition of the material and the fabrication parameters include the welding method, heat input and the restraint condition. In order to correctly predict weld residual stresses and distortions, the significance of each of the above factors needs to be known so that models can be developed that are both accurate and least demanding in terms of time and computer capability (i.e. simplified and not overcomplicated with largely insignificant features).

Historically, addressing the fundamental physics and mechanics underlying the development of weld-induced residual stress and distortion used rather crude analysis procedures by today's standards.

As suggested by Dong and Brust in their review [19], perhaps the first attempt to predict the residual stresses generated by welding was carried out by Rodgers and Fletcher in 1938 [14] using an analytical approach for butt-welded plates, employing linear shell theory with both measured and calculated temperature history for the thermal loading. The time-incremental residual stresses ($\Delta\sigma$) in the direction parallel to the weld are derived from thermal strains, and consist of a compressive stress generated by the cooler surrounding material plus a uniform tensile stress arising from the thermal expansion of the considered transverse cross section as a whole, as follows:

$$\Delta\sigma = E\alpha \Delta T(x) + \frac{1}{w} \int_{-w/2}^{+w/2} E\alpha \Delta T(x) dx \quad (2.1)$$

where E is Young's modulus, α is the coefficient of thermal expansion (both of which are considered to be constant over the increment), and ΔT is the temperature change during the time increment, which varies only in the x -

direction, across the width of the two welded plates (w). At the end of each time increment, the calculated residual stresses are superimposed on the previous stress distribution and the system is brought into equilibrium by superimposing the force necessary to produce uniform straining of the plate, the assumption being that all cross sections normal to the weld line remain plane.

A number of other correlative models based on experimental and/or analytical solutions were developed from the late 1930s through to the early 1970s to predict welding distortions and residual stresses (most notable are those by Rykalin, Tall, Okerblom and Masubuchi, see [7] for details). These approaches were quite novel and often provided reasonable predictions when compared with experimental measurements, but were often limited to single pass welds [19]. However, the fundamental understanding gained through these simple analytical solutions and systematic experimental investigations, gave a great deal of insight into the mechanisms underlying residual stress and distortion development. As discussed in the book by Masubuchi [7], it was established that longitudinal residual stresses (those parallel to the weld, σ_l) tend to be invariant (and often reach or exceed yield point, σ_y) along the weld except at its initiation and termination (Figure 2.1). In contrast, the transverse residual stresses (those perpendicular to the weld, σ_{tr}) were found to exhibit a strong dependence, both in terms of distribution and magnitude, on factors such as welding procedures, joint geometry and restraint conditions (Figure 2.2). Such observations led to a series of innovative developments on controlling or mitigating some of the detrimental effects of residual stress and distortions on welded structures, examples of which are discussed later.

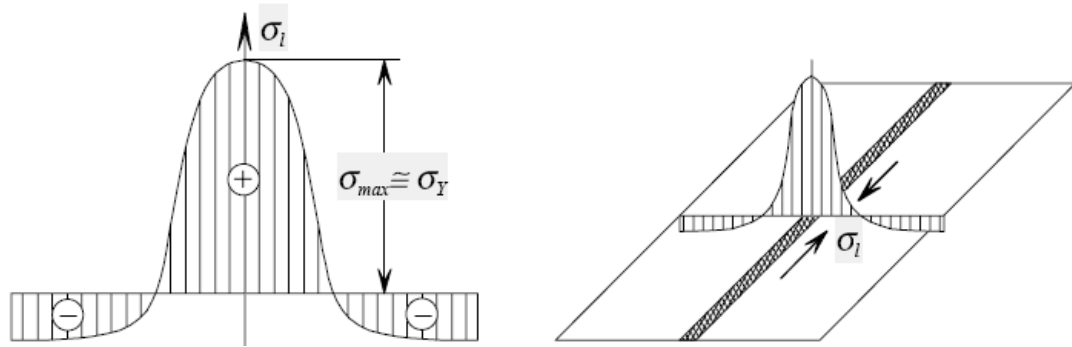


Figure 2.1: Typical longitudinal residual stress profile due to welding [20]

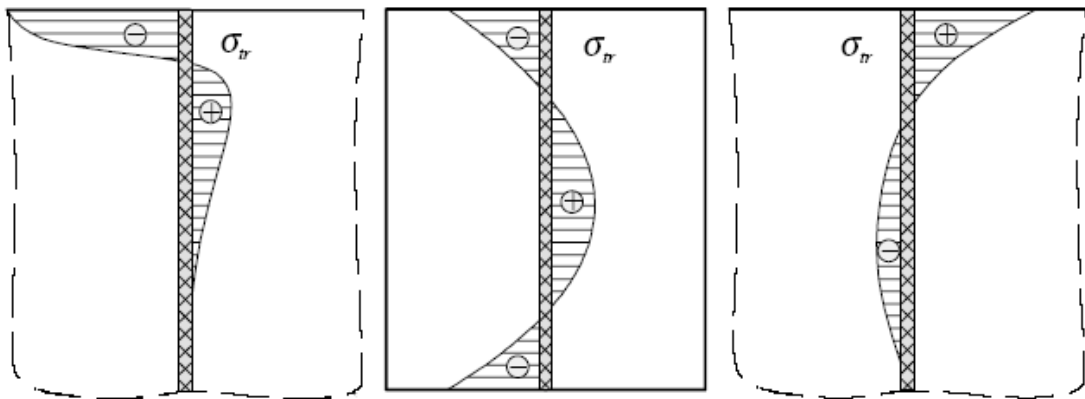


Figure 2.2: Example transverse residual stress profiles due to welding [20]

The analytical approaches were replaced by more flexible numerical approaches in the early 1970s as the versatility and capability of the finite element method (FEM) was realised. This numerical method is particularly suited to modelling the welding process since it is readily adapted to include both geometric and material nonlinearities [5]. As discussed by Friedman [21]: The complexity of performing analytical studies of welding stresses and distortions for various weldment configurations, when considering factors such as transient multidimensional temperature distributions, effects of weldment fixturing and surround structure on heat sink and constraint characteristics, and realistic models of inelastic material behaviour in the vicinity of the weld line, among others, suggests the use of numerical methods of analysis –in particular, the widely adaptable finite element method– for predicting transient and residual stresses and distortions.

Ueda and Yamakawa in Japan (1971) [22], Hibbitt and Marcal (1973) [5] and Friedman in the USA (1975) [21] published some of the earliest finite element (FE) models developed for predicting the residual stresses and distortions induced by the welding process. These models contained necessary simplifications due to the lack of computing power available, and two-dimensional (2D) planar analyses were most commonly performed with sections normal to the weld direction, under *quasi-stationary* thermal conditions. However, the early numerical models did include features that were often previously unaccounted for such as temperature-dependent material properties, through thickness temperature variations, irregular weldment geometries and nonuniform heat source distribution, all of which the purely analytical models struggled to cope with. Although full three-dimensional (3D) analyses would have been even more beneficial, the numerical techniques developed initially yielded valuable data that had previously been unobtainable. Several researchers (McGuire and Groom in 1979 and Brust *et al.* in 1981) at the Centre for Welded Structures Research, Battelle Memorial Institute, USA, extended the early models to account for multiple pass welds and additional features such as material re-melting and annealing, phase changes and heat sinks [19]. While originally developed to predict weld-induced transient and residual stresses and distortions, the nature and characteristics of the numerical thermal models used in the analyses enabled their use in predicting cooling rates, peak temperature distributions, changes in metallurgical structure and effects such as fixturing [21], underlining the importance of their conception.

In recent times, weld process models have been extensively developed and improved, and are being used by several different organisations throughout the world. A very good literature review, modelling background and recent published applications of computational welding mechanics, can be found in

Lindgren [23]. As general-purpose commercial FE codes have become readily available during the last few decades, the use of such codes for residual stress analysis has become highly desirable. This is mainly because procedures based on commercial codes are readily transferable to industrial applications and are easily modified to suit specific cases of interest. For example, there are now a wide range of add-on packages available for use with the commercial FE codes to model features such as crack propagation (e.g. Zencrack, Zentech International Limited) and complex processes such as heat treatment (e.g. DANTE, Deformation Control Technology, Inc.). SYSWELD (ESI Group) is a stand-alone multiphysics engineering package and claims to be the leading tool for the simulation of heat treatment, welding and welding assembly processes.

Although the ever-increasing power and capability of computer systems means that detailed, full 3D computational simulations are feasible to some extent, they require a large amount of data input. For example, thermophysical and mechanical temperature-dependent properties, and any changes due to phase transformation are necessary, and these are not straightforward to obtain experimentally. Even with adequate input data, simplifications are often still required to overcome numerical problems and non-convergence, and the models can be very computationally expensive. It is with the aim of alleviating some of the problems mentioned here, that drives ongoing research into simplified models for distortion prediction and mitigation (see [24-29]). An overview of some commonly used “computationally efficient models” is presented in the paper by Camilleri *et al.* [30]. These models attempt to keep computation times within a reasonable industrial time frame and to minimise the amount of data input required. Whilst still satisfying these aims, the models should be able to

provide adequate information for the welding engineer in the design stage, enabling design optimisation long before fabrication is due to commence.

2D simplified models concentrate on the thermal contraction of a transverse plane strain slice during cooling after the welding torch has passed (Figure 2.3); 3D models are able to include the length of this region.

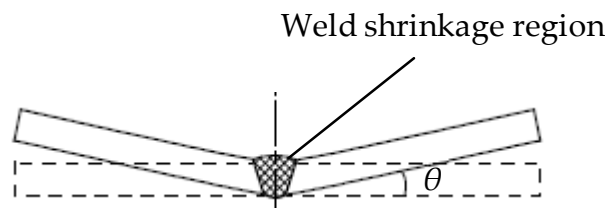


Figure 2.3: Two-dimensional plane strain section showing nonuniform shrinkage region and resulting angular distortion, θ

Using this simplified method, the need to determine a complex transient temperature field and any complicated features such as microstructural changes are eliminated, and often a uniform initial melting point temperature is prescribed to the weld, circumventing the need for any spatial-dependent temperature history input. It is reasonable to assume that only a small shrinkage region needs to be considered since the surrounding temperature gradients are high and the extreme temperatures that are required to cause significant plastic deformation during the cooling phase are confined to the local area in and around the weld. Therefore, the computation and data input times are reduced significantly and large, highly complex welded structures can be modelled within a reasonable time frame [24]. Neglecting the heating phase can be justified since when the material in the shrinkage region melts, it enters what some researchers call the mechanically molten state, in which all stresses are relaxed (or annealed). Only when the material cools is it able to regain its stiffness and produce the residual stresses and distortions that are of interest. Since the transverse

width of the weld fusion zone typically varies across the thickness, the contractions in the shrinkage region are nonuniform and so cause angular deformation. The contractions are resisted by the surrounding cooler material, and this results in the formation of residual stresses, some of which are accommodated by the distortions until equilibrium is achieved. A simplified analytical approach can be used to predict the local deformations, and the resulting thermo-elastic-plastic (i.e. thermoelastic-thermoplastic) algorithms can be incorporated into larger elastic FE models [25].

Because welding is a transient process, the cooling of the welded material does not occur simultaneously at all positions along the weld (see Figure 2.4).

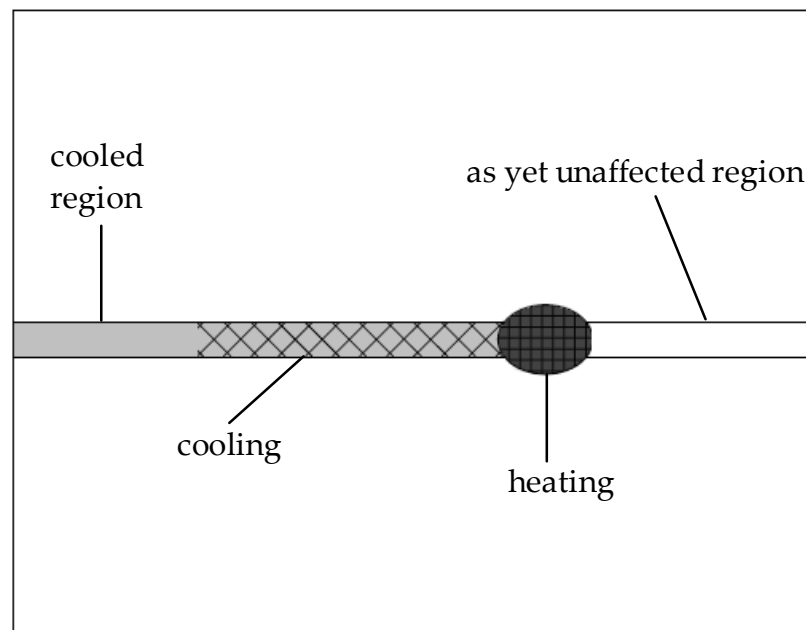


Figure 2.4: Distinct regions of thermal activity during transient welding

The regions closer to the start of the weld cool and regain their stiffness while the regions further along the weld line are still molten. Similarly, when the regions further along the weld line cool and regain their stiffness, the regions preceding them will already have cooled and will therefore restrict the

shrinkage of the cooling regions. This effect cannot be considered in a standard 2D model but it can be included in a 3D model by prescribing a spatially-dependent temperature history. The challenge when developing simplified weld simulation models is to capture all of the effects mentioned above without resorting to more computationally expensive and user intensive nonlinear thermal and elastic-plastic FE analyses.

Other recent efforts have been made to reduce the computation time for large-scale FE welding simulations. For example, Nishikawa *et al.* [29] use an interactive substructure method for a 3D analysis of a Hastelloy-X engine component, where the model is split into one strongly nonlinear region around the heat source and a weakly nonlinear region elsewhere (Figure 2.5). This method only requires calculation of the inverse stiffness matrix at the start of the analysis unless the stiffness changes significantly. Therefore, the rest of the computation is reduced to the small-scale strongly nonlinear region, which moves with the heat source.

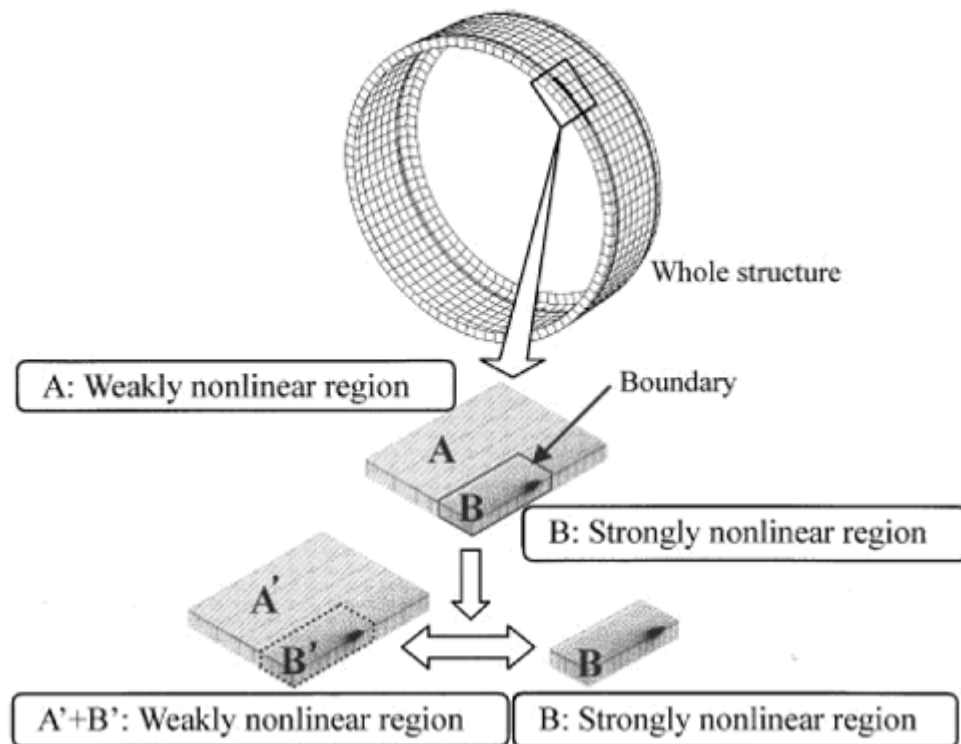


Figure 2.5: Iterative substructure method [29]

Adaptive and dynamic types of remeshing are other techniques that can be employed to allow a fine mesh around the weld source to move during the analysis while a coarser mesh is used elsewhere, thus maintaining solution accuracy but reducing computation time (Figure 2.6 and Figure 2.7). The difference between adaptive and dynamic remeshing is that in the former, the global mesh is automatically updated (i.e. refined in some regions and coarsened in others) depending on the solution obtained during each time increment, whereas in the latter, the mesh design (e.g. refinement) remains unaltered but the location of the fine region moves throughout the model. Inherent shrinkage strain models have also been developed in which firstly, thermal elastic–plastic analyses are used to estimate inherent deformations for different typical welding joints. Then these deformations are applied to an elastic analysis to predict welding distortion for large welded structures based on the obtained inherent deformations (see [31] for example).

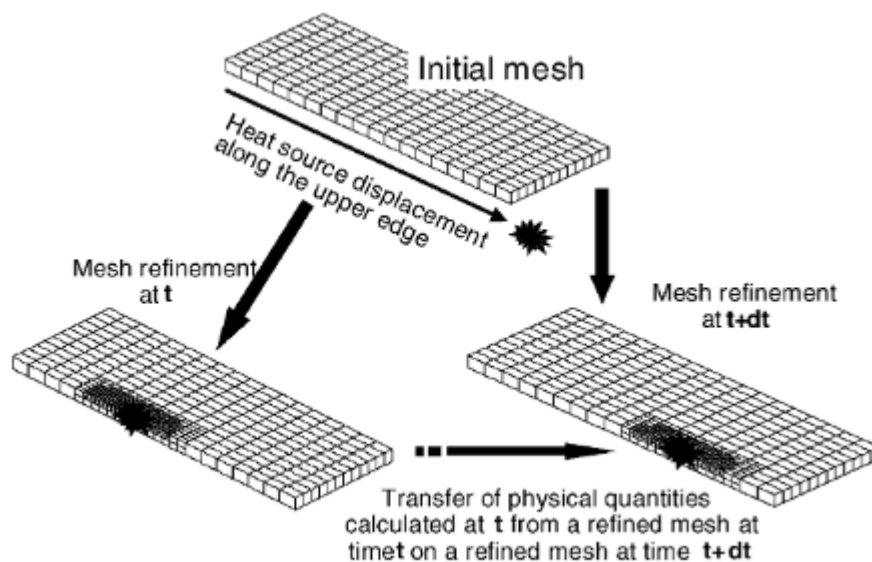


Figure 2.6: Adaptive remeshing procedure [32]

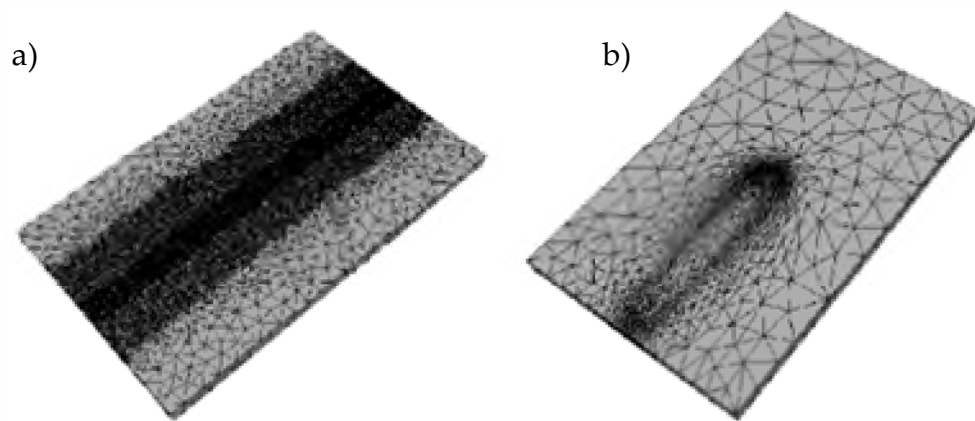


Figure 2.7: Adaptive remeshing example (from [33])
 a) reference mesh b) adapted mesh

2.4 Residual stress and distortion mitigation

As emphasised by Mollicone *et al.* [26]: For a given material and structural configuration, the magnitude of distortion depends primarily on the specific thermal energy input of the welding process (the energy per unit length of weld). Significant reductions cannot therefore be made without changing to a welding process with less heat input and this may not always be practicable. With this point in mind, residual stress and distortion mitigation techniques were developed and employed to try to make the best reductions possible without changing the welding process.

Possibly the earliest use of residual stress mitigation techniques focussed on ship structures, and was performed by Greene and Holzbaur [34] in 1946. They reduced welding-induced residual stresses by applying a controlled temperature field in two strips parallel to a longitudinal butt weld. This imposed temperature field exerts an equivalent tensile overloading (thermal tensioning) effect on the weld region, reducing longitudinal residual stresses once the weld cools back down to room temperature [35]. The temperatures required within the heated strips were typically below 400°F (204°C) in applications performed under ambient room temperature conditions. The

key element in this technique is that the direction of the thermal stresses induced by the imposed local heating is the same as that of the weld residual stresses that are to be reduced (e.g. longitudinal in this case).

Most of the recent residual stress and distortion mitigation techniques, although developed much later and optimised using numerical methods, can be viewed as variations of the principles defined by Greene and Holzbaur [34]. For example, backlay welding (BW) was developed by Brust and Rybicki in 1981 [36] for mitigating tensile residual stresses on stainless steel piping weld inner surfaces, where intergranular stress corrosion cracking was a major concern for the nuclear power industry during the 1970s and 1980s. BW consists of heating the circumferential weld region by depositing one or more layers of axial welds along the outer surface of the pipe. A model was implemented that made use of closed form analytical solutions to construct accurate high-speed weld thermal analysis procedures that had been developed for finite thickness (including thin) plates. Work such as this probably represented the first industrial application of a weld process model to solve a manufacturing problem and some of the early models are still used in many industries today [19].

As numerical procedures became more elaborate, so did the residual stress and distortion mitigation techniques. Critical controlling parameters were established, for example, Low Stress No Distortion (LSND) welding was conceived and published in 1994 by Guan *et al.* [37]. This technique introduced a trailing heat sink for welding thin gauge aluminium alloys and the method was conceptualised in 2006 by van der Aa *et al.* [38]. A further extension of this concept is to mechanically stretch the weld on cooling using rollers; this can eliminate both residual stresses and buckling distortions [35]. Mechanical and thermal tensioning can be used to avoid triggering buckling

modes [39, 40] and similarly, thermal compression (cooling with a trailing heat sink) can be effective in preventing hot cracking [41].

2.5 Numerically modelling the welding process

Modelling the welding process can be a tedious and nontrivial task due to the complex nature of the process, which involves several physical phenomena. A fully detailed process model would need to include: accurate temperature history input or calculation (heat flux and boundary conditions), temperature-dependent material properties, addition of filler material (if any), mechanical effects such as distortion and clamping (if any), metallurgical transformations during heating and cooling phases, melt pool phenomena such as fluid flow and electromagnetic forces, chemical interaction with shielding gases etc.. In order to reduce the demands of modelling such a complicated process, some simplifications are necessary. Fortunately, most models can be simplified without loss of accuracy since if the material is homogenous and the geometry and welding heat source (and therefore temperature distribution and thus stresses and distortions) are symmetric about the weld centreline, then only half of a weldment need be modelled.

The modelling of welding phenomena can be achieved using two distinct approaches, the choice of which depends on the resources available (time, expertise and tools), the scope of the investigation and the particular phenomena of interest [42]. Firstly, it is possible to focus on the complex fluid and thermodynamics local to the weld pool and the heat-affected zone; and secondly it is possible to model the global thermomechanical behaviour of the welded structure. In the first approach, the governing equations of fluid flow and heat transfer (i.e. the conservation of mass, momentum and heat, together with the latent heat of fusion and surface boundary conditions)

are used to define the thermodynamics of the weld pool. Significant progress has been made in modelling the size and shape of the weld pool based upon a consideration of the arc and fluid physics (see [43] for example). However, these models are highly complex, currently commercially unavailable and require sensitive parameters such as molten metal surface tension that are difficult to measure. Therefore, in practical industrial terms, the first approach is of limited use. In the second approach, a simplified heat source model is employed with heat transfer by conduction only. A variety of heat sources can be used for the simulation of welding and, as shown as early as 1973 by Hibbitt and Marcal [5], the accuracy of the model is totally reliant on the parameters which describe the weld pool size and shape. These parameters can be obtained from a combination of experimental and calculated data and mainly depend upon the welding process employed and the material that is being welded. Taylor *et al.* [42] use both approaches with the aim to estimate and verify the parameters associated with the simple heat source models in order to achieve consistency with the predictions of the thermodynamical approach. With this aim satisfied, it is then possible to transfer thermal data between analyses of the weld pool and the welded structure via the model parameters.

Numerical models are generally used for the purposes of process simulation or process understanding. However, these two requirements place differing demands on the modelling strategy. Whilst process simulation typically implies a quick, largely interactive and approximate approach, process understanding requires the model to duplicate closely the complex physics of the process. Attempting to model the complex physics of welding (the interaction of the heat source with the weld pool) to the maximum possible detail constitutes an 'unintelligent solution' when one is interested in the

global mechanical effects of welding, particularly since the distribution of pressure from an arc source and the precise effects of surface tension, buoyancy forces and molten metal viscosity are difficult to quantify and interpret. Whereas the intelligent approach is to model only the dominant parameters that influence weld behaviour in a given process. The selection of a particular modelling approach is, therefore, critically dependent not only on the desired output accuracy but also on the required solution time and the anticipated model complexity [24].

Taylor *et al.* [42] also point out, if the heat source is moving at a constant velocity then the temperature distribution can be assumed stationary with respect to a moving coordinate system, whose origin coincides with the point of application of the heat source [21]. This is termed the Eulerian or heat source frame. In this frame, it is only necessary to model a transverse section of the structure, which can be achieved by applying a generalised plain strain boundary condition in the welding direction and by using the simplified heat source model. This implies that all sections normal to the weld line remain plane during the entire welding process. However, the mechanical analysis only rarely reduces to a steady-state problem, and often it is the starting and stopping transients that are of interest. For the analysis of these effects it is the Lagrangian frame, where the heat source is moving, that is the most appropriate [44]. The Eulerian frame is more suitable when modelling the localised fluid dynamics of a weld pool associated with a moving heat source [42].

The characterisation of heat transfer in the weld puddle itself is a formidable problem. Unless the mechanisms of heat flow in the puddle are known accurately, only estimates of the molten metal thermal characteristics can be made by specification of appropriate values of conductivity and specific heat

to be used in the FE analysis. It is realistic to increase the effective conductivity of the molten material in order to simulate the heat transfer mechanisms in the puddle, and thus lower the molten weld metal temperatures than those otherwise predicted. Material properties are often extrapolated for temperatures beyond those that measurements have been recorded for, the adequacy of the assumptions made are of course open to question, and only the experimental determination of the required high temperature data can serve to test their validity [21].

As mentioned briefly above as a way of simplifying weld process modelling, two-dimensional (2D) models analyse sections normal to the welding direction. The plane section normal to the direction of travel of the welding heat source is assumed to be in a state of plane strain. This implies that motion is completely restrained in the weld, or longitudinal direction, therefore, all sections normal to the weld line remain plane during the entire welding process. Though this assumption is probably adequate in regions somewhat removed from the weld puddle, it may not be valid in the neighbourhood of the molten metal. This approach therefore prevents calculation of distortions ahead of the welding arc, and may inhibit accurate computations of deformations in the immediate vicinity of the weld puddle. It nevertheless enables the essential features of the mechanical response during cool-down to be modelled, and the resultant residual stresses and distortions in the plane to be calculated [21]. The weldment is completely free to expand and bend in the transverse direction, and so the transverse bending (angular) distortions that are characteristic of thin weldments can be illustrated using 2D models. However, the plane strain approach used in the 2D models prevents characterisation of the longitudinal cambering mode of distortion that is also commonly found in thin weldments (Figure 2.8). A 2D generalised plane strain model ([45]) can consider the effects of longitudinal

extension and cambering. This approach relaxes the plane strain requirement by allowing the longitudinal strain to follow a linear function of longitudinal extension and rotation about the plane strain axes.

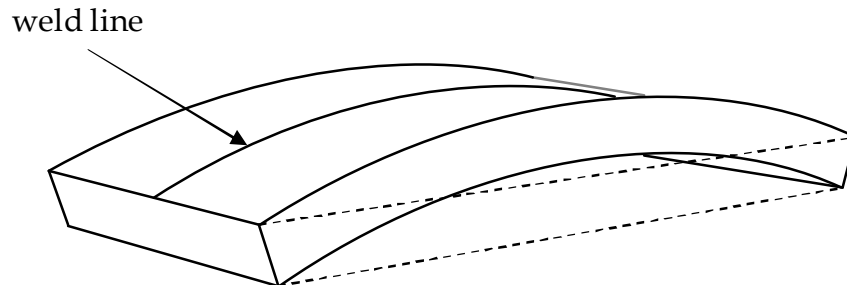


Figure 2.8: Cambering distortion

Two-dimensional models are useful if the approximation is valid. They require a steady state/homogenous temperature field where each cross section has the same thermal history (which will give a homogeneous residual stress field). This is true in the case of thick plates or thick walled pipes with low (i.e. negligible) conductivity ahead of the heat source, or in high speed welding, where heat does not accumulate ahead of the source, which would otherwise result in an increase in peak temperature along the weld (i.e. a varying temperature profile) [46]. Therefore, 2D models are not always suitable for thin plate welding since in a 2D plane normal to the welding direction, the heat flow in the direction of welding is neglected.

2.5.1 Simplified welding heat source models

In order to predict the development of residual stress and distortion, along with any metallurgical changes that may occur during welding, a temperature-time history is required. Theoretically, if both the thermal process and the response of the welded material to this process are known, predictions are possible. Therefore, a significant amount of research has

been undertaken with the aim of producing suitably accurate temperature-time histories. Some of the most notable simplified welding heat source models that have been used to generate such data are discussed in this section.

Most of the earliest analytical treatments of temperature transients during welding assumed that the effective thermal energy supplied by the heat source was deposited in such a narrow band of material that it might be idealised as a point or a line source, depending on the geometry of the weld [21]. One of the pioneers of the classical point or line source solution was D. Rosenthal.

In the mid to late 1930s (and more widely published in English during the 1940s), Rosenthal [47, 48] applied the basic theory of heat flow developed by Fourier to a moving heat source model in order to calculate the temperature distribution resulting from heat flowing from a welding torch into and throughout a welded part. Rosenthal [47] defines the state of a welded piece where the welding is performed over a sufficient length as *quasi-stationary* (or quasi-steady, i.e. steady-state with respect to a moving coordinate system): To an observer stationed at the source of heat input during welding, no change in the temperature distribution around the heat source will be noticeable. The temperature distribution will move along the surface of the welded piece without changing in intensity, size or shape. Consequently, the traces left on the surface by different isotherms will become straight lines parallel to the direction of welding. The zones of different colour that form on a work piece during welding clearly show the establishment of the quasi-stationary state. The different colours indicate the maximum temperature reached in a given zone, and these zones become parallel to the direction of welding when the thermal state is quasi-stationary (Figure 2.9).

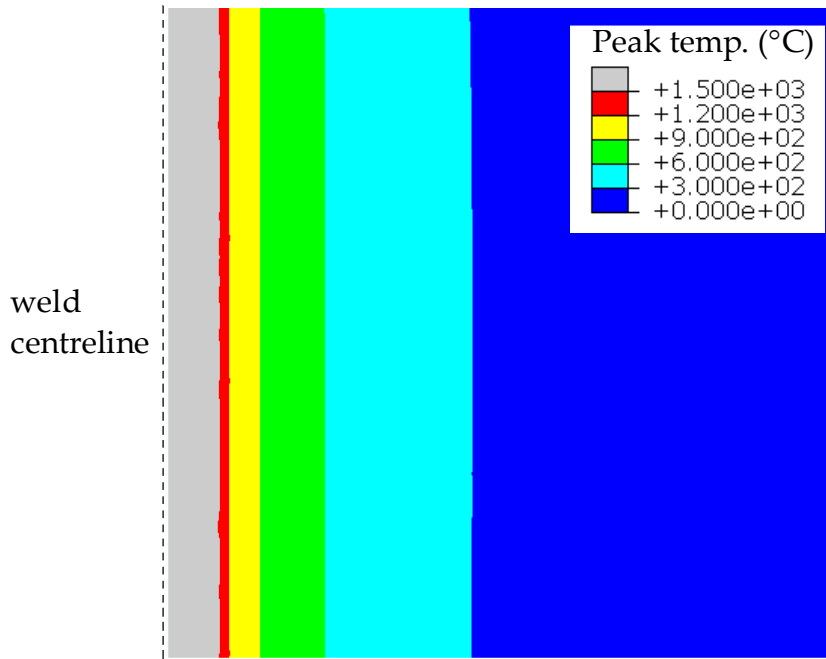


Figure 2.9: FE predicted peak isotherms
(details of the FE modelling can be found in Chapter 3)

Although inaccurate in the regions closest to the heat source, due to the use of a point or line source that assumes an infinite temperature at the point or line of application, Rosenthal's solution can yield quite accurate results elsewhere [46]. In addition, since the temperature and heat flux is assumed infinite at the source, the temperature distribution obtained has many similarities to the stress distribution around a crack tip in linear elastic fracture mechanics. Therefore, many of the FE techniques developed for fracture mechanics can be readily adapted to the Rosenthal model and by using a numerical method, some of the limitations inherent in the analytical method can be overcome.

In 1969, Pavelic *et al.* [49] suggested that the welding heat source model should follow a given distribution to account for the significant amount of heat that transfers from the arc to the material without passing through the molten zone. A radially symmetric Gaussian (or normal) surface distribution of flux was proposed and this was subsequently expressed in a coordinate

system that moves with the heat source by Friedman [21], for thermomechanical FE analysis of the welding process. Although more input data is required because of the empirical approach used to predict the size and shape of the weld pool, significantly better temperature distributions were calculated in the fusion and heat-affected zones with Pavelic's 'disc' model than those computed with the Rosenthal model. Distributed heat source models are also able to capture through-thickness variations in temperature distribution as opposed to a vertical line source of heat, which yields no thickness variations whatsoever. The localised temperature nonuniformity that occurs during welding drives the variation of shrinkage through the thickness during cooling, and thus causes the characteristic bending distortions, which are accompanied by a nonuniform accumulation of plastic strain in the weld metal and heat-affected zones [21].

An extension of Pavelic's model was put forward by Goldak *et al.* in 1984 [46]. The authors suggested that the heat should also be distributed throughout the depth of the molten zone to reflect more accurately the digging action of the arc. A nonaxisymmetric three-dimensional heat source model was proposed, taking the form of a 'double ellipsoid'. This model is more accurate, based on molten zone observations, and more flexible than its predecessors –which in fact are special cases of this model– and is still in frequent use today. With the added depth dimension, both shallow and deep penetration welds can be accommodated, in addition to asymmetrical situations that were now possible, and the ability to vary the temperature distribution in front and behind the heat source. The latter was desirable since it was discovered that the temperature gradient calculated in front of the heat source using a single ellipsoid distribution, was not as steep as expected and the gentler gradient at the trailing edge of the molten pool was steeper than that measured experimentally. Goldak *et al.* [46] also considered

the complexities of weld puddle distortion and the stirring effect generated by the interaction of the heat source (arc, electron beam, laser) with the weld pool, and developed a volumetric distribution of heat input to take these phenomena into account.

The distributed heat source models are more realistic than point source models due to the distribution of heat input over an area or a volume as opposed to a singular point. However, these models are still a form of idealisation, which is necessary to achieve a simple solution without the need to model the weld pool free boundary position, the applied tractions, and the convective and radiative conditions between the weld pool and the arc.

Since not only the magnitude, but also the distribution of heat input, influences the dimensions of the fusion zone (FZ) and heat-affected zone (HAZ), the cooling rates, peak temperature distribution and the temperature gradients, the choice of heat source model and the parameters used are critical to the accuracy of a weld process model [21].

The volume source developed by Goldak *et al.* [46] was intended to be very flexible in order to accurately capture the variety of temperature distributions that are commonly found during different types of welding. The size and shape of the 'double ellipsoid' can be determined by matching with an observed molten or fusion zone (FZ) (i.e. the region bounded by the melting point isotherm, which is situated at the solid-liquid interface). This method has been repeatedly used by many researchers and can be reasoned since there is little superheating in the molten zone [46], and so the material melting point is the critical temperature in terms of model validation. Likewise, since the accuracy with which a heat source model predicts the size and shape of the FZ is the most stringent test of the performance of the

model, the Goldak *et al.* [46] model has been shown to give the most accuracy when the ellipsoid size and shape is equal to that of the weld pool. Goldak *et al.* [46] also argue that a Gaussian distribution of power density is more realistic physically than constant power density throughout the molten zone since the stirring velocity must decay to zero at the FZ boundary and rise to a maximum at the arc-weld interface. It is also undesirable mathematically to have a large step change in the power density at the FZ boundary since a FE analysis would require a fine mesh in order to converge and obtain accurate results, and this increases the computation expense. However, it should be noted that Dye *et al.* [44] achieved suitably accurate results using a circular source of constant power density for modelling the welding of thin plates. The model suggested in [44] is implemented in the work presented in Chapter 3 of this thesis.

2.5.2 Welding filler addition -element activation

Two different techniques can be used to model the addition of welding filler in a FE analysis: “quiet” elements or “born dead”. When using quiet elements, the filler elements are active during the whole analysis but the stiffness and the thermal conductivity are initially very low so that the “inactive” elements do not affect the rest of the model. With the other method, born dead elements, the elements that are inactive are not part of the system of equations until they are specifically activated. In A. Lundbäck’s thesis [50], the born dead technique is used exclusively. The thermal and mechanical activation is separated to enable the element to be heated up thermally but not contribute to the mechanical stiffness. The criterion when an element is to be activated is set as a distance relative to the position of the origin of the heat source. The plastic strain should be zeroed as long as the element is in liquid phase. Lindgren *et al.* [51] compared the two methods for a multipass welding analysis of a thick plate. They found that both methods

gave very similar results but the method of born dead elements was somewhat more effective with respect to computational cost. Different problems may arise depending on which method is used. Decreasing the stiffness of the quiet elements too much will yield an ill-conditioned stiffness matrix with numerical problems as a result. On the other hand, when using the born dead technique, if the nodes are completely surrounded by inactive elements then these nodes will not follow the movements of the active neighbour nodes. This can result in severely distorted, or even collapsed, elements. Lindgren *et al.* [51] solved this problem using a smoothing technique.

2.5.3 Equivalent plastic strain as an indicator of damage

Equivalent plastic strain characterises permanent deformation and may be used as an indicator of cumulative ‘damage’ in the weld metal (fusion) and heat-affected zones (FZ and HAZ, respectively) during the welding process. The maximum equivalent plastic strain exists at the FZ-HAZ interface (Figure 2.10). This is because plastic straining is greater closer to the weld centreline, since the maximum temperature reached increases as this line is approached, except in the weld metal itself as this region necessarily exceeds melting point temperature and therefore undergoes plastic stain relaxation. Maximum damage is thus expected to occur along the FZ-HAZ interface. The concept of using plastic strain as an indicator of ‘damage’ enables the use of FE analysis for damage assessment as well as for predicting residual stresses and distortions [21].

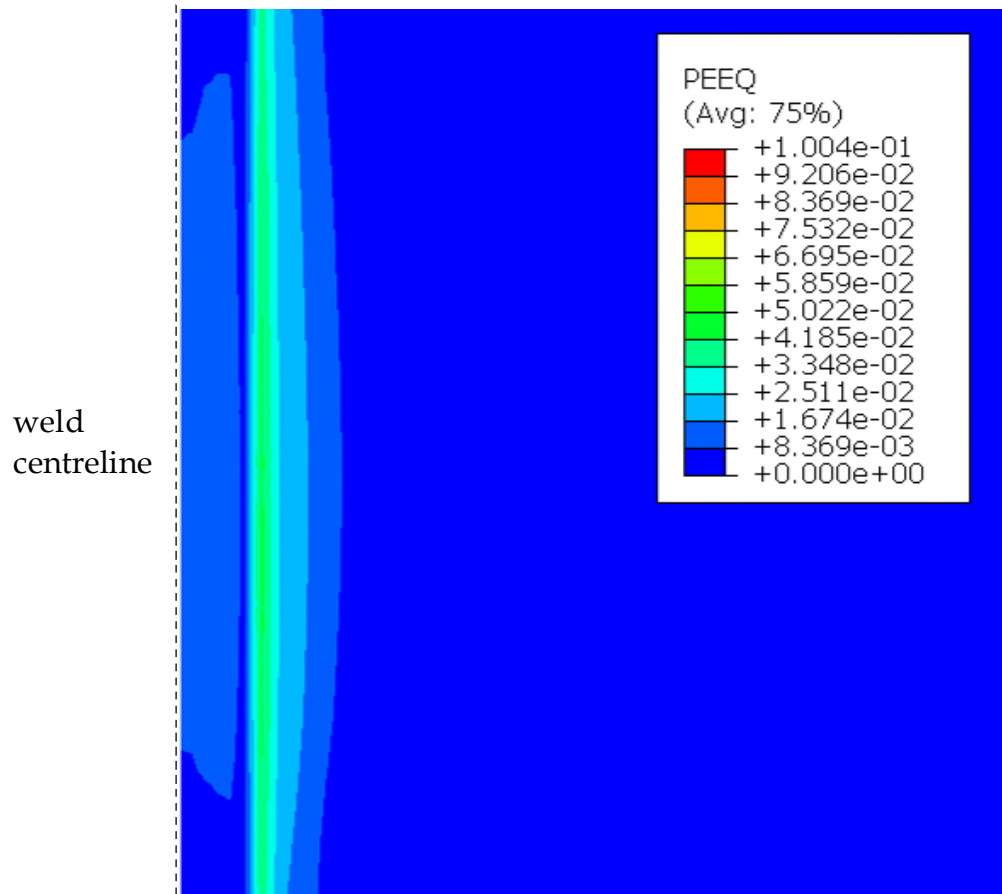


Figure 2.10: FE equivalent plastic strain
(details of the FE modelling can be found in Chapter 3)

2.6 Welding distortion

Distortion problems are often caused at the design stage and may be partially solved during fabrication through experience, or with postweld correction procedures such as flame straightening. Eliminating or mitigating distortion early in the design and fabrication process rather than afterwards will increase industrial competitiveness in terms of both cost and time. Proper understanding of the distortion mechanism and the different types and causes, enables the development of suitable predictive tools and mitigation controls. It is also important to note that improper control may lead to an increase in distortion.

2.6.1 Distortion mechanism

The geometrically nonuniform heating and cooling that occurs during welding causes nonuniform thermal expansion and contraction, which in turn produces transient stress and plastic deformation. The presence of plastic deformation results in the development of residual stresses, which remain after the welding is complete. If the residual stresses are unable to be supported by the structure, they will be necessarily relieved through distortion until a structurally-sustainable stress-state is reached. Therefore, the stiffness of the structure and any imposed restraint conditions are fundamental in governing the global response of the structure, and consequently control the general characteristics of the residual stress field [52]. The lack of supporting material in thin parts and low stiffness of long parts makes them both particularly prone to distortion. Since the heat imposed when welding with a single source cannot be uniformly distributed through the thickness of a weld, the subsequent residual stresses are also nonuniformly distributed; this is the cause of bending or cambering distortion. Essentially, all welding induced distortions are driven by compressive shrinkage forces, which are generated due to the nonuniform thermal loading. Depending upon the distribution of the shrinkage forces and the geometry (e.g. rigidity) and material characteristics of the welded structure, various types of distortion, such as bending, rotation and buckling may take place (Figure 2.11). A combination of these different modes of distortion can cause twisting.

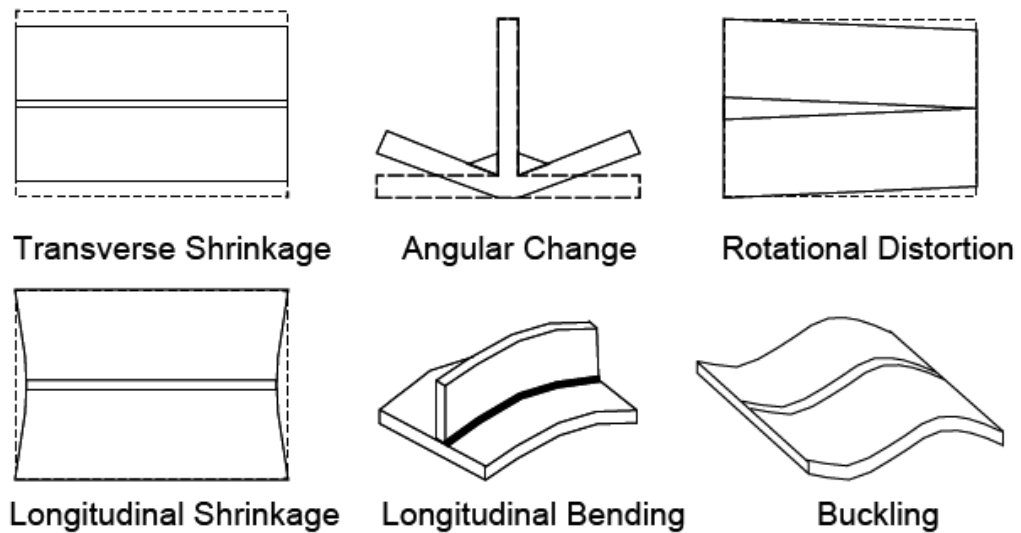


Figure 2.11: Different types of welding distortion ([53])

2.6.2 In-plane shrinkage

One of the fundamental dimension changes that occur due to welding is in-plane shrinkage. This shrinkage takes place in both transverse (perpendicular) and longitudinal (parallel) directions with respect to the weld line. Of these two, the transverse shrinkage is generally of much higher magnitude, and the majority of this shrinkage is due to contraction of the base metal rather than the weld metal itself [54]. The latter point can be justified since the HAZ is significantly larger than the FZ.

Mandal [54] explains that a plate undergoing welding can be divided into two zones, depending on the relative location with respect to the weld line. The zone closest to the weld is called *nearfield* and is considered to be thermo-elastic-plastic; the other zone is termed *farfield* and is considered to remain fully elastic throughout the entire heating and cooling cycle (Figure 2.12). The nearfield is directly affected by the thermal cycle and hence experiences substantial expansion during heating, and contraction during cooling. The surrounding colder (and therefore stiffer) material in the farfield, which is not directly (or at least less) affected by the thermal cycle and therefore does

not undergo significant expansion or contraction, resists the expansion of the nearfield and acts like an elastic restraint. By constraining this expansion, compressive forces are generated and these can be modelled by a set of springs along the nearfield-farfield boundary that store the energy that is exerted by the expansion that is trying to occur. The compressive stress that develops here during heating is supported by tensile stresses over the rest of the welded part, as is necessary for equilibrium. Mandal [54] suggests that the 350°C isotherm is a suitable boundary (for most metals) for distinguishing between the two zones (Figure 2.12). Therefore, thermal expansion of material that reaches a peak temperature not exceeding 350°C is considered negligible.

During the cooling phase, contraction of the nearfield takes place and simultaneously the energy stored in the 'springs' is released, thus increasing the contraction forces. Under the action of these forces, the base metal and the weld metal –initially with reduced yield stress due to elevated temperature– yield and plastically strain resulting in residual shrinkage distortion and thickening of the welded joint. The material in the farfield resists excessive contraction, and as the nearfield cools, it regains its stiffness and is able to support higher stresses. Therefore, after cooling is complete, residual tensile stresses are present in the nearfield with balancing compressive stresses in the farfield.

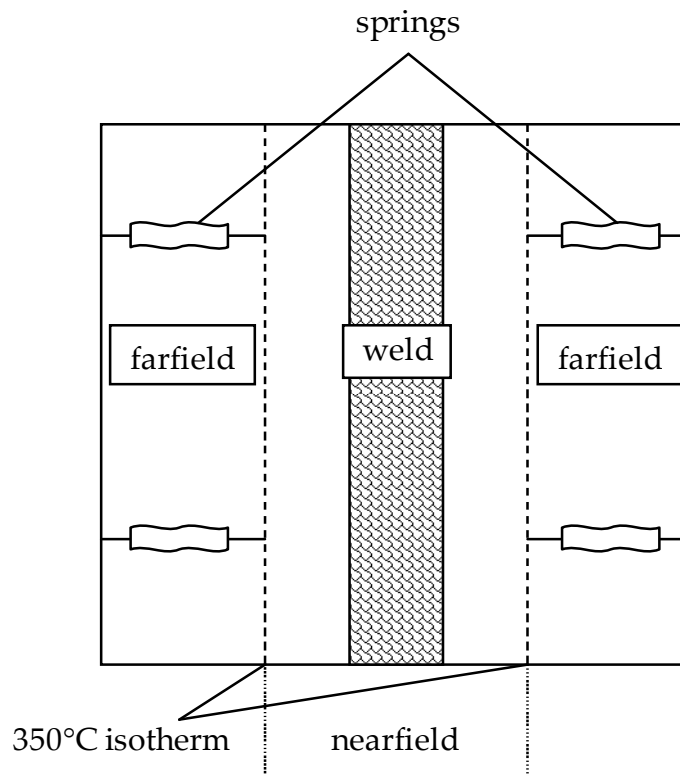


Figure 2.12: Nearfield and farfield zones during welding

The effects of in-plane shrinkage are important since it can cause problems with component alignment and assembly, and it is the driving force behind the other modes of distortion. Unfortunately, by restricting in-plane shrinkage with restraints such as clamps, the residual tensile stresses in the weld are increased and this can cause cracking during the cooling phase, in addition to exacerbating the associated long-term service problems that occur due to residual stress.

Due to the relatively uncomplicated physical basis of thermal distortion, it is possible to use empirically determined formulae for practical predictions (good examples are presented in [54] and [7]). Since the thermal contractions are governed mainly by the maximum temperature reached and the geometry of the HAZ, weld-induced distortions can be related to the heat input (heat energy supplied / welding speed), and the cross sectional area of

the welded part. However, difficulties such as coping with the localised plasticity around the welding heat source, heat losses due to convection and radiation, and the definition of realistic boundary conditions often require simplification or neglect, which results in less accurate predictions.

2.6.3 Angular distortion

Angular distortion occurs due to the bending moment caused by nonuniform shrinkage across the plate thickness, in the regions near the weld line. It is characterised by the angular change that results.

The plastic deformation that occurs due to the nonuniform shrinkage is localised to a small area around the weld; the rest of the part does not deform but merely follows the distortion of the deformed area.

The magnitude of angular distortion clearly depends upon the extent of in-plane shrinkage, which is governed mainly by the maximum temperature reached and the geometry of the HAZ. Therefore, since a square butt joint produces a more uniform heat distribution in thinner plates than a single V groove joint for example, the square joint will yield less angular distortion. In a double V groove joint (achieved by welding from both sides), the heat distribution should be symmetrical about the axis where the two welds meet and so no angular distortion should be produced [54].

It has been observed that maximum angular distortion (e.g. 4-5°) occurs in fillet-welded steel plates of 8-10mm thickness. The reason is that the heat distribution is more uniform through the thickness of a thinner plate, therefore the bending moment is reduced and plates thicker than 10mm have enough rigidity to restrict the angular distortion.

2.6.4 Buckling distortion

In the direct vicinity of a weld, the postweld residual stresses are tensile; self-equilibrating compressive residual stresses develop over the rest of the welded part. Consequently, welding of stiffeners to thin panels (stiffened panels) can cause corrugations that are often observed in bottom or side shells and buckling as the weld cools even before load is applied, if the compressive residual stresses induced exceed the critical buckling stress of the panels. If buckling does not occur during the welding process, the weld-induced distortions and residual stresses will still adversely affect the buckling strength of the structure.

The magnitude of buckling distortion is much greater than the other modes of distortion and there is more than one stable deformed shape. Therefore, it is paramount that buckling due to welding is avoided. The best way to mitigate buckling distortion is to properly select structural parameters such as plate thickness, stiffener spacing and welding parameters. Similar to a beam buckling experiment, there exists a critical buckling heat input for a given test condition. This critical heat input decreases as the plate thickness decreases and the free span increases. Simplified closed-form analytical solutions have been proposed for the prediction of the critical buckling load when welding and some are presented in [7]. However, these solutions are limited to idealised cases and cannot be directly applied to practical instances. More detailed eigenvalue analyses can also be performed to determine the critical buckling load and the buckled mode shape.

The initial, or preweld, stress state can be significant in terms of buckling during welding. Small tensile stresses not only can diminish distortion but can also prevent buckling. Conversely, small compressive stresses cause not only a substantial increase in postweld distortion but also promote buckling.

Both compressive and tensile stresses can form as a result of the sheet rolling process and require adequate mangling for removal. These stresses can also form when parts are forcibly tack welded before being fully welded.

2.6.5 Rotational distortion

During butt welding of plates, the “unwelded” portion of the joint ahead of the torch tends to open or close depending on the welding method. The magnitude of this rotational distortion is dependent upon both the heat input and the welding speed.

Rotational distortion can be avoided by fixing the plates, either by tack welding or clamping. Tack welds are difficult to implement with robotic welding and are usually made manually, which results in additional labour and cost. Often less attention is paid to tack welding and tack welds can produce problems for the full weld. It can be difficult to completely consume the tack weld and this can cause lack of penetration along with other types of weld defect. In submerged arc butt-welding of long and comparatively thick plates, the forces acting on the tack welds can be great enough to break them. The overall impact of rotational distortion is resulting mismatch of the joint.

2.6.6 Distortion control

With the appropriate measures taken, postweld distortion can be minimised. However, improper control may actually lead to an increase in distortion. The simplest way to reduce distortions is to modify the welding process so the heat input is changed. Heat sinks can also be used to quickly remove heat from the welded region. Out-of-plane distortion due to buckling can be avoided by suitably choosing plate thickness and stiffener spacing. Increasing the plate thickness and reducing stiffener spacing effectively increases the critical buckling stress of a panel. For simple structures, the

critical values can easily be calculated to ensure that buckling will not occur for a given set of welding conditions. For complicated structures, more advanced numerical models are necessary, see [55] for example.

Joint mismatch should be avoided since these joints require increased weld metal deposition in order to form a sound joint and therefore distortion will be increased. Elastic prestressing can be effectively used for mitigating angular distortion caused by longitudinal stiffener fillet welds, provided the necessary degree of prebending can be predicted. For example, a plate may be deflected around a round bar and clamped at the edges prior to welding.

Thermal or mechanical tensioning are other techniques that can be used to reduce weld-induced buckling distortion by generating a tensile stress in the weld as it cools. The optimisation of weld sequences can also have a significant effect on distortion.

2.7 Welding processes

The localised heating required for welding can be achieved in several different ways, examples include the use of an electric arc, a gas or plasma flame, an electron beam (EB) or a laser beam (LB). These processes vary in power density and depth penetration. The latter two examples provide high intensity and penetration, producing a characteristic metal vapour keyhole shape through the thickness of the weld. By contrast, tungsten inert gas (TIG) arc welding (also called gas tungsten arc welding (GTAW)) is a relatively low power density process. Consequently, heat is distributed over a larger region and less is delivered to the molten zone, therefore a greater heat input must be used per unit volume of weld (molten) metal. This results in greater heating of the material surrounding the weld, which is

generally undesirable and limits the thickness of material that can be welded in a single pass.

Although both LB and EB processes are extremely fast, and can be easily automated, which makes them highly productive, their primary disadvantages are very high equipment costs (though these are decreasing) and a susceptibility to thermal cracking. In addition, fit up must be precise and locating the parts with respect to the beam must be perfect, due to small distribution of the heat source. EB welding also requires the use of a vacuum in an evacuated chamber since the fast moving electrodes could be rapidly dispersed if they were to collide with air or gas molecules, resulting in a loss of energy. This necessity restricts the use of EB welding compared with arc welding, which is more easily performed manually and in the field. The ability to field repair components greatly reduces overall costs and increases product (e.g. aero engine) availability.

2.8 Tungsten inert gas (TIG) welding

Although many of the topics and the methodologies presented in this thesis are largely independent of the welding method, this work concentrates solely on TIG welding due to industrial considerations. The following background to TIG welding refers extensively to the excellent collection of material in the book, *Welding and Distortion Control*, by Mandal [54], where more details may be found.

TIG welding is an electric arc welding process that uses a nonconsumable tungsten electrode to produce the weld and an inert gas for shielding from atmospheric contamination (Figure 2.13). C.E. Jackson defines a welding arc as 'a sustained electrical discharge through a high-temperature conducting

plasma producing sufficient thermal energy so as to be useful for the joining of metals by fusion' [56].

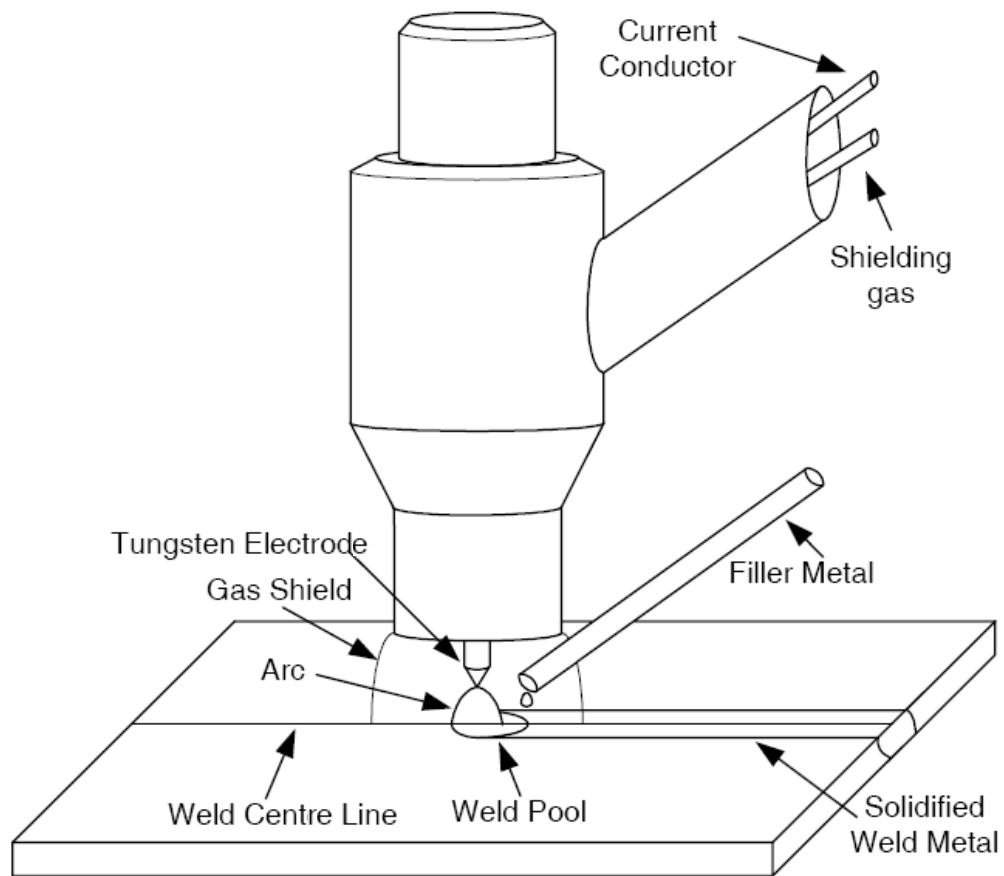


Figure 2.13: TIG welding schematic ([57])

A tungsten electrode is used since tungsten has the highest melting temperature among pure metals (3422 °C). As a result, the electrode is not consumed during welding, though some erosion (called burn-off) can occur. Certain stable higher density metal (e.g. zirconium, thorium, lanthanum) oxides are often alloyed with tungsten to produce an electrode with superior properties to that of pure tungsten (minimum 99.5% by weight with no internal alloying elements). The oxides lower the work function of the electrode, which effectively means a reduction in the amount of energy required to give off an electron (i.e. to allow current to flow), lowering the voltage necessary to strike an arc (thus making it easier). Since the oxides are

insulators and pure tungsten is a metallic conductor, oxide addition also increases the current carrying capability of the electrode [54].

The key advantage of TIG welding is that it allows for high precision, pure welds that are highly resistant to corrosion and cracking over long time periods. This makes TIG the welding procedure of choice for critical welding operations like sealing spent nuclear fuel canisters before burial. TIG welding creates no slag² and no spatter³ since both are contained by the inert gas that shields the weld, making TIG welding a relatively clean and time efficient process.

Maximum quality is assured by maintaining the cleanliness of the operation –all equipment and materials used must be free from oil, moisture, dirt and other impurities, as these cause weld porosity and consequently a decrease in weld strength and quality. To remove oil and grease, alcohol or similar commercial solvents may be used.

The concentrated nature of the TIG arc is one of its strong points. Welds of great strength and quality can be made with thin materials, light materials, dissimilar materials, in most available metals, and all with minimal distortion or corruption of the adjoining base metal.

However, TIG welding does have disadvantages. Low heat input, caused by low welding current or high welding speed, can limit penetration and cause the weld bead to lift away from the surface being welded. Conversely, too

² a rough coating left over the weld that must be chipped away before polishing or finishing

³ tiny little balls of steel that, like slag, must be chipped away from around the weld

much heat input causes the weld bead to grow in width while the likelihood of excessive penetration (burn-through) and spatter increase.

Manual GTAW is often considered the most difficult of all the welding processes commonly used in industry since great care and skill are required to control the amount of current used, and prevent contact between the electrode and the workpiece, while maintaining a short arc length. Although some welds combining thin materials can be accomplished without filler metal (known as autogenous welds), unlike other welding processes, GTAW normally requires two hands; since most applications require that the welder manually feed a filler metal into the weld area with one hand while manipulating the welding torch in the other. These disadvantages can be avoided by automating the welding process and so this option is very favourable.

Theoretically, an extremely thin fused layer might be sufficient for connecting the parts to be joined. The fusion layer should not be thicker than necessary in order to avoid wasting of energy, edge burn-off, sagging of the weld pool and deep weld end craters [58]. Control of weld bead shape is essential since this shape has a direct effect on the mechanical properties of the weld [6]. Therefore, it is clear that precise selection of the process parameters is necessary.

The principle operating variables for GTAW are:

- arc voltage (arc length),
- welding current,
- welding speed (and filler wire feed rate if applicable), and
- shielding gas (inert gas such as argon or helium)

All of these variables interact with each other very strongly; therefore, they cannot be treated as independent variables while establishing welding procedures for fabricating specific joints.

2.9 Weld material properties

Fusion welding requires localised input of intense heat and usually involves the deposition of molten filler metal. The melting of the local base or parent metal and intermixing with filler metal will result, upon cooling, in the formation of a different microstructure to that of the parent metal. Since the area of parent metal adjacent to the weld is subject to a somewhat different heating and cooling cycle during welding, the weld (fusion zone – FZ) and the surrounding material (heat-affected zone – HAZ) will each have different microstructures, and hence, the mechanical properties will vary across the weldment.

The understanding and modelling of the mechanical response of welds requires knowledge of the variation in material properties between all the different microstructural regions of the weldment, i.e. the FZ, the HAZ and the parent metal. The global response of a welded structure can then be determined by successfully implementing the constitutive stress-strain response for each weld region, together with any residual stress information, into numerical modelling codes [59].

Impression creep testing can be used to determine creep properties in the narrow zones (e.g. HAZ) within weldments (e.g. [60]). There are many publications concerned with investigating the effects of the welding process on the mechanical properties and performance of welded components during service (including service at elevated temperature), a good literature review can be found in the PhD thesis by W. Sun [60].

2.10 Metallurgical effects of welding

Weld solidification bears some similarity to casting but there are some key differences, such as the large temperature gradient across the melt and the dynamic nature of the welding process, which means that the solidification behaviour is dependent on the welding velocity. The material adjacent to a weld is also subjected to a rapid heat treatment cycle, and so various microstructures are formed as a result of welding (see Figure 2.14 for example).

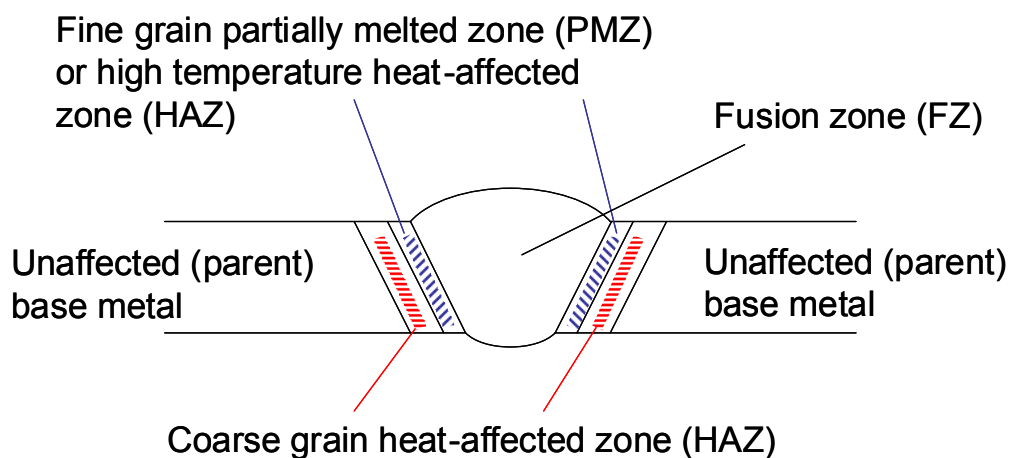


Figure 2.14: Microstructural zones formed by the fusion welding of a metal alloy

The different microstructures formed govern the strength and toughness properties, including fatigue and creep behaviour, of the zones within a weldment.

2.10.1 Weld pool solidification

In fusion welding, initial solidification occurs epitaxially; therefore, the initial crystal size of the weld metal is inherited directly from the base metal. This planar front solidification is difficult to maintain in alloys with a large solidification range due to constitutional supercooling, resulting in a transition from planar to cellular growth. Protrusions form and develop into long arms of cells that grow approximately parallel to the direction of

maximum heat flow [61] (Figure 2.15). These large elongated columnar grains are very different in size and shape from the grains of the base metal, which are normally equiaxed (Figure 2.18). The size of the columnar grains is significant since yield strength decreases as grain size increases.

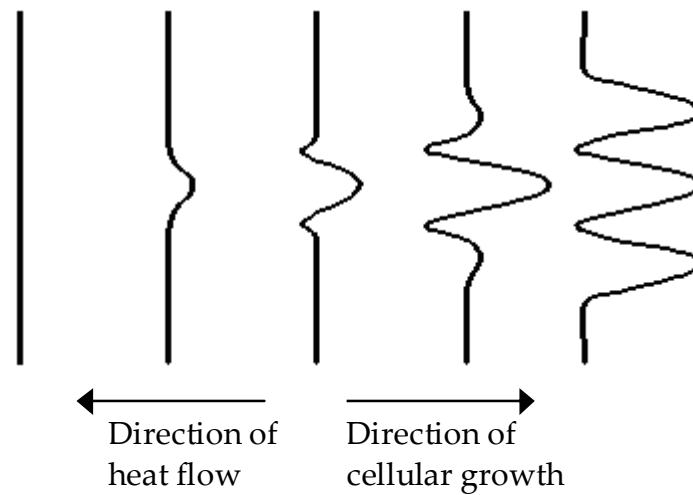


Figure 2.15: Transition from planar to cellular growth

The cellular microstructure is also only conditionally stable, and as the temperature gradient reduces, the walls of the primary cells become unstable and develop secondary and tertiary arms, thus a dendritic structure forms [61] (Figure 2.16 and Figure 2.17).

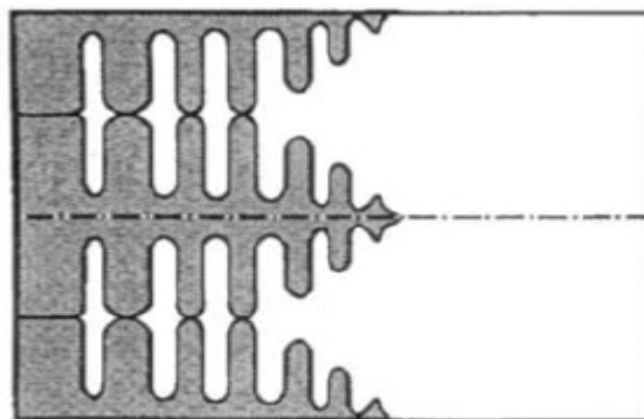


Figure 2.16: Columnar dendritic growth (from [62])

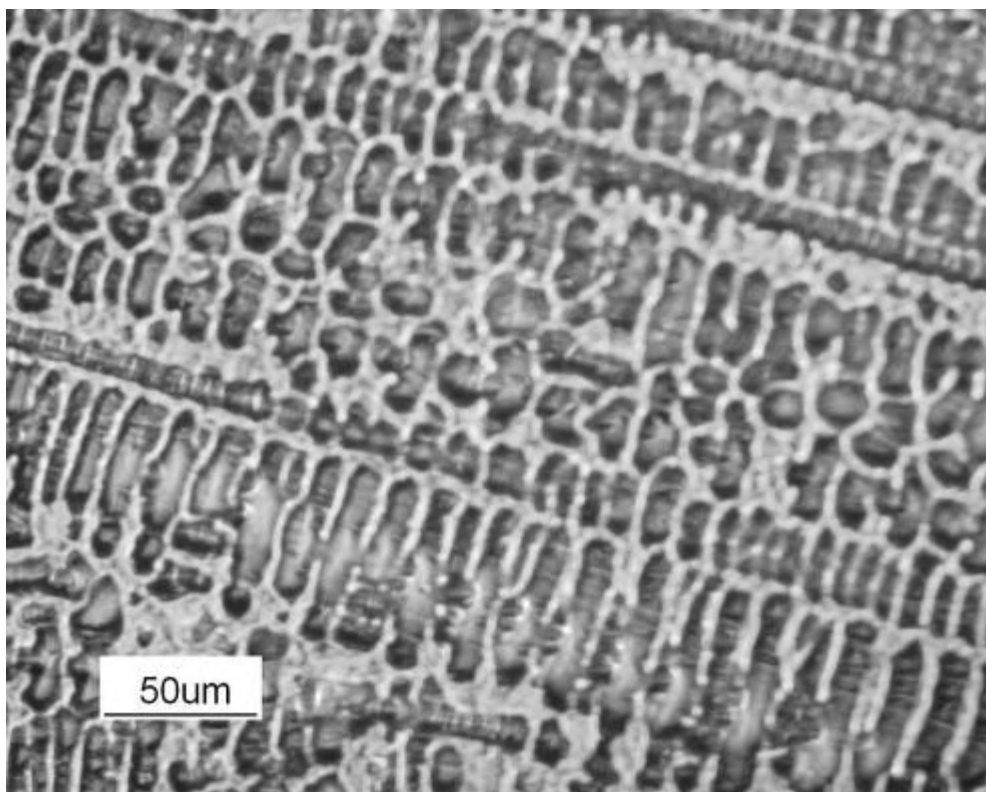
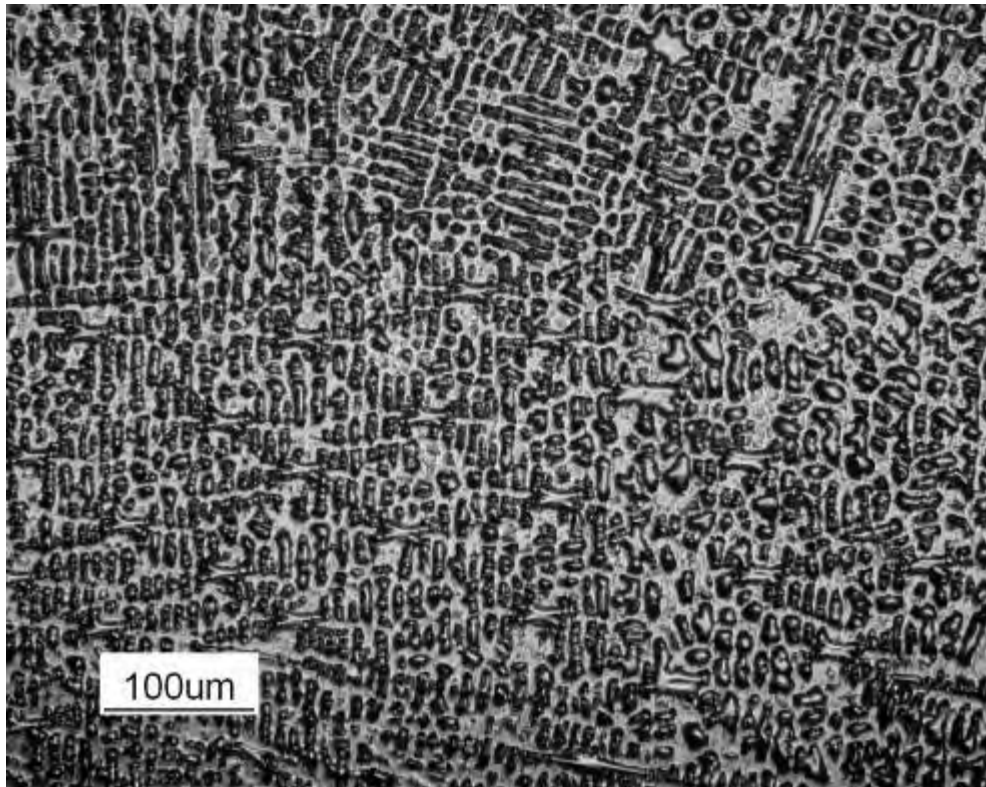


Figure 2.17: IN718 weld fusion zone dendritic microstructure

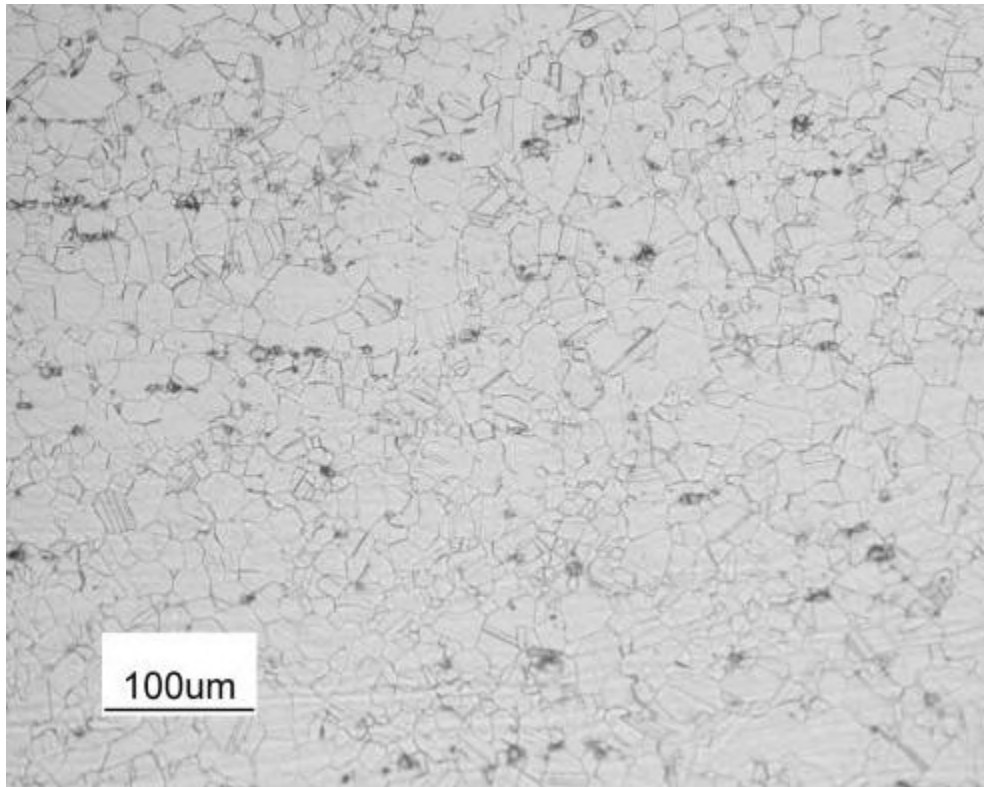


Figure 2.18: IN718 base/parent equiaxed microstructure

In the region immediately surrounding the weld pool, the peak temperature is between solidus and liquidus. Therefore, this region experiences partial melting and is referred to as the partially melted zone (PMZ) (Figure 2.19) [63].

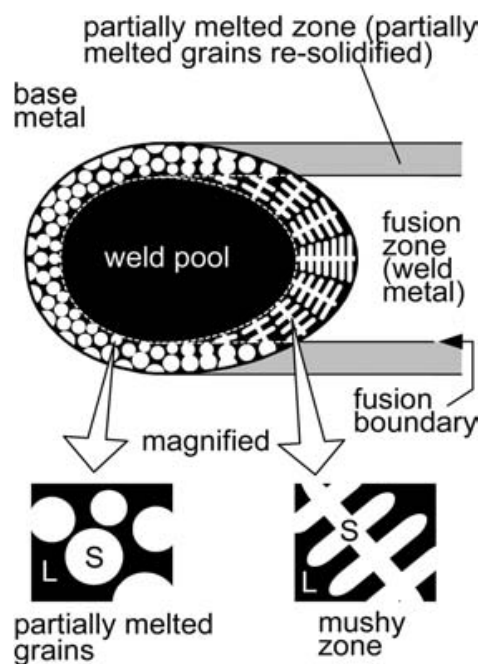


Figure 2.19: Partially melted base-metal grains around the weld pool of an alloy during welding (from [63])

2.10.2 The heat-affected zone (HAZ)

In the region directly adjacent to the fusion zone (FZ) exists base metal that undergoes a severe thermal cycle without melting. As a result, the microstructure and properties of this heat-affected zone (HAZ) change undesirably. The HAZ can be divided into a number of subzones, the total number and type depends on the material being welded. Each subzone refers to a different type of microstructure. Common changes in microstructure are recrystallisation and grain growth. In IN718 welds, there are two HAZ regions: one coarse-grained and one fine-grained (Figure 2.14 and Figure 2.20). Grain growth is less pronounced in the fine-grained region directly adjacent to the FZ due to grain boundary segregation and the subsequent pinning of the grains, since temperatures are lower in the other subzone, grain growth is not restricted in this way. The HAZ is a critical region in a weldment and is often the site of failure.

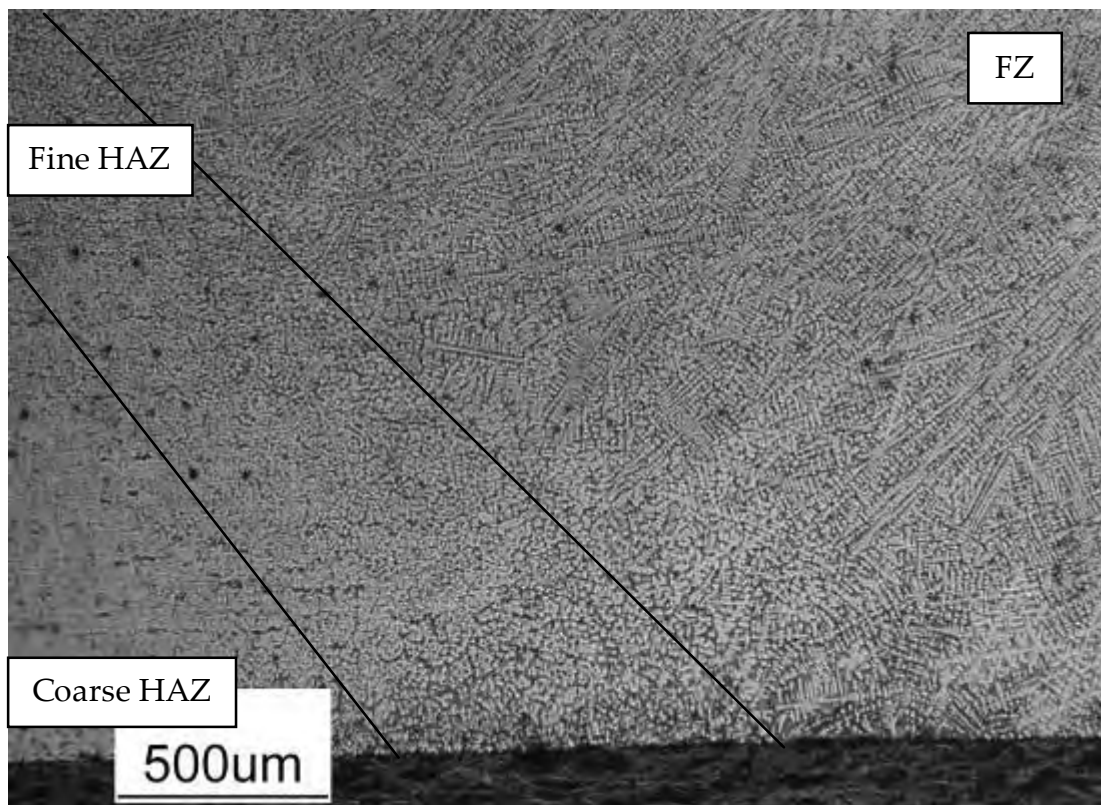


Figure 2.20: IN718 weld microstructural zones

The fine-grained HAZ could also be referred to as a PMZ due to the incipient melting/liquation of the grain boundaries (Figure 2.21).

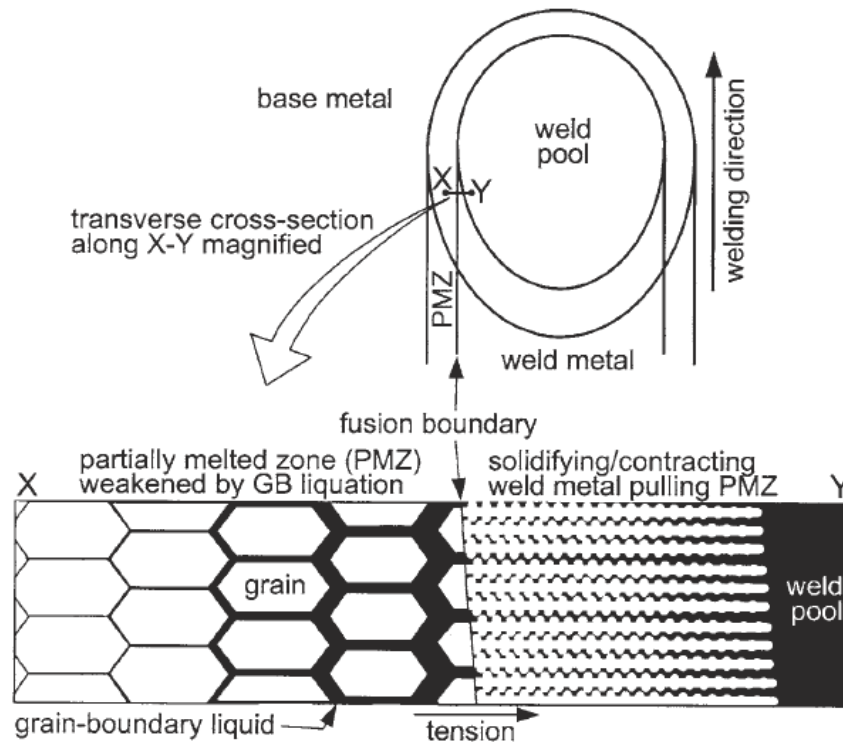


Figure 2.21: Grain boundary liquation (from [63])

2.10.3 Solid-state phase transformation

During the postsolidification cooling of weld metal and cooling of the surrounding HAZ, additional modifications in microstructure are likely to occur, even in single-phase metals. In polyphase metals (in particular carbon, low alloy and stainless steels), phase transformations may occur. The extent of these transformations depends upon the composition of the metal, the maximum temperatures reached and the cooling rate. One major example of a solid-state phase transformation that occurs during welding is the austenite–martensite transformation in steels. Deng *et al.* [18] looked at the effects of solid-state austenite–martensite transformation during cooling of welded parts made from particular steels. They concluded that, for steels with significant carbon content, this transformation does have a marked effect on weld-induced residual stress and deformation. Since this thesis is

concerned with the nickel-base alloy IN718, which remains as single-phase austenite from melting point to room temperature [64], no further details will be presented on welding solid-state phase transformation (there is a wealth of literature published in this area, for example see [65]).

2.10.4 Weld cracking

The severe thermal cycle and high restraint involved during the welding of high strength metals can cause cracks to develop. Some common types are:

- solidification/hot cracking –occurs in the weld as it solidifies due to the influence of tensile residual stress acting on low temperature melting phases that form as a result of segregation
- liquation cracking/microfissuring –occurs at grain boundaries in the HAZ due to segregation aggravated by the melting of the boundaries
- cold cracking (or hydrogen-induced stress-corrosion cracking) –occurs over time in the HAZ due to hydrogen embrittlement and tensile residual stress
- reheat/strain-age cracking –occurs during multipass welding or postweld heat treatment due to creep cracking of susceptible microstructure under high residual stress

For more details on weld integrity, see the book by S. Lampman [66].

2.11 INCONEL 718

2.11.1 Introduction

Extensive research has been published on INCONEL 718 (IN718). A general profile of the alloy can be found in the review by Song *et al.* [1]. Their review focuses on the principles of the strengthening and heat-resistant properties of the alloy at high temperature, the grain size and composition effects on its mechanical properties, and its fatigue and creep properties and failure

mechanisms at high temperature. Some information about IN718 that is relevant to the work in this thesis is presented in this section. Particular attention is given to publications concerned with IN718 welds.

2.11.2 Background

IN718 (also known as Inco 718 or alloy 718) is a precipitation-hardenable, niobium-modified, nickel-base superalloy used extensively in the aerospace, petrochemical, and nuclear industries since it exhibits good strength, excellent resistance to oxidation at high temperatures, and favourable weldability [1, 67-70]. IN718 was introduced in the late 1950s and is often used in critical high temperature creep resistant applications up to 650°C [1, 67, 71-75]. The alloy is also used in the field of cryogenics for its low temperature ductility and in offshore oil and heat exchangers for its corrosion resistance. One example of application within the aerospace industry is the gas turbine engine, where IN718 is used for turbine disc forgings and shell structures such as the combustor [2]. IN718 is also widely used in the space shuttle main engine for its excellent strength and ductility over a large temperature range [76].

The principle of the hardening of IN718 is the precipitation of two intermetallic phases, gamma prime (γ') and gamma double prime (γ''), during aging [77]. γ' [$\text{Ni}_3(\text{Al}, \text{Ti})$], the first of the two phases to precipitate during heat treatment, is a coherent, ordered, face-centred cubic (FCC) phase with a volume fraction of approximately 4%. This phase is a strengthening component of most nickel- and nickel-iron-based alloys. Unlike most nickel-base superalloys, IN718 is primarily hardened by the more effective body-centred tetragonal (BCT) phase, γ'' (Ni_3Nb) [78], which precipitates coherently as ellipsoidal, disc-shaped particles on {100} planes of the FCC

matrix. γ'' has a volume fraction of 15-20% [77]. The success of nickel-base alloys as high-temperature materials is due to the two-phase structure, which combines the good ductility provided by the FCC-austenitic γ matrix and the strength of the γ' (γ'' in the case of IN718) precipitate [79].

The time–temperature–precipitation (TTP) characteristics of the γ' phase and carbides in IN718 introduce complexities in the creep behaviour of the alloy. Although the γ'' phase helps to strengthen IN718, it possesses a higher lattice misfit with the γ phase than the γ' phase. This higher lattice misfit increases the tendency towards precipitate instability and thus coarsening with long term exposure at elevated temperatures [73]. The rapid coarsening and eventual conversion of the γ'' phase to δ is believed to be responsible for the degradation in the properties of IN718 above 650 °C [78, 80]. The kinetics of particle coarsening in IN718 has been characterised in [78] and [81], for example.

2.11.3 INCONEL 718 welds

The sluggish precipitation kinetics of the γ'' phase makes IN718 relatively easy to weld, avoiding the cracking problems associated with alloys hardened by the more rapidly precipitating γ' phase [82]. IN718 also has a good resistance to (strain-age) cracking during postweld heat treatment (PWHT) since the precipitation is slow enough to allow welding residual stress relief to occur before significant aging [83, 84].

During welding of aged IN718, the γ' and γ'' hardening precipitates dissolve causing the weld to soften [61]. By applying a PWHT, the hardness is regained somewhat and the effects of a solution heat treatment (SHT) followed by a PWHT have an even more beneficial effect, but the creep and fatigue (and to some extent the tensile strength) properties are not regained

due to the elongated size and columnar dendritic shape of the grains in the weld fusion zone. The same results by welding IN718 in the SHT condition and then aging.

Both electron beam (EB) welding and tungsten inert gas (TIG) arc welding are used as major fabrication routes for the manufacture of some IN718 structural parts. In the work of Radhakrishna and Prasad Rao [75], it was found that EB welding results in a better rupture life than TIG welding, however TIG welding does have advantages over EB welding, such as less stringent fit-up requirements [2].

Although IN718 is one of the most weldable high strength superalloys available, the alloy is still susceptible to weldability problems, including solidification cracking in the fusion zone (FZ) and microfissuring in the heat-affected zone (HAZ) [16]. An overview of the metallurgy of IN718 applicable to weldability issues such as strain-age cracking and microfissuring, can be found in [85].

In the case of wrought IN718, the ingots are homogenised at the solution heat-treatment temperature and then thermomechanically processed in order to obtain a fine-grained equiaxed structure, so segregation is not a problem. However, segregation is a common problem in solidified structures such as castings and welds, although little research has been conducted on segregation in IN718 welds. Segregation causes chemical inhomogeneity in the structure and hence is detrimental to the mechanical properties [75], but since the solidification process and the extent of segregation differs between castings and welds, studies available on castings cannot be directly applied to welds. The nonequilibrium thermal cycles experienced during welding

also make a direct comparison with casting difficult [86]. Therefore, further studies into IN718 welds are necessary.

In common with other nickel-base alloys such as Hastelloy C-4 and C-276, IN718 was developed to not contain any topologically close-packed (TCP) phases in the SHT condition. However, after welding, TCP phases such as σ and Laves appear in the weld metal microstructure, either as a result of nonequilibrium solidification or after prolonged exposure to elevated temperatures. These phases can lead to weld metal hot cracking and adversely affect the mechanical and corrosion properties [87].

Laves phase $[(\text{Ni,Cr,Fe})_2(\text{Nb,Mo,Ti})]$ which forms in the interdendritic regions of the weld metal as a result of niobium segregation and is an unavoidable terminal solidification phase in IN718 [88], is an important aspect of IN718 welds since it affects structural integrity and can lead to premature failure during service [75]. Although the addition of silicon improves the weldability of IN718, it has been shown to adversely affect the mechanical properties by promoting the formation of the brittle Laves phase, which was detrimental to the rupture life of welds compared to the base metal counterpart [75].

Vincent [89] describes the precipitation in the HAZ around EB welds. A high proportion of Laves phase was found inside the welds and at boundaries in the HAZs (attributed to boundary liquation). It is stated that although the welds may show no loss of strength under normal testing procedures (e.g. tensile test), the long-term creep, fatigue and corrosion resistance could still be adversely affected under extreme service conditions. Huang *et al.* [90] studied the effect of homogenisation heat treatment on the microstructure and microfissuring of the HAZ of EB welded cast IN718. The segregation of

boron at the grain boundaries was identified as the cause of microfissuring. HAZ microcracking in welded IN718 was also investigated by Lucas and Jackson [83] and a mechanism driven by incipient melting was proposed.

2.11.4 INCONEL 718 weld mechanical properties

While many publications are available relating to the microstructure and mechanical properties of wrought IN718, little research has been conducted on how welding affects these properties [88].

Gordine [82] obtained room temperature mechanical property data for IN718 TIG weldments. Although they showed good tensile strength (also observed by Mayor [91]), the welds exhibited lower impact strength and ductility relative to the wrought material. An improvement in these properties was obtained by the dissolution of Laves phase through a modified PWHT that included a high temperature solution treatment, although it is noted that this may cause excessive grain growth and therefore decrease the fatigue and tensile strength properties of the base metal.

Hardness testing is a quick and simple technique that has been used for many decades as a criterion of weld and parent material property variation with respect to strength. Hardness measurements are essentially a measure of the plastic behaviour of metals since they introduce high levels of plasticity (locally this may be as high as 30%). Several empirical relationships between hardness and yield strength have been proposed, however it has been shown that when weld hardness testing is used to determine if any strength loss in the weld is apparent, assuming that the hardness change is proportional to the change in yield stress can be misleading [92].

The mechanical properties of IN718 weld material have been shown to be significantly less than that of the base material. The room temperature 0.2% proof stress of both TIG and EB welds calculated using electronic speckle pattern interferometry (ESPI) are presented by Kyriakoglou *et al.* [92]. Although only a 5% drop in micro hardness was measured (similar to [93]), the TIG welds studied showed nearly a 30% reduction in proof stress.

Huang *et al.* [94] found that Laves phase decreased the ductility of tensile-tested IN718 EB welds and offered a preferred crack propagation path. Ram *et al.* [88] also studied the microstructure and mechanical properties of IN718 EB welds and the effects of different postweld heat treatments. It was found that the tensile and stress rupture properties of the welds were inferior in relation to the base metal due to the presence of Laves phase, even after an improved heat treatment. Ram *et al.* [95] studied the effects of using pulsed-current to reduce niobium segregation when TIG welding IN718. They found a corresponding improvement in the stress rupture properties, although the welds were still significantly inferior relative to non-welded material.

James and Mills [96] studied IN718 TIG weldments through fatigue-crack growth tests at temperatures ranging from 24-649°C. Compact specimens were used with notches centred in the weld metal; the resulting crack propagation was parallel to the direction of welding. It was found that, in general, the fatigue-crack growth rates were slightly higher in the weldments than in corresponding wrought material. It is also pointed out that IN718 weldments have inferior fracture toughness, but no time to crack initiation data can be derived from this work. The microscopic analysis presented in Mills and James [97] attributed the increased crack growth rates of IN718

welds to Laves particles nucleating extensive microvoid coalescence ahead of the advancing crack front.

2.11.5 Life assessment of welded INCONEL 718 at high temperature

It is stated in [75] that while extensive data on the stress rupture/creep behaviour of wrought IN718 is available, the data on the creep/stress rupture behaviour of IN718 weldments is rather scarce.

Song *et al.* [98] obtained creep rupture data for TIG butt-welded sheet IN718 at 620°C but the creep properties of the weld material were not determined. In [93] the creep data was used for failure predictions using continuum damage mechanics modelling. The welded specimens in the work by Song *et al.* had significant out-of-plane distortion and included stress-concentrating weld bead excess, which caused the failure location to occur at the toe of the weld underbead. Both the amount of distortion and weld bead geometry varied from specimen to specimen, making the effects of welding on the material properties difficult to assess [93]. This also meant that the results of any analysis were dependent on the precise geometry of the individual specimen. A parametric study of the stress concentrations in the vicinity of the weld bead fillet, with various bead geometries and distortion angles is presented in [4]. The aim of the work presented in this thesis was to improve on that by Song *et al.* by determining IN718 weld material data at high temperature via mitigating the distortion and subsequently removing the weld bead excess.

Life assessment covering creep and high temperature fatigue has been reported for non-welded IN718 (mostly in terms of crack growth behaviour) for example [3, 68, 69, 71, 73, 99-108], but assessment for welded thin-section

structures is more complex due to the residual stresses, deformations and material microstructural changes caused by the welding process. The weld bead geometry must also be considered since the sharp fillet radii result in high stress concentrations at the weld bead and parent interface. Due to these factors, the weld has a direct effect on the creep and fatigue life [4]. The residual stresses also interact with the deformations to produce out-of-plane distortions in the welded part; this compromises uniaxial testing and makes life prediction difficult.

Finite element welding simulation

3.1 Summary

Finite element (FE) arc welding simulations capable of calculating the evolution of stress and deformation, and predicting the residual stresses and distortions that occur as a result of the welding process are presented in this chapter. Sequentially-coupled nonlinear thermal and elastic-plastic ABAQUS FE flat plate analyses are employed and successfully validated using experimental and numerical results from literature. The heat input from the welding torch is modelled using a simplified heat source approach. The simulations have added complexity, particularly since the effects of restraint are considered, and the addition of filler is included, along with the formation of the typical weld underbead that forms during the welding of thin plates.

3.2 Introduction

The geometrically nonuniform heating and cooling that occurs during welding causes nonuniform thermal expansion and contraction, which in turn produces transient stress and plastic deformation. The presence of plastic deformation and the shrinkage of any weld filler upon cooling, results in the development of residual stresses, which, if unable to be supported by the structure, will be necessarily relieved through distortion until a structurally-sustainable stress-state is reached. Therefore, the stiffness of a structure and any imposed restraint conditions are fundamental in governing its global response during welding, and consequently control the general characteristics of the residual stress field [52]. The lack of supporting material in thin parts and low stiffness of long parts render them particularly

prone to weld-induced distortion. The aim of the numerical modelling described here is to calculate the final state of stress and distortion after the welding process has been completed and the weld has cooled.

Since the heat imposed when welding with a single source cannot be uniformly distributed through the thickness of a weld, the subsequent residual stresses are also nonuniformly distributed; this is the cause of bending and angular distortion. Essentially, all welding induced distortions are driven by compressive shrinkage forces, which are generated due to the nonuniform thermal loading. Depending upon the distribution of the shrinkage forces and the geometry (e.g. rigidity) and material characteristics of the welded structure, various types of distortions, such as bending, rotation and buckling may take place.

Postweld reduction and rectification of weld-induced residual stresses and distortions can require time consuming and expensive procedures such as flame straightening, and in some cases, attempts at these may fail and the component may not be fit for service and have to be scrapped. Eliminating or mitigating distortion early in the design and fabrication process rather than afterwards will increase industrial competitiveness in terms of both cost and time. Proper understanding of the distortion mechanism, and the different types and causes, enables the development of suitable predictive tools and mitigation controls. It is also important to note that improper control may lead to an increase in distortion. It is for reasons such as those mentioned here, that it is an engineering obligation to obtain a good understanding of weld-induced residual stresses and distortions present in structural components, and how best to reduce their prevalence.

3.3 Modelling approach

Due to the relatively uncomplicated physical basis of thermal distortion, it is possible to use empirically determined formulae for practical predictions (see [54] for details and examples). Since the thermal contractions are governed mainly by the maximum temperature reached and the geometry of the heat-affected zone (HAZ), weld-induced distortions can be related to the heat input (heat energy supplied / welding speed), and the cross sectional area of the welded part. However, difficulties such as coping with the localised plasticity around the welding heat source, heat losses due to convection and radiation, and the definition of realistic boundary conditions often require simplification or neglect, which results in less accurate predictions than those that can be produced using numerical procedures such as the finite element (FE) method.

The plastic deformation generated by welding is a function of structural, material and fabrication parameters. The structural parameters include the joint type and the dimensions of the welded material. The material parameters reflect the metallurgical condition of the material and the fabrication parameters include the welding method, heat input and the restraint condition [18].

In addition to the more obvious considerations of geometry and any clamping or restraint conditions, thermophysical and mechanical temperature-dependent properties are required, and any significant changes due to phase transformation should be included in a numerical model of a welding process. The distribution and magnitude of heat input needs to reproduce the effects of the physical heat source, whether it is an arc, an electron beam or a laser etc... The addition of any filler material also requires attention.

The modelling of welding processes has received a lot of attention over the past 30 years; predicting the residual stress field and any possible distortions being the main focus (e.g. [23]). However, an all-encompassing fusion welding model that includes both the physical fluid flow in the weld pool and the mechanical effects of the welding process is still not feasible. With the increase in computer capability, more parameters and effects are able to be included in models that instead use a simplified heat source based upon prior knowledge of the weld pool shape.

3.4 Model definition

One approach to modelling welding distortion is the coupled temperature-displacement shrinkage volume method favoured by Bachorski *et al.* [24], which concentrates on the linear thermal contraction of a nominal volume. This method is not very satisfactory since it relies heavily on the accuracy of the size and shape used to represent the fusion zone and is unsuitable for butt welds with small V-angles unless the actual shape and size of the fusion zone is known (see Figure 3.1).

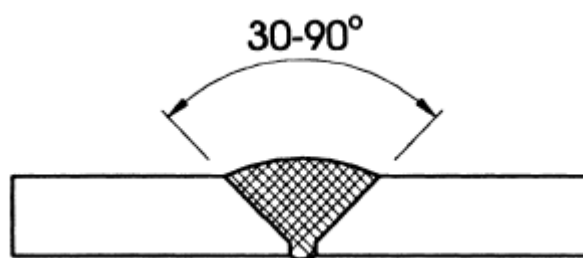


Figure 3.1: Assumed fusion zone for a typical V-joint modelled using the shrinkage volume approach

Instead, the FE arc welding simulations presented here are based on a two-dimensional (2D) pipe welding model adopted by Brickstad and Josefson [10], and a three-dimensional (3D) IN718 plate welding analysis performed

by Dye [2, 44]. Sequentially-coupled nonlinear thermal and elastic-plastic FE analyses are used to generate a welding simulation model, capable of calculating the evolution of stress and deformation, and predicting the residual stresses and distortions that occur as a result of the welding process. The coupling procedure is illustrated in Figure 3.2.

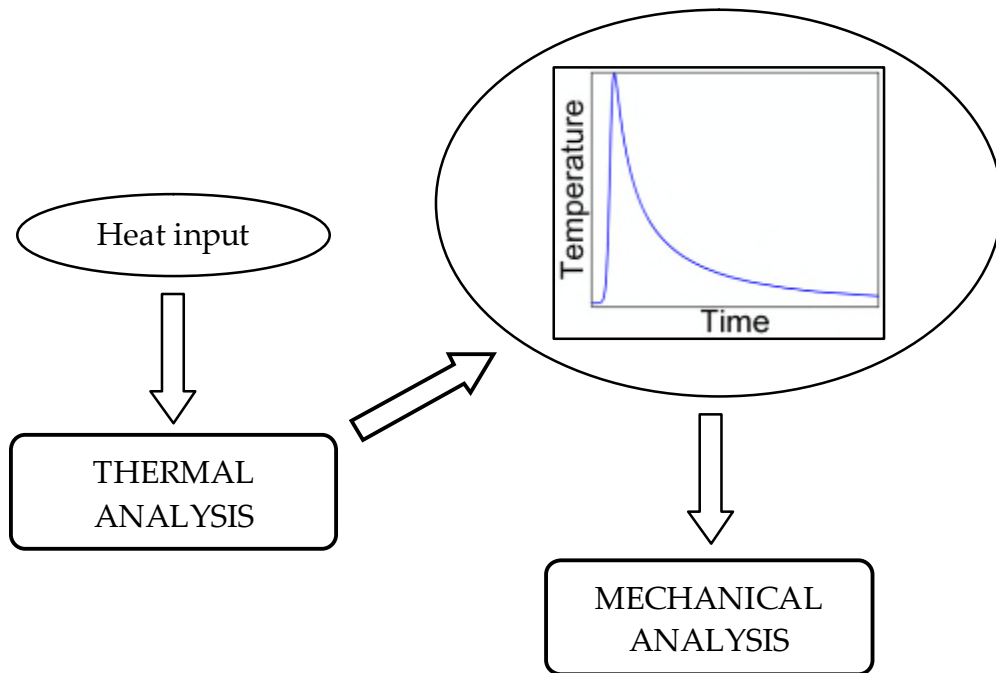


Figure 3.2: Sequential coupling of the thermal and mechanical analyses

First, a conduction-based thermal analysis is run to determine the entire temperature history for each node in the FE mesh. This data is then used as input for a mechanical (stress-displacement) elastic-plastic analysis, which allows the thermal history and its mechanical effects to be equated via thermal expansion, hence changing thermal effects into mechanical behaviour. Any microstructural changes can also be determined using the temperature history and implemented in the mechanical analysis.

Each analysis uses an identical FE mesh, and both require temperature-dependent material properties. Due to large deformations occurring during

the mechanical analysis, a large-displacement formulation (NLGEOM in ABAQUS) is used to account for geometric nonlinearity. Elements with additional incompatible bending modes (e.g. C3D8I in ABAQUS for 3D) are also employed in order to accurately capture distortion [109].

Single pass, gas metal arc welding of flat plate, nickel-base superalloy IN718, has been simulated in 2D (plane strain) and 3D using the ABAQUS FE software suite. In particular, the modelling of tungsten inert gas (TIG) bead-on-plate autogenous welding of IN718 by Dye *et al.* [44] has been recreated and the results analysed in order to validate the technique used. Validation was achieved using the numerical results, thermocouple measurements, coordinate measurement scans and neutron diffraction measurements presented in [44]. The results obtained for an identical case show the same residual stress distribution and the predicted distortion also agrees well with the computed and experimental data in [44].

After validation, the model was advanced with added complexity, particularly since the effects of restraint are considered, and the addition of filler is included, along with the formation of the typical weld underbead that forms during the welding of thin plates.

Only one plate for a butt weld and half of the single plate for a bead-on-plate weld need to be modelled because of symmetry about the weld centreline. The modelling approach can easily be applied to bead-on-plate or V-angle butt welds and both autogenous (no addition of filler material or with filler of the same material as the material being welded) and nonautogenous welding. The ABAQUS USDFLD FORTRAN user subroutine can be used to model the deposition of molten filler as discussed in section 3.14.

3.5 Thermal analysis

The thermal analysis is based on the early work of Rosenthal [47, 48] since the heat diffuses from a defined source. The analysis appeals to the fundamental governing equation of heat transfer (from [110]):

$$\rho C_p \frac{\partial T}{\partial t}(x, y, z, t) = -\nabla \cdot q(x, y, z, t) + \dot{Q}(x, y, z, t) \quad (3.1)$$

where ρ is the density of the material, C_p is the specific heat capacity, T is the current temperature, q is the heat flux vector, \dot{Q} is the rate of internal heat generation, x , y and z are the coordinates in the reference system, t is the time, and ∇ is the spatial gradient operator.

The nonlinear isotropic Fourier heat flux constitutive equation is employed so that:

$$q = -k\nabla T \quad (3.2)$$

where k is the temperature-dependent thermal conductivity. Therefore, the material properties required for the thermal analysis are density, specific heat capacity and thermal conductivity. The properties used for IN718 are given later in the material properties section (section 3.8).

The heat input from the welding torch is modelled as a distributed heat flux (DFLUX in ABAQUS) focused around the weld centreline; this heat then transfers throughout the rest of the plate by conduction. After the torch passes, the plate cools back down to ambient temperature using a thermal boundary condition (Newton's law of cooling):

$$q_{bc} = h(T - T_{bc}) \quad (3.3)$$

where h is a combined convective and radiative cooling coefficient, T is the local temperature and T_{bc} is the ambient temperature, which is assumed to be constant (20°C in this work). Conduction to a welding jig or a backing plate

may also occur and would therefore need to be modelled (as in sections 3.15 and 3.16, respectively), but no contact will be assumed here unless specified.

A variety of heat flux (or heat source) models can be used to simulate the heat input from the welding torch, e.g. triangular [10], conical [111], ellipsoidal [46], split (surface and volume) [24], with the use of the ABAQUS DFLUX FORTRAN user subroutine (e.g. Figures 3.3-3.6). The choice of heat source depends upon the type of welding process, for example, a volumetric distribution is more suited to modelling the deep keyhole-shape fusion zone produced during electron beam welding.

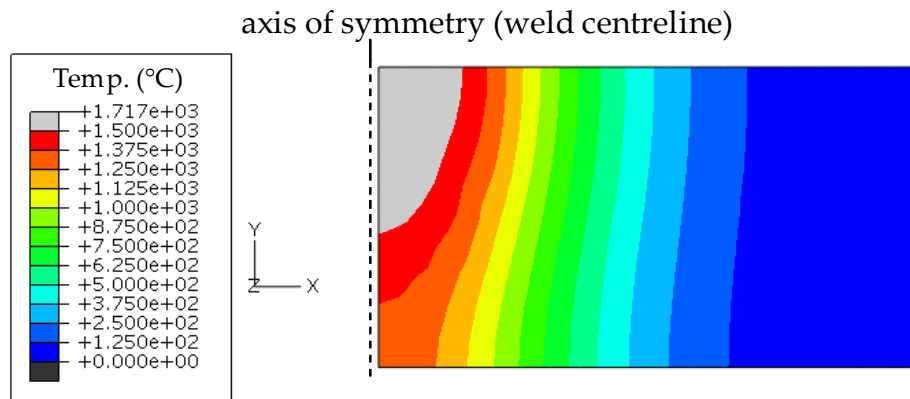


Figure 3.3: Conical heat source (side view)

The most popular heat source model is the 3D Ellipsoidal Power Density Distribution developed by Goldak *et al.* [46] (Figure 3.4 and Figure 3.5, when $c_1 = c_2 = c$), which uses the following equation for describing the heat flux:

$$q(x, y, z, t) = \frac{6\sqrt{3}Q_p}{abc\pi\sqrt{\pi}} e^{-3x^2/a^2} e^{-3y^2/b^2} e^{-3[z+v(\tau-t)]^2/c^2} \quad (3.4)$$

where: Q_p is the energy or power input (W)

$a b c$ are the semi-axes defining the ellipsoid

v is the welding speed (m/s)

τ is a lag factor (to define source position at $t = 0$)

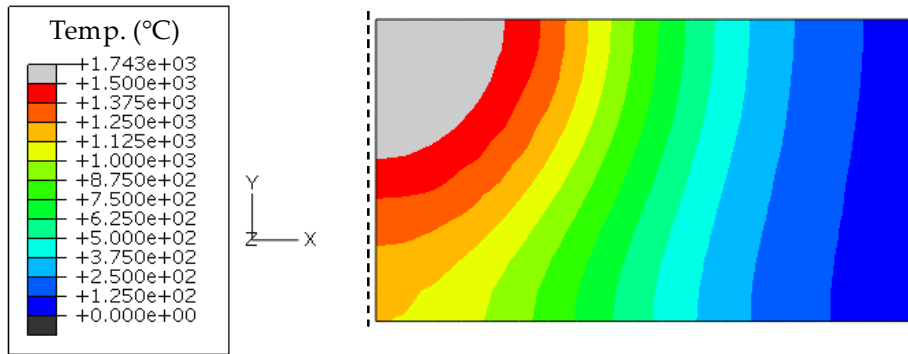


Figure 3.4: Gaussian ellipsoidal heat source (side view)

In the double ellipsoidal model, the heat is distributed through two different ellipsoids, one front and one rear, hence the introduction of c_1 and c_2 (e.g. Figure 3.5). This heat source by Goldak *et al.* is widely used ([110], [112] are just two examples) since it has many parameters and so is very flexible.

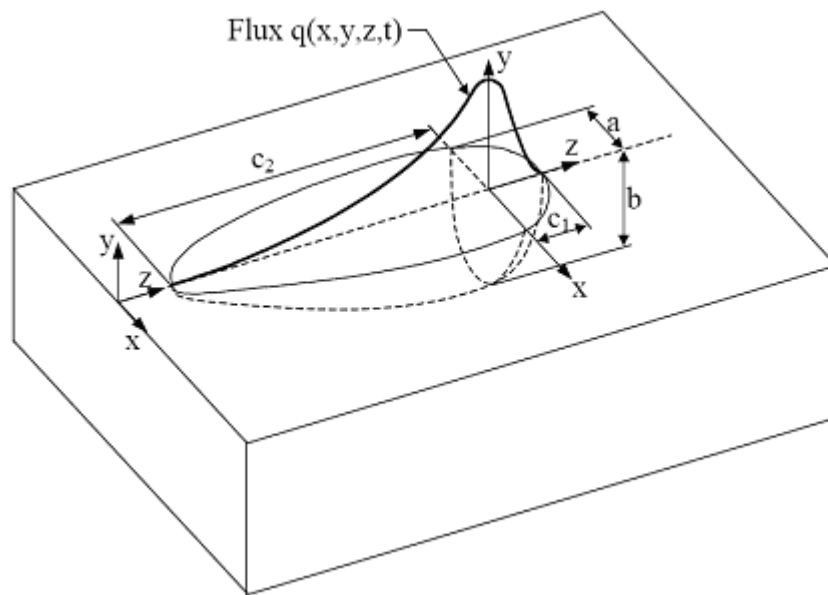


Figure 3.5: Double ellipsoidal heat source definition ([46])

In order to model the corresponding rise in temperature of surrounding material due to the addition of molten filler, a 'split' heat source can be used. This source consists of a Gaussian surface distribution combined with a uniform heat source in the weld region (Figure 3.6).

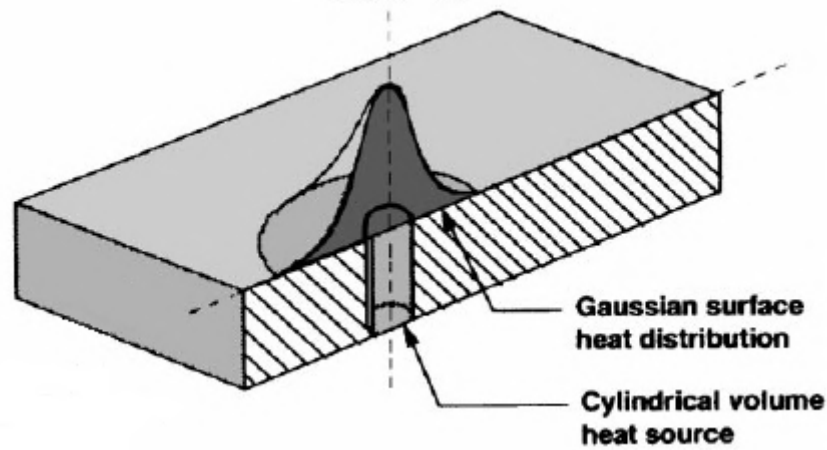


Figure 3.6: Split heat source (from [24])

For the case of a thin plate (a thickness of approximately 3mm is used here), it can be assumed that transfer of energy from the welding torch to the workpiece occurs within a circular source (radius a) of constant power density [44]:

$$q = \frac{\eta Q_p}{\pi a^2} \quad (3.5)$$

where η is the thermal efficiency of the welding process and Q_p is the absolute power of the source.

The circular source moves with the welding velocity, v , such that the circle is defined in the x - z plane at time t by (Figure 3.7):

$$x^2 + (z + a - vt)^2 = a^2 \quad (3.6)$$

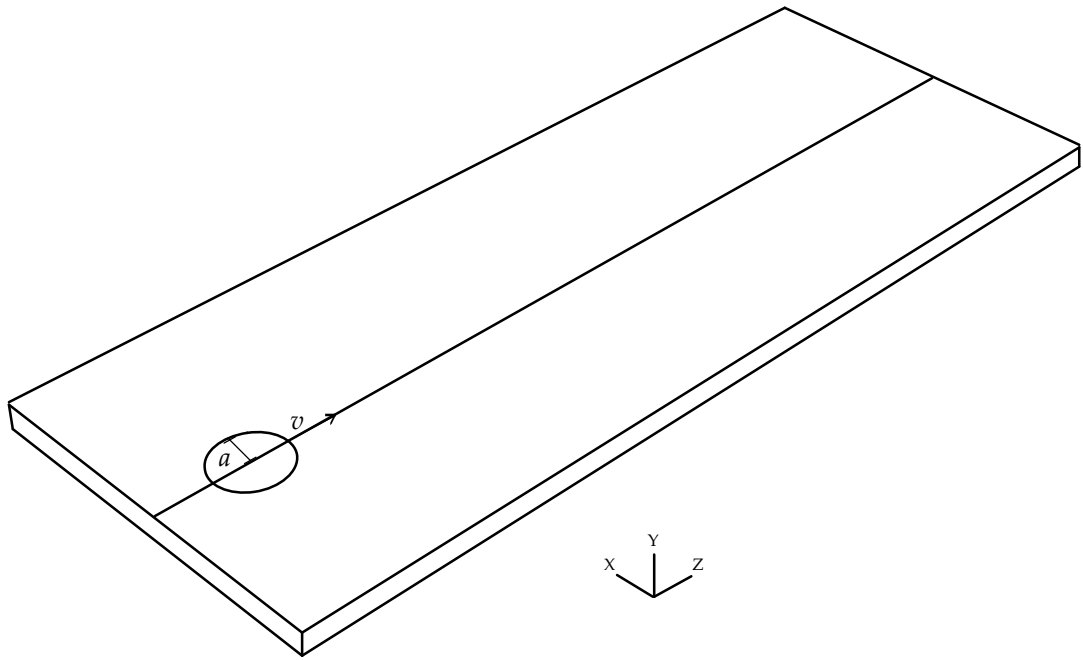


Figure 3.7: Circular heat source definition

η , Q_p , a and v are approximated using values from literature for similar cases (see [44]) and then refined using the FE model until the calculated weld fusion zone geometry is satisfactory when compared with experiments. The values used for this IN718 TIG welding analysis were $\eta = 0.57$, $Q_p = 1000$ W, $a = 4$ mm and $v = 1.6$ mm s⁻¹. With the value of the cooling coefficient in equation (3.3), $h = 35$ W m⁻² K⁻¹.

Figure 3.8 shows the temperature history for a point on the top surface at the weld centreline for a sample FE weld model. The maximum temperature is achieved after approximately 10s and cooling is complete after approximately 1000s. The temperature distribution approximately midway through the welding process is shown in Figure 3.9.

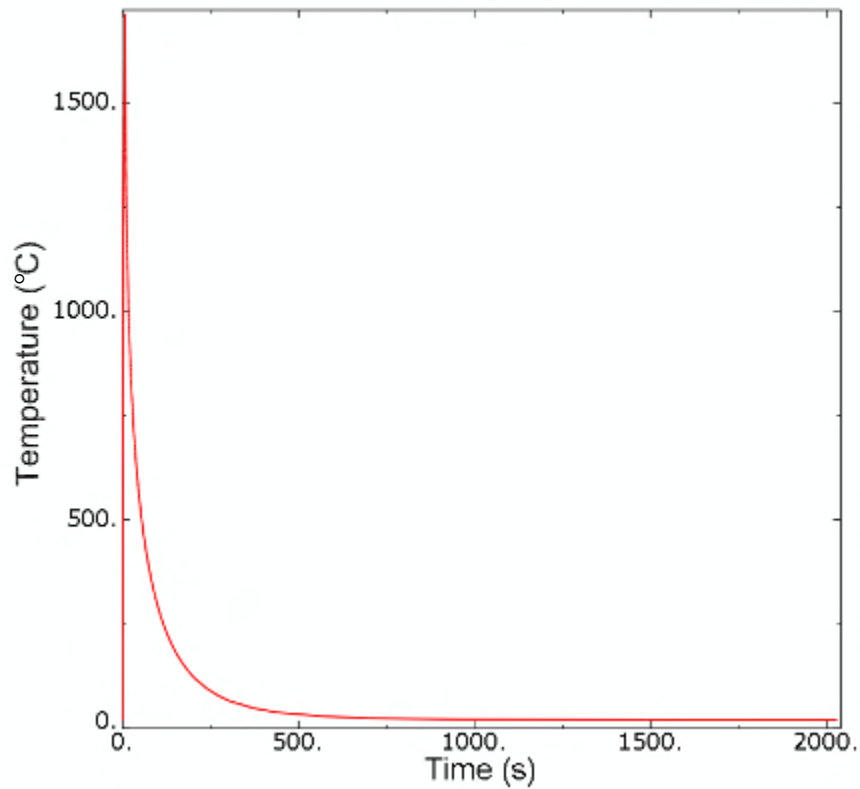


Figure 3.8: Temperature history for the top of the weld centreline

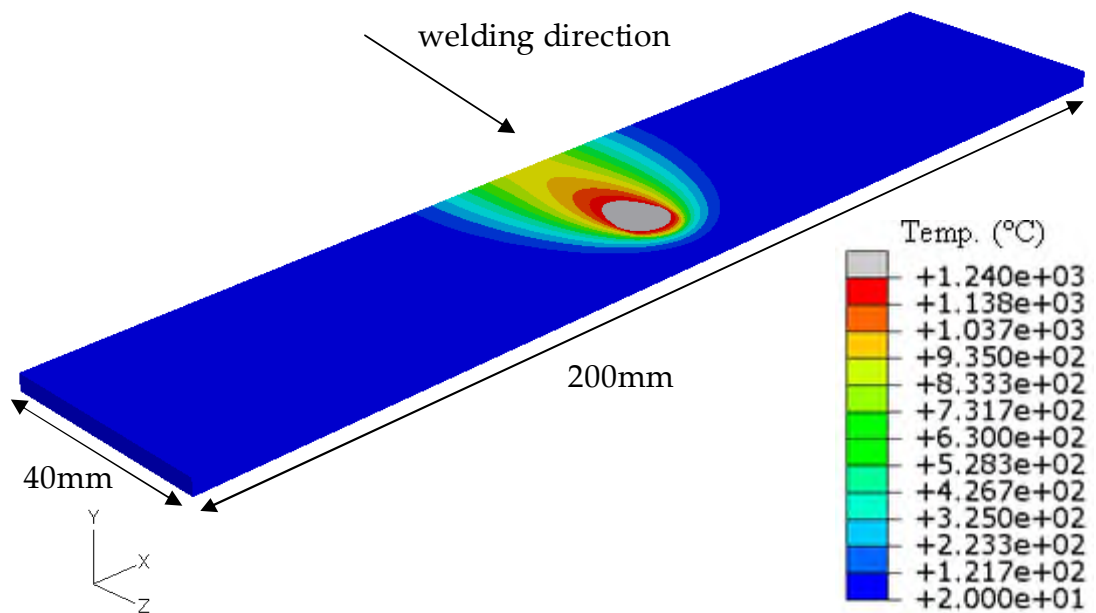


Figure 3.9: Temperature distribution midway through the welding process (the mirror imaging facility introduced in ABAQUS v6.6 is used to reflect the results across the weld centreline (the axis of symmetry))

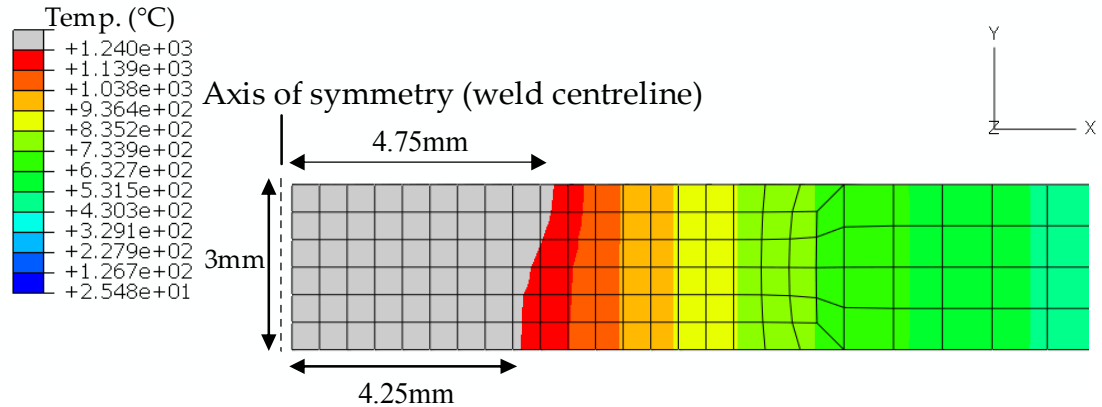


Figure 3.10: Maximum temperatures achieved in a cross section transverse to the weld; white/grey region indicates the fusion zone

The half width of the fusion zone (FZ) (temp. > 1240 °C –the melting point of IN718) here is ≈4.75mm for the top surface and ≈4.25mm for the bottom surface (see Figure 3.10), which compares well with measurements of half an actual weld (top surface ≈5.0mm, bottom surface ≈4.0mm (to the nearest 0.5mm)). It is more beneficial and crucial that the size and shape of the FZ is predicted accurately and used for validation than comparisons of the lower temperatures found in the far field, which may be measured more easily with thermocouples, but have less effect on the stress and distortion magnitudes. It also follows that if the FZ is accurately predicted, it is likely that the temperature profiles elsewhere are also accurate.

The maximum temperature that occurred during this analysis was 1720 °C. This is slightly higher than for a 2mm plate (e.g. [44], max. 1620 °C) but this is expected since more heat input is physically required for the greater thickness of plate used here (3mm), therefore the top surface will necessarily heat up more.

Steady-state conditions were achieved over a central 14mm-long portion of the 40mm weld. This is an important consideration since the required width of the test specimens' gauge length is 12.5mm (see Chapter 4), and therefore

to ensure validity of the tests, it is imperative that the temperature profiles do not vary significantly across this region.

3.6 The need for a three-dimensional model

Prior to the development of computers with sufficient processing capability to enable reasonable 3D welding analyses to be performed, it was generally accepted that a 2D plane strain analysis through the section of the weld provided adequate residual stress predictions. However, the plane strain assumption is often unsuitable and inaccurate. For instance, because welding is a transient process, the cooling of the welded material does not occur simultaneously at all positions along the weld. The regions closer to the start of the weld cool and regain their stiffness while the regions further along the weld line are still molten. Similarly, when the regions further along the weld line cool and regain their stiffness, the regions preceding them will already have cooled and will therefore restrict the shrinkage of the cooling regions. This effect cannot be considered in a standard two-dimensional model.

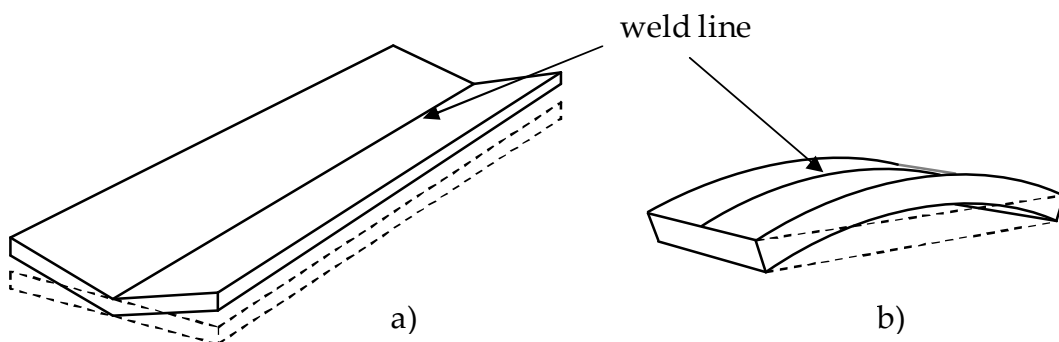


Figure 3.11: Two primary modes of distortion:
a) angular 'butterfly' and b) cambering

Two primary modes of distortion; angular 'butterfly' (bending around the weld centreline) and cambering (bending around a transverse axis), can

occur as a result of welding thin plates (Figure 3.11). Since these modes occur in geometric planes perpendicular to each other, a three-dimensional model is necessary in order to give accurate predictions of both residual stress and distortion.

3.7 Finite element mesh

It is important when using any numerical method to minimise computation time as much as possible without compromising the accuracy of the solution. Therefore, the design of the FE mesh used requires attention. As a matter of course, in welding, the highest temperature gradient occurs closest to the weld. Consequently, it is necessary to refine the mesh in this region. Conversely, away from the weld, a relatively coarse mesh may be used. The 3D symmetrical graded mesh presented in Figure 3.12, which consists of multiple cells like that shown in Figure 3.13, vastly reduces the computation time compared with an ungraded mesh. Regular hexahedra perform most accurately in large strain and deformation problems such as that encountered here [109].

The mesh design and refinement (Figure 3.14), along with the time incrementation used, is based on a set of guidelines employed by Dye *et al.* [44]. On the weld centreline, the element size should be no larger than 1 x 1 x 0.5mm in order to adequately simulate the heat source, whilst in the far field elements of size 4 x 4 x 1mm are acceptable. Two elements through the thickness are deemed adequate to model bending. The geometry of the weld underbead used in section 3.14 is also shown in Figure 3.14.

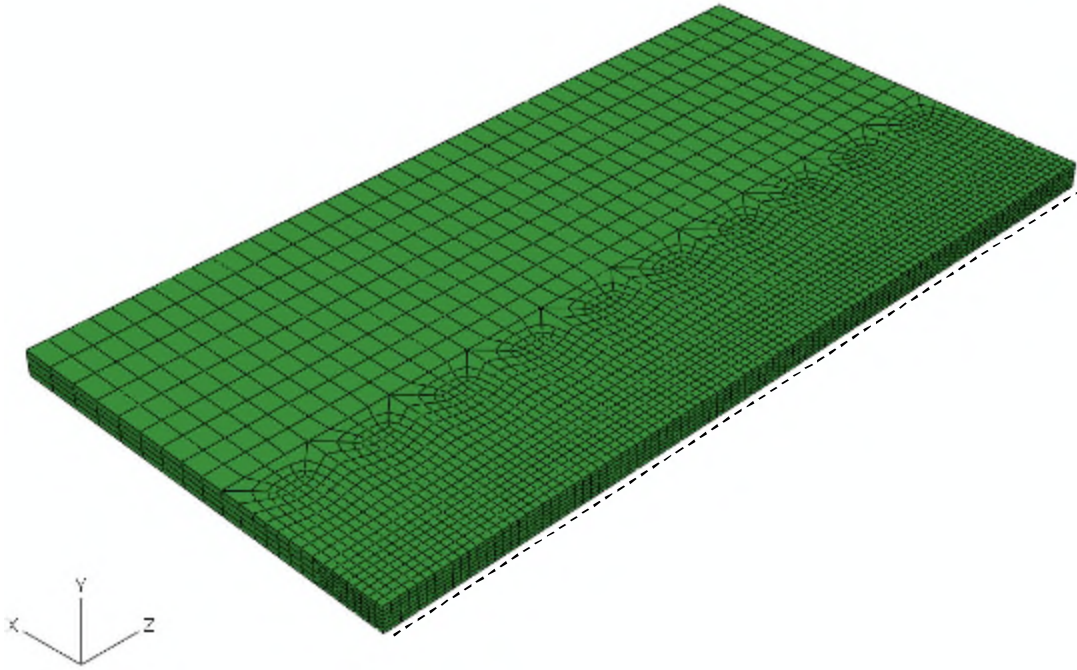


Figure 3.12: 3D graded finite element mesh (10520 elements), consisting of multiple cells

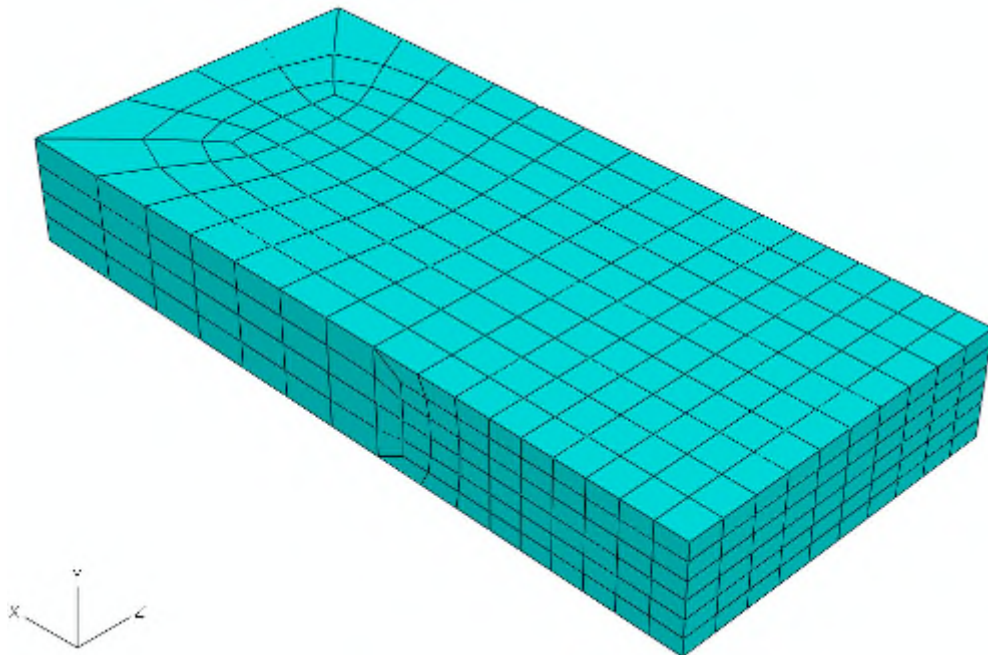


Figure 3.13: One of the cells used to make up the full mesh

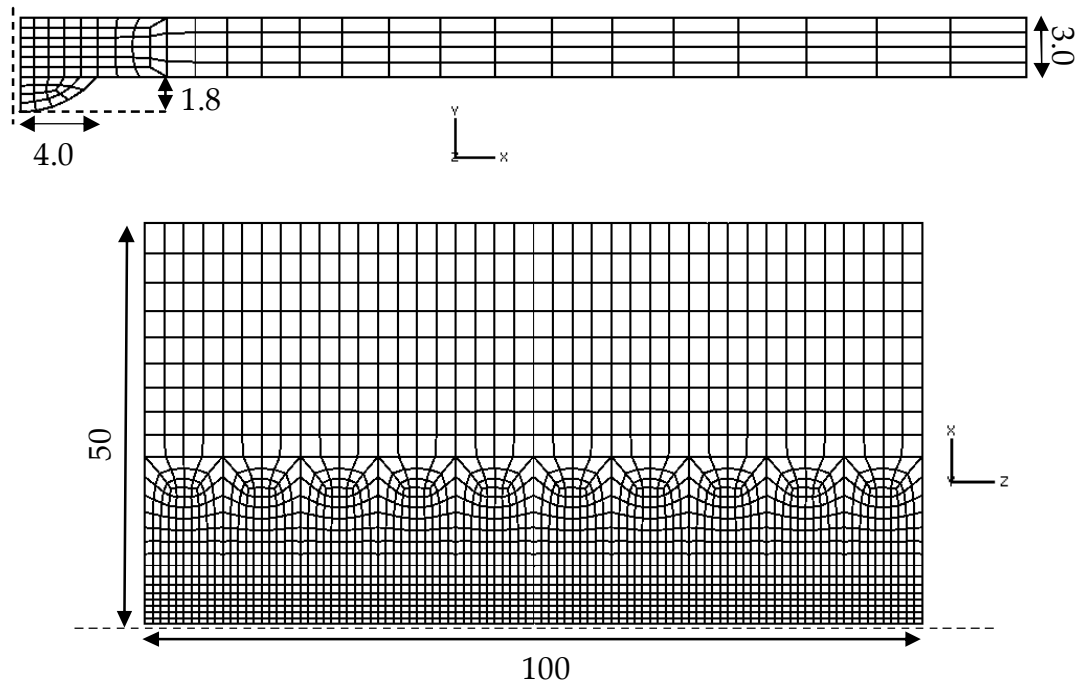


Figure 3.14: Finite element mesh design (dimensions in mm)

Symmetry about the weld centreline means it is only necessary to model one-half of a bead-on-plate weld or one plate during butt-welding. It is assumed here that there is no separation of the plates during the welding process. Artificial mechanical boundary conditions must be imposed to prevent rigid body motion if clamps are not present or are neglected in the model. Here, the two corner ends farthest from the weld centreline are fixed in both the y and z directions (see Figure 3.15).

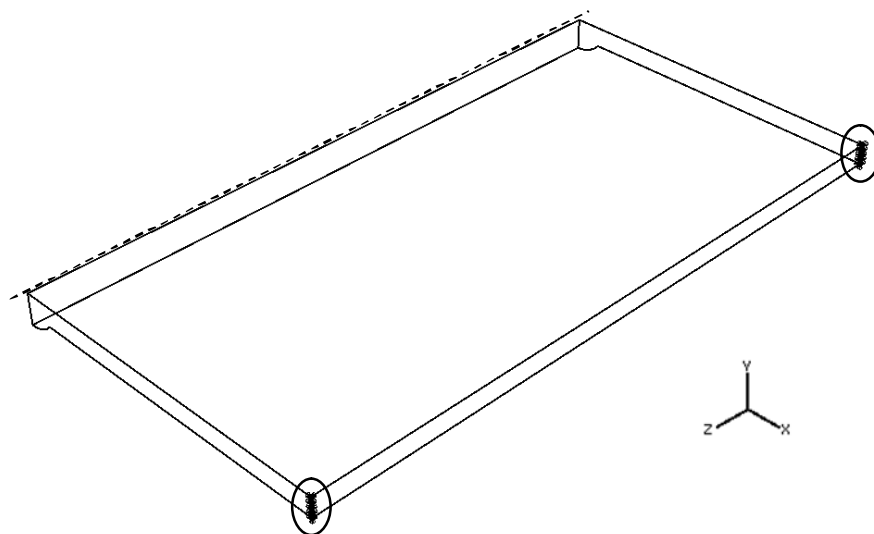


Figure 3.15: Artificial mechanical boundary conditions (circled)

While regular linear diffusive heat transfer elements were used for the thermal analysis (e.g. DC3D8 in ABAQUS for 3D), fully integrated linear elements with additional incompatible bending modes (e.g. C3D8I for 3D) are employed in the mechanical analysis in order to accurately capture the distortion. The additional modes eliminate the parasitic shear stresses that cause the response of regular first-order displacement elements to be too stiff in bending. In addition, these modes eliminate the artificial stiffening due to Poisson's ratio effect in bending (which is manifested in regular displacement elements by a linear variation of the stress perpendicular to the bending direction).

Because of the added internal degrees of freedom due to the incompatible modes (e.g. 13 extra for C3D8I), these elements are somewhat more expensive than the regular first-order displacement elements; however, they are significantly more economical than second-order elements. The incompatible mode elements use full integration and thus, have no hourglass modes. The incompatible mode elements perform almost as well as second-order elements in many situations if the elements have an approximately rectangular shape [109].

A time step of 0.16s, equivalent to a travel distance of 0.25mm (one quarter of the element length), was used for the thermal analysis. After the heating step was completed, a step with automatic time incrementation and a maximum allowable temperature change per increment of 160°C was used to allow the weld to cool back to ambient temperature. Automatic time incrementation with default ABAQUS controls was used throughout the mechanical analysis.

3.8 Material properties

The following temperature-dependent material properties are required for the simulation of welding:

- Thermal analysis
 - thermal conductivity (κ)
 - specific heat capacity (C_p)
 - density (ρ)

- Mechanical analysis
 - coefficient of thermal expansion (α)
 - Poisson's ratio (ν)
 - stress-strain data (σ - ϵ)

Values obtained from literature [44] and during the testing programme (mentioned in more detail in Chapter 5), for solution heat-treated (SHT) IN718, are presented in Figure 3.16 and Figure 3.17.

The release of latent heat during solidification does not need to be accounted for due to the empirical nature of the modelling of the weld pool [44].

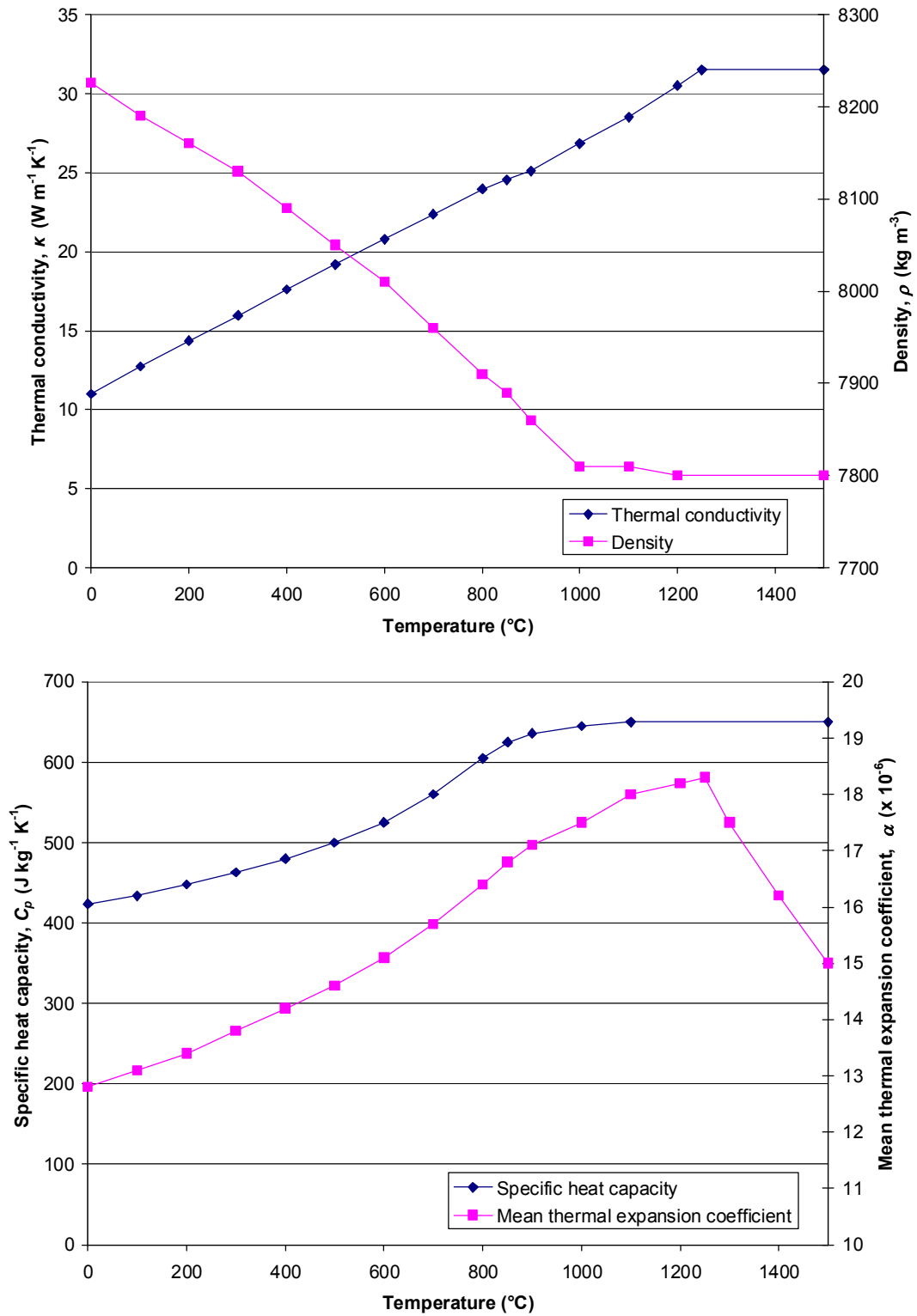


Figure 3.16: IN718 temperature-dependent material properties [44]

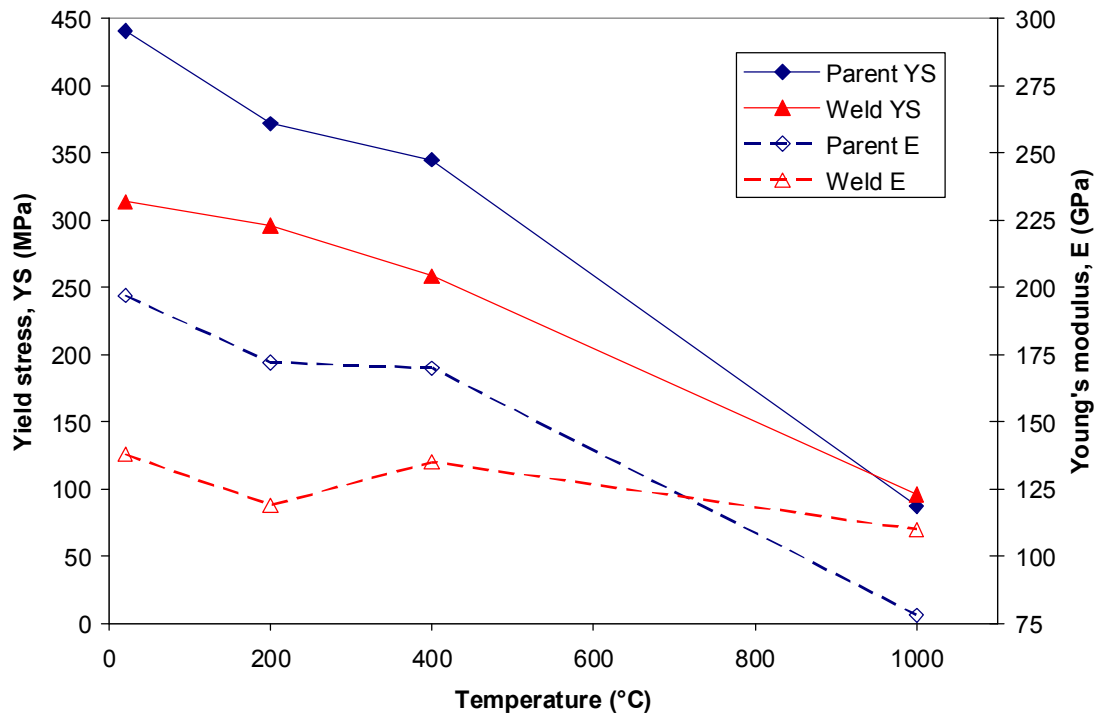
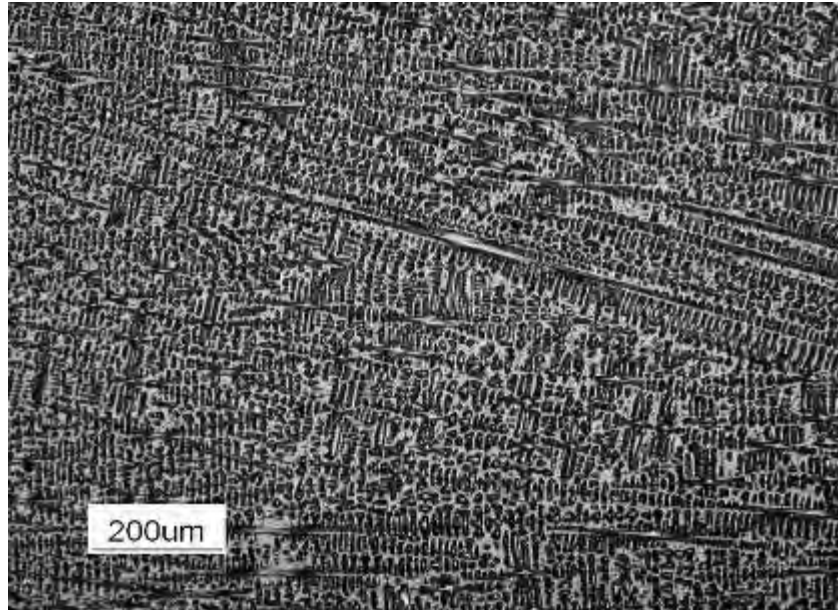


Figure 3.17: SHT IN718 temperature-dependent mechanical properties

In this work, full experimental stress-strain curves were used as input to the FE analysis with isotropic hardening (the testing procedure and results can be found in Chapter 5). Since IN718 remains as single-phase austenite from melting point to room temperature [64], no solid state phase transformations occur during welding. Precipitation hardening will occur at temperatures above approximately 600°C but this process is slow in relation to welding time [113, 114]. However, weld fusion zones in IN718 are known to exhibit poor mechanical properties in relation to the base metal as a result of extensive interdendritic Nb segregation and consequent formation of Nb-rich, brittle, intermetallic Laves phase during weld metal solidification [115].

Figure 3.18(a) shows that the microstructure of the weld contains columnar grains that are very different in texture, size and shape to the equiaxed wrought parent grains in Figure 3.18(b). Clearly, these microstructural differences will have a pronounced effect on the mechanical properties of the weld.

a)



b)

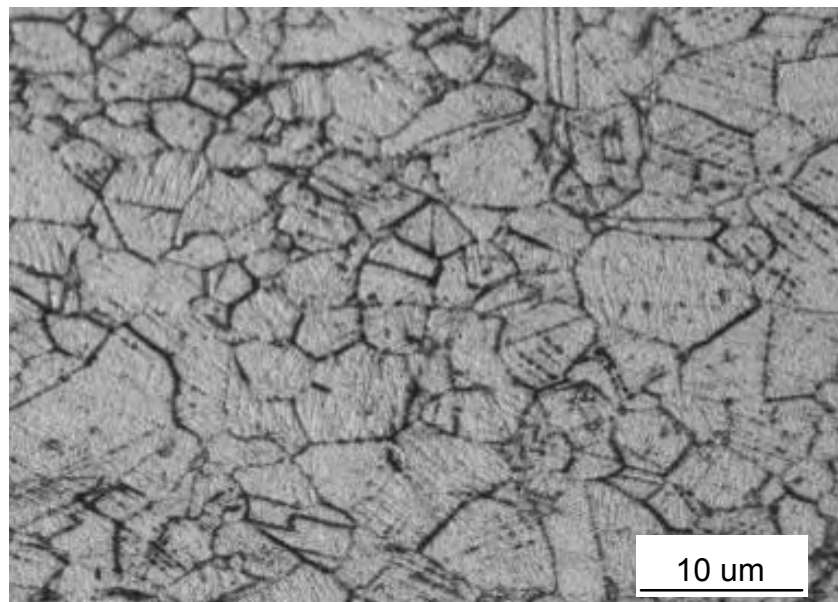


Figure 3.18: a) IN718 weld microstructure b) IN718 parent microstructure

It has been shown that the yield stress of IN718 weld material may be as much as 25% lower than that of the parent material [92]. Correspondingly, stress-strain curves for the weld material at different temperatures were resolved by calculating the difference in strain of non-welded and cross-welded specimen tensile tests, and determining what the properties of the weld must be in order to give the measured test results (see Chapter 6 for more details). The effect the change in material properties during welding has on the residual stress and distortion states is discussed in section 3.11. The properties in the heat-affected zone (HAZ) also differ to those of the parent material due to grain growth. The HAZ is approximately a third of the weld width each side with properties that vary linearly from weld to parent [92]. This variation is ignored in these analyses. It should also be noted that due to precipitation hardening, it is difficult to obtain test data above 600°C that are representative of solution heat-treated IN718. However, the lack of appropriate high temperature data has been shown not to substantially influence the distortion and residual stress fields since they only become significant when the material regains most of its strength after cooling [44].

3.9 Mechanical analysis

In the elastic-plastic mechanical analysis, the total strain is given by [54]:

$$\varepsilon_{ij} = \varepsilon_{ij}^e + \varepsilon_{ij}^p + \varepsilon_{ij}^{th} \quad (3.7)$$

where ε_{ij}^e is elastic strain, ε_{ij}^p is plastic strain and ε_{ij}^{th} is thermal strain. The stress is related by the following constitutive law (for an isotropic thermoelastic material):

$$\sigma_{ij} = C_{ijrs}^e (\varepsilon_{ij}^e - \varepsilon_{ij}^p - \varepsilon_{ij}^{th}) \quad (3.8)$$

where C_{ijrs}^e denotes the component of the elastic constitutive tensor.

Therefore, using the temperature history exported from the thermal analysis as input for the mechanical analysis, thermal strains are generated, which result in stress and distortion. Mechanical boundary conditions are required, as shown in Figure 3.15.

The predicted distortion modes for a 200mm long x 50mm wide x 2mm thick bead-on-plate weld are presented in Figure 3.19 and Figure 3.20.

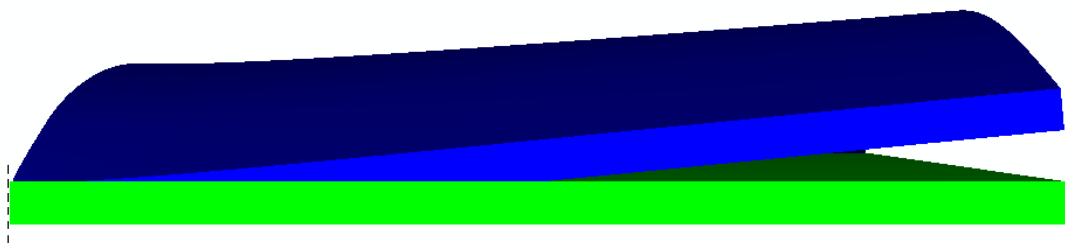


Figure 3.19: 5.6° Predicted angular distortion (in blue)



Figure 3.20: 6mm Predicted cambering (in blue)

The predicted longitudinal residual stress distribution and both cambering and angular modes of distortion for a 200mm long x 100mm wide x 2mm thick bead-on-plate weld are presented in Figure 3.21. A cross section transverse to the weld is shown in Figure 3.22 and a plot of the longitudinal stress on the bottom surface in Figure 3.23. The (minimal) through-thickness residual stress is shown for the cross section in Figure 3.24.

A plan view and a transverse cross section showing the predicted transverse residual stress are shown in Figure 3.25 and Figure 3.26, respectively. A plot of the transverse residual stress at the mid-plane of the cross section is presented in Figure 3.27.

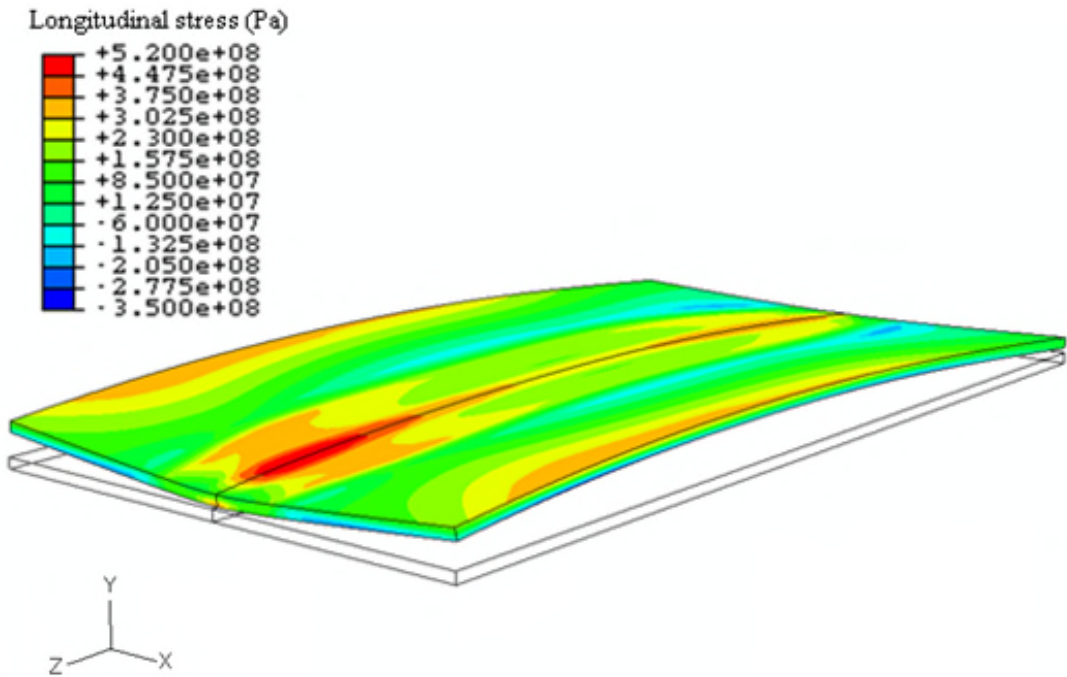


Figure 3.21: 200mm long x 100mm wide plate, longitudinal residual stress (results mirrored about weld centreline for illustrative purposes)

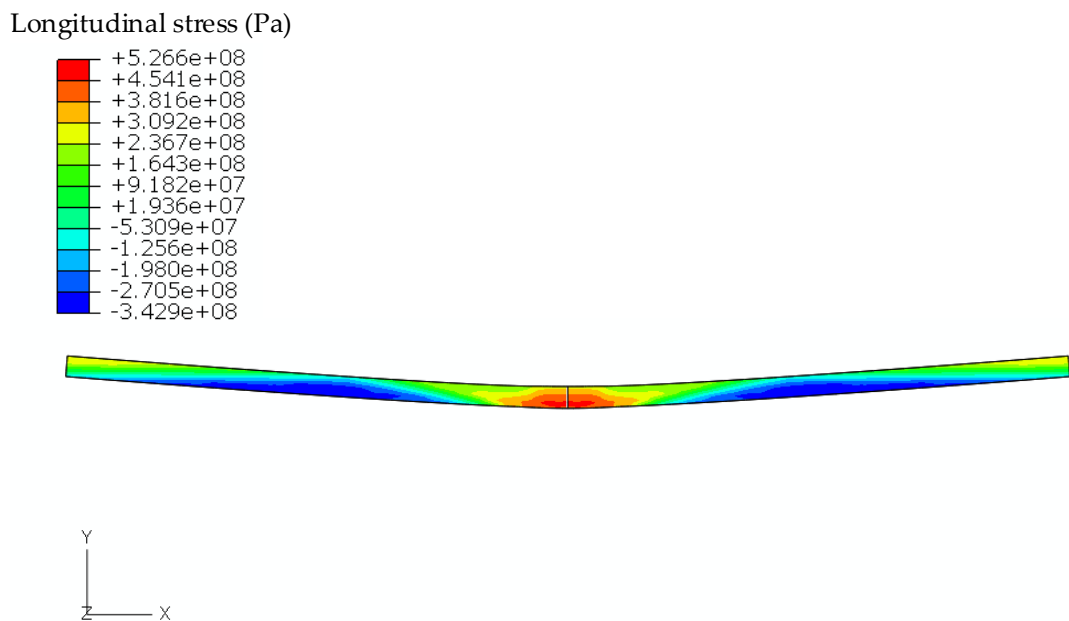


Figure 3.22: 200mm long x 100mm wide plate, mid-length transverse cross section, longitudinal residual stress

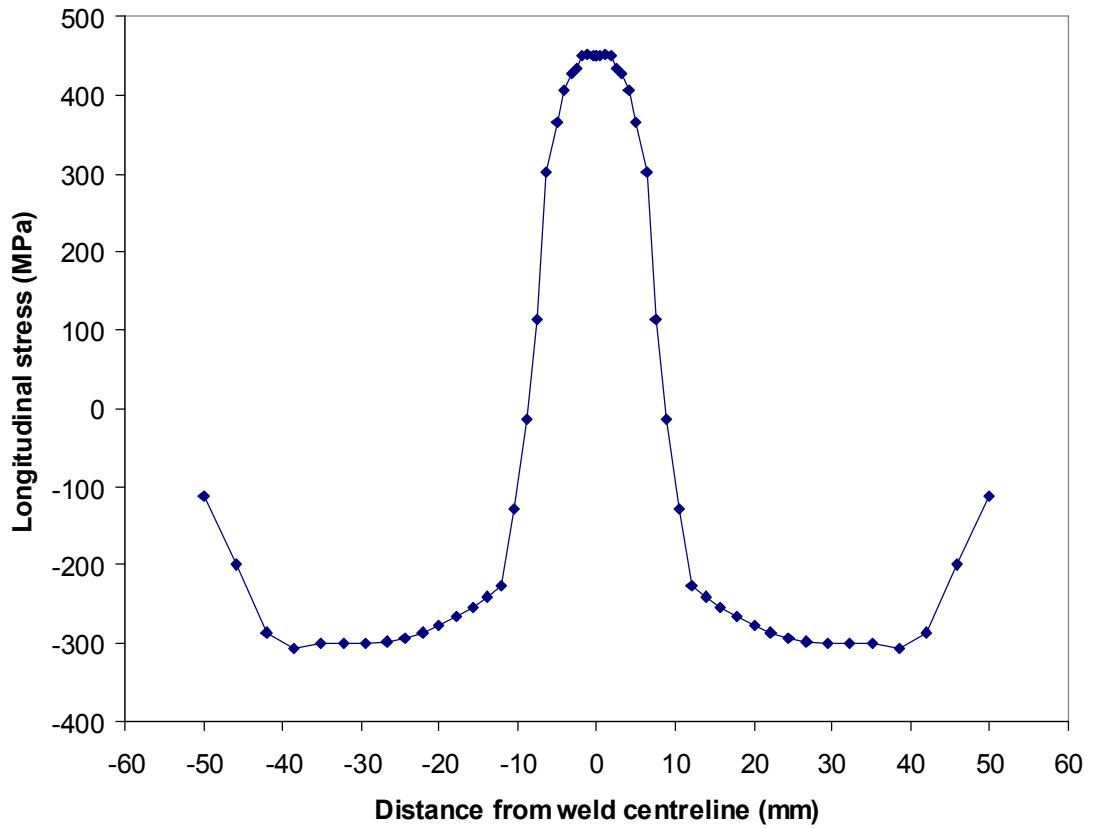


Figure 3.23: 200mm long x 100mm wide plate, mid-length transverse cross section, bottom surface, longitudinal residual stress

Through-thickness stress (Pa)

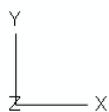
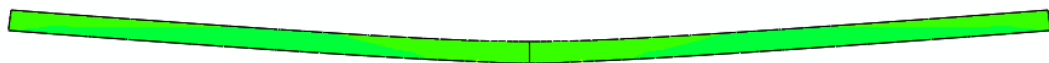
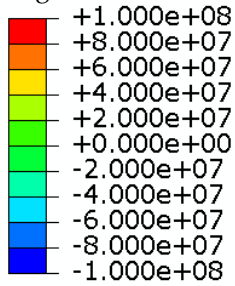


Figure 3.24: 200mm long x 100mm wide plate transverse cross section, (minimal) through-thickness residual stress

Transverse stress (Pa)

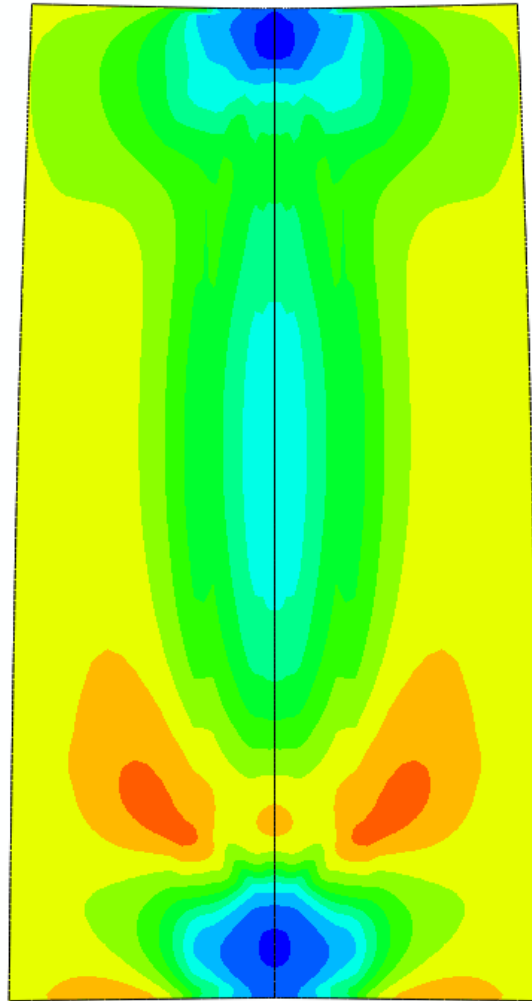
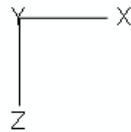
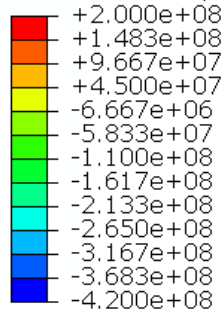


Figure 3.25: 200mm long x 100mm wide plate, transverse residual stress

Transverse stress (Pa)

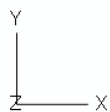
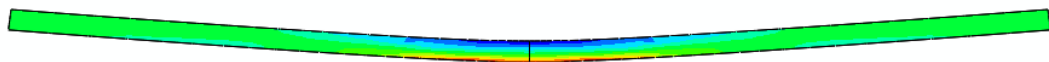
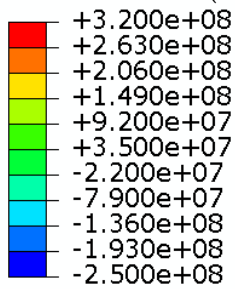


Figure 3.26: 200mm long x 100mm wide plate, mid-length transverse cross section, transverse residual stress

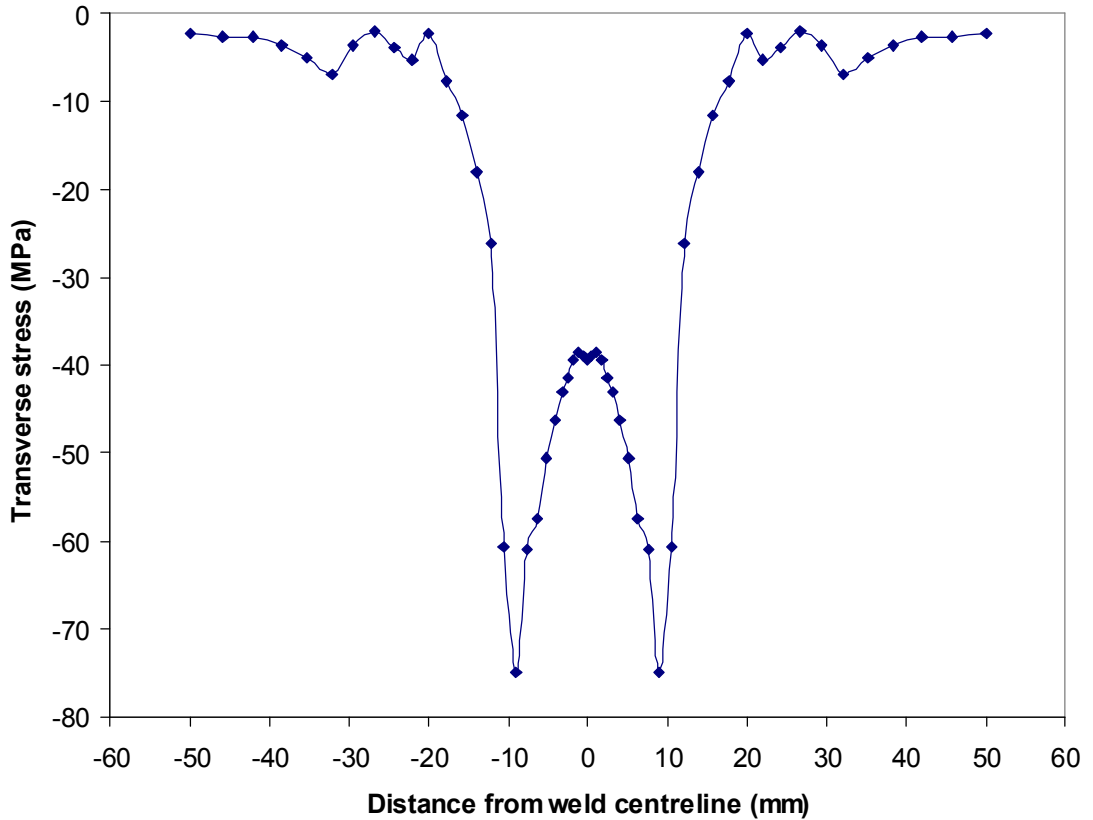
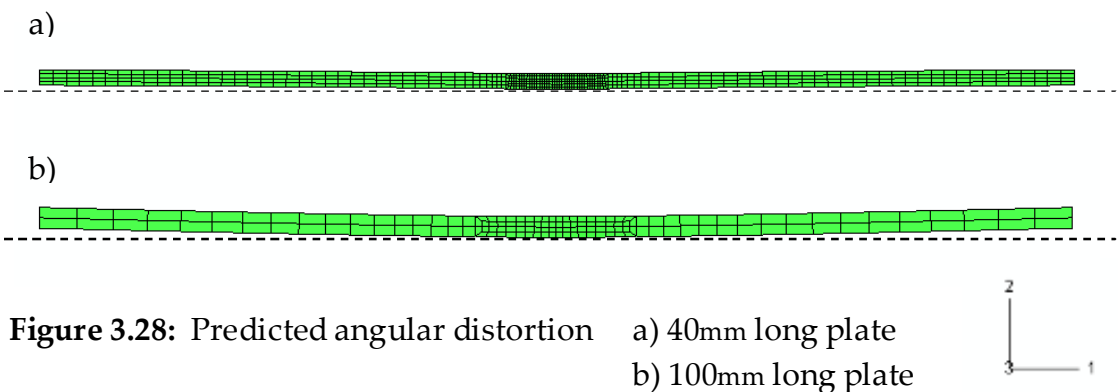


Figure 3.27: 200mm long x 100mm wide plate, mid-length transverse cross section, mid-plane, transverse residual stress

Both the transverse and the longitudinal residual stresses are largely invariant within the central portion of the weld (e.g. Figure 3.25), but there is a large variation through the thickness (e.g. Figure 3.26). There is no significant stress in the through-thickness direction (Figure 3.24). Figure 3.23 illustrates that there is a tensile longitudinal stress of yield stress magnitude around the weld centreline, balanced by compressive stress elsewhere. The change in sign of transverse residual stress (i.e. from compressive to tensile) through the thickness of the cross section (Figure 3.26) relates to the angular distortion of the plate. These results are comparable with those of Dye *et al.* [44].

Different size plates were modelled to evaluate both the effect of the length of weld and the width of the plates. In general, the distribution of residual stress was the same for all models but the tensile longitudinal residual stresses were slightly higher for smaller plates and the compressive stresses occurred slightly closer to the weld centreline. The compressive longitudinal residual stresses were also slightly higher for smaller plates, which is necessary to balance out the higher tensile stresses. Tensile transverse residual stresses were also higher for smaller plates since they are stiffer and can therefore support more stress without distorting as much (0.3° compared with 1.4° –see Figure 3.28), the decrease in welding time also has a beneficial effect on distortion.

A comparison of the angular distortion between a 40mm long plate (0.3°) and a 100mm long plate (1.4°) is shown in Figure 3.28. The distortion of the larger plate is more evident.



3.10 Effects of annealing/plastic strain relaxation

Since the mechanical analysis treats molten material as a soft-solid, artificial plastic strain will accumulate during heating and will lead to physically unrealistic predictions of residual plastic strains and stresses [19, 44]. Upon melting, any plastic strains should be completely relieved. At temperatures below the melting point, the plastic strain may also be reduced by annealing processes [21]. This phenomenon can be accounted for in a numerical model by resetting any plastic strains accumulated at a point in the material during the heating phase to zero when (or if) the temperature at that point reaches the material's melting (or annealing) temperature, therefore any work hardening history is lost [109] (see Figure 3.29).

In these analyses, the annealing temperature is assumed to be the same as the melting (solidus) temperature (1240°C). The coefficient of thermal expansion is also chosen to decrease with increasing temperature so that heating beyond the melting temperature does not lead to further expansion [44].

The annealing of plastic strains can have a significant effect in the residual strains and stresses predicted, especially when no molten filler material is added during the welding process as in the case of the 2D autogenous bead-on-plate weld example shown in Figure 3.29, Figure 3.30 and Figure 3.31 (all deformations are scaled by a factor of 5 for illustrative purposes).

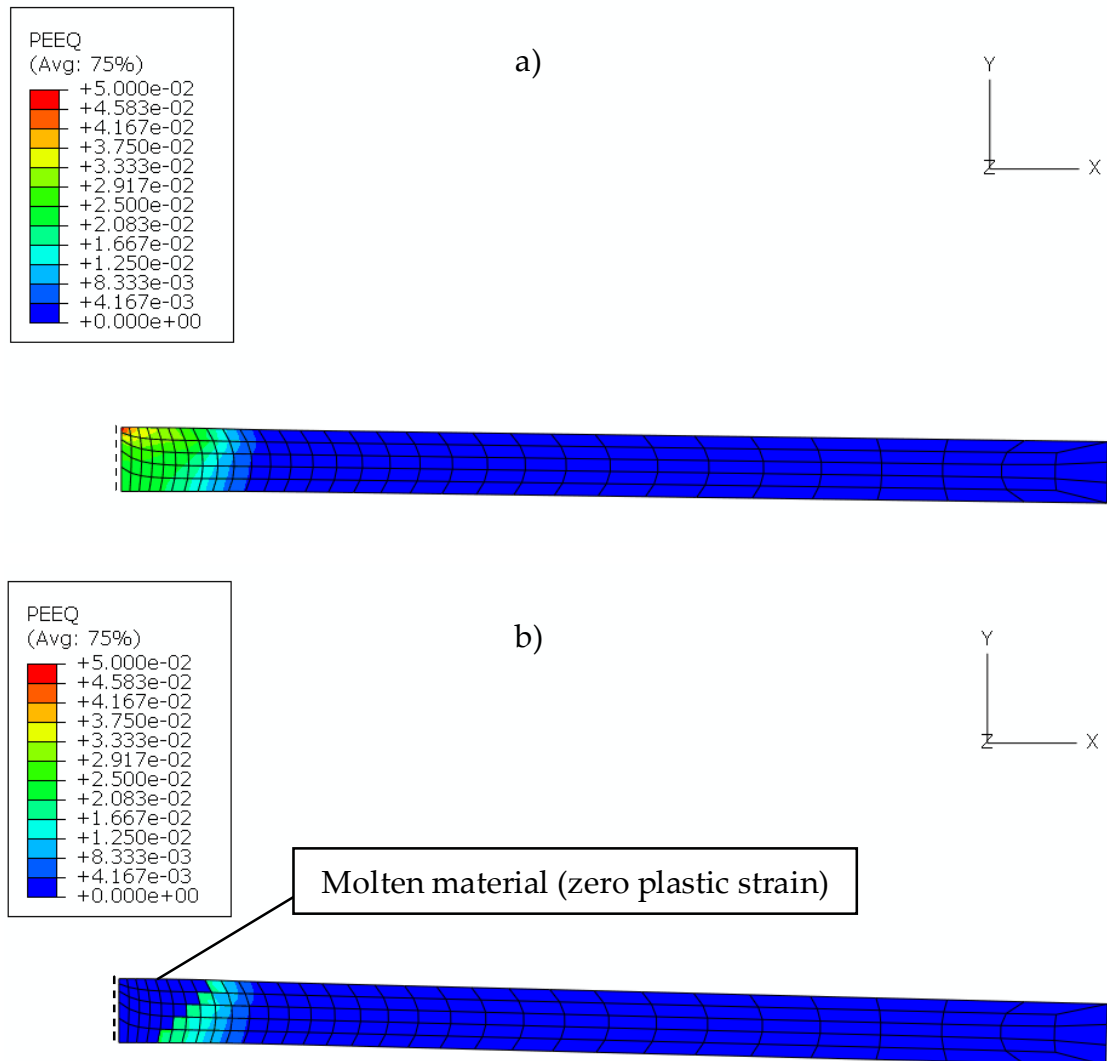


Figure 3.29: Annealing of equivalent plastic strain during heating:
 a) without plastic strain relaxation
 b) with plastic strain relaxation
 (deformation scaled by a factor of 5)

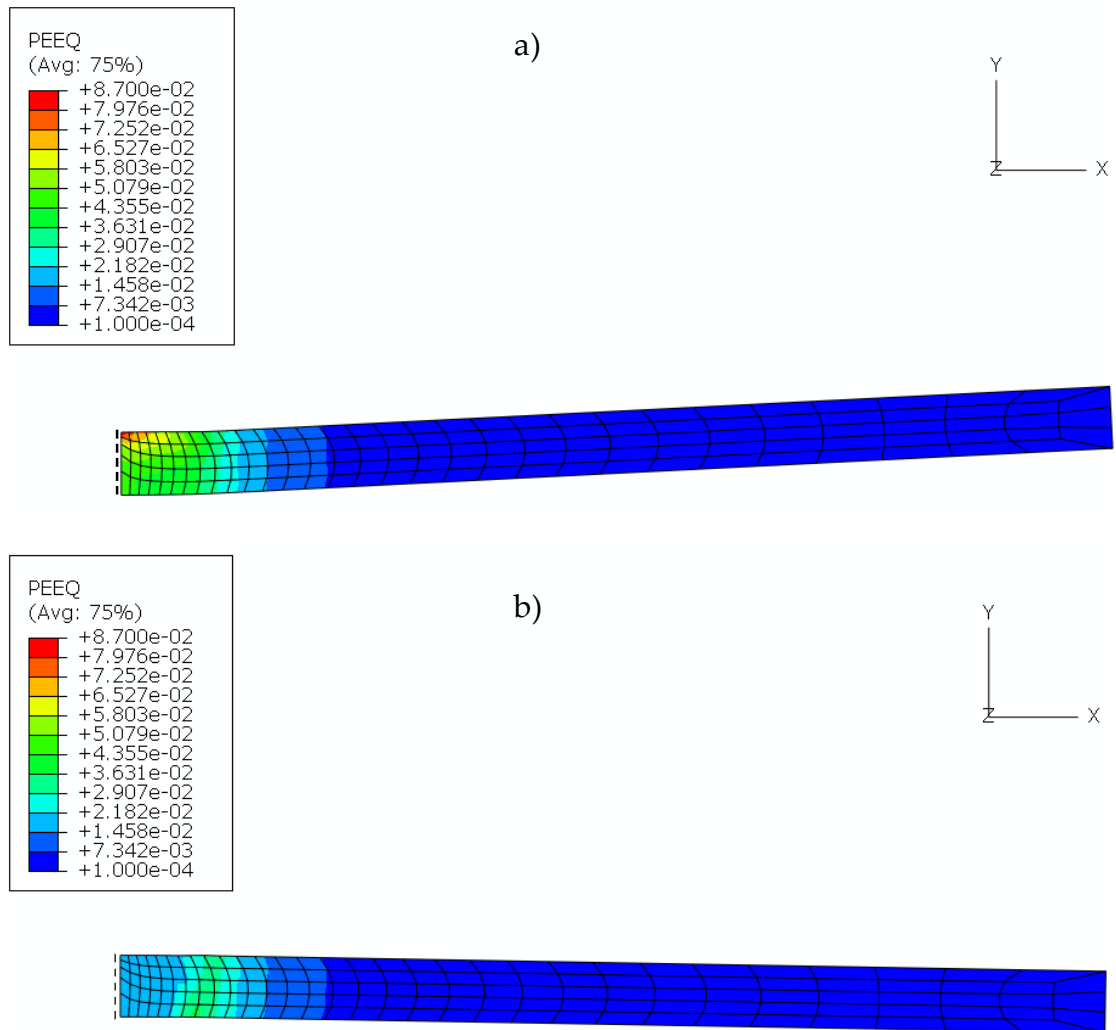


Figure 3.30: Final equivalent plastic strain:
 a) without plastic strain relaxation
 b) with plastic strain relaxation
 (deformation scaled by a factor of 5)

The final state equivalent plastic strains are identical, except for the region that melted during the heating phase in the annealed case (b) (Figure 3.30). Because of the plastic strain relaxation, the average strain here is half of that in the non-annealed case (a).

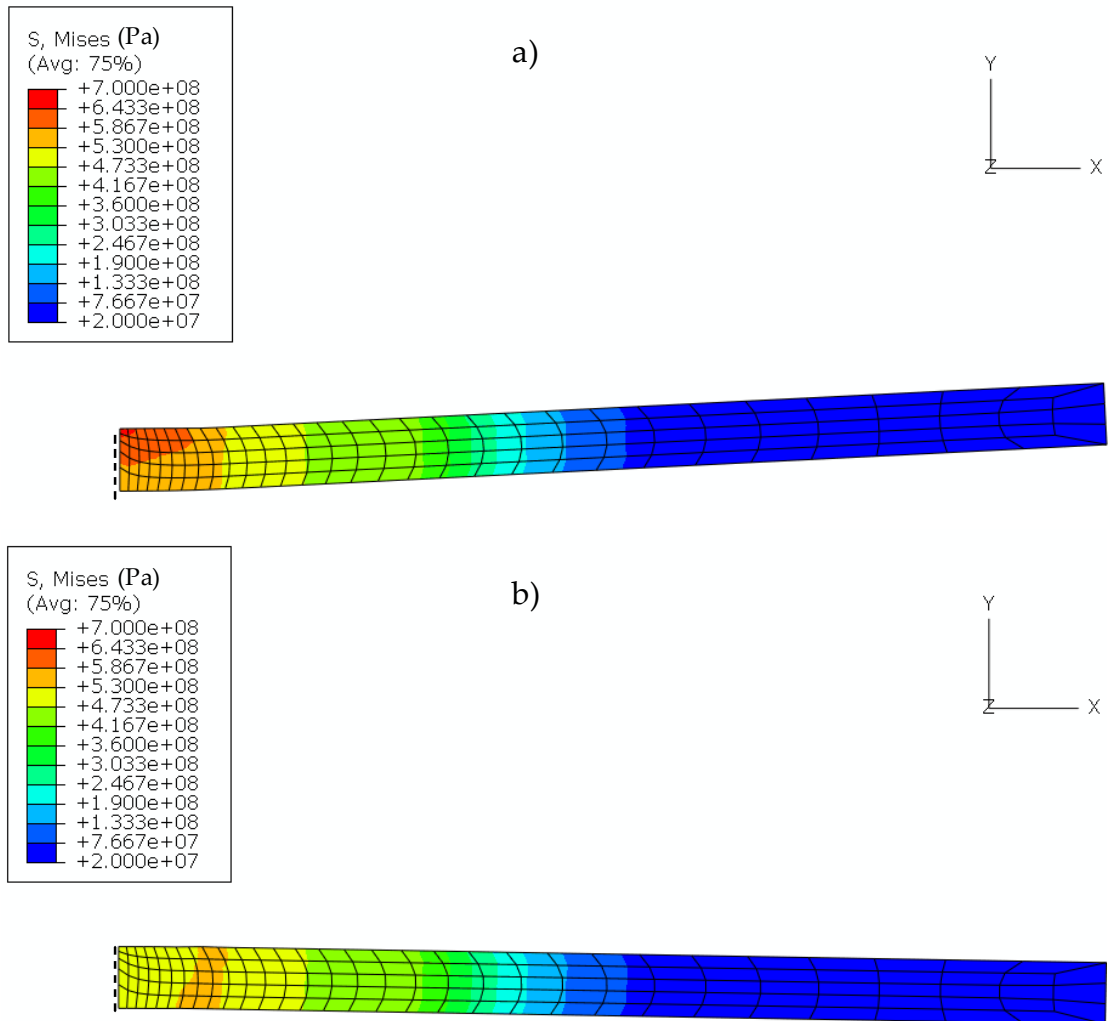


Figure 3.31: Final von Mises stress:
a) without plastic strain relaxation
b) with plastic strain relaxation
(deformation scaled by a factor of 5)

The von Mises stress distribution remains practically the same for both cases until cooling begins and the material starts to contract. In relation to the equivalent plastic strain, the final state von Mises stresses are also identical, except for the region that melted during the heating phase in the annealed case (b). Because of the plastic strain relaxation, the average stress here is about 20% less than that in the non-annealed case (a).

Most significantly, the inclusion of plastic strain relaxation (annealing) has resulted in a reverse in the direction of angular distortion in this 2D example.

The peak residual stress and plastic strain occur in the parent material for the annealed case, not in the weld, and the distribution is biased towards the bottom of the plate rather than the top. This results in a reverse of the direction of angular distortion. This highlights the importance of including the effects of plastic strain relaxation.

3.11 Effect of using different weld mechanical properties

The effect of substituting the mechanical properties of the material upon melting only has a slight effect on the residual stress (-7%) and deformation (-2%) for the case of IN718 (Figures 3.32-3.34).

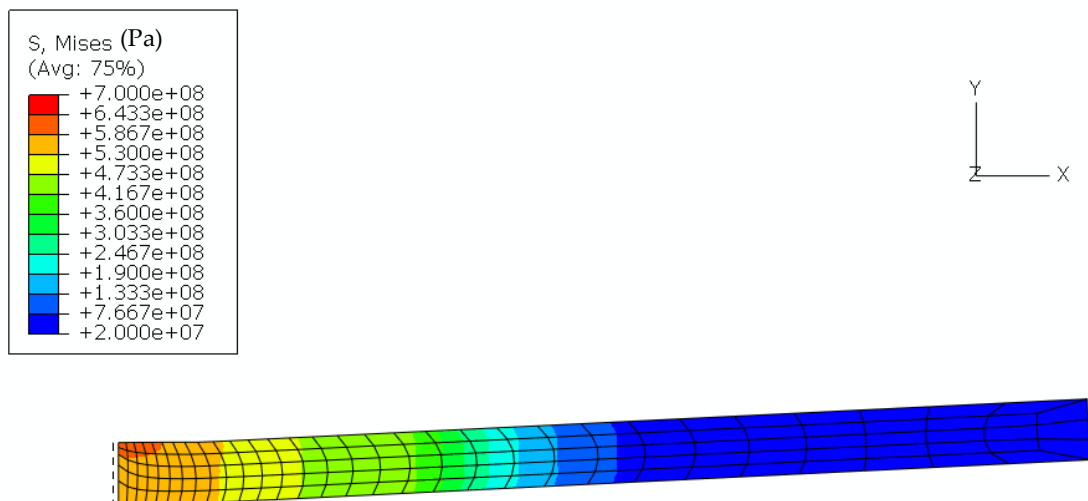


Figure 3.32: Final von Mises stress (deformation scaled by a factor of 5)

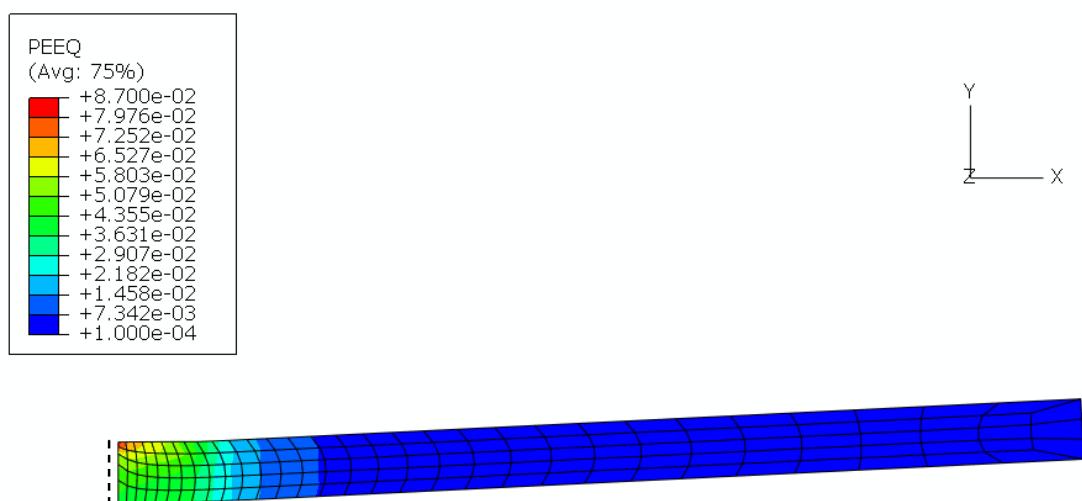


Figure 3.33: Final equivalent plastic strain (deformation scaled by a factor of 5)

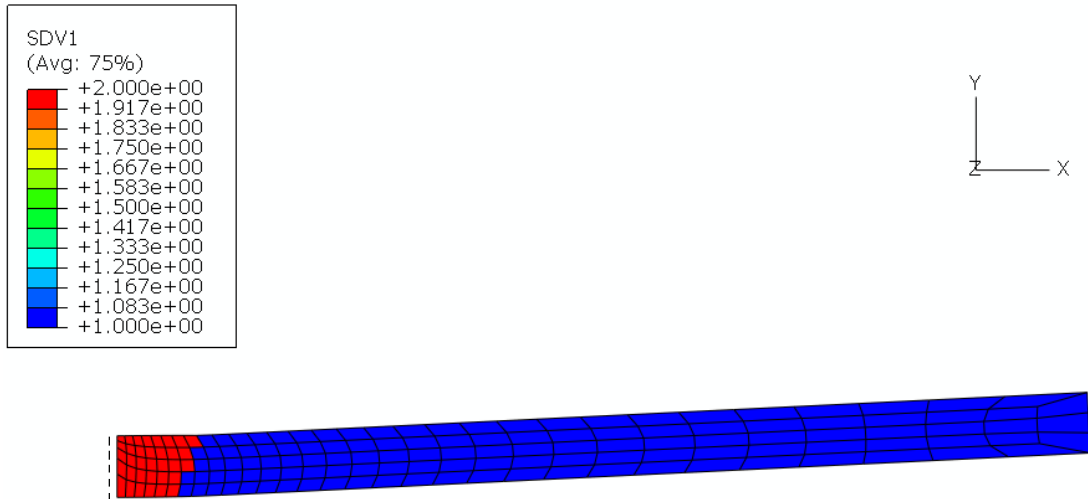


Figure 3.34: FE solution-dependent state variable (tracks material property change from 1=parent to 2=weld) (deformation x5)

Figure 3.35 shows a comparison of the residual von Mises stress across the top surface for the base case, annealed case and the above example with the change in mechanical properties upon melting.

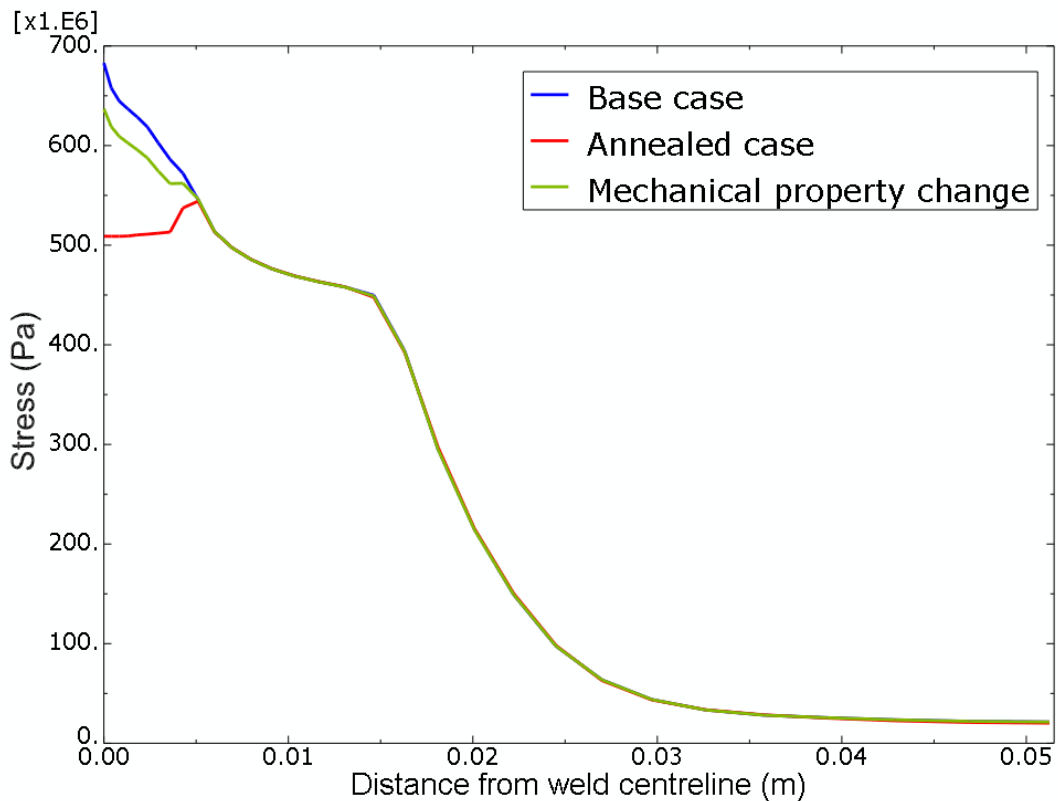


Figure 3.35: Final von Mises stress, top surface

3.12 Presetting for distortion mitigation

In order to try to mitigate distortion, predictions produced when autogenous welding plates that have been preset have been calculated (Figure 3.36 and Figure 3.37).

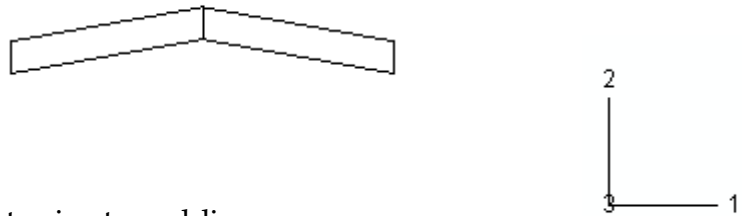


Figure 3.36: Plates preset prior to welding

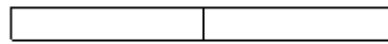


Figure 3.37: Plates after welding (as intended)

Unfortunately, presetting did not have the desired effect of reducing the angular distortion. Instead, the FE model predicts angular and also cambering distortion, in the opposite direction to the standard case, thus presetting was actually detrimental in this instance (see Figure 3.38 and Figure 3.39). As expected, presetting the plates in the converse sense to that shown in Figure 3.36 just increased the amount of angular distortion that was found in the standard case.

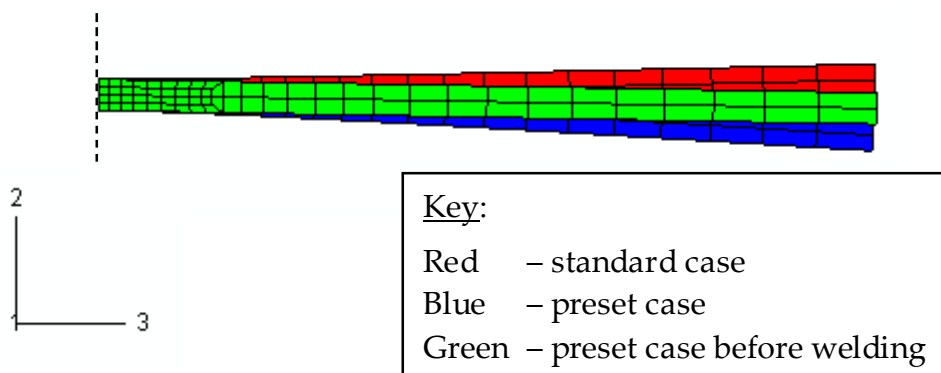


Figure 3.38: Predicted angular distortion

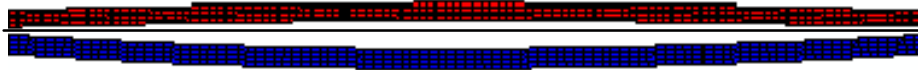


Figure 3.39: Predicted cambering distortion (Blue – preset case)

This example shows the instability of the distortion modes and that their predictions are therefore a nontrivial task, particularly since the direction of the distortions depends upon the welding process, setup and weld bead geometry.

3.13 Effects of restraint (clamping)

This section investigates the effects of clamping the plates, in terms of the stresses and distortions produced during and after welding.

3.13.1 G-type clamped model

Initially, G-type clamps are represented using two groups of nodes with pinned boundary conditions, which are relaxed after welding and cooling is complete (see Figure 3.40). It was found that both the transverse and the longitudinal stresses were higher before the clamps were released, but afterwards the residual stresses were lower and only slight angular distortion was predicted ($\approx 0.03^\circ$ as opposed to $\approx 0.9^\circ$) (Figure 3.43 and Figure 3.44). There was hardly any noticeable cambering distortion. The magnitude of the necessary restraining force was found to be reasonably large (see Figure 3.41), but only slight plastic straining was introduced around the clamps (Figure 3.42).

It appears that since clamping delays the onset of distortion, it forces both the primary modes (angular and cambering) to occur simultaneously. These modes therefore compete and this has the net effect of reducing the residual stresses and distortions.

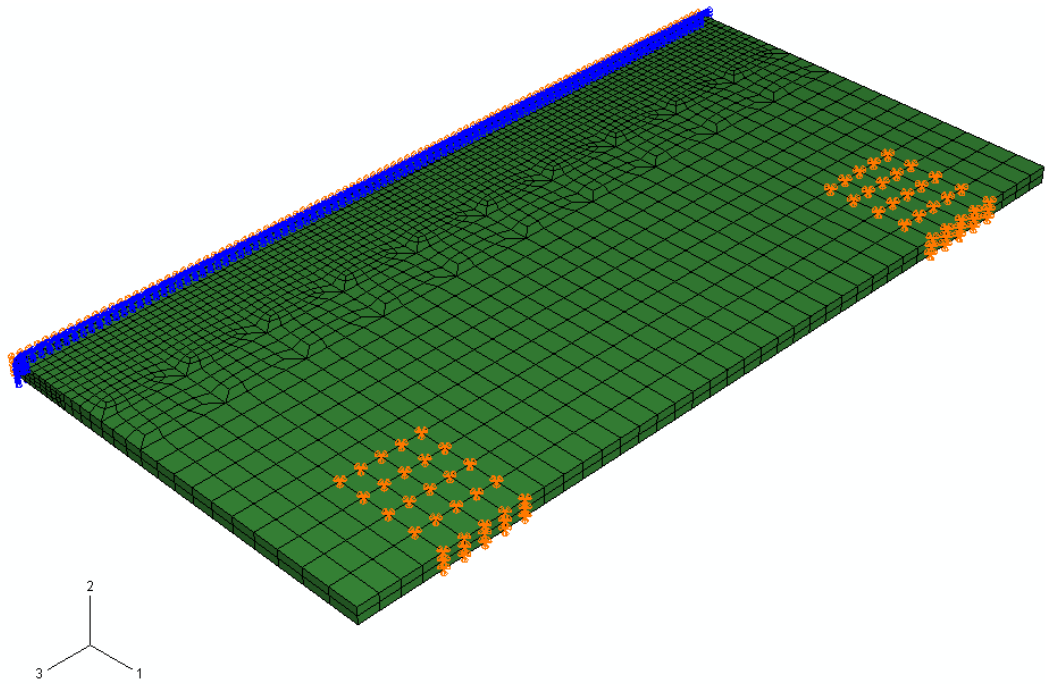


Figure 3.40: Boundary conditions: weld centreline symmetry boundary condition and two 10 x 10 mm clamps positioned 10 mm from plate ends

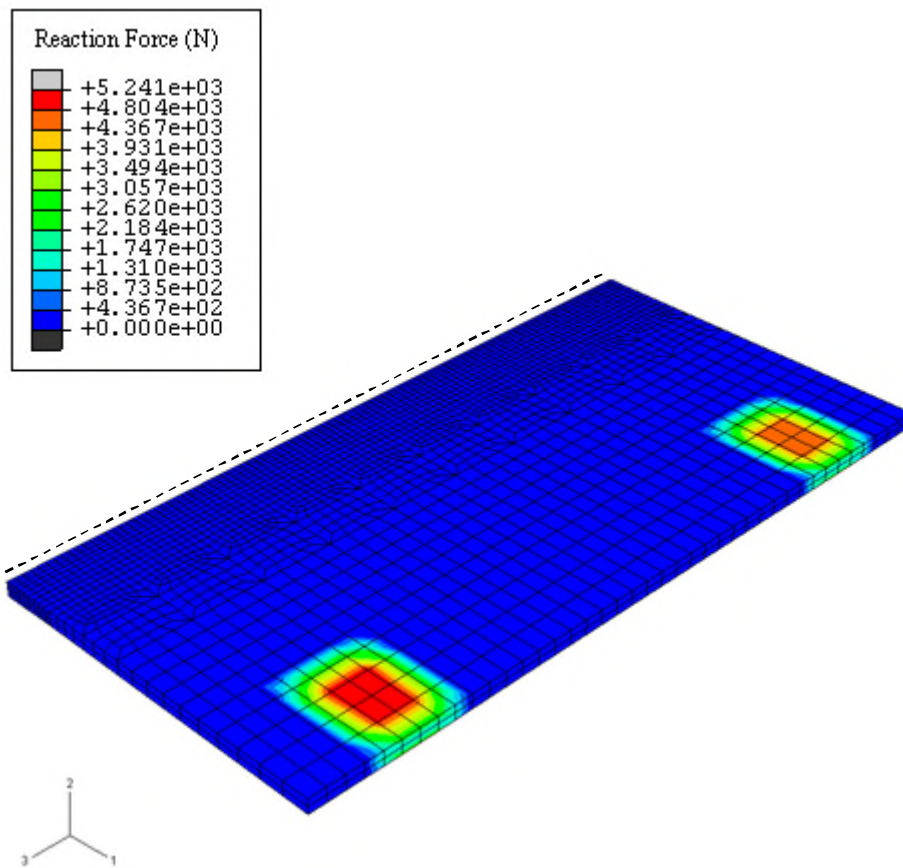


Figure 3.41: Peak reaction forces required to restrain the nodes

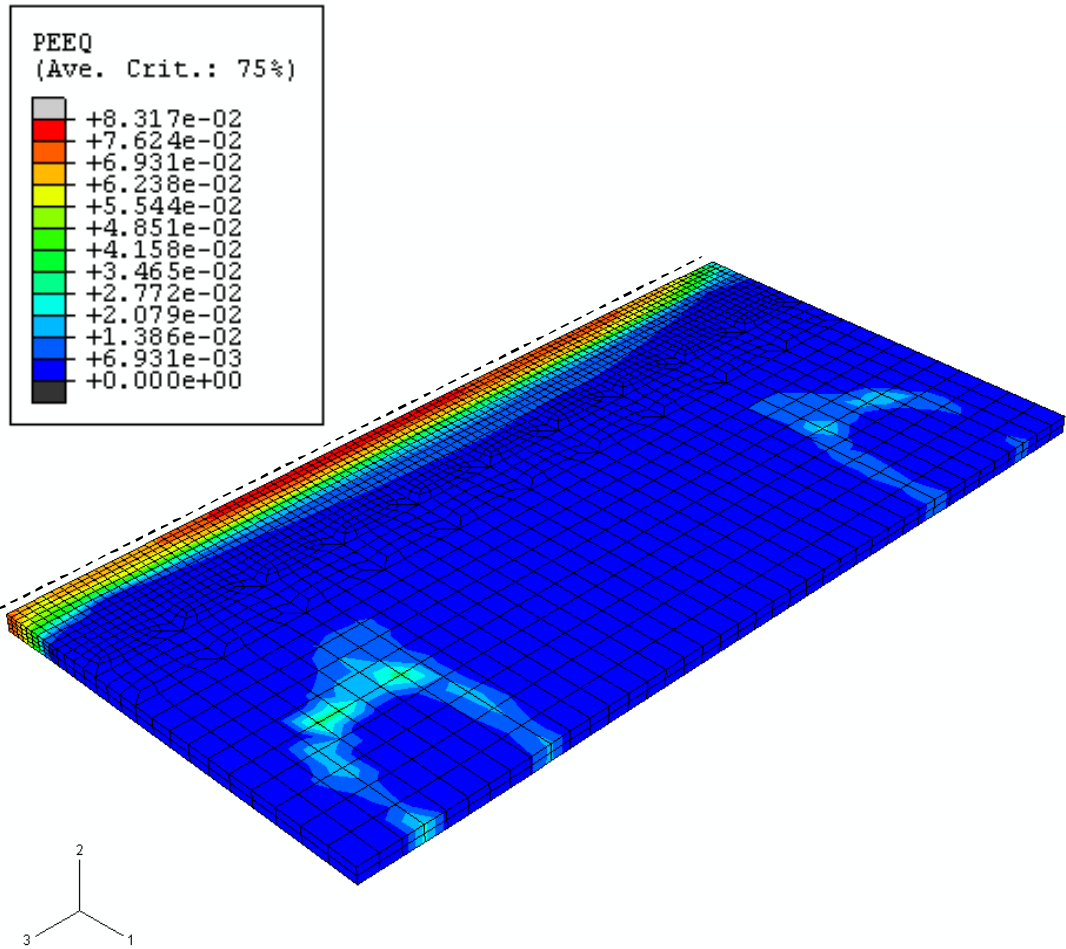


Figure 3.42: Equivalent plastic strain

After clamp removal, the highest region of equivalent plastic strain around the clamps is 3.3%. This is significantly lower than that experienced in the weld (8%).

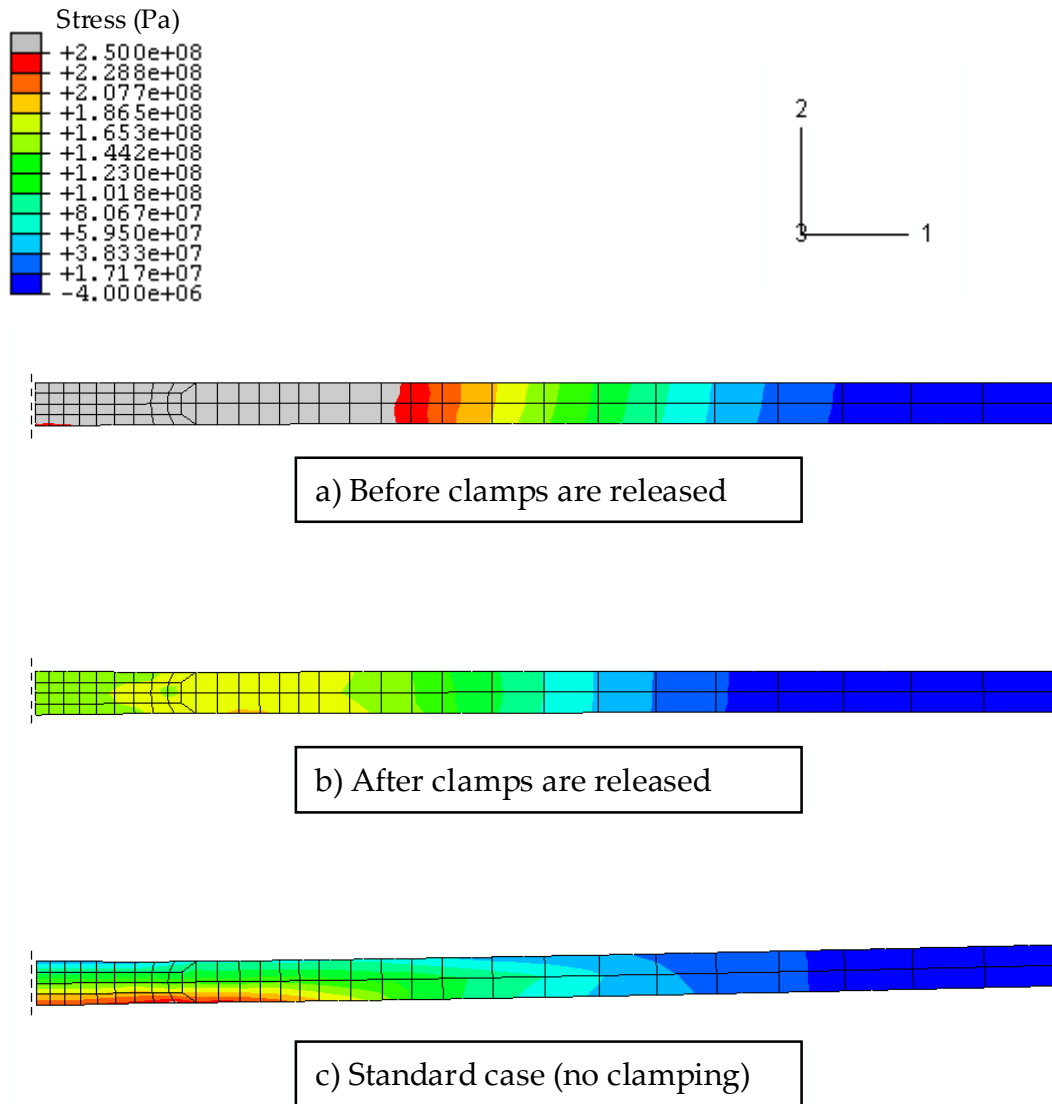


Figure 3.43: Predicted transverse stress distributions on a cross section, showing the effects of clamping

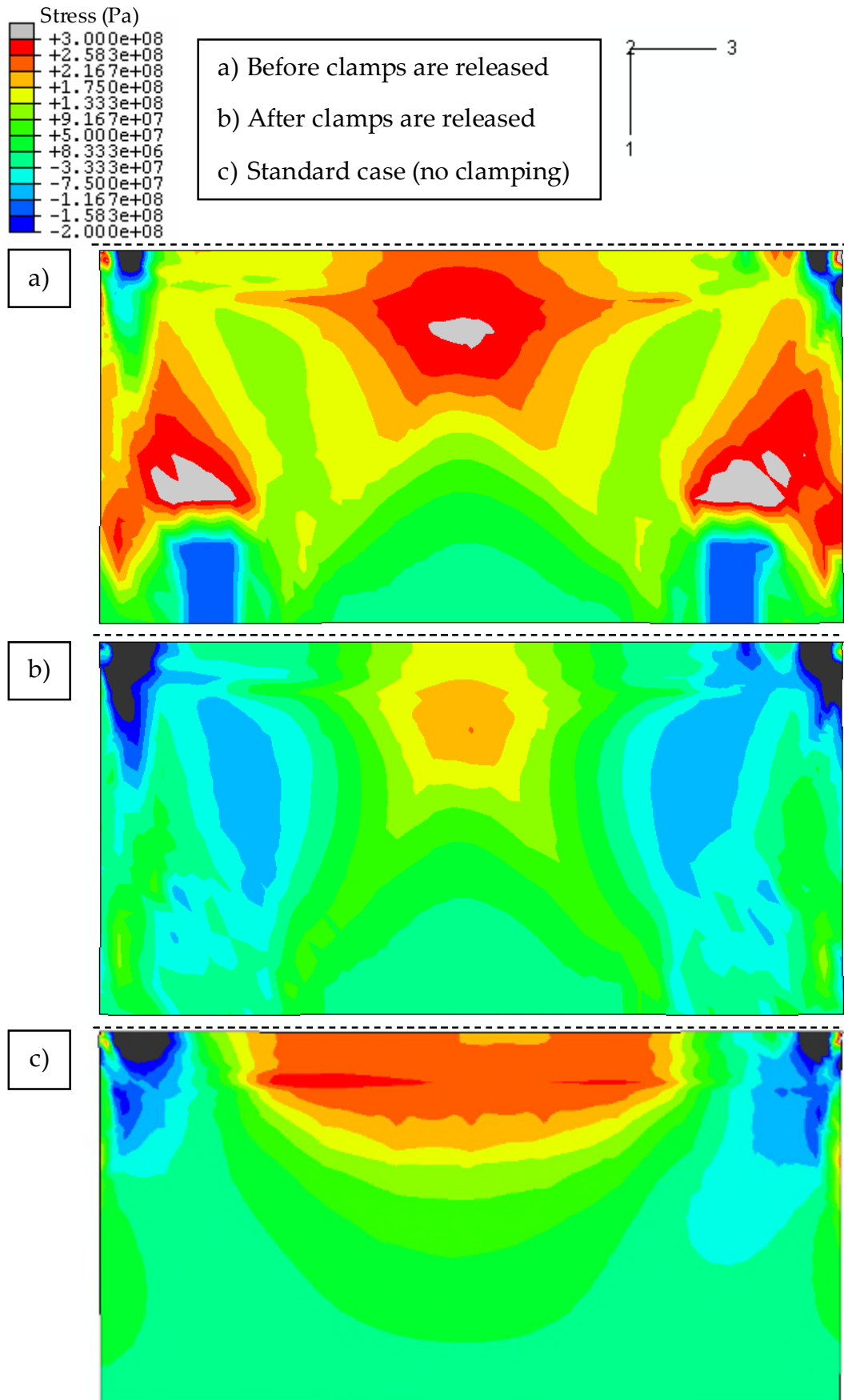


Figure 3.44: Predicted transverse stress distributions, showing the effects of clamping

3.13.2 Flat clamped model

Another model, with clamps more representative of those conventionally used during welding of plates (Figure 3.45) was also studied to evaluate the advantages and disadvantages of restraint.

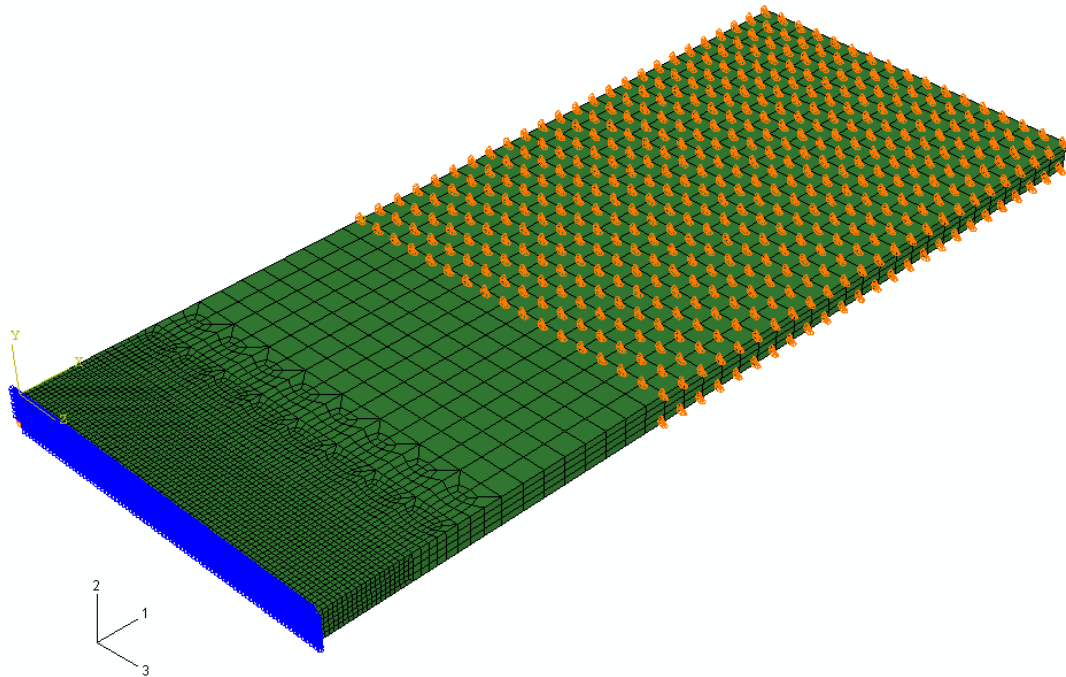


Figure 3.45: Boundary conditions: pinned (encastre) top and bottom surface, 40mm away from weld centreline

The small size of the plates (40mm x 100mm) and the restraint condition successfully mitigated any angular distortion (Figure 3.46).

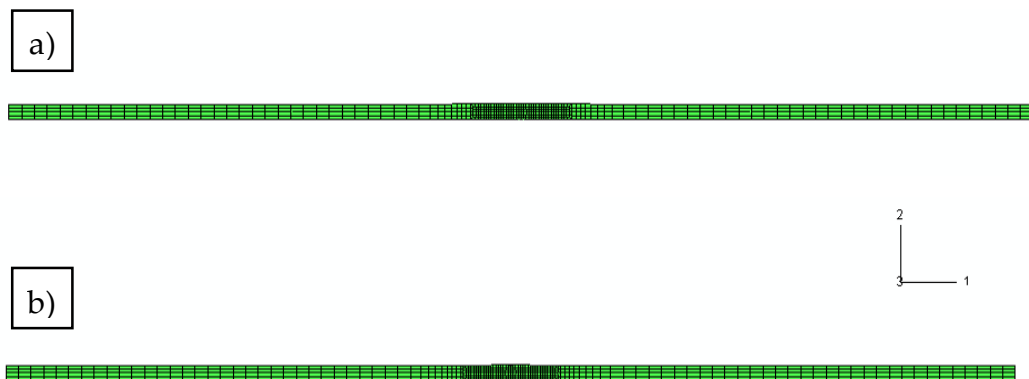
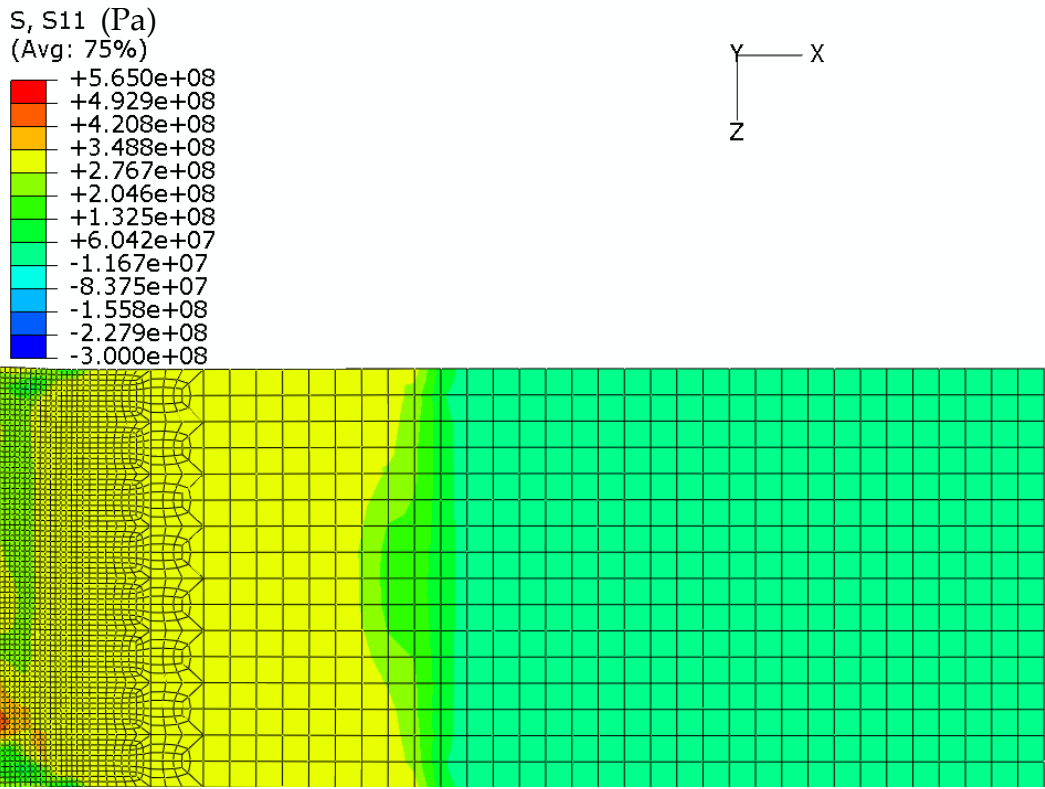


Figure 3.46: Angular distortion: a) before clamps are released
b) after clamps are released

As in the G-type clamp model, high tensile stress is generated in the unrestrained region (Figure 3.47a), which relaxes after the clamps are released (Figure 3.47b). The residual transverse stress is low across the weld (<80 MPa), rising slightly near its end (150MPa). A small band of compressive stress (100-150MPa) distinguishes the clamped (to the right) and unclamped areas (to the left) (Figure 3.47b).

The longitudinal stress only shows a slight change in distribution across the clamped/unclamped interface when the clamps are released (Figure 3.48). This is expected since these plates are less prone to cambering since they are short, and therefore relatively stiff.

When considering the suitability of shorter plates for producing tensile specimens, it should be noted that the slight difference in residual stress across the width of gauge length seen here will redistribute during postweld heat treatment and subsequent machining of the specimen.



a): Transverse stress distribution before clamps are released

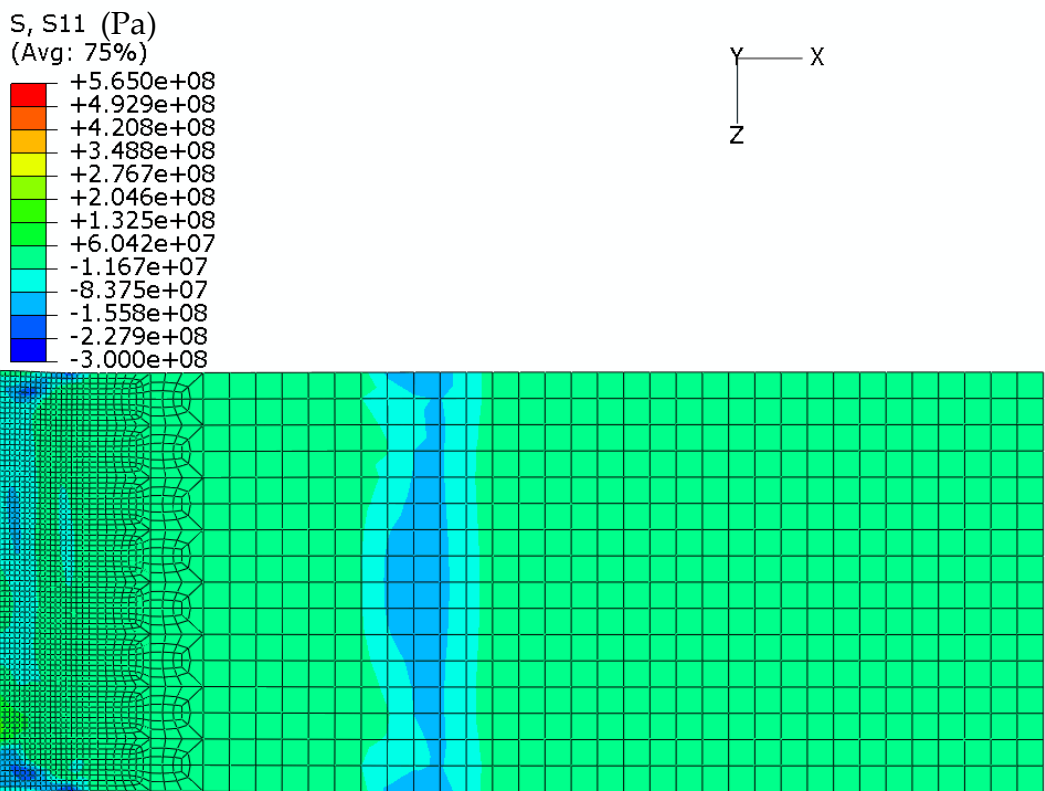
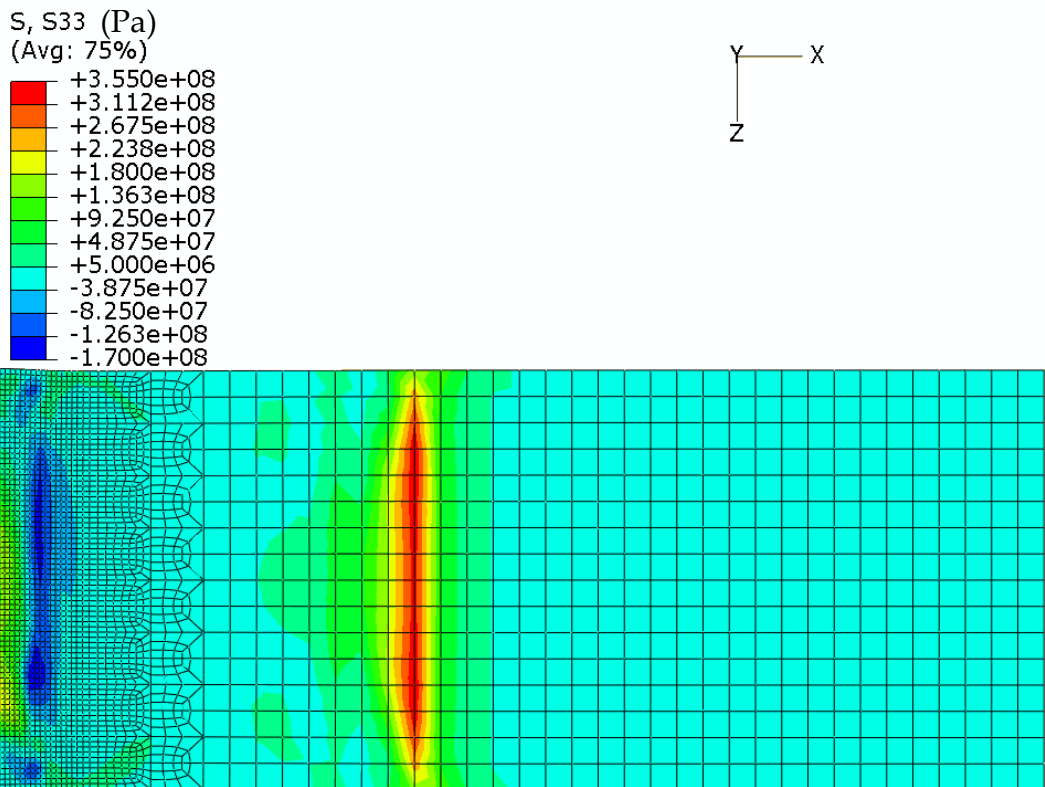


Figure 3.47 b): Transverse stress distribution after clamps are released



a): Longitudinal stress distribution before clamps are released

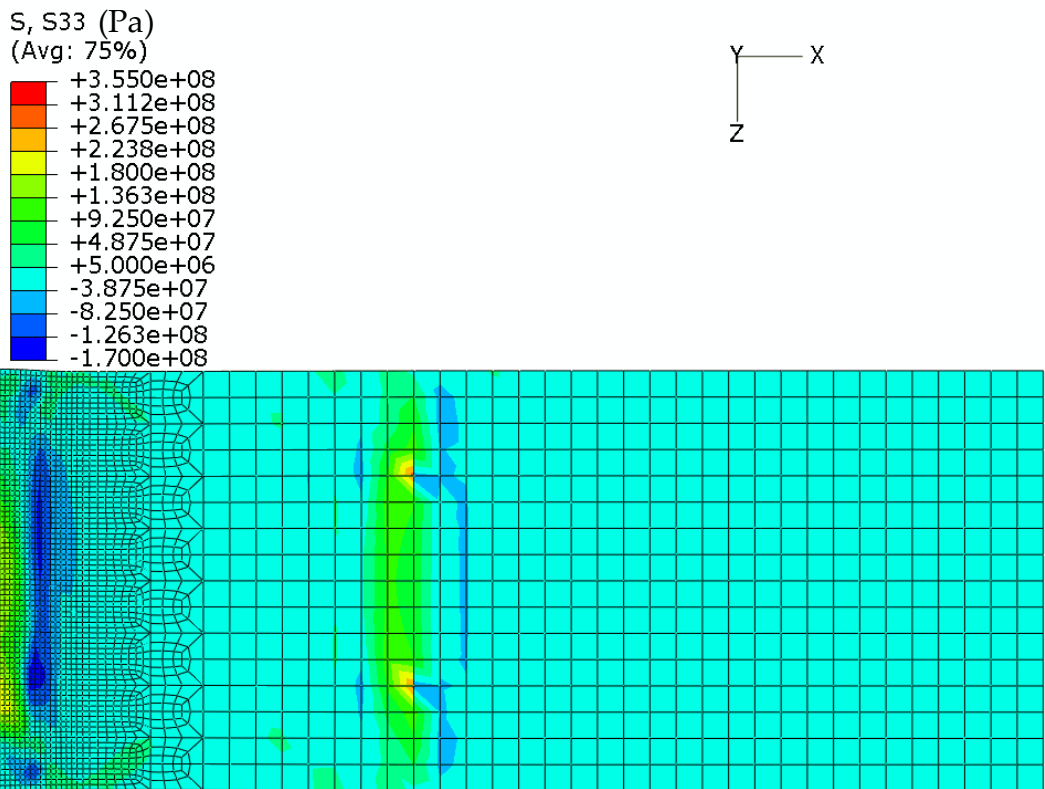


Figure 3.48 b): Longitudinal stress distribution after clamps are released

The maximum equivalent plastic strain occurs after cooling (Figure 3.49 and Figure 3.50); there is little change during clamp release. The maximum occurs at the top surface due to greater shrinkage.

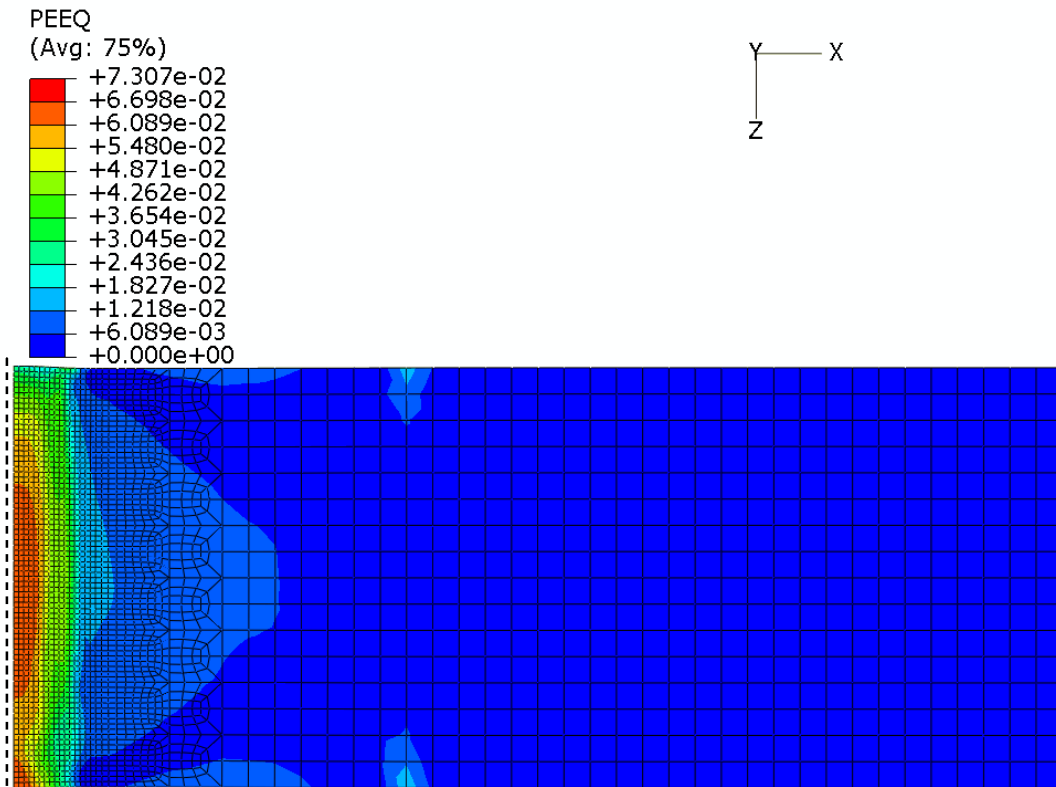


Figure 3.49: Equivalent plastic strain after clamps are released

Clamping slightly increases the plastic strain but the maximum remains lower than that found in larger welded plates that distort (e.g. 200mm-long plate, Figure 3.51 and Figure 3.52).

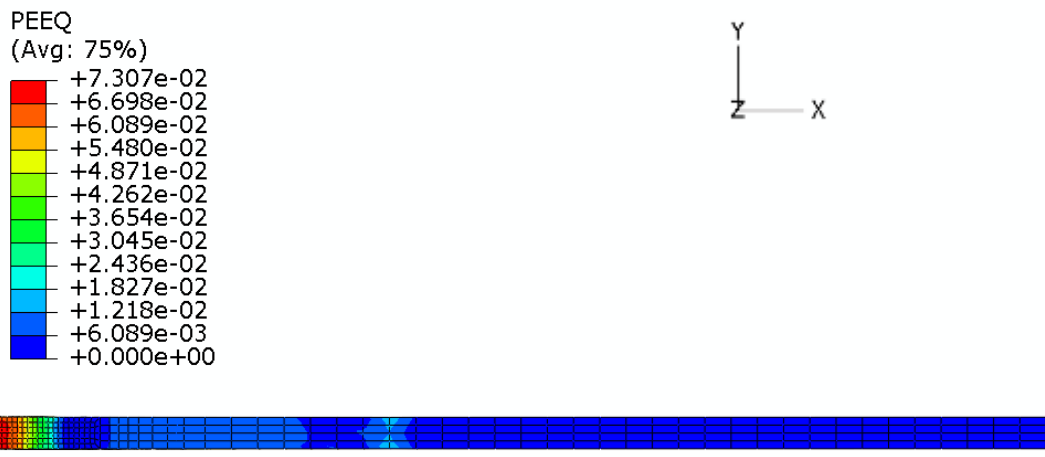


Figure 3.50: Equivalent plastic strain after clamps are released (transverse cross section)

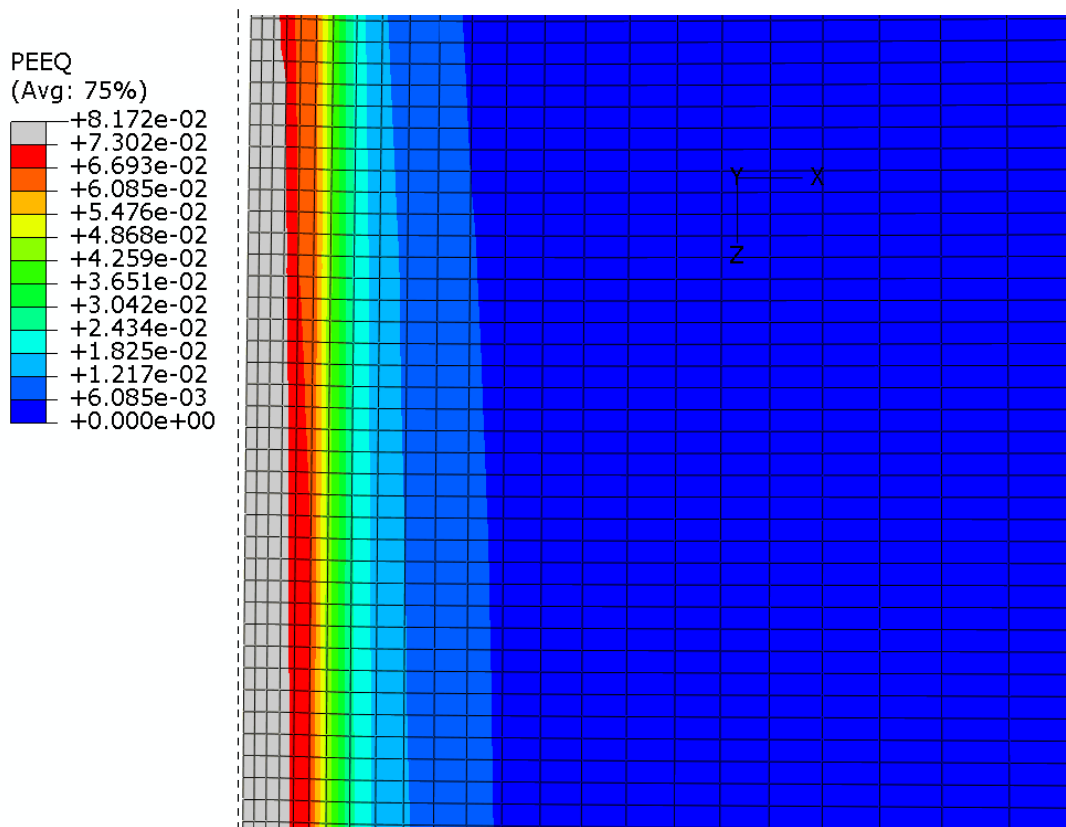


Figure 3.51: Equivalent plastic strain without clamping, 200mm-long plate (central portion of model)

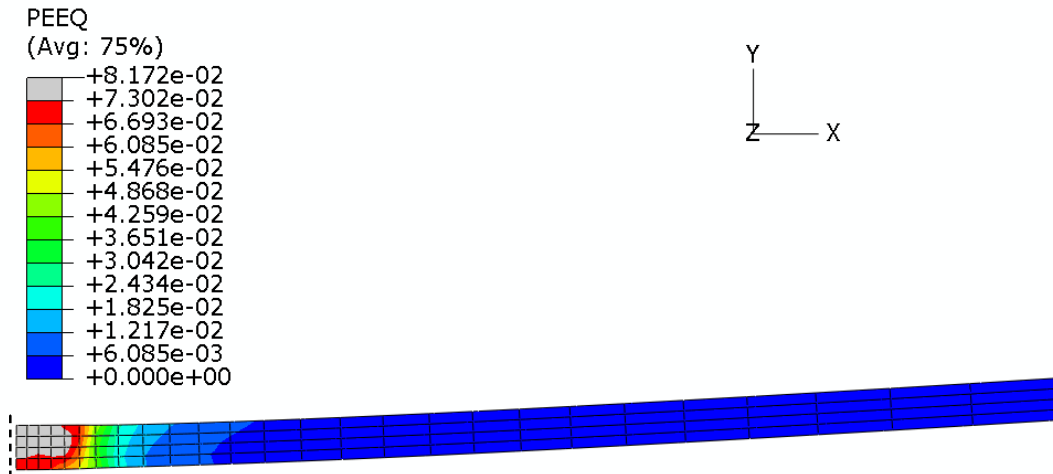


Figure 3.52: Equivalent plastic strain without clamping, 200mm-long plate (transverse cross section)

3.14 Modelling filler addition and underbead formation

A technique has been developed using the USDFLD FORTRAN user subroutine in ABAQUS to model the addition of filler during the welding process. This routine enables the user to define field variables at a material point as functions of time or of any of the available material point quantities. Therefore, USDFLD can be used to introduce solution-dependent material properties since such properties can easily be defined as functions of field variables [109]. Elements in the FE mesh that represent the filler are initially assigned material properties equivalent to those of air along with an initial melting point temperature condition and zero conductivity. This ensures that no heat is transferred to or from these elements and they also do not affect the stresses or deformations in the model until the time is reached when they exist as molten material. At this time, the subroutine switches the field variable corresponding to a change in material properties from air to the plate material. The user subroutine FILM is also used in the thermal analysis to represent the change in position of the convection boundary surface when the filler is activated.

Underbeads are often produced during the welding of thin plates due to the sagging of molten material under gravity. The technique used for modelling underbead formation is very similar to that mentioned above for welding with filler, except it is the underbead elements that undertake a change in material properties.

The following results are from a FE simulation of welding including the addition of filler and formation of an underbead. Figure 3.53 shows a region of high tensile longitudinal residual stress stretching from the top of the weld centreline to the corner where the underbead meets the plate. Lower stresses exist in the weld underbead since it is molten upon activation and therefore does not expand during the heating phase of the analysis but does shrink during cooling (Figure 3.53 and Figure 3.54). The region of increased residual stress therefore balances the region of low residual stress in order for the plate to remain in equilibrium.

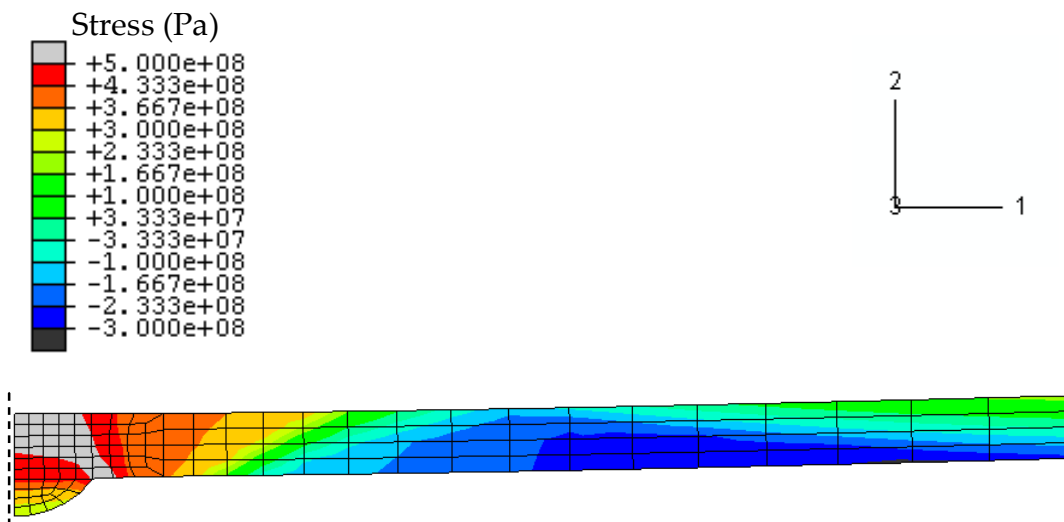


Figure 3.53: Predicted longitudinal stress distribution

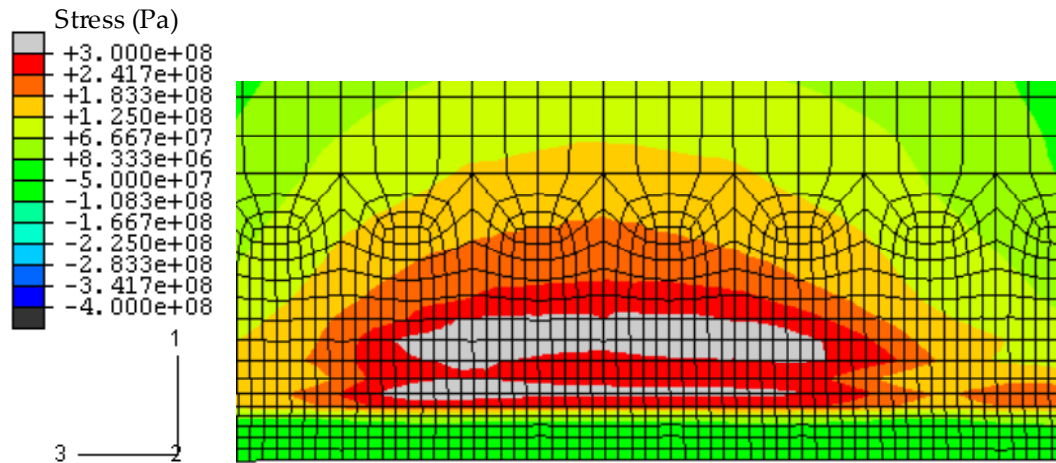


Figure 3.54: Predicted transverse stress distribution

The angular distortion for this example ranges from 1 - 2° above horizontal, varying with the distance along the plate in the welding direction. This compares well with FE models without the addition of filler or an underbead. Therefore, these effects do not significantly alter the direction or magnitude of distortion.

Figures 3.55-3.66 show detailed results from a 3D FE IN718 thin-plate arc butt-welding simulation that includes the features mentioned previously in this chapter: filler addition and weld underbead formation, annealing, and material property changes due to resolidification after melting. The results are mirrored about the weld axis of symmetry for illustrative purposes.

Figure 3.55 shows the evolution of plastic strain during the heating phase of the welding process. The annealment of plastic strain in the molten region behind the heat source can be seen. The small area around the molten region that heats up significantly but does not melt retains its plastic strain. The regions of high plastic strain at the edges of the weld underbead in Figure 3.56 indicate a potential failure site under load.

Figure 3.57 and Figure 3.58 show the peak temperatures reached during welding. The fusion zone ($>1240^{\circ}\text{C}$) is shown in white.

Figure 3.59 and Figure 3.60 show the FE-calculated region that experiences the material property change due to resolidification after melting.

Figures 3.61-3.64 show the predicted residual stress distributions, and Figure 3.65 and Figure 3.66 the predicted, angular and cambering distortions, respectively.

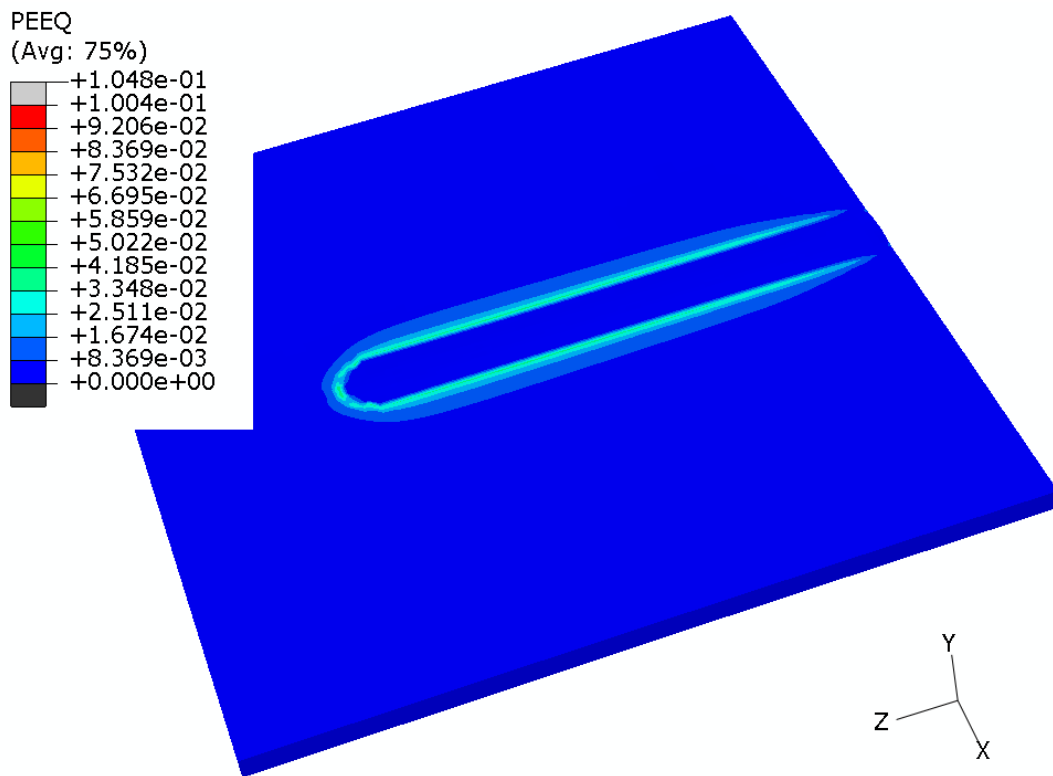


Figure 3.55: Evolution of plastic strain during welding

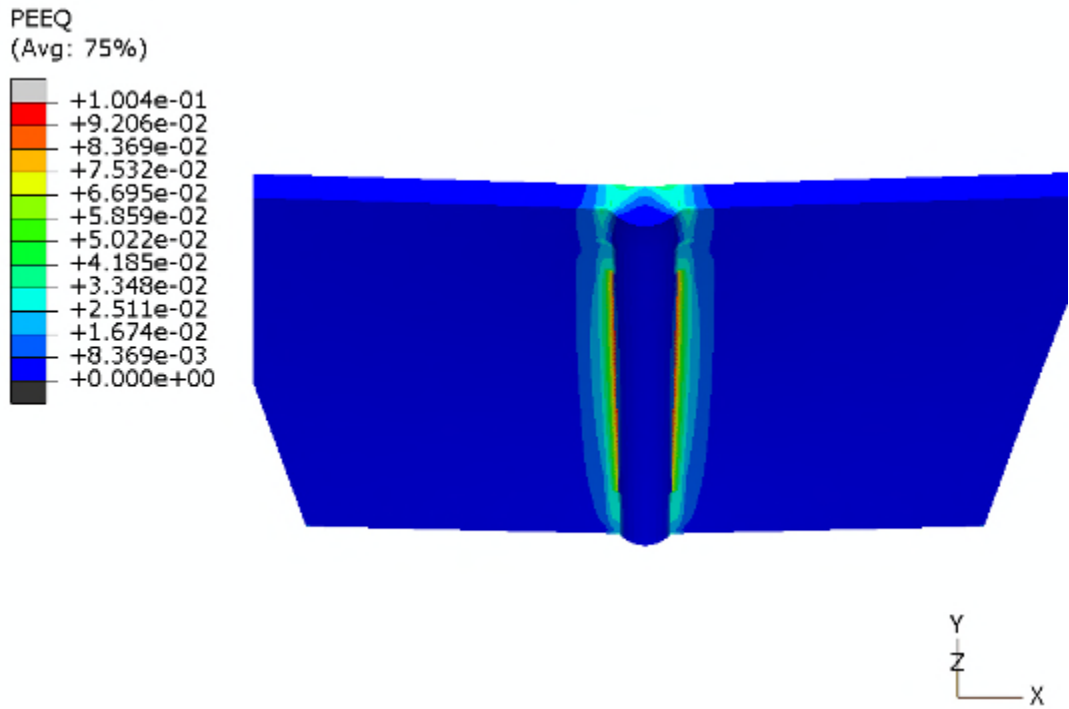


Figure 3.56: Final plastic strain state (underside)

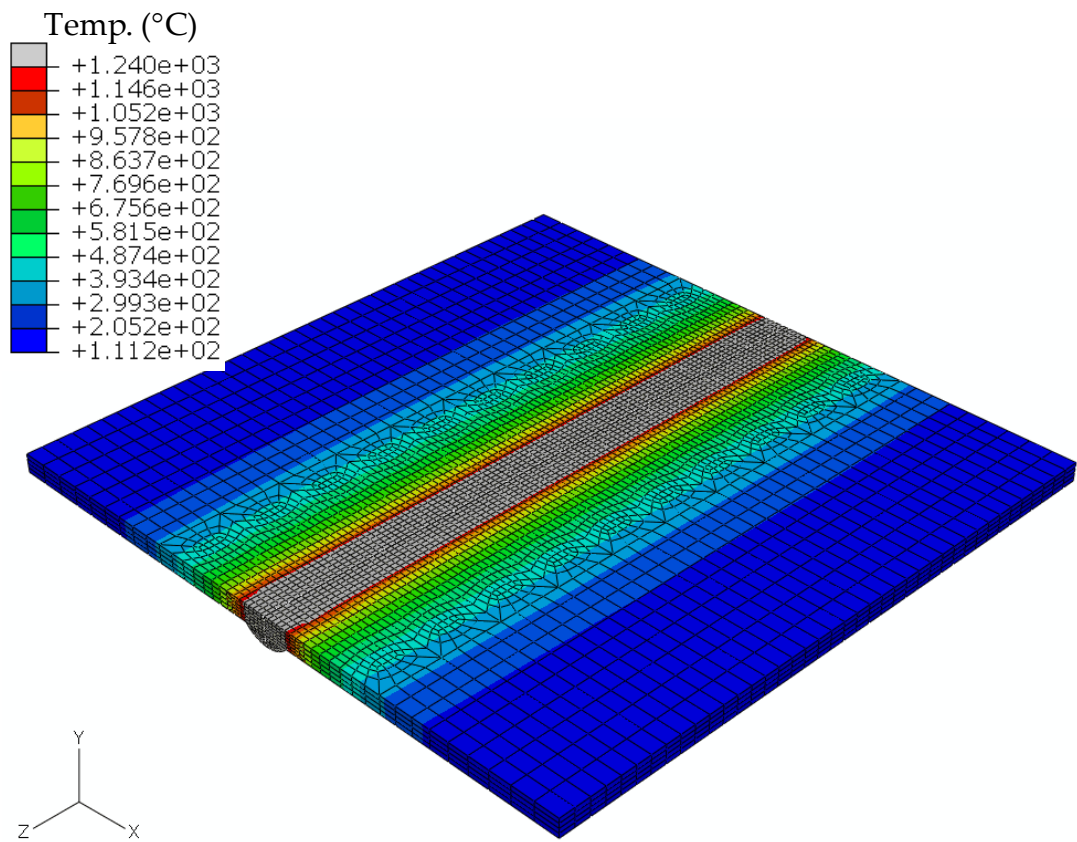


Figure 3.57: Peak temperatures reached during welding, the fusion zone is shown in white

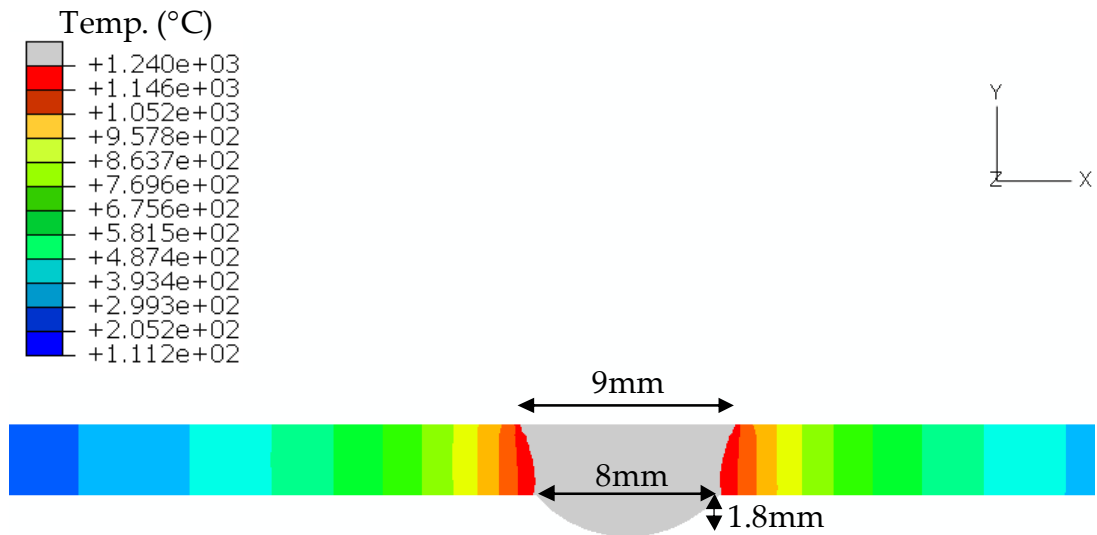


Figure 3.58: Peak temperatures reached in a transverse cross section

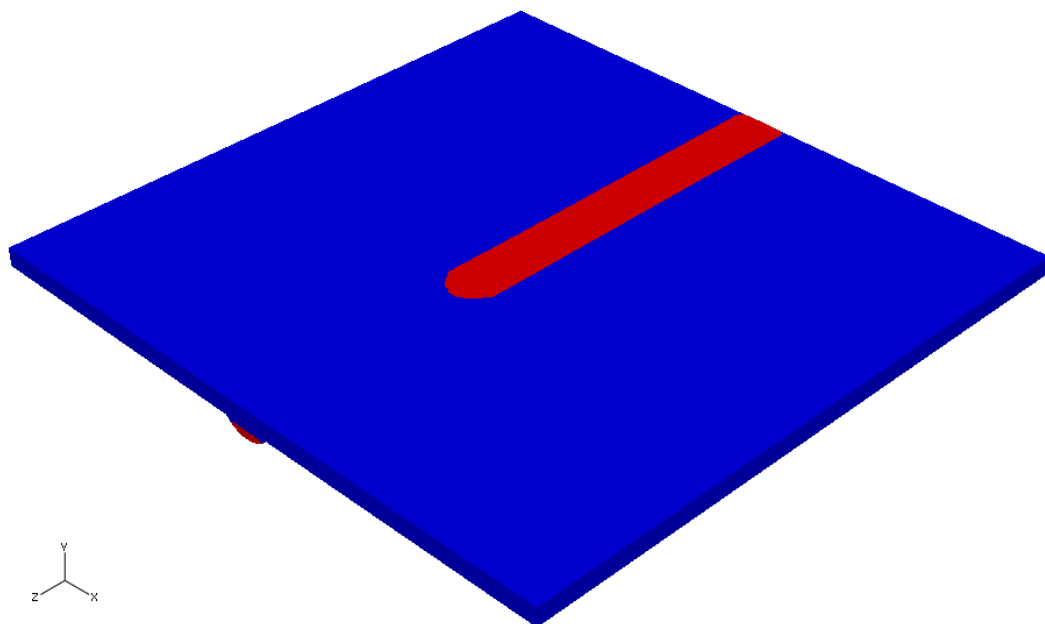


Figure 3.59: Fusion zone material property change: blue – parent IN718
red – weld IN718



Figure 3.60: Fusion zone material property change, transverse cross section

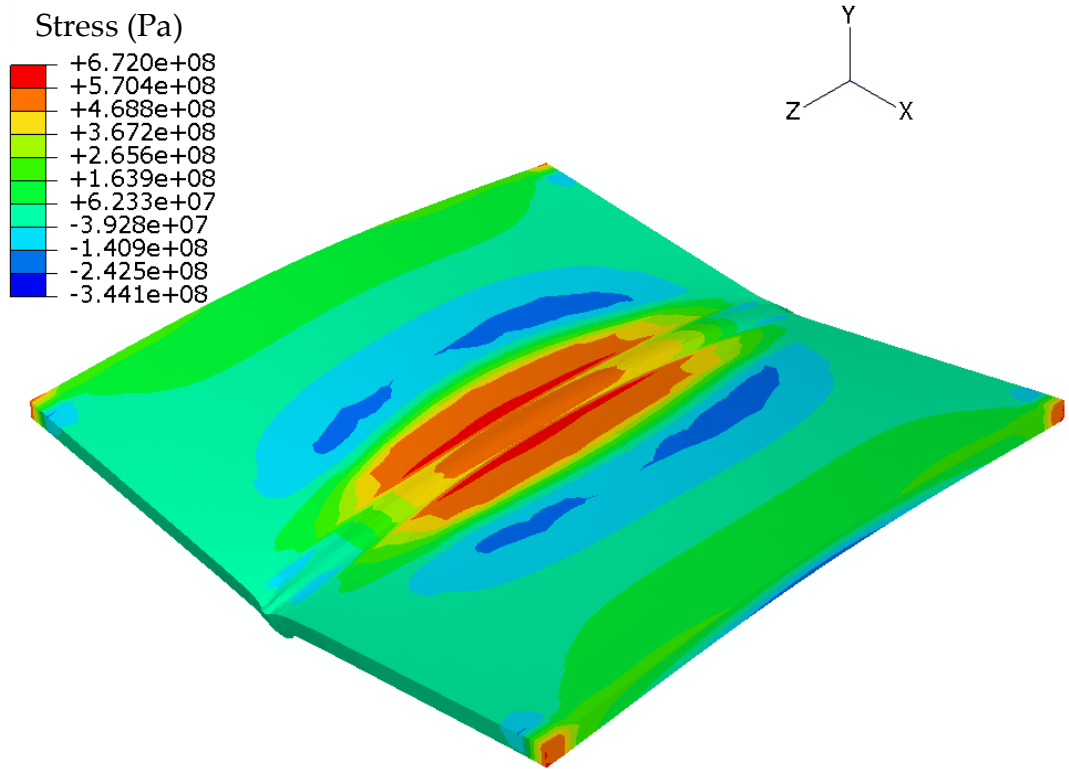


Figure 3.61: Longitudinal residual stress distribution (topside)
-deformation scaled by a factor of 5

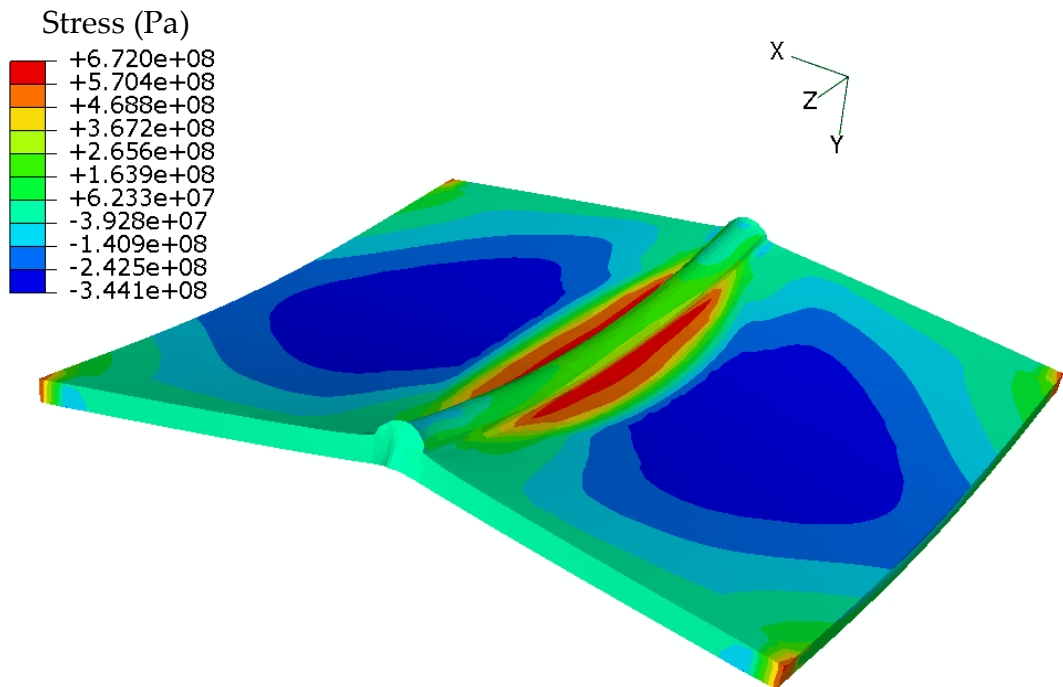


Figure 3.62: Longitudinal residual stress distribution (underside)
-deformation scaled by a factor of 5

The regions of tensile longitudinal stress in and directly around the weld (Figure 3.61 and Figure 3.62) are due to the restriction of shrinkage of the weld by colder surrounding material during cooling. The greatest stress is not contained within the weld itself because of plastic strain relaxation. Further from the weld centreline, balancing compressive stresses can be seen. The weld underbead experiences relatively low stress since it is less constrained and able to contract more freely than the weld edges. The difference in magnitude of residual stress through the thickness relates to the cambering of the plates.

Figure 3.63 shows tensile residual stress around the weld, balanced by compression in the far field, with the exception of the compressive stress around the curvature of the weld bead. The difference in stress from the top to the bottom surface relates to the angular distortion of the plates.

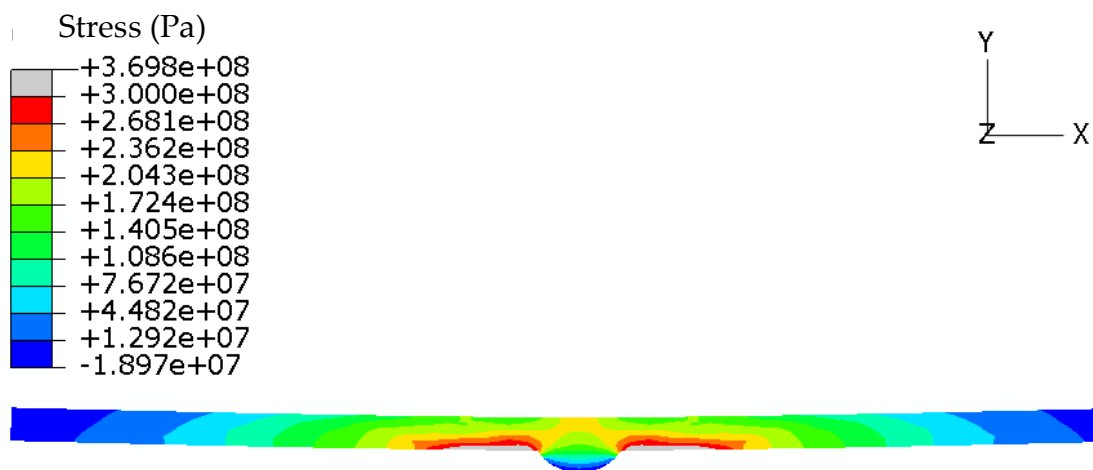


Figure 3.63: Transverse residual stress distribution at the weld midpoint (transverse cross section)

Figure 3.64 shows tensile residual stress along and around the central portion of the weld, balanced by compressive stress at the ends of the weld.

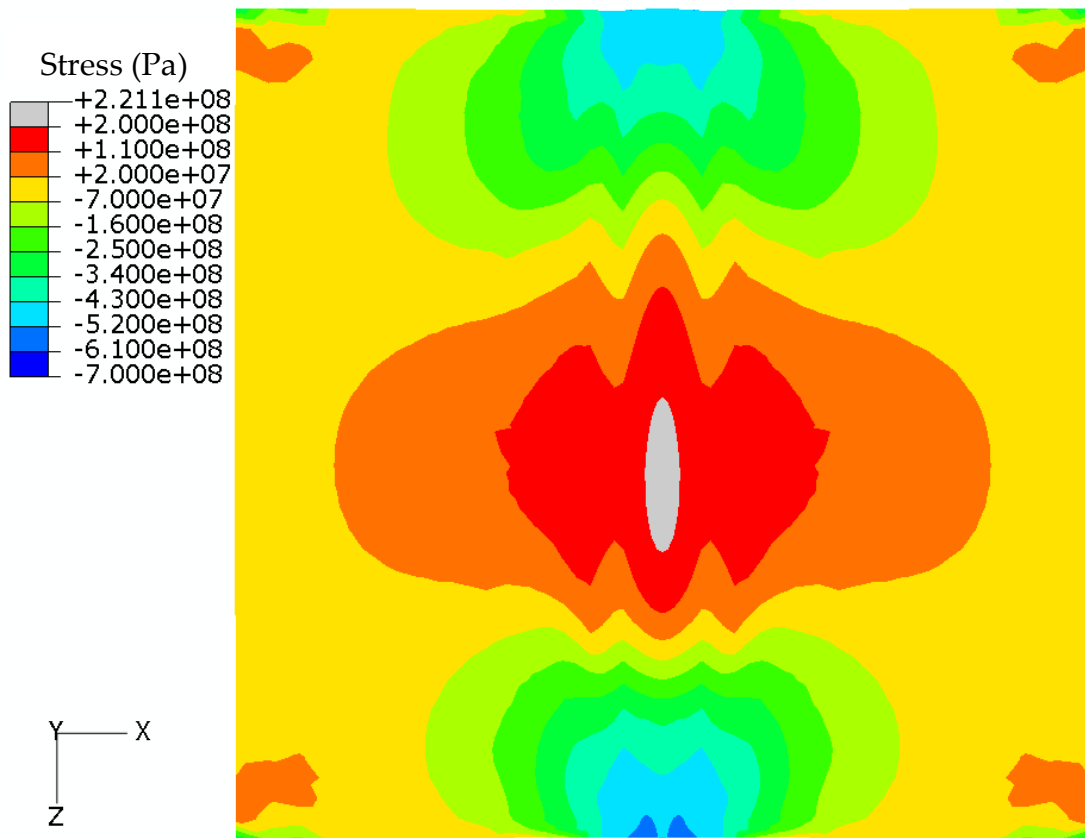


Figure 3.64: Transverse residual stress distribution (topside)

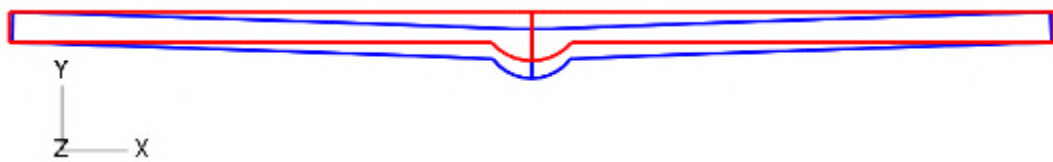


Figure 3.65: 1.9° Peak angular 'butterfly' distortion (blue)



Figure 3.66: 0.9mm Cambering distortion (blue)

3.15 Welding model including jig

The models presented previously in this chapter have not considered the effects of heat transfer to a backing plate or welding jig, or to the clamps used in the mechanical analysis. In the next two sections, a realistic steel welding jig is included in the thermal analysis, with and without clamps. The results of these models are directly relevant to the later work presented in this thesis since they simulate the actual welding process used to produce the butt-welded tensile specimens (see Chapter 4). Therefore, this modelling gives an indication of the likelihood of any distortions and magnitude of residual stresses, along with the effects of the clamps and how conductive heat losses might affect the shape of the fusion zone.

By ensuring that the fusion zone (FZ) does not make contact with the jig, the extreme heating is localised around the weld and does not diffuse into the jig (Figure 3.67). The area of the jig closest to the weld centreline heats up to a maximum of 390°C (Figure 3.68); this is well below the melting point of the material ($\approx 1400^\circ\text{C}$).

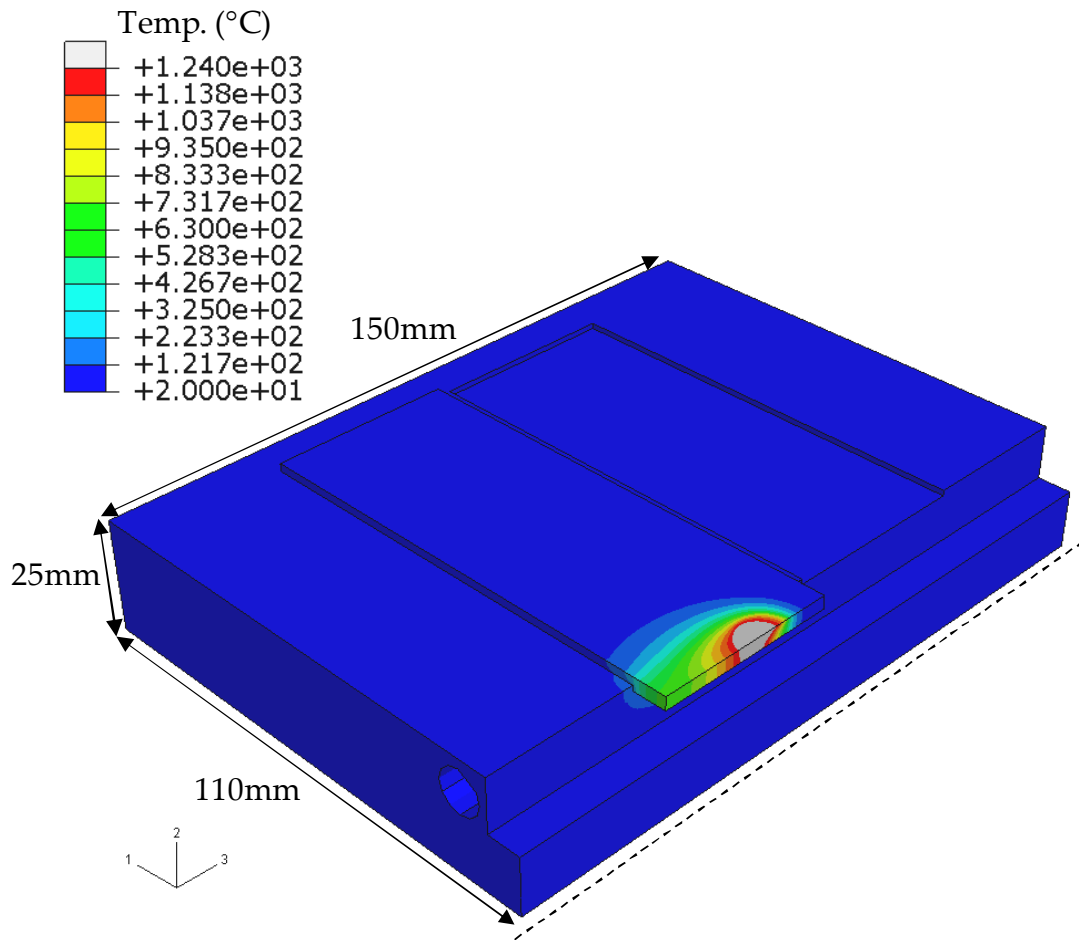


Figure 3.67: Temperature distribution during welding

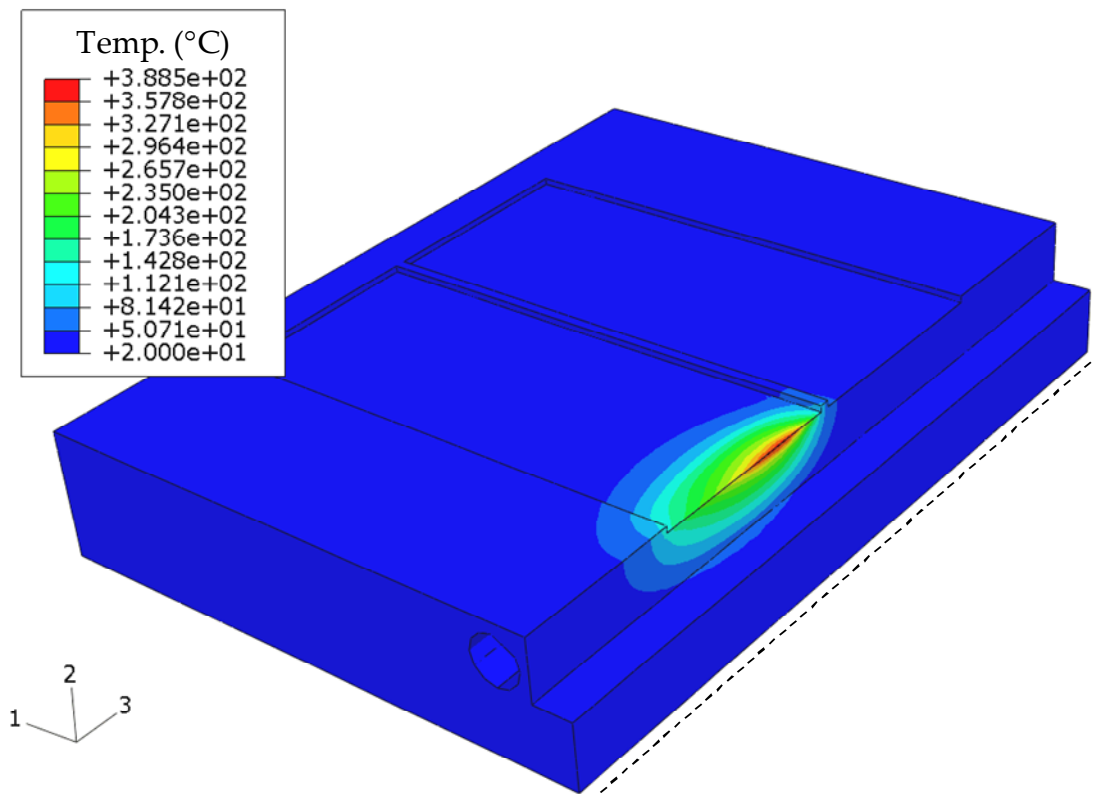


Figure 3.68: Temperature distribution in jig during welding

Both plate and jig cool to approximately 30°C, 75 seconds after completion of the weld (Figure 3.69).

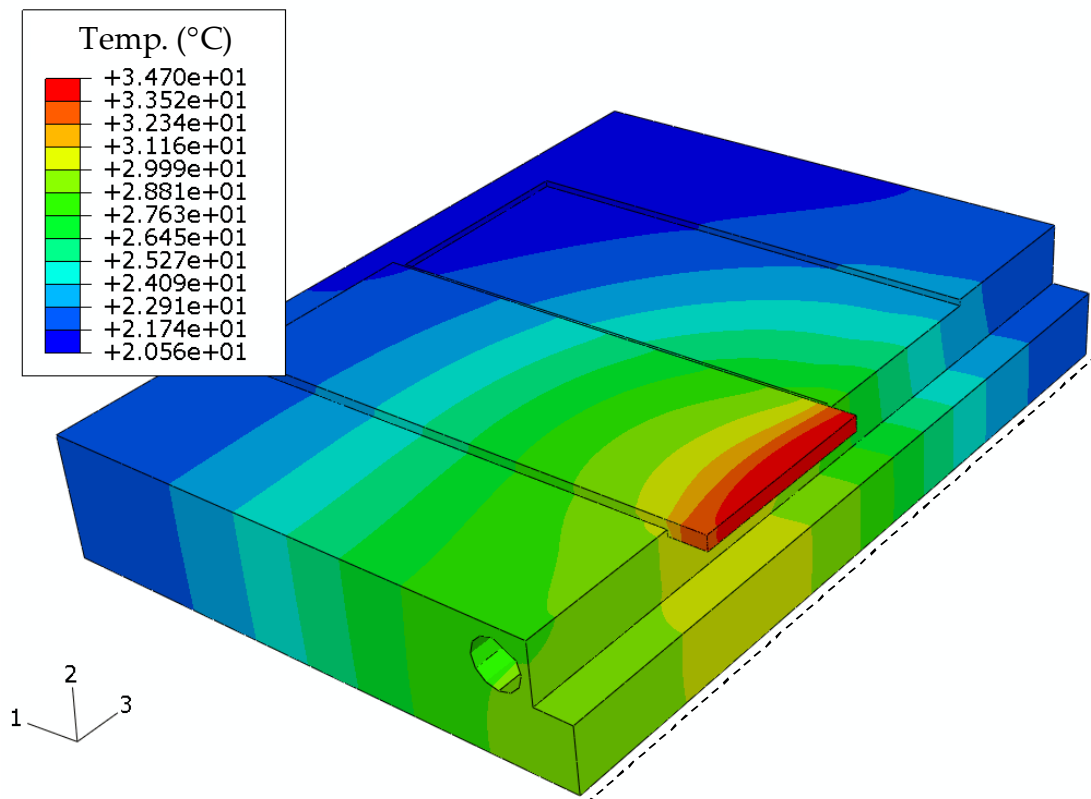


Figure 3.69: Temperature distribution during cooling

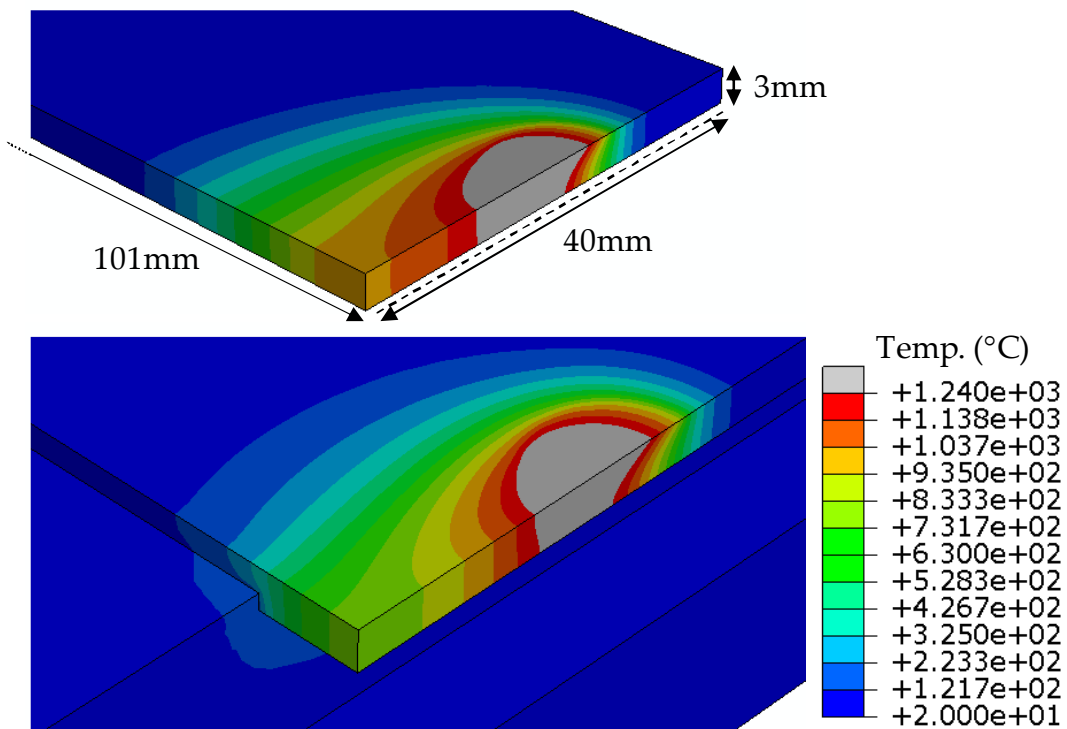


Figure 3.70: Different temperature profile when jig is included (bottom)

Figures 3.70-3.72 show that the temperature profile is noticeably different when conduction to the welding jig is included in the thermal analysis. The plate-jig interface can be clearly seen when looking at the bottom surface of the plate (Figure 3.72). The peak temperature is reduced and so is the size of the FZ and HAZ, consequently this will have an effect on the residual stresses and distortion and the overall quality of the weld. The heat input in the analysis would need to be increased to obtain the same size FZ as that determined experimentally when welds were produced with this jig.

Without jig



With jig

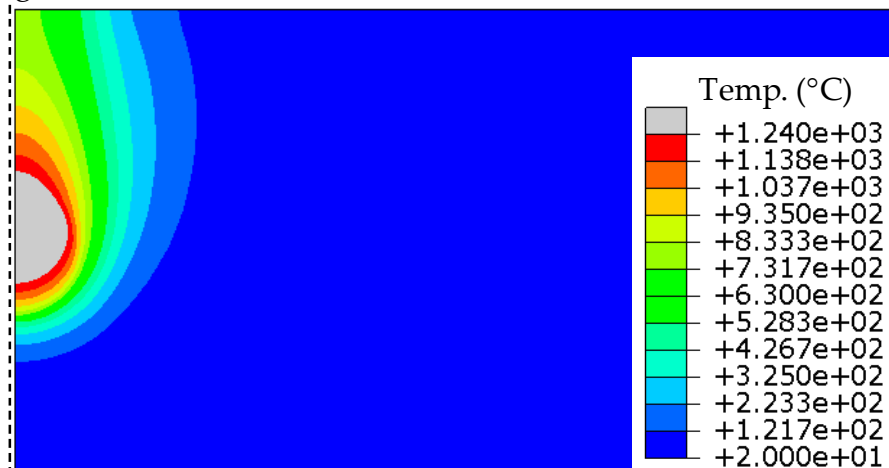
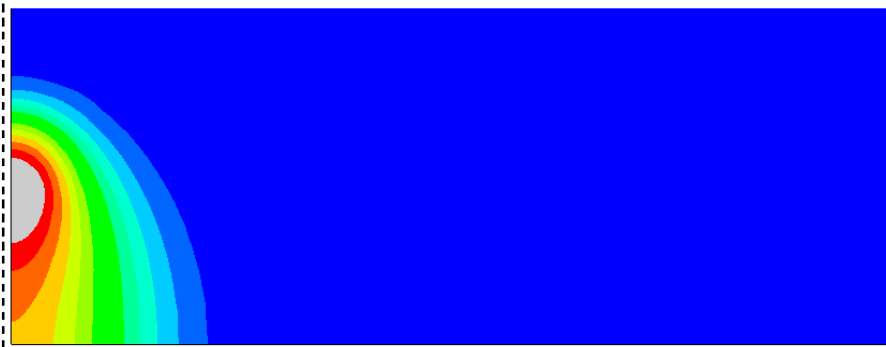


Figure 3.71: Temperature profile, top surface (fusion zone in white)

Without jig



With jig

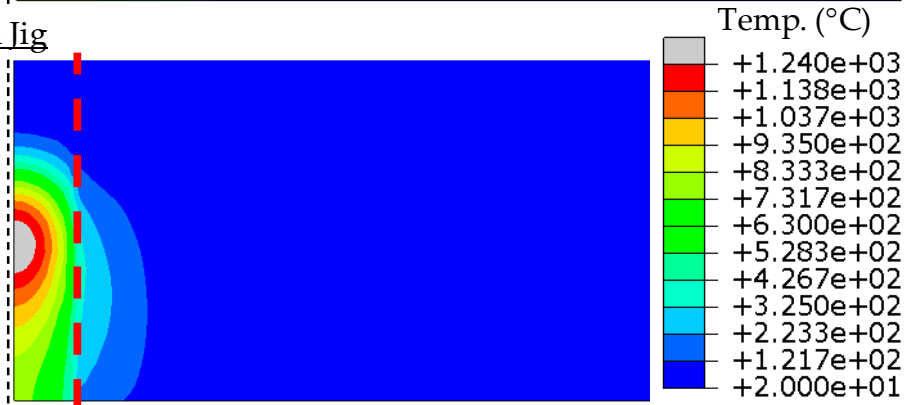


Figure 3.72: Temperature profile, bottom surface (fusion zone in white, red dotted line indicates plate-jig interface)

Figure 3.73 shows that including the clamps with the jig (Figure 3.74) has little effect on the temperature profile.

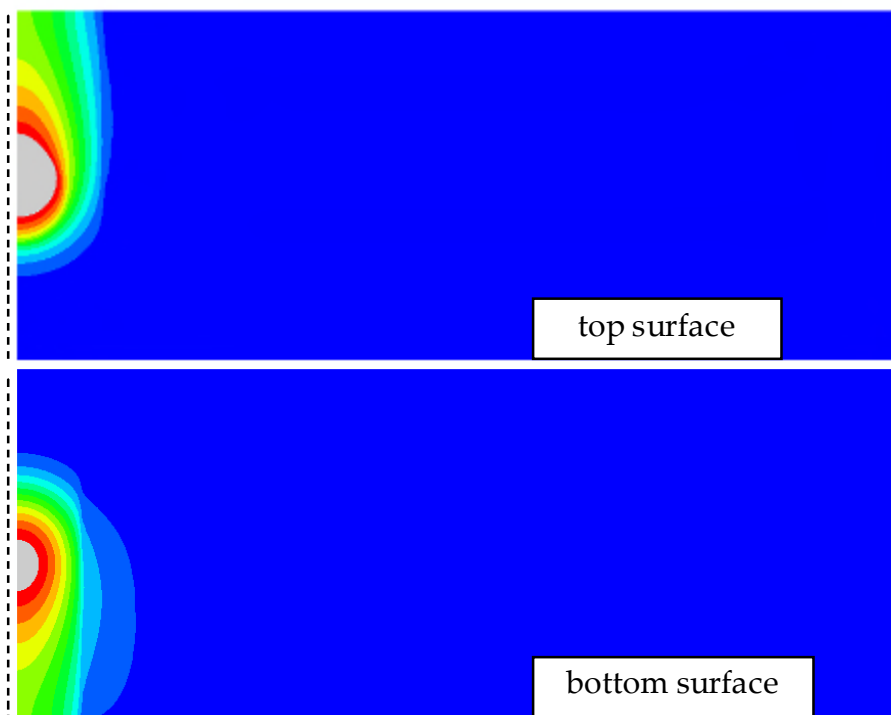


Figure 3.73: Temperature profile for jig with clamps

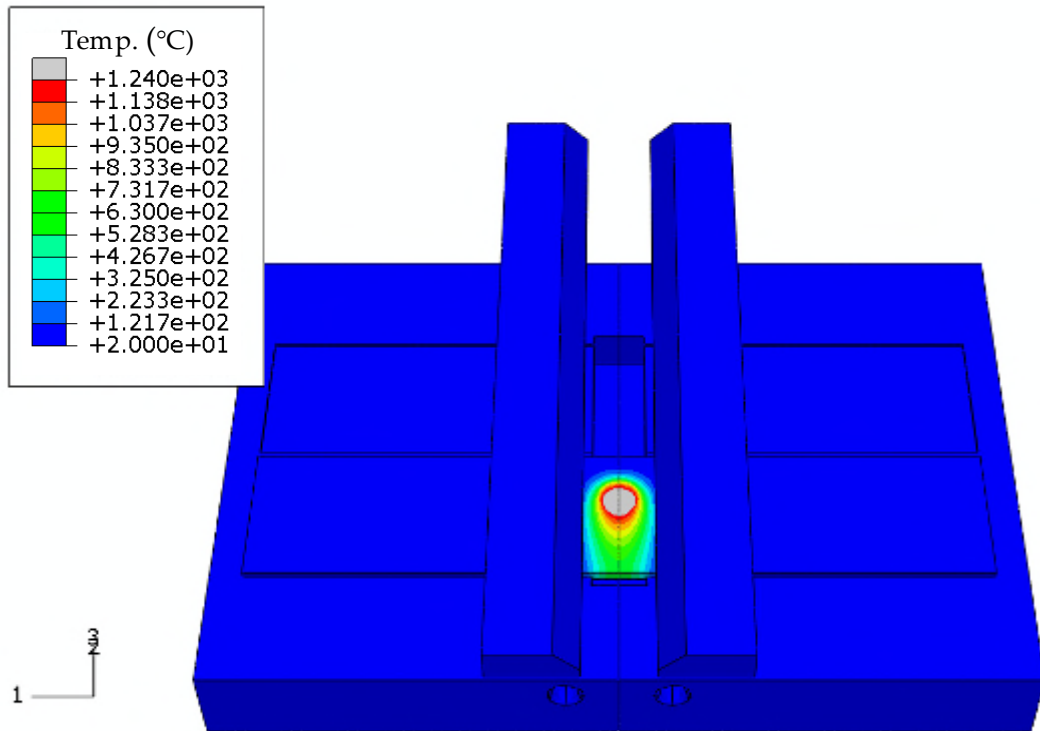


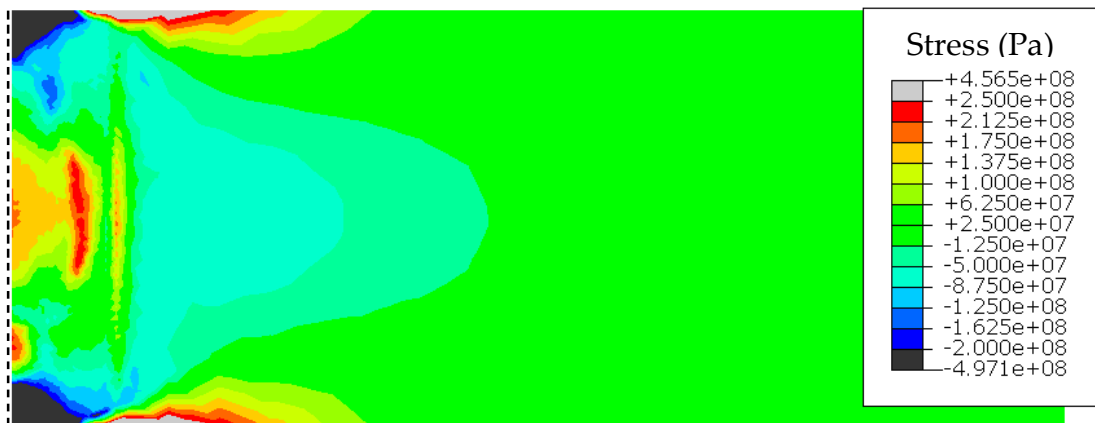
Figure 3.74: Temperature distribution for jig with clamps model

The residual stress profiles produced from the mechanical analysis of the jig with clamps model are shown for the top surface in Figure 3.75 and Figure 3.76.



Figure 3.75: Longitudinal residual stress distribution (jig with clamps)

Before clamps are released



After clamps are released

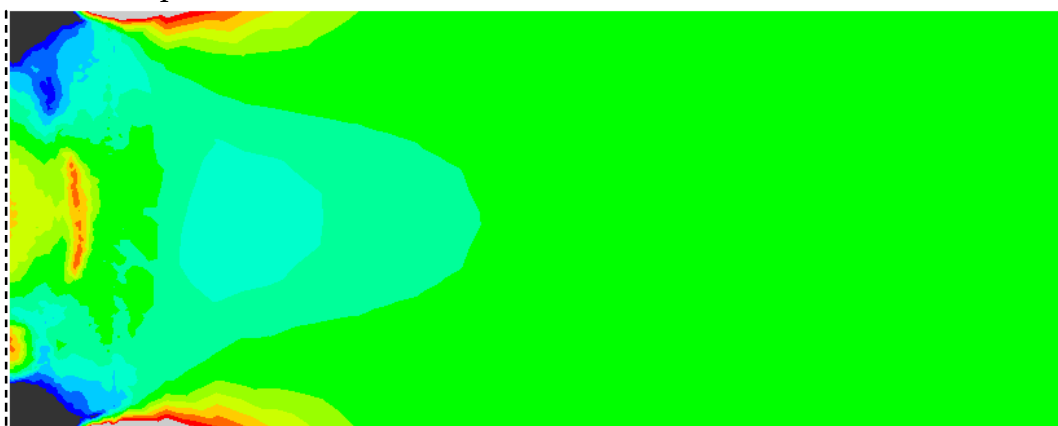


Figure 3.76: Transverse residual stress distribution (jig with clamps)

There was no noticeable distortion and the residual stresses are no higher than in previous models. Little additional plastic straining (less than that found in larger plate models) was produced, except at the end of the weld, which is removed during machining of bow tie shape specimens (Figure 3.77).



Figure 3.77: Equivalent plastic strain distribution (jig with clamps)

As in section 3.13, the clamps were modelled using zero-displacement boundary conditions in the mechanical analysis to avoid unnecessary complicated and computationally expensive contact analyses. This simplification is appropriate since deformation due to contact is minimal in this case. A small slip of 0.25mm was recorded under the clamps if the boundary conditions were not used in the FE model.

3.16 Welding model with a ceramic backing plate

By removing the thermal boundary condition on the bottom surface of the plate, welding with a low-conductivity ceramic backing plate can be simulated. As expected, welding with a ceramic backing plate results in an increase in peak temperature and FZ size (Figure 3.78 and Figure 3.79).

The results obtained for all of the different thermal cases analysed are presented in Figure 3.78 and are summarised below in decreasing peak temperature order:

Ceramic backing plate > free plate > plate and jig > plate, jig and clamps

There is less difference in the peak temperature of the ceramic backing plate and free plate cases since convection has a smaller effect than conduction, which is why the peak temperatures of the plate and jig / plate, jig, and clamps cases are lower. There is also less difference in the cooling rate of the plate and jig / plate, jig and clamps cases since conduction to the clamp is insignificant (Figure 3.78).

In general, it is shown that a reduced peak temperature and increased cooling rate leads to a reduced FZ.

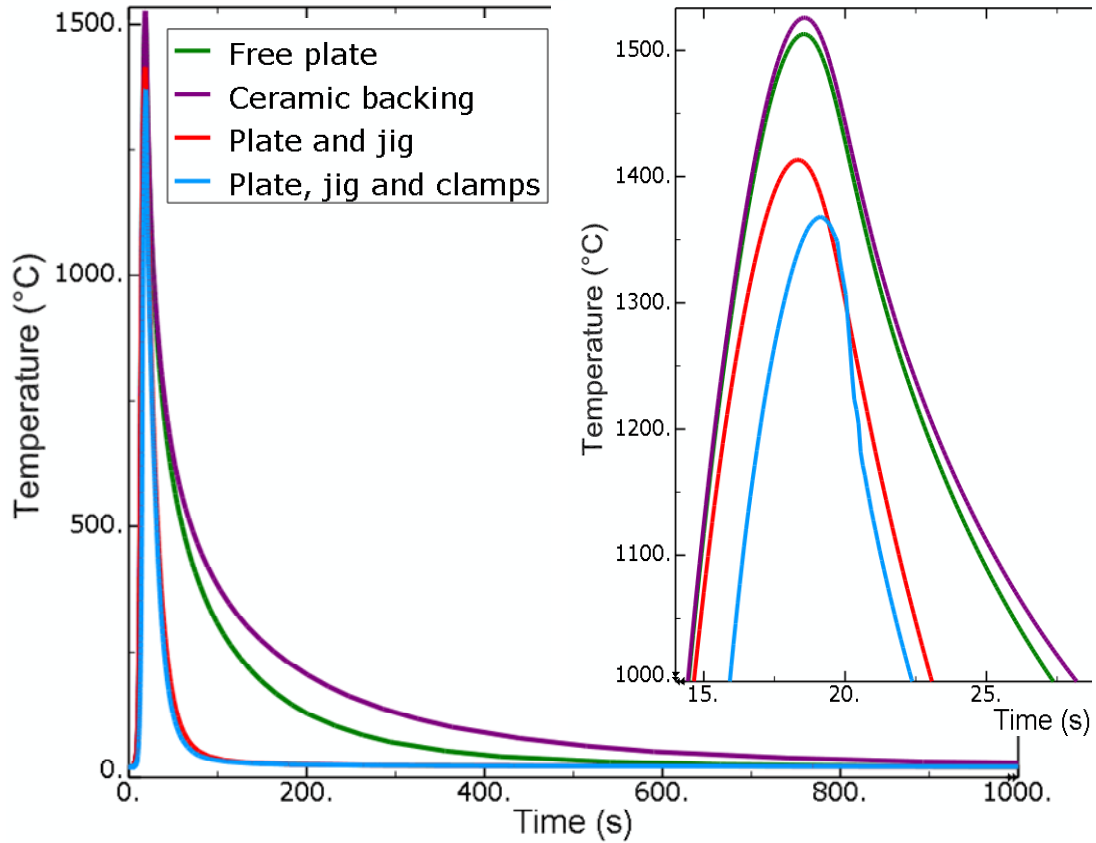


Figure 3.78: Peak temperature history for the different cases analysed

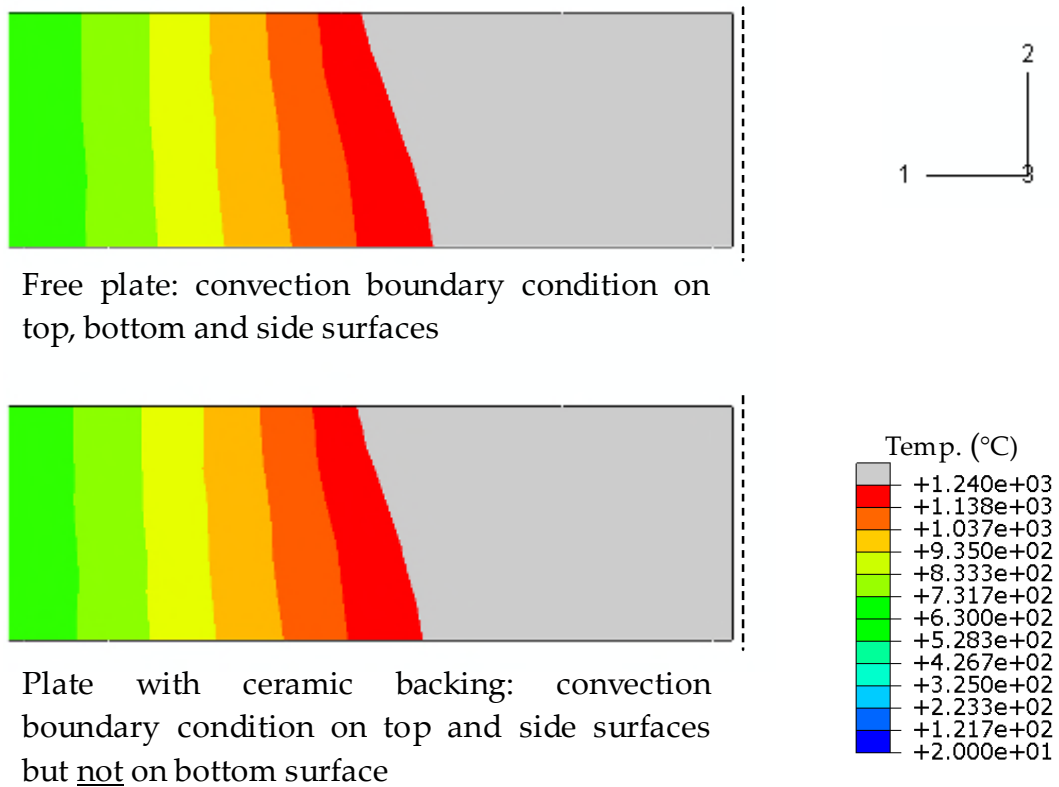


Figure 3.79: Peak temperature profiles (fusion zone shown by white contour)

3.17 Discussion and conclusions

The welding of thin plates can produce out-of-plane distortions that compromise uniaxial testing and make life prediction difficult. An ABAQUS finite element numerical arc welding model was developed and used to understand the development of weld-induced distortions and residual stress, and determine the effects of distortion mitigation techniques. The need for a three-dimensional model was argued since a plane strain assumption is often unsuitable and inaccurate for modelling transient welding with multiple distortions modes occurring simultaneously. The importance of including the effects of plastic strain relaxation was also highlighted in terms of residual stress and distortion. For a simple two-dimensional case, it was found that the residual stress in the molten region was significantly reduced and the direction of angular distortion was reversed when plastic strain relaxation was accounted for.

The complications of presetting and the effects of using different types of clamping, and the possible heat loss to a welding jig or backing plate were analysed. Presetting did not reduce the amount of distortion predicted but clamping was more successful. It was decided that the weld-induced distortions could be effectively mitigated by only welding small plates that are just large enough to form one tensile test specimen. The small size increases the relative stiffness of the plates, and reduces the welding time and therefore the total time for which nonuniform thermal contraction exists, which is the driving force of the distortions. Unlike other methods of distortion prevention, such as those involving trailing heat sources or sinks, this solution does not modify the effects of the welding process on the thermal history of the material and so is ideal for test specimens designed to compare welded and non-welded material. If the plates remain flat after welding, the weld bead excess can be removed by a finishing process. This

step is important since the sharp fillet radii of the weld beads result in high stress concentrations at the weld bead and parent interface. This theoretical welding procedure was put into practice during the experimental work (Chapter 4) and resulted in welds free of distortion as predicted by the numerical model.

Chapter 4

Test specimen manufacture

4.1 Introduction

This chapter documents the manufacture of the thin rectangular section, TIG butt-welded and non-welded IN718 test specimens used for the uniaxial tensile, creep and high temperature fatigue testing presented in Chapter 5. The welding procedure was devised using the finite element welding simulations from Chapter 3, in order to produce welded specimens free of distortion.

4.2 Material procurement

Via Rolls-Royce plc, Haynes International Ltd supplied four pieces of 2.317m x 0.164m x 3.2mm (thick) Haynes® 718 Alloy (equivalent to IN718). The material had been given a solution heat treatment (SHT) consisting of heating to the single-phase field temperature (950-980°C) for 1 hour to take all elements into solution (homogenisation), followed by rapid cooling. The chemical composition is given in Table 4-1. This material was used for all tests: welded and non-welded, and with or without additional (age hardening) heat treatment.

Table 4-1: Chemical composition of the IN718 sheets in weight %

Ni + Co	Cr	Fe	Nb + Ta	Mo	Ti	Al	Mn	Si	C	Cu	B	S
54.1	17.7	Bal	5.29	3.04	1.01	0.51	0.24	0.08	0.05	0.03	0.003	0.002

VBC Group Ltd supplied a 10kg spool of 0.9mm diameter VBC alloy 0220 welding wire, which is also equivalent to solution heat treated IN718. The chemical composition is given in Table 4-2. This wire was fed in during the welding process using a purpose built KUKA welding robot.

Table 4-2: Chemical composition of the IN718 wire in weight %

Ni + Co	Cr	Fe	Nb + Ta	Mo	Ti	Al	Mn	Si	C	Cu	B	S
53.0	17.4	19.9	5.13	2.99	0.96	0.48	0.03	0.07	0.05	0.04	0.003	0.001

4.3 Postweld heat treatment (PWHT)

Any reference to heat treatment or postweld heat treatment (PWHT) refers to the following:

- clean thoroughly with water, detergent and methanol
- ramp up heating at $\approx 10^{\circ}\text{C}/\text{min}$ to 720°C
- hold at 720°C for 8hrs
- furnace cool ($50^{\circ}\text{C}/\text{hr}$) to 620°C
- hold at 620°C for 8hrs
- air cool to room temperature

This is a standard precipitation (ageing) heat treatment for IN718. The temperature is not high enough to take all elements into solution and so Laves phase that forms during the fusion welding of IN718 will still be prominent, which will have a detrimental effect on the material's properties. However, this heat treatment does harden both the parent and weld material as well as effectively relieving welding-induced residual stresses [92].

It is worth noting that, as mentioned by Ram *et al.* [88], Laves phase (formed after weld solidification) can be eliminated by re-annealing after welding, prior to ageing as follows:

- Anneal (SHT) at 1065°C (20 mins) then air cool to room temp. followed by the standard ageing of 720°C (8 hours), furnace cool to 620°C (8 hours)

But temperatures above 995 °C can cause grain coarsening in IN718 which also causes degradation in material properties so Ram *et al.* [88] suggest a compromise:

- Anneal (SHT) at 980 °C (20 mins) then air cool to room temp. followed by the standard ageing of 720 °C (8 hours), furnace cool to 620 °C (8 hours)

High temperature heat treatments are also undesirable for large components due to the impracticality of the furnace size required and since the structure may distort under its own weight when in a low strength condition.

The PWHT was conducted in air, which resulted in slight oxidation of the material surface, but this will not affect the subsequent tests, which will also be conducted in air. It was important to thoroughly clean the specimens before PWHT in order to remove the lubricant used during the machining process; otherwise dark patches developed on the specimen surface.

4.4 Weld material property testing

IN718 and welded IN718 thermomechanical and thermophysical material properties need to be determined for temperatures ranging from ambient to melting point before PWHT (for FE welding simulation) and at relevant temperatures after PWHT (for creep and high temperature fatigue FE analysis and lifetime prediction).

Before PWHT, the weld fusion zone material properties are more like those of cast IN718. It is difficult to find adequate cast properties from research literature and cast IN718 is not in sheet form, so it is highly desirable to mechanically test the welds themselves.

Using a Gleeble thermomechanical simulator is impractical since the material requires melting in order to recreate the actual welding conditions.

Below are some other suggestions for obtaining IN718 weld material properties:

- a) Weld some specimens across the width, test as for the non-welded specimens (see Figure 4.1), and calculate the properties of the weld material by comparison

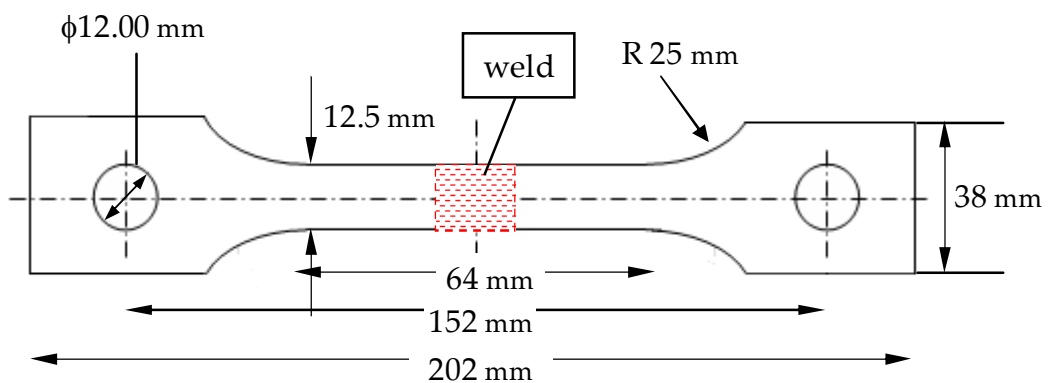


Figure 4.1: Suggested uniaxial specimen, formed from two plates butt-welded across the width

- b) Weld some specimens along the full length and test as for the non-welded specimens (see Figure 4.2)

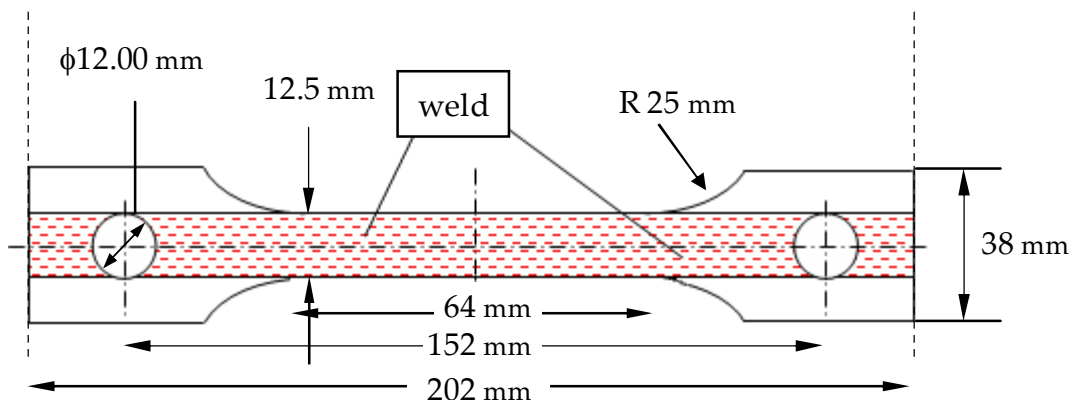


Figure 4.2: Suggested uniaxial specimen, welded along the full length

- c) Hardness test a IN718 weld to obtain a room temperature yield stress estimate and then extend this to other temperatures (and produce other properties) by comparing with tensile tests of the non-welded specimens

- d) Perform image correlation tests (as in [92]) to obtain the room temperature yield stress and then extend this to other temperatures (and produce other properties) by comparing with tensile tests of the non-welded specimens

It was decided to pursue option (a) since this is the most attractive approach that provides an indication of the weld properties without added complications. It is however, limited because the gauge length of the specimen includes some non-welded material, although with the use of numerical analysis the effects this has on the testing can be evaluated.

Option (b) would involve a large change in the welding setup and will only provide material properties along the weld, but the properties across the weld are of most interest to this work. Options (c) and (d) require additional tests and will only provide material properties at room temperature, which is a disadvantage compared with option (a).

4.5 Thermomechanical material property testing

- The elastic modulus, yield stress and hardening modulus will all be measured from one uniaxial tensile test carried out at each of the following temperatures: 20*, 200, 400, 620[†], 700, 800, 1000 °C

* depending on (ambient) room temperature

[†] the temperature chosen for the creep and high temperature fatigue tests

Poisson's ratio cannot be easily tested at high temperatures so values from literature will be used.

The following properties are largely invariant with respect to the heat treatment (condition) of the material and a full set is costly and difficult to obtain. Therefore, data acquired from research literature will be used in place of the following test and all of the thermophysical property tests:

- The coefficient of linear thermal expansion can be tested using thermomechanical analysis (TMA) but this requires a cylindrical specimen, which may be too large to be cut out of the sheet material. An alternative test may be performed using a Gleeble thermomechanical simulator.

4.6 Thermophysical material property testing

- The specific heat capacity (temperature dependent), latent heat capacity, solidus and liquidus temperatures can all be measured using one differential thermal analysis (DTA) test.
- The thermal conductivity can be measured at the National Physical Laboratory (NPL) or possibly using a Gleeble thermomechanical simulator.
- The density can be obtained by Helium pycnometry performed at room temperature. The result of this test can be used along with the coefficient of linear thermal expansion to calculate the density at the other temperatures in the required range.

An overview of the material property testing required is given in Table 4-3.

Table 4-3: An overview of the material property testing required

<u>CATEGORY</u>	<u>PARAMETER</u>	<u>SI UNITS</u>	<u>EXPERIMENT</u>
<u>Thermomechanical Properties</u> (All are temperature dependent)	Elastic Modulus	Pa	Uniaxial tensile test
	Yield Stress	Pa	
	Hardening Modulus	Pa	
	* Coefficient of Linear Thermal Expansion	K ⁻¹	Thermomechanical Analysis (TMA)
(Temperature dependent) <hr/> <u>Thermophysical Properties</u>	* Specific Heat Capacity	J/(kgK)	Differential Thermal Analysis (DTA)
	* Latent Heat Capacity	J/kg	
	* Solidus Temperature	°C	
	* Liquidus Temperature	°C	
(Temperature dependent)	* Thermal Conductivity	W/(mK)	Thermal Diffusivity
	* Density	kg/m ³	Helium Pycnometry

* Tests not performed (data obtained from literature)

4.7 Tensile, creep and high temperature fatigue testing

All the specimens except those specified for as-received/as-welded tensile testing, were given the same postweld heat treatment (PWHT –see section 4.3), so that a fair comparison could be made between the welded and non-welded material. Each weld joins two small plates (equal width but half the length of the bow tie specimen) to form a full size specimen with a weld in the middle, across the entire width (see Figure 4.3).

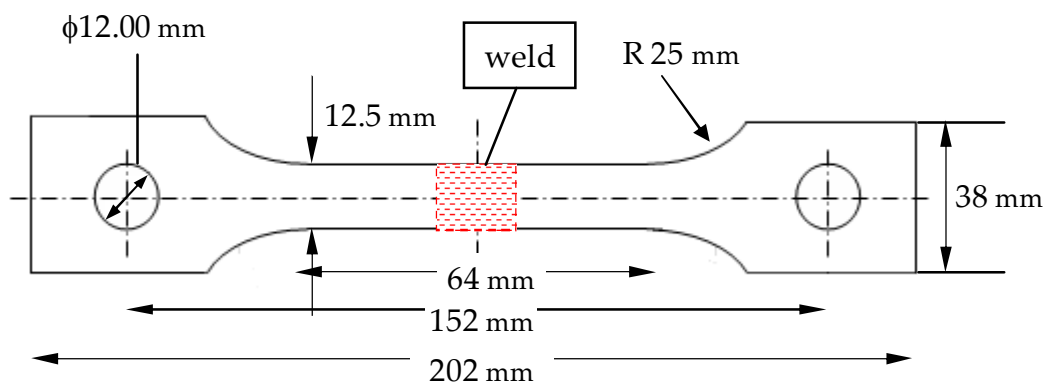


Figure 4.3: Uniaxial tensile, creep and high temperature fatigue test specimen, formed from two plates butt-welded across the width (geometry as per BS 3500 : Part 3 [116])

4.8 Welding

The initial work for this thesis concerned the development and application of a numerical arc welding simulation model, capable of calculating the evolution of stress and deformation, and predicting the residual stresses and distortions that occur as a result of the welding process. An ABAQUS finite element model incorporating user subroutines, was formulated and validated using experimental results obtained from research literature for the case of welded thin IN718 plates [44] (Chapter 3).

One of the aims of the numerical modelling was to help decide how to mitigate, or at least minimise, the angular distortion that had hampered previous uniaxial tests of welded specimens. In terms of large-scale welded

structures, complicated methods that include the use of trailing heat sources or sinks, or postweld flame straightening have been used for research and industrial purposes. These methods necessarily have a direct effect on the thermal history of the material, which is undesirable since the subsequent material behaviour will then depend on the specific parameters used for the minimisation or correction of the distortion. It is worth noting that presetting and prestressing of welded parts can mitigate postweld distortion, but these methods are unreliable and tend to produce variable results, so were also not considered suitable for this work. A less complicated solution was devised, which does not involve any additional heat input or corrective procedure, but simply makes use of the relative stiffness of the material, along with clamps that enable the welded metal to cool and regain its stiffness before it is required to support any stress.

Since axial stiffness k , is defined as:

$$k = \frac{A \times E}{L} \quad (4.1)$$

where A is the cross sectional area, E is Young's modulus and L is the length of the structure. It is evident from equation (4.1) that a reduction in length results in an increase in stiffness. Therefore, reducing the size of the part to be welded will reduce the amount of postweld distortion. Also, reducing the size of the part decreases the welding time and subsequently, the total heat input, which also leads to a reduction in distortion. In addition, since less time is taken to weld smaller plates and the heat flow due to conduction within the material is confined to a smaller volume, the total welding time is less and so is the time taken for a uniform temperature distribution to occur throughout the plates. This results in a reduced time of nonuniform heating and cooling, and corresponding nonuniform thermal expansion (the driving force for the distortions). Both experimental and numerical analysis results

have shown that less distortion occurs when welding smaller plates than larger ones [44].

It was decided to weld plates that were only large enough to form one tensile test specimen coupon (approx. 200mm x 40mm), in order to reduce postweld distortion. A jig was designed to allow for easy positioning of the plates prior to welding, suitable clamping, and holes for the injection of shielding gas (see Figure 4.4 and Figure 4.5). Particular importance was placed on ensuring that the position of the weld centreline was consistent, so that the weld was always formed along the intersection of the two plates, without requiring much adjustment for each weld run. Therefore, it was important that the plates had straight parallel sides and at least one was 101mm –half the width of the finished welded coupon.

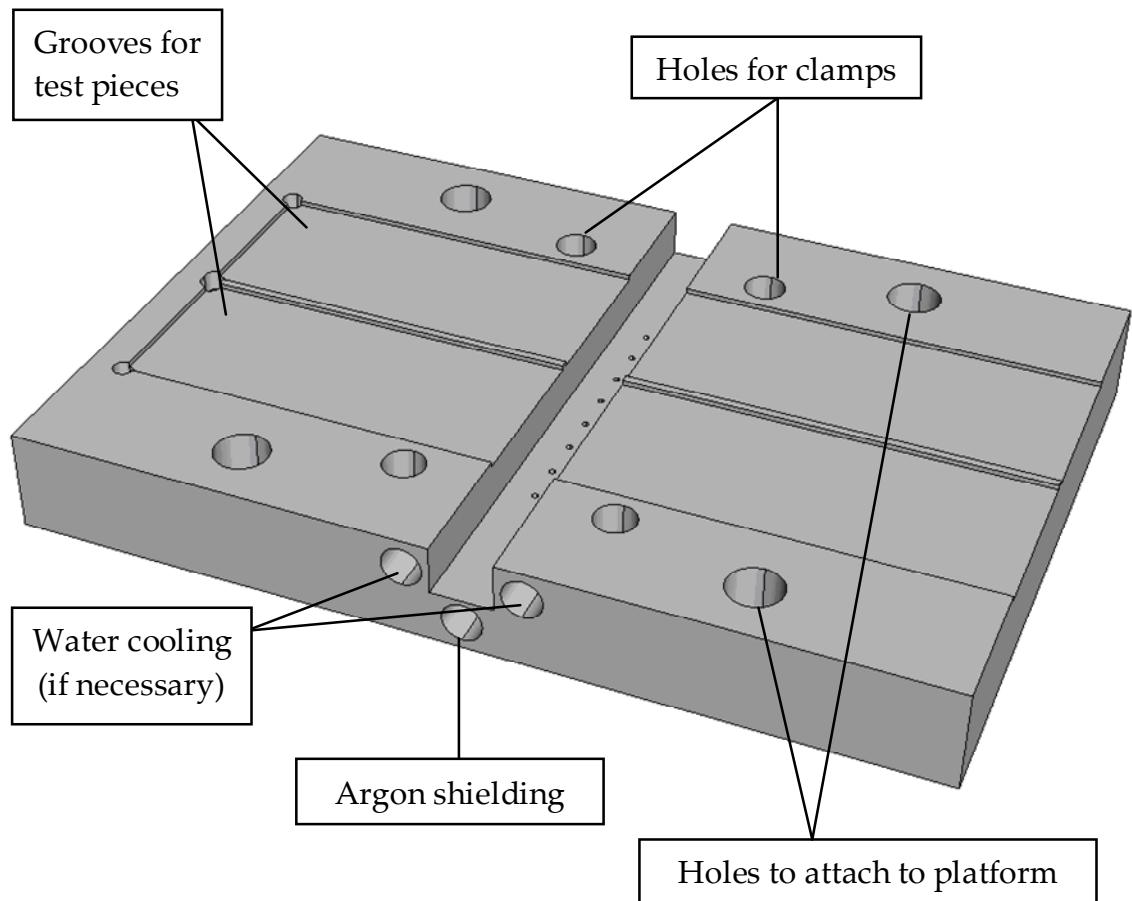


Figure 4.4: Welding jig, schematic



Figure 4.5: Welding jig, photograph

The welding parameters were adjusted to produce acceptable welds. The final parameters chosen are given below:

Mechanised fully penetrating single pass TIG butt welds on a jig with clamps

Joint preparation:	Square edge, closed butt, waterjet then ground and cleaned with acetone
Welding current:	100A
Polarity:	DCEN (Direct current electrode negative)
Travel speed:	1.33 mm/sec (80 mm/min)
Filler wire:	IN718 ϕ 0.9 mm
Wire feed speed:	650 mm/min
Shielding gas:	High purity argon
Flow rates:	18 l/min Torch, 30 l/min Shielding
Electrode:	1% Lanthanated ⁴ tungsten ϕ 2.4 mm
Arc length:	3 mm

The welding robot and setup used are shown in Figure 4.6 and Figure 4.7. The purpose of the robot was to ensure as much reproducibility as possible.

No temperature measurements were made during the welding since:

- arc welding causes interference with most thermocouples
- thermographic cameras require accurate emissivity data that is difficult to obtain and may be unreliable
- temperature measurements cannot easily be made in the fusion zone, which is the area of most interest for validation purposes, measurements taken too far from the weld centreline are less sensitive to the welding process/parameters and therefore are of less use

⁴ Low erosion rate, wide current range, no spitting, best DC arc starts and stability [117]

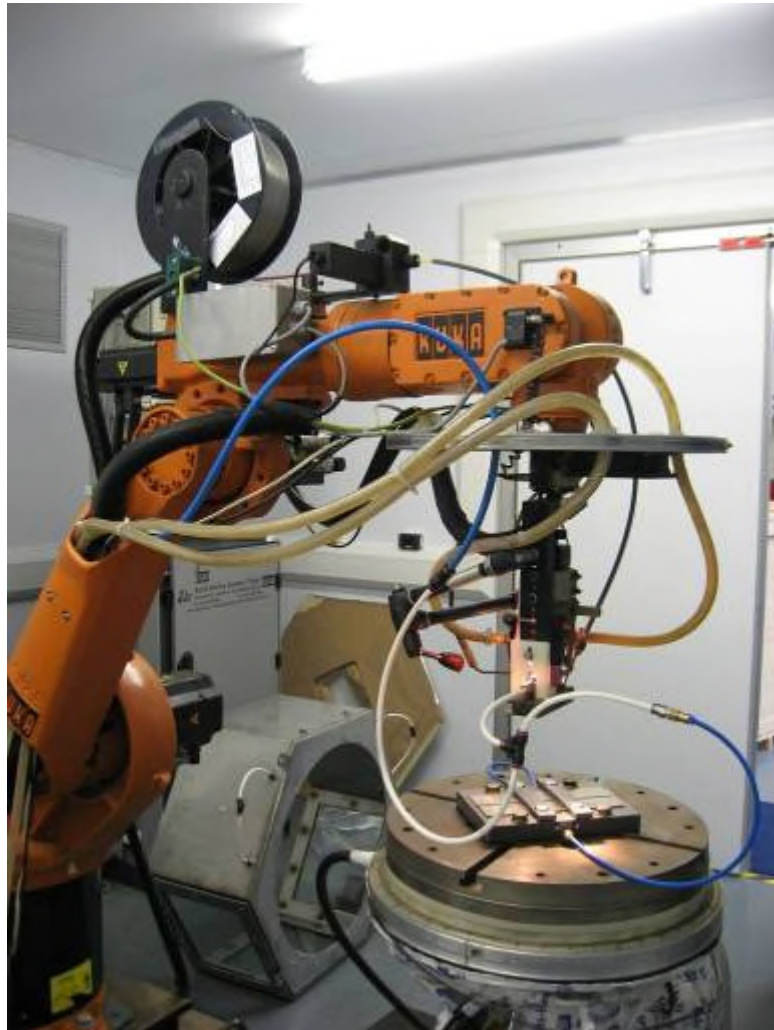


Figure 4.6: Welding setup

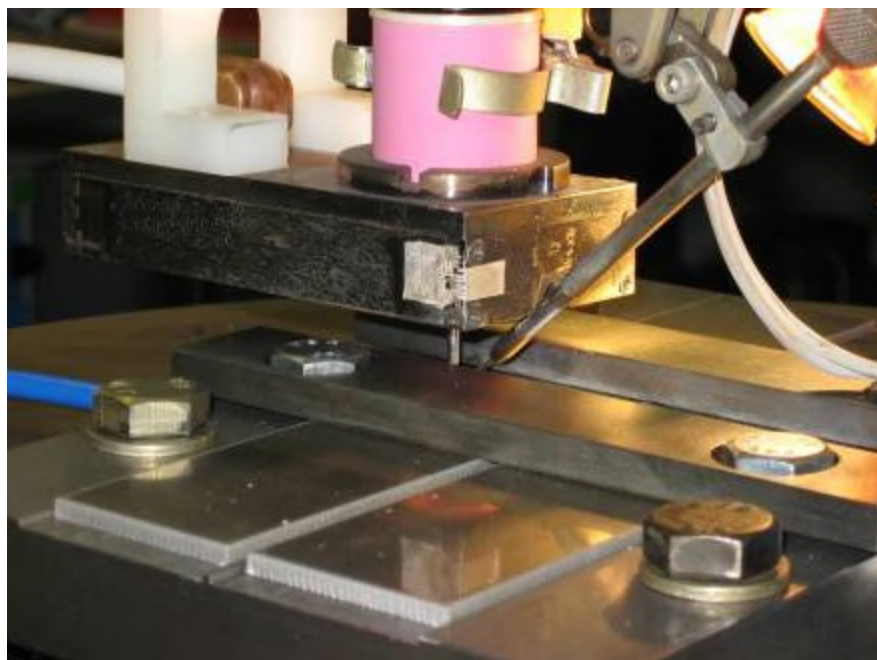


Figure 4.7: Welding setup close up

The welding jig performed as desired, and all of the welds produced were free of distortion, both before and after postweld heat treatment (PWHT –see section 4.3) (Figure 4.8).



Figure 4.8: Welded blank (before specimen profiling)

Before PWHT, the small welded plates had the weld bead excess (top and bottom) ground flush and were profile-machined to the bow tie tensile test specimen shape shown in Figure 4.3 (detailed in section 4.9). The finished specimens were free from out-of-plane distortion (Figure 4.9).



Figure 4.9: Welded bow tie specimen (after profiling)

Some of the welds were sectioned for optical microscopy (Figure 4.10a) and some were sent for X-ray inspection at NDT Services Ltd., Kegworth, UK (Figure 4.10b). There was no evidence of any defects such as cracking or porosity, before or after PWHT.

The holes of the fatigue specimens were thoroughly polished using wet and dry paper wrapped around a spindle in a bench drill and finished by hand (it was important to remove the chamfered edges that resulted from the machining process). The test sections were slightly polished using the bench drill and then thoroughly finished by hand.

4.10 Summary

Both thin rectangular section non-welded and thin rectangular section TIG butt-welded, bow tie tensile, creep and high temperature fatigue specimens were manufactured from 3.2mm solution heat-treated sheets of IN718 provided by Haynes International Ltd. The welds were mechanised, fully penetrating, single pass TIG, square-edge, closed butt welds, between the short sides of 100mm x 40mm coupons with matching IN718 filler wire and argon shielding.

The small welded plates did not distort and so the weld bead excess could be removed without difficulty by finishing. Some welds were sent for X-ray inspection at NDT Services Ltd, Kegworth, UK and some were cross-sectioned and examined with an optical microscope. No evidence of any defects such as cracking or porosity was found. After bow tie profiling, all specimens except those specified for as-received/as-welded tensile testing, were given the same precipitation heat treatment before testing, consisting of: 720°C/8hrs, 50°C/hr furnace cool to 620°C/8hrs, air cool. This heat treatment also effectively relieves welding-induced residual stresses.

Chapter 5

Tensile, creep and high temperature fatigue testing

5.1 Summary

This chapter documents the experimental work. The testing setup and procedures are discussed and the results of uniaxial tensile, creep and high temperature fatigue tests on both TIG butt-welded and non-welded, thin-section IN718 specimens are presented. The main objectives of the testing are to determine the effect the welds have on life, analyse any differences in their failure behaviour, and obtain material properties for input into finite element analyses for welding simulation and life prediction purposes.

Tensile tests at temperatures from 20°C to 1000°C resulted in both the 0.2% proof stress and the ultimate strength of most of the welded specimens exceeding 90% of the values of the non-welded specimens. However, the strains to failure for the welded specimens were significantly less than those of the non-welded specimens.

Constant load creep tests at 620°C also showed noticeably lower total strains to failure for the welded specimens than the non-welded specimens. The time to failure for a given load was also markedly less for the welded specimens. The welded specimen creep failures occurred in a coarse-grained heat-affected zone (HAZ) where large grains were unable to accommodate large straining by grain boundary sliding, leading to premature fracture.

Low cycle fatigue tests at 620°C, with a trapezoidal (1-1-1-1) form, load frequency of 0.25 Hz and zero stress ratio, resulted in lower failure times for the welded specimens than the corresponding non-welded values for any given nominal stress. This was attributed to the presence of brittle Laves phase at fine-grained HAZ boundaries, which is known to decrease ductility and life.

In conclusion, it was found that although welded IN718 exhibits comparatively little loss of tensile strength, its creep and high temperature fatigue properties are severely compromised.

5.2 Welded specimen results classification

A weld is an inhomogeneous structure, but distinct zones with homogeneous properties within a weld can be identified. The welded test results presented in this chapter refer to the specimen as a whole and should be viewed akin to those of a composite material, where the measured strain is the total for the gauge length of the specimen, which includes parent, HAZ and weld (fusion zone) material. The properties of the welds themselves are determined in Chapter 6. It should also be noted that the applied nominal stress values are quoted here and the effects of residual stress would have consistently modified the actual stress experienced by the welded specimens. All welded specimens were tested in the direction transverse to the weld.

5.3 Extensometer

In order to withstand test temperatures of up to 1000°C (and particularly the longer term creep tests performed at 620°C –see section 5.6), the extensometer used in the tests was made of Nimonic 80. During the tests, the extensometer was not subjected to any loads, except self-weight, and hence was able to move rigidly and freely following the movement of the

specimens. The gauge length for all of the tests was accurately set to 50 mm (see Figure 5.1a). A side view of the extensometer's installation is shown in Figure 5.1b.

Deformations of the gauge length were measured by displacement transducers mounted in the extensometer (see Figure 5.1a). The transducers were inductive LVDT transducers, the plungers of which had a stroke of about 12 mm, of which 5 mm was in the linear range where the measurement is most reliable. During the tests, the transducers were always set up in the linear working range.

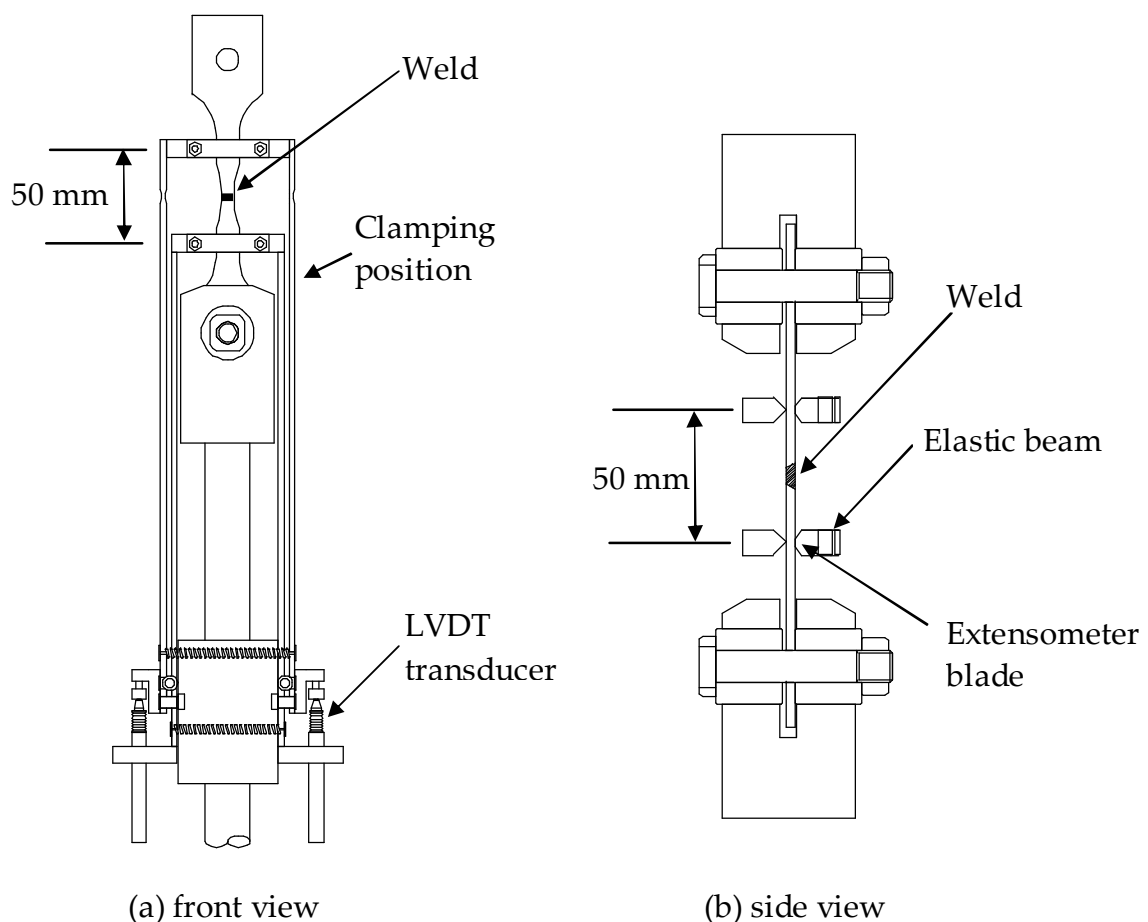


Figure 5.1: Illustration of the extensometer setup

The extensometer was attached to the specimens by knife-edge blades that were tightened by screws. During the heating of the specimen to the test

temperature, the pressure on the extensometer increased as the specimen expanded, whilst during the test, the extensometer loosened due to stress relaxation and the deformation of the specimen. To maintain sufficient contact pressure with the specimen in order to obtain all the deformation information, a special elastic beam clamping mechanism was used as in previous high temperature testing performed at the University of Nottingham. The dimensions of the elastic beam and its installation on the extensometer are shown in Figure 5.2. The beam was made from Nimonic 115 in order for it to withstand repeated use at high temperatures. The Nimonic 115 elastic beam has two cantilever arms. When the screws are tightened, the cantilever arm elastically deforms and applies a force on the blade, which clamps the extensometer to the specimen. When the specimen thickness changes during the tests, due to large deformations or creep stress relaxation, the elastic beam will still keep a force on the extensometer blade as long as the pre-stressed deformation of the elastic beam is larger than the deformation of specimen thickness.

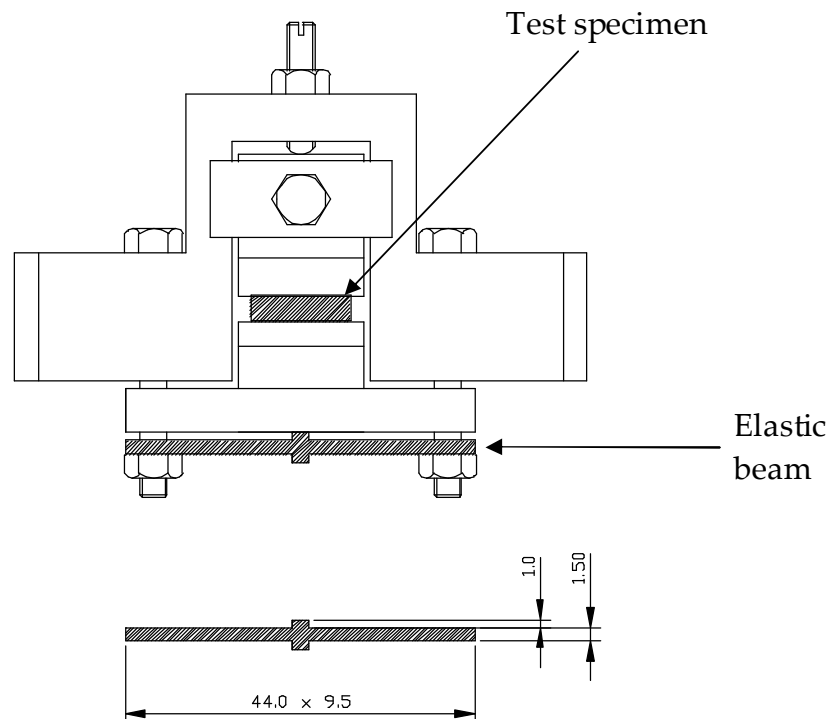


Figure 5.2: Top view of the extensometer grips and Nimonic 115 elastic beam

5.4 Temperature measurement

Twisted wire thermocouples were attached around the specimens in order to monitor their temperature throughout the tests. The specimen gauge length was automatically maintained at the test temperature throughout each test. There was no noticeable variation in the thermocouple readings during the tests.

5.5 Tensile testing

Slow strain rate (constant 0.05mm/s displacement), uniaxial tensile tests were performed on a Mayes Universal Servo-electric Test Machine (Figure 5.3), mainly in order to obtain the necessary material properties required for finite element analysis. Tests were carried out on heat-treated (PWHT –see section 4.3) and as-received, welded and non-welded IN718 specimens at temperatures from 20-1000°C. The specimen geometry is shown in Figure 4.3.

5.5.1 Tensile testing setup and procedure

The specimens were mounted in the Mayes Universal Test Machine using Nimonic 80 high temperature fixtures. An advantage of using specimens with holes is that the pin joint arrangement negates the need for accurate alignment, since it allows the specimen to freely align with the loading direction. The extensometer was attached with the gauge length accurately set to 50 mm. Three twisted wire thermocouples were attached around the top, bottom and centre of the specimen gauge length. The furnace was brought up to temperature while a minimal load was applied to allow the machine's cross head to move with the expansion of the specimen. With a computer running NI LabVIEW logging readings from the extensometer and load cell, a constant displacement rate of 0.05mm/s was applied and the test run until specimen failure.



Figure 5.3: Mayes Universal Servo-electric Test Machine

5.5.2 Tensile test results

The results of uniaxial tensile tests performed at room temperature (20°C) and the specified high temperature (620°C) used for the creep and fatigue testing, are presented and discussed first to allow a simple comparison between the welded and non-welded material. These specimens were given the same PWHT as discussed in section 4.3.

As shown in Table 5-1, the welded specimen tested at room temperature exceeds all of the minimum levels specified by AMS 5596 [118] for an equivalently-aged wrought IN718 sheet, except for a lack of ductility as indicated by a significantly lower strain to failure.

Table 5-1: Tensile test results at 20°C and 620°C

Specimen Ref.	Temp. (°C)	0.2% Proof stress (MPa)	Ultimate strength (MPa)	Young's modulus (GPa)	Failure strain (%)
T1 – NW HT	20 (RT)	1161	1383	205	22.8
W28 – W HT	20 (RT)	1087	1292	201	7.5
T2 – NW HT	620	992	1163	166	21.8
W23 – W HT	620	920	1064	165	5.7
AMS 5596	20 (RT)	1034	1241	200	12.0

NW – non-welded, W – welded, HT – heat-treated, RT – room temperature

The tests at 620°C show a decrease in strength for the welded and non-welded material. These tests also have serrated stress-strain curves, which illustrates the Portevin-Le Chatelier effect [119], whereby the applied stress fluctuates due to the motion of dislocations as the material strains (Figure 5.4).

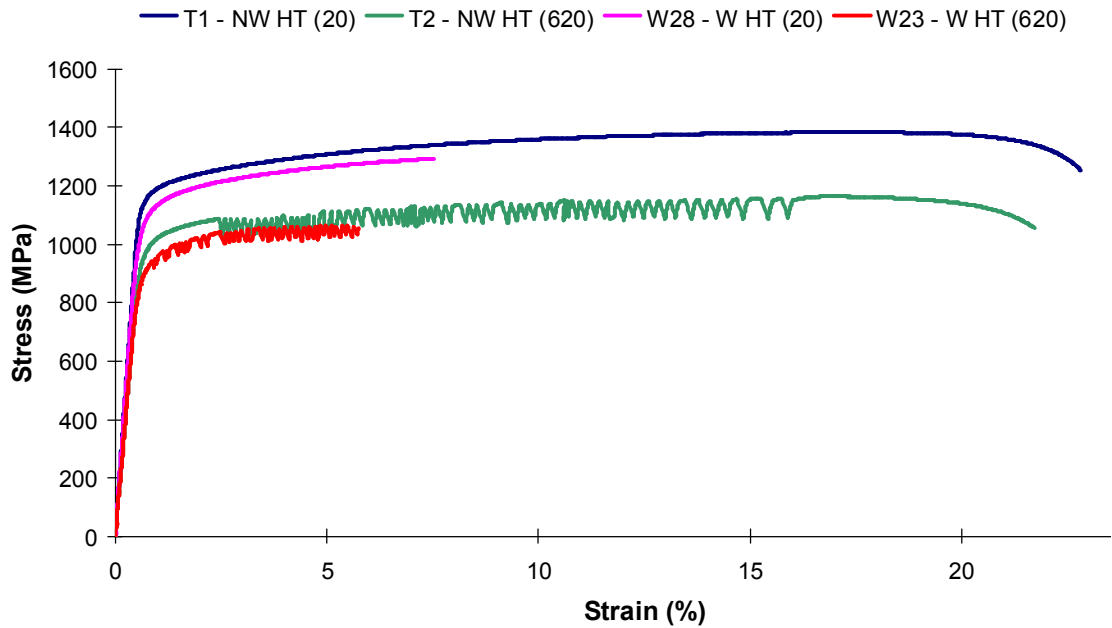
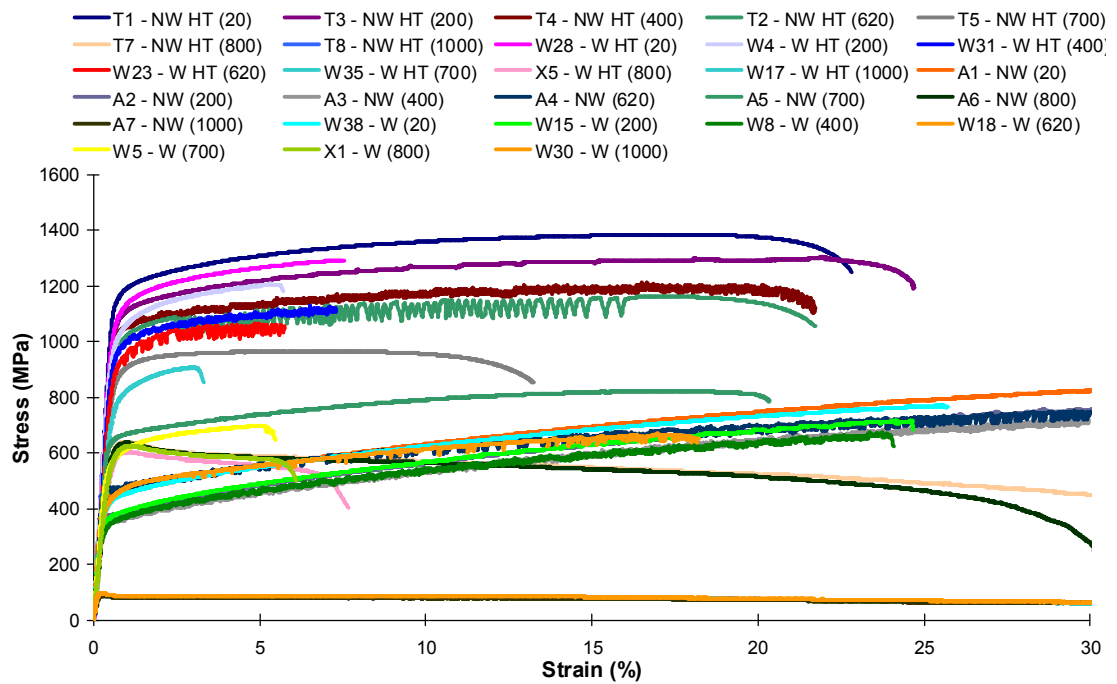


Figure 5.4: Tensile test results (stress-strain relationship) at 20°C and 620°C

Both the 0.2% proof stress and the ultimate strength of the welded specimens are above 90% of the values of the non-welded specimens for tests at ambient (20°C) and elevated (620°C) temperature. The Young's modulus of the welded specimens is very similar to the corresponding non-welded specimen test values. The strain to failure for the welded specimens is significantly less than that of the non-welded specimens. These dissimilarities are due to the differing microstructure of the weld compared to that of non-welded IN718, about which details can be found in the literature review and sections 5.8 and 5.9.

The results of the full tensile testing programme of heat treated and as-received, welded and non-welded IN718 at temperatures from 20-1000°C are presented in Figure 5.5. The mechanical material properties calculated using these results are presented in Figure 5.6 and Table 5-2. The general trend is for the properties to decrease steadily with increasing temperature until the characteristic severe loss of properties starts to occur at 600°C [1].

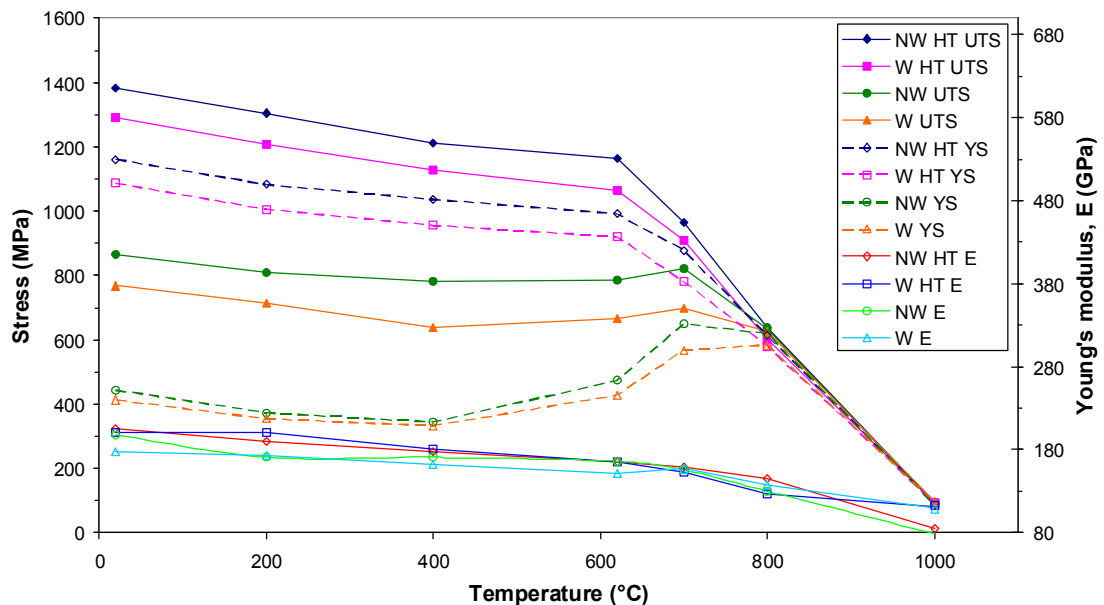


Test temperature shown in brackets (°C)

W – welded, NW- non-welded, HT – heat treated

A – as received (non-welded, not heat treated), T – non-welded, heat treated

Figure 5.5: Full tensile test results (stress-strain curves)



NW – Non-welded

HT – Heat treated

YS – Yield stress (0.2% offset)

W – Welded

UTS – Ultimate tensile strength

E – Young's modulus

Figure 5.6: Variation of welded and non-welded IN718 mechanical material properties with temperature

Table 5-2: Tensile mechanical material properties (test data)

Specimen ref.	Temp. (°C)	E (GPa)	UTS (MPa)	Yield stress (MPa)	Failure strain (%)
T1 - NW HT	20	205	1383	1161	22.8
T3 - NW HT	200	190	1305	1083	24.7
T4 - NW HT	400	178	1211	1036	21.7
T2 - NW HT	620	166	1163	992	21.8
T5 - NW HT	700	159	966	878	13.2
T7 - NW HT	800	145	638	613	38.8
T8 - NW HT	1000	85	91	91	N/A
A1 - NW	20	198	866	443	47.1
A2 - NW	200	171	808	373	48.0
A3 - NW	400	171	782	344	52.8
A4 - NW	620	166	785	474	44.6
A5 - NW	700	156	821	649	20.3
A6 - NW	800	130	636	619	30.1
A7 - NW	1000	79	87	87	N/A
W28 - W HT	20	201	1292	1087	7.5
W4 - W HT	200	201	1209	1006	5.7
W31 - W HT	400	181	1127	956	7.3
W23 - W HT	620	165	1064	920	5.7
W35 - W HT	700	153	907	781	3.3
X5 - W HT	800	126	603	579	7.7
W17 - W HT	1000	112	92	92	N/A
W38 - W	20	177	768	413	25.7
W15 - W	200	173	715	354	24.7
W8 - W	400	162	637	333	24.0
W18 - W	620	151	667	428	18.2
W5 - W	700	157	697	568	5.5
X1 - W	800	137	625	584	6.1
W30 - W	1000	109	96	96	N/A

The heat-treated welded material shows good but slightly lower strength when compared to the non-welded heat-treated material. Like the non-welded material, without any postweld heat treatment, the welded material lacks strength but the strength increases as the temperature reaches that of the recommended heat treatment (600-700°C) due to age hardening of the material during the test. The Young's moduli do not differ much between the different conditions of specimens tested.

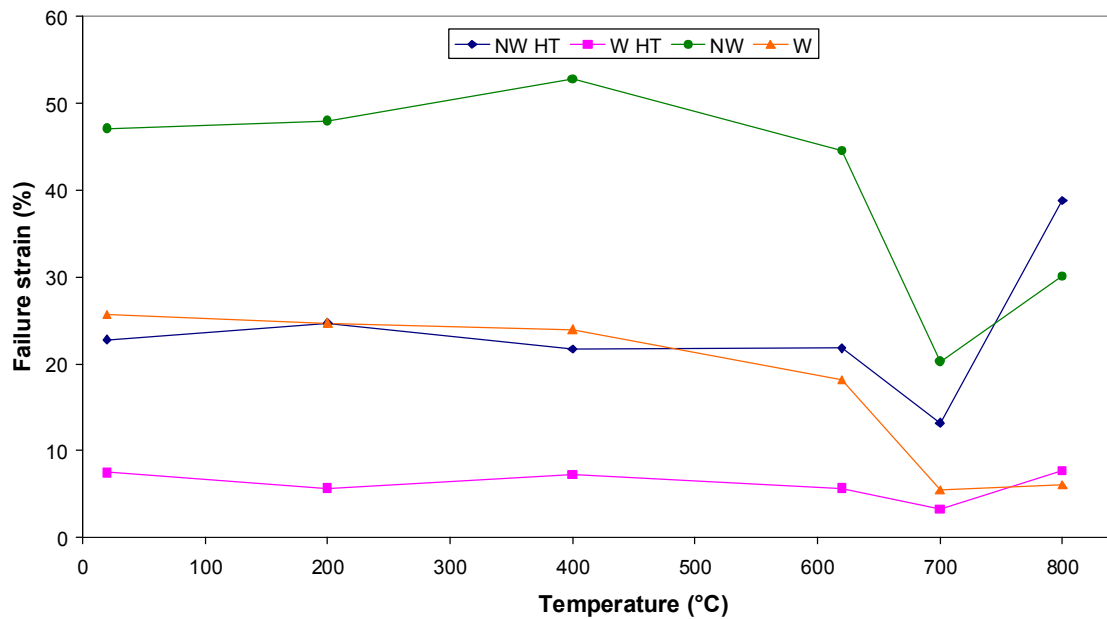


Figure 5.7: Tensile test failure strains against temperature

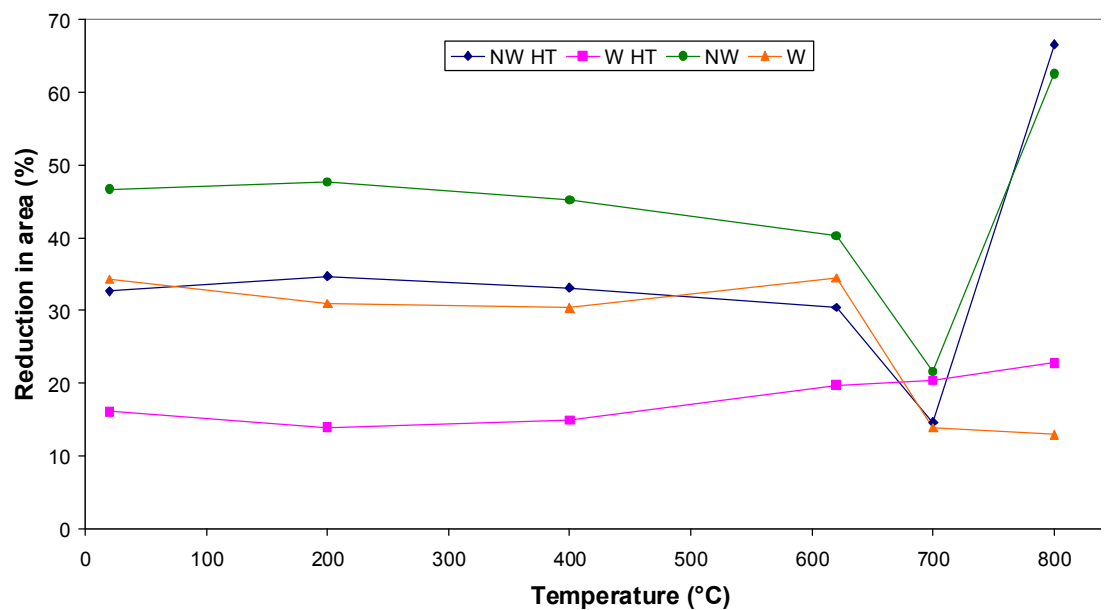


Figure 5.8: Tensile test reductions in area at failure against temperature

The welded material is less ductile than non-welded (or parent). This is shown by the lower extensions at failure and reductions in area of the welded specimens. The welded material also has a lack of superplasticity at very high temperature compared to non-welded. This is evident since the failure strains and reductions in area of the welded specimens do not significantly increase at 800°C, whereas the corresponding values of the non-

welded specimens do. Further indication that the non heat-treated material hardens around 600-800°C is shown by the corresponding decreases in extensions at failure and reductions in area of the specimens tested at 700°C (Figure 5.7 and Figure 5.8, respectively).

All welded specimens failed in the weld region (Figure 5.9). Optical microscopy was performed on some of the failed, welded and non-welded tensile specimens, the results of which are discussed and compared with those of the creep and fatigue specimens in section 5.8. Some low magnification photographs of the common tensile shear failures observed are shown in Figures 5.9-5.11.

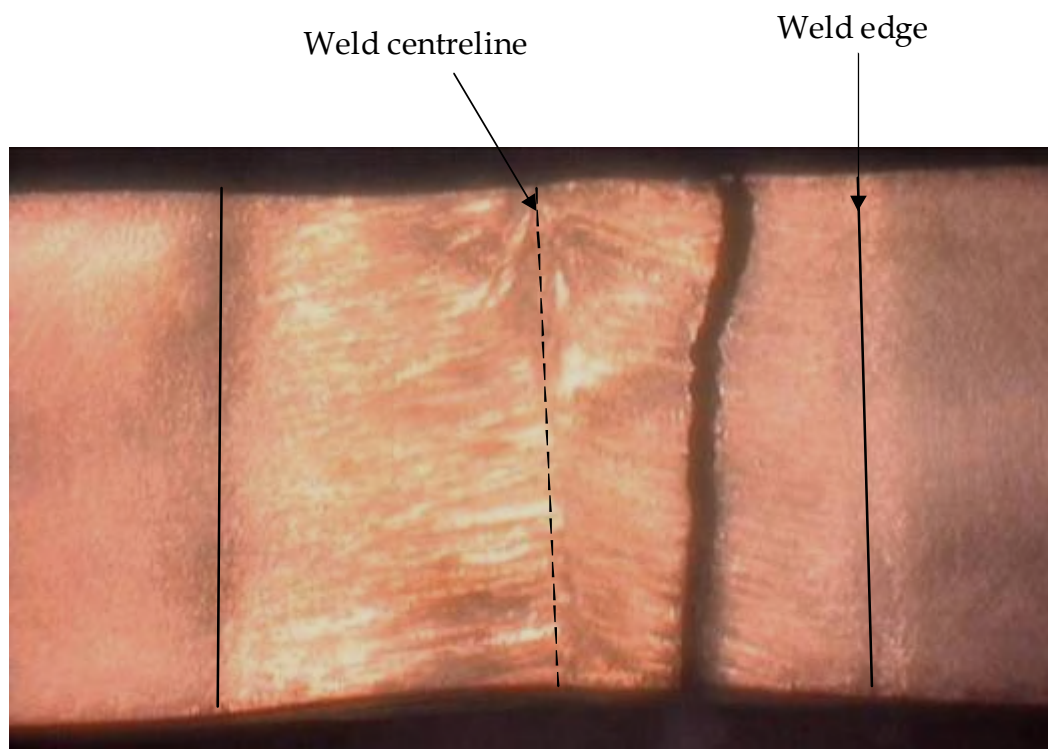


Figure 5.9: Failed welded tensile specimen W8 –photograph (top view), the approximate locations of the weld centreline and edges are marked



Figure 5.10: Failed welded tensile specimen W8 –photograph (side view)

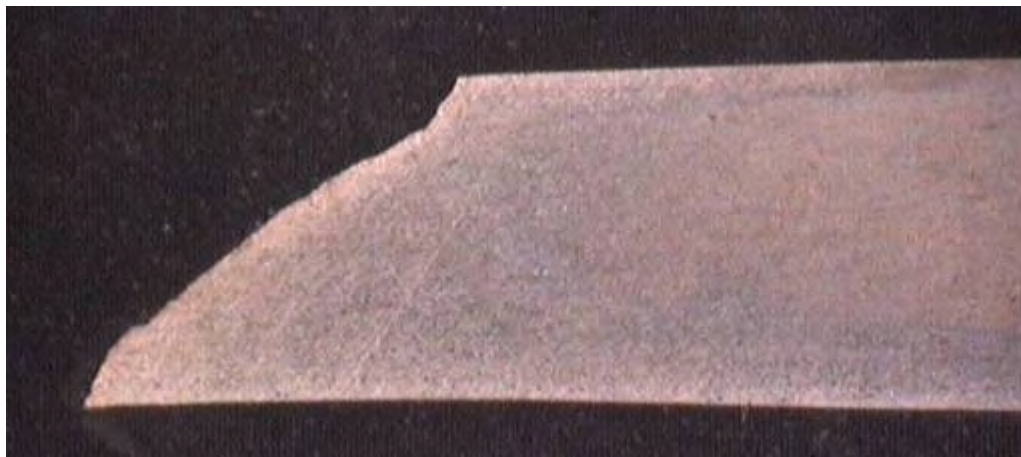


Figure 5.11: Failed non-welded tensile specimen T1 –photograph (side view)

5.6 Creep testing

Uniaxial constant load creep tests were performed at 620°C, the results of which are used in Chapter 6 to provide the material constants required for creep and damage constitutive equations. 620°C was the chosen temperature for all the creep and also the high temperature fatigue tests since this is the temperature limit permitted for many critical applications of the material [1, 78]. Rapid coarsening of the primary hardening phase in IN718, body-centred tetragonal (BCT) Ni_3Cb , γ'' phase and its eventual conversion to δ is believed to be responsible for the degradation in properties of IN718 above 650°C [78, 80].

Creep tests were carried out on both welded and non-welded, and also notched welded and notched non-welded IN718 specimens, at a variety of different nominal stress levels. The purpose of the notched tests was to obtain multiaxial stress material behaviour properties. All specimens were given the same heat treatment (referred to as PWHT –see section 4.3).

5.6.1 Creep testing setup and procedure

The creep tests were carried out on Denison machines (see Figure 5.14) in which a constant load is applied through a lever system. The specimen geometry was the same as that used for the tensile tests (Figure 4.3), except for the notched tests (Figure 5.12 and Figure 5.13). The specimens were mounted in the machine using Nimonic 80 high temperature fixtures (Figure 5.15). The extensometer (with Nimonic 115 elastic beam as mentioned in section 5.3) was attached with the gauge length accurately set to 50mm (Figure 5.16). A Solartron SI 13350 data logging system was used to automatically record the output from the LVDT transducers. A muffle-type furnace was used to heat the specimen up to the required temperature. The furnace was lowered to surround the specimen. A minimal load was applied to the specimen as the furnace was heated to the test temperature. With the data logger taking readings from the extensometer, the test load to give the required stress was applied and the test run until specimen failure.

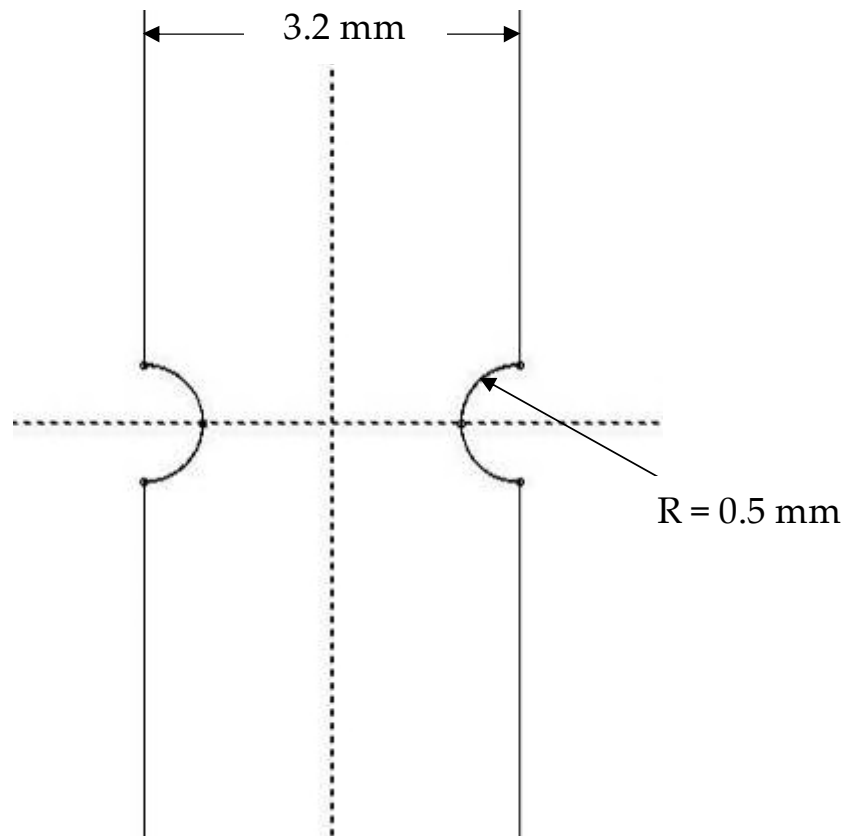


Figure 5.12: Notched creep specimen (side view)

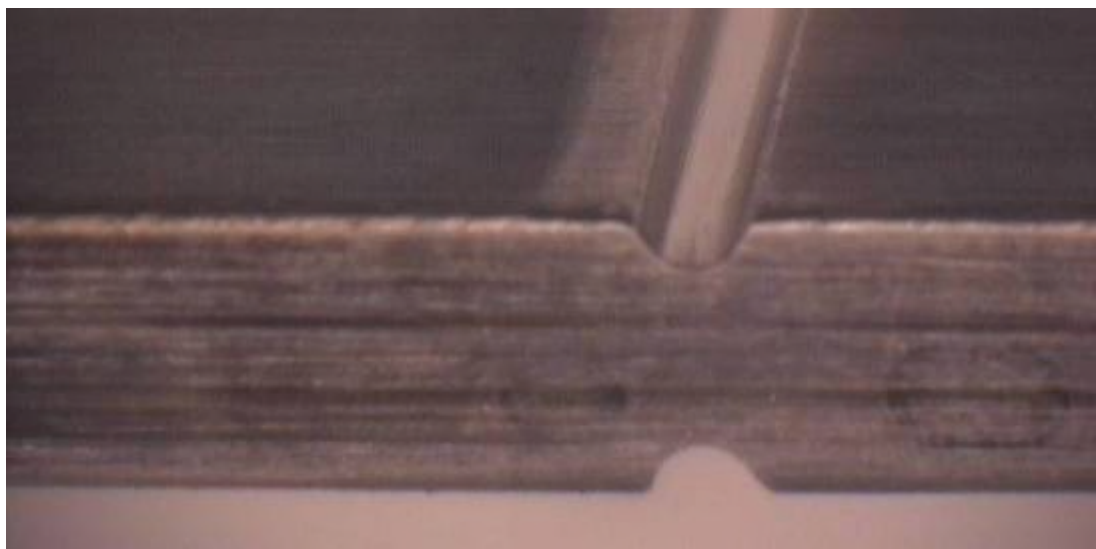


Figure 5.13: Notched creep specimen photograph (side view -after polishing)



Figure 5.14: Denison creep testing machines

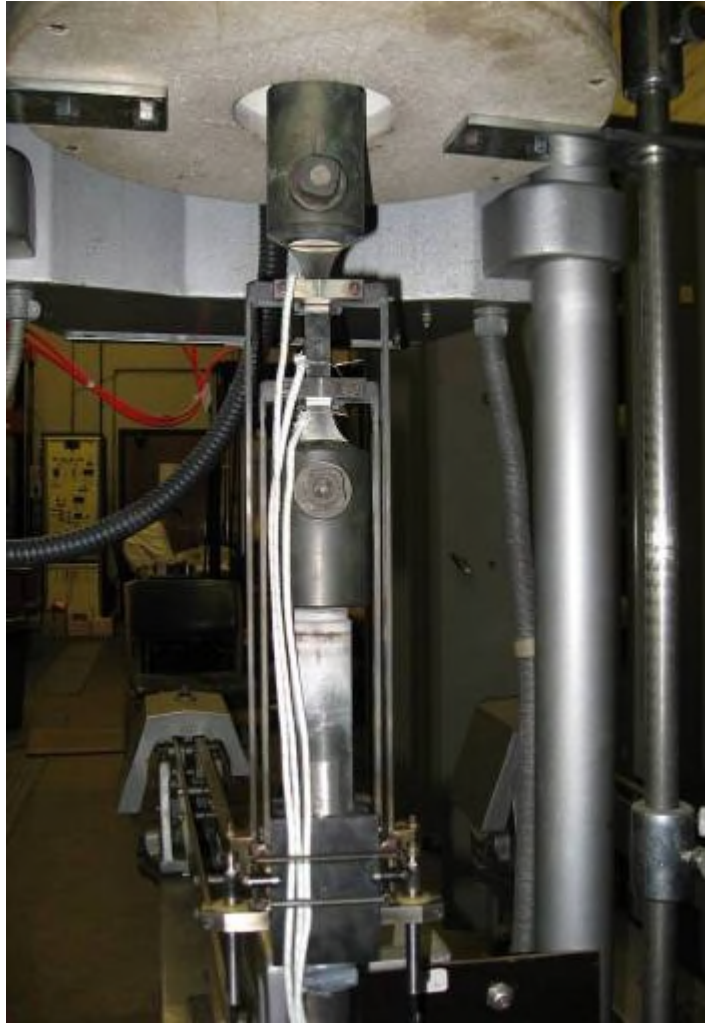


Figure 5.15: Creep specimen installation

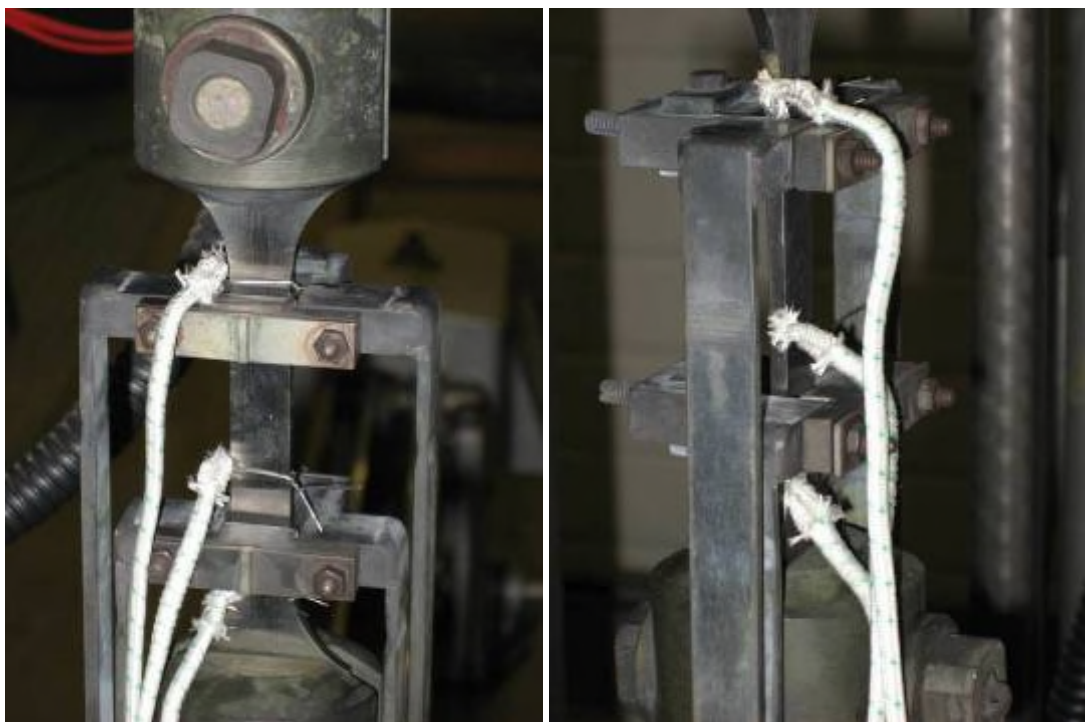
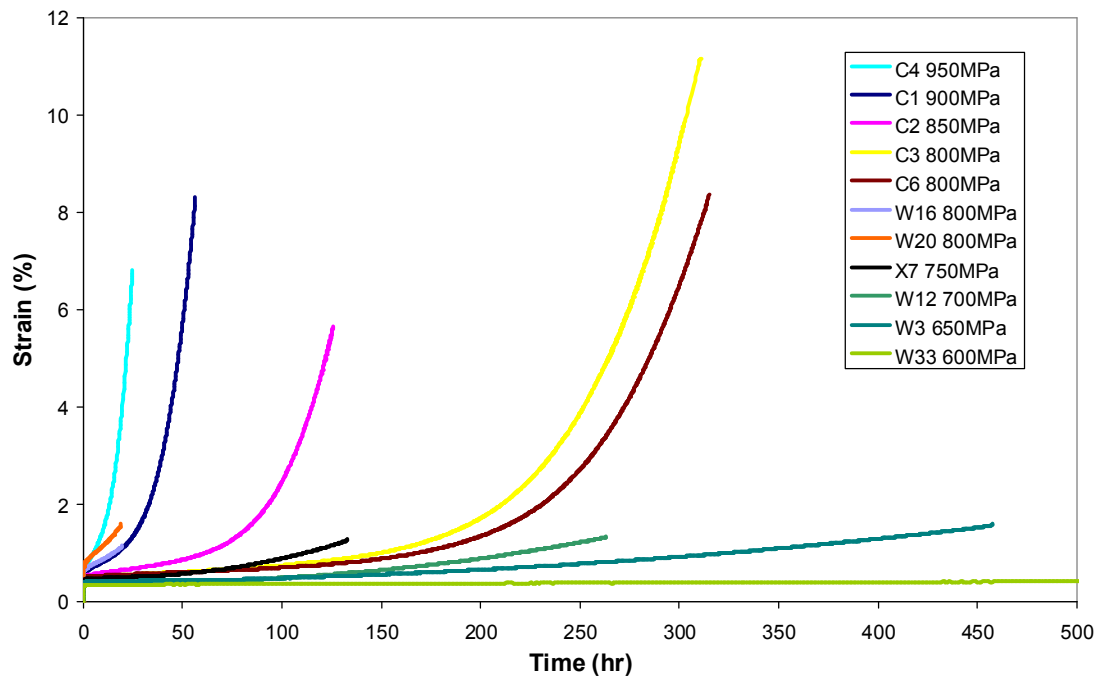


Figure 5.16: Extensometer attached to creep specimen

5.6.2 Creep test results

The resulting creep test strain-time curves are presented in Figure 5.17. As for the tensile test results, the total strains to failure of the welded specimens are noticeably less than those of the non-welded specimens. The time to failure for a given load is also markedly less for the welded specimens. The failure times consistently decrease as the applied load increases for both types of specimen.



W/X – welded, C – non-welded

Figure 5.17: Creep strain curves against time

The creep rupture (or failure) times are plotted (using logarithmic scales) against nominal applied stress in Figure 5.18 and tabulated in Table 5-3. The data obtained during this work is compared with results from similar testing performed previously at the University of Nottingham, but where weld bead excess was not removed and the welded specimens were distorted [93].

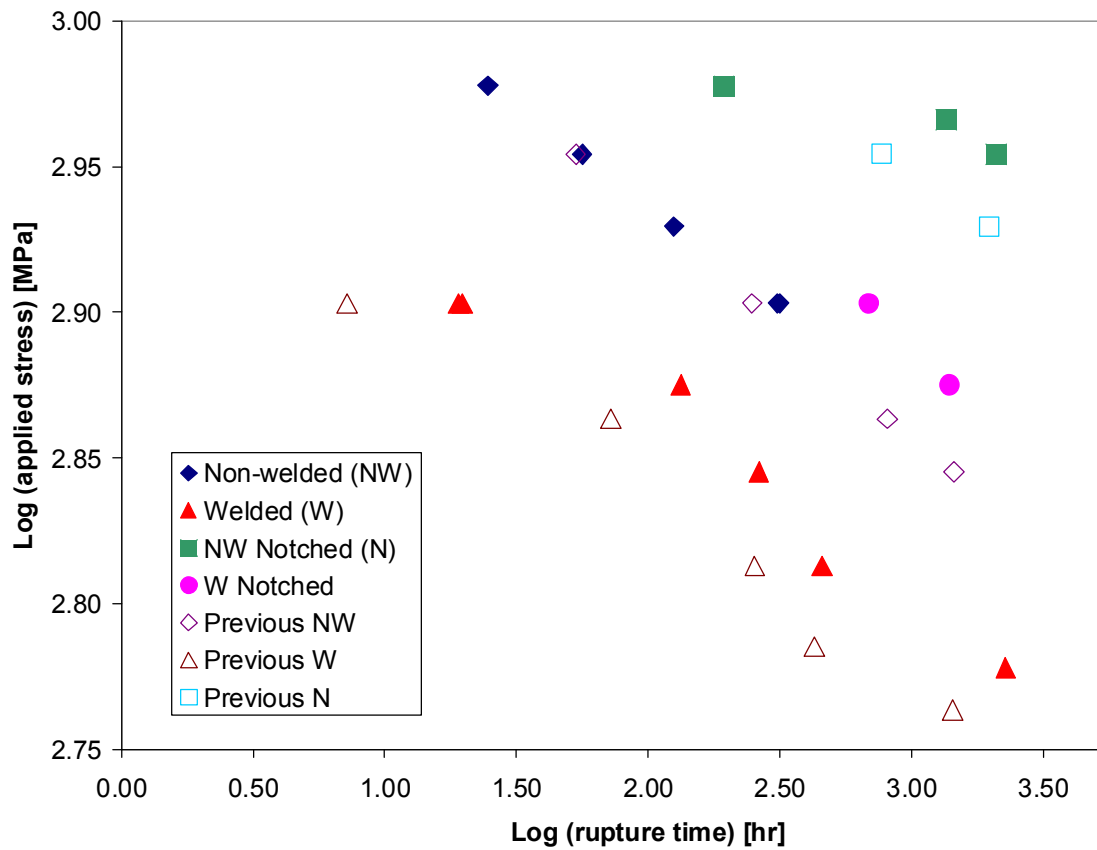


Figure 5.18: Log-log creep rupture times for applied stress at 620°C (compared with similar previous testing where weld bead excess was not removed and the welded specimens were distorted [93])

Table 5-3: Constant load creep rupture lives (hr) (compared with [93])

Nominal stress (MPa)	Non-welded	Previous Non-welded	Welded	Previous Welded
560	–	–	–	1440
610	–	–	–	429
600	–	–	2280	–
650	–	–	458	254
700	–	1456	263	–
730	–	814	–	72
750	–	–	133	–
800	310	249	20	7
850	126	–	–	–
900	56	53	–	–
950	25	–	–	–

In terms of creep life (i.e. time to rupture), the results of the creep testing compare well with those from the previous testing programme. The welded specimens performed slightly better than before since weld bead excess was removed and the specimens were not distorted. The non-welded specimen results follow a linear trend when plotted using logarithmic scales (Figure 5.19), but the welded specimen results follow a more complex sinusoidal distribution, although a linear trend line can be fitted to the intermediate stress tests (i.e. 650MPa, 700MPa and 750MPa) (Figure 5.20).

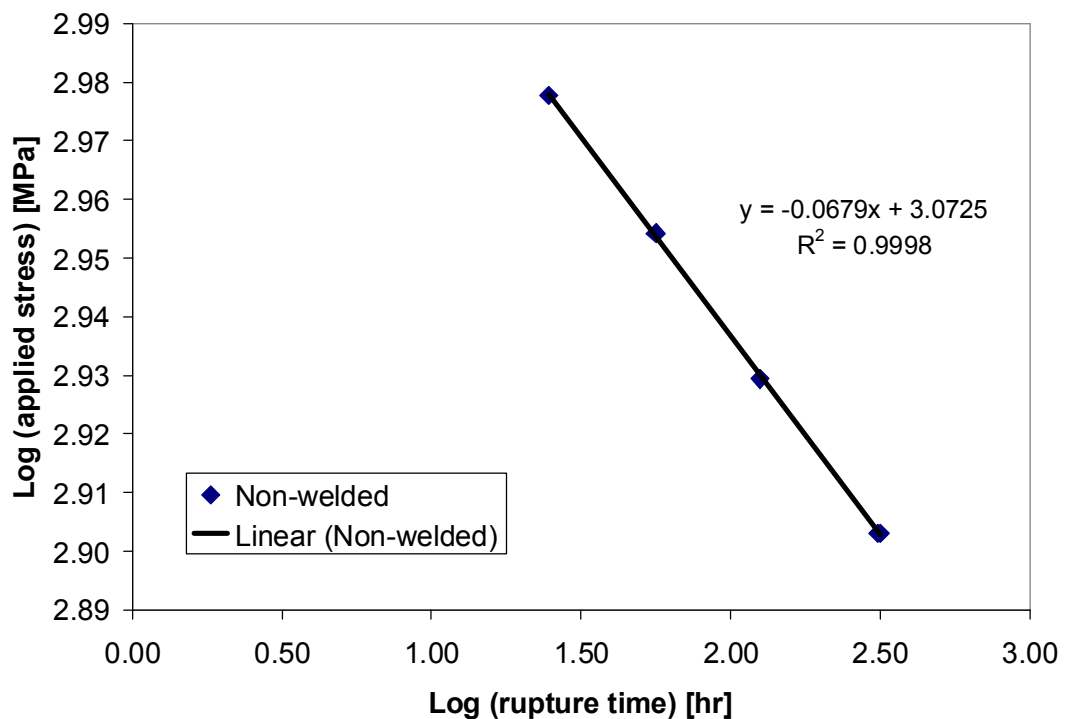


Figure 5.19: Log-log applied stress against rupture time plot for non-welded IN718 creep tests at 620°C

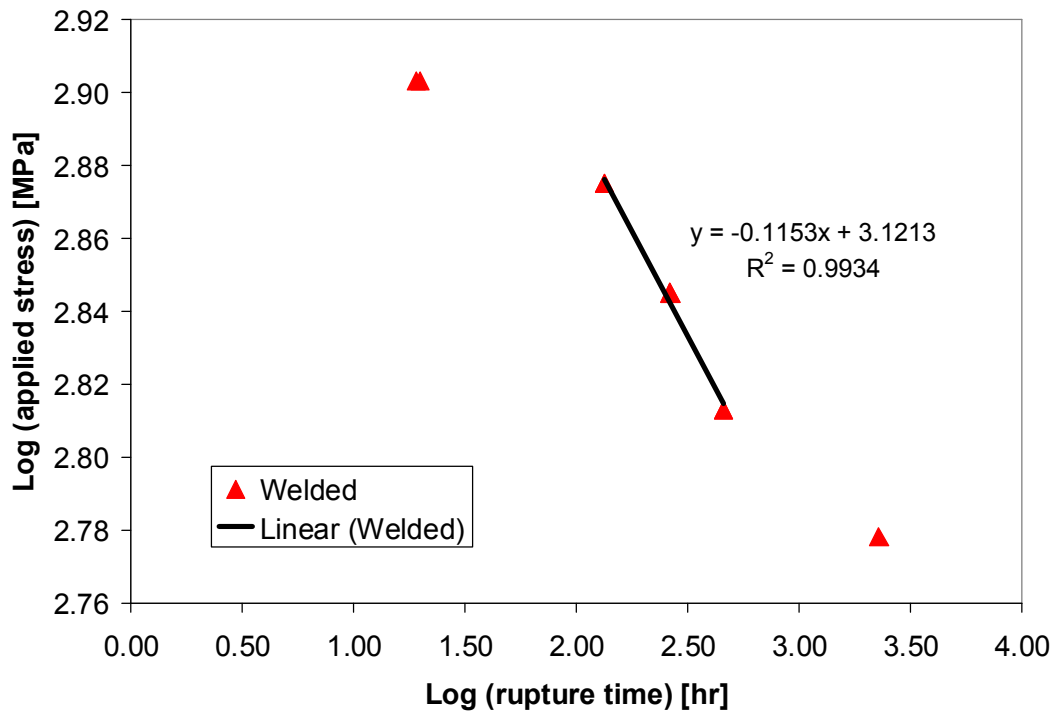


Figure 5.20: Log-log applied stress against rupture time plot for welded IN718 creep tests at 620°C

All welded specimens failed in the heat-affected zone. Creep cracks propagated perpendicular to the loading direction, followed by tensile overload fracture along a 45° plane to the specimen surface, which indicates shear failure. Optical microscopy was performed on some of the failed, welded and non-welded creep specimens, the results of which are discussed and compared with those of the fatigue and tensile specimens in section 5.8. Some low magnification photographs of the common creep failures observed are shown in Figures 5.21-5.23.

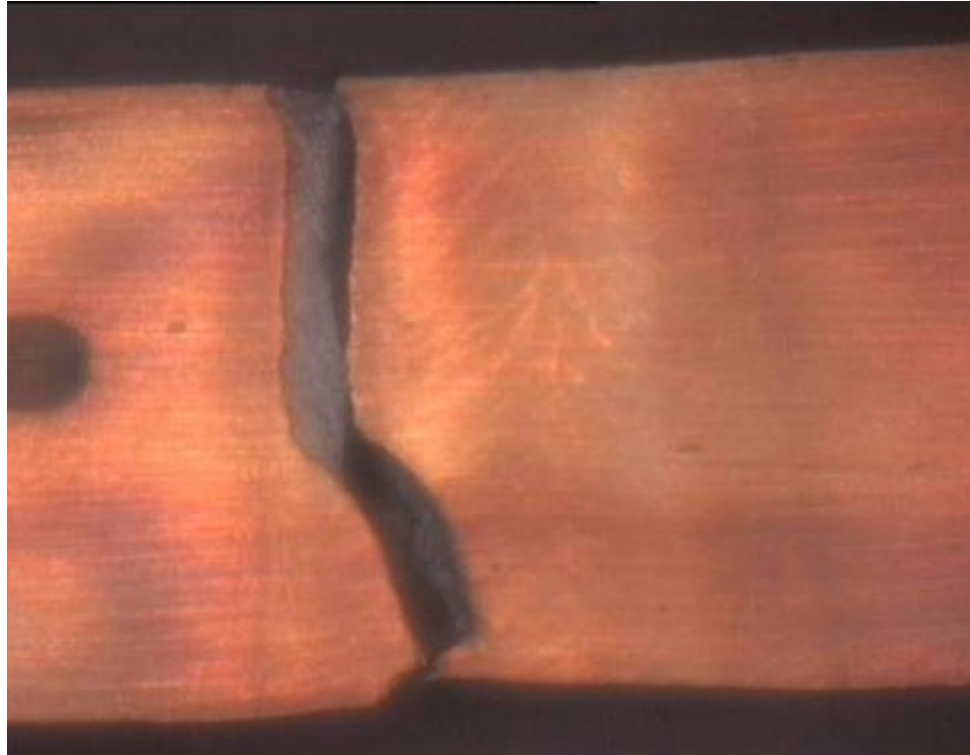


Figure 5.21: Failed welded creep specimen W12 –photograph (top view)



Figure 5.22: Failed welded creep specimen W12 –photograph (side view)



Figure 5.23: Failed non-welded creep specimen C2 –photograph (side view)

5.7 High temperature fatigue testing

High temperature fatigue tests with dwell periods are essentially cyclic loaded creep tests, combining the effects of creep and fatigue and are therefore often termed ‘creep-fatigue’ tests. Significant creep-fatigue interaction may occur or one of the processes may be dominant and the other can often be neglected for the purposes of life assessment. The tests performed here were load-controlled and low-cycle due to the high applied load, which causes plasticity and leads to a low number of cycles before failure. The tests were also uniaxial and isothermal (620C° -the temperature also chosen for the creep tests, see section 5.6). Tests were carried out on both welded and non-welded specimens, at a variety of different nominal (maximum on-load) stress levels. All specimens were given the same heat treatment (referred to as PWHT –see section 4.3).

5.7.1 High temperature fatigue testing setup and procedure

The high temperature fatigue tests were performed on the same Mayes Universal Test Machine as that used for the tensile tests (Figure 5.3). The machine is electromechanical, servo-controlled, screw-driven and has a maximum loading capacity of 250 kN. It is fitted with a muffle type furnace and has the facility for cyclic loading over a range of frequencies using programmable waveforms.

Again, the specimens were mounted in the Mayes Universal Test Machine using Nimonic 80 high temperature fixtures and the extensometer was attached with the gauge length accurately set to 50 mm (see Figure 5.24). The furnace was closed around the specimen and brought up to temperature while a minimal load was applied to allow the machine's cross head to move with the expansion of the specimen. The machine's ramp cycle generators were then started and the upper and lower loads were refined to the required levels using feedback from a computer running NI LabVIEW. The cycle rates were also adjusted to give an acceptable frequency commensurate with the limitations of the machine. Cycles to failure were counted and recordings of load and extension were logged at intervals throughout the test.

All cycles had a trapezoidal (1-1-1-1) form with a load frequency of 0.25 Hz (i.e. 1sec ramp up/1sec dwell at max. load/1sec ramp down/1sec dwell at min. load) and a stress ratio ($\sigma_{\min} / \sigma_{\max}$) of *approximately* zero (a minimum load of 0.5kN was used to avoid slack in the fixtures) (see Figure 5.25). This loading waveform is the same as that used in similar previous tests performed by the University of Nottingham and Rolls-Royce plc, and is used to replicate high temperature, fluctuating on-off load service conditions.



Figure 5.24: Fatigue specimen installation

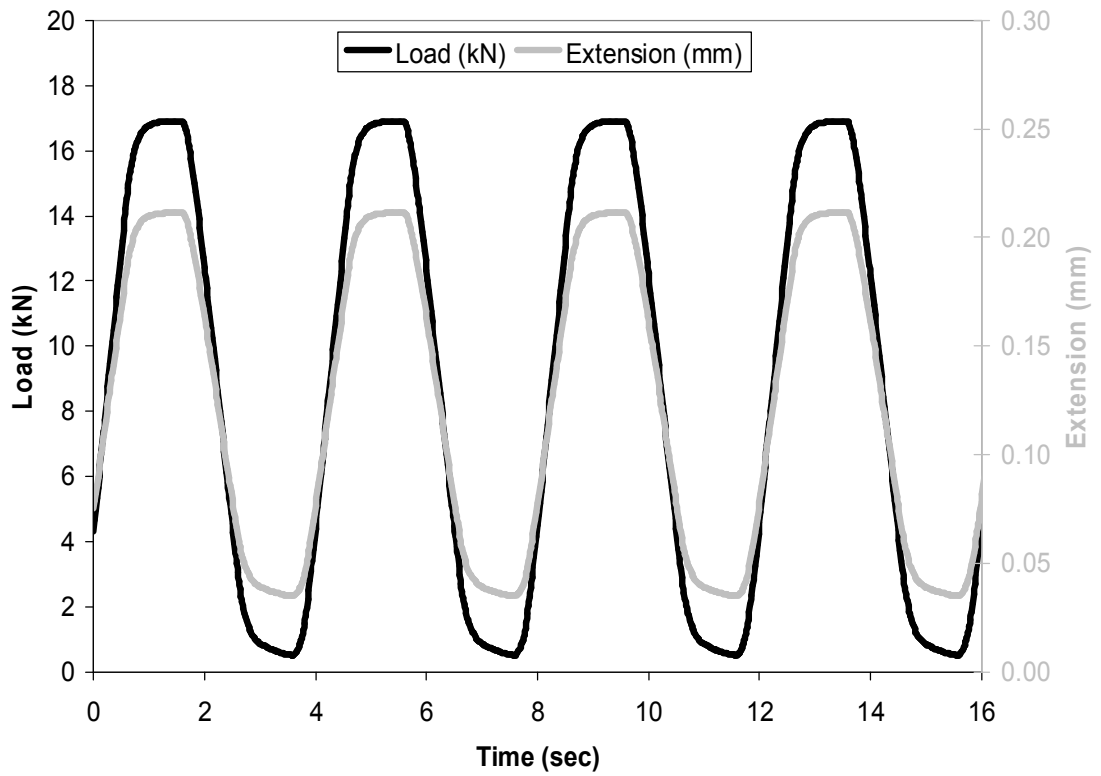


Figure 5.25: Fatigue test cycle data from a welded specimen tested at a nominal (on-load) stress of 825MPa (stress ratio ≈ 0 , trapezoidal (1-1-1) form, load frequency = 0.25 Hz)

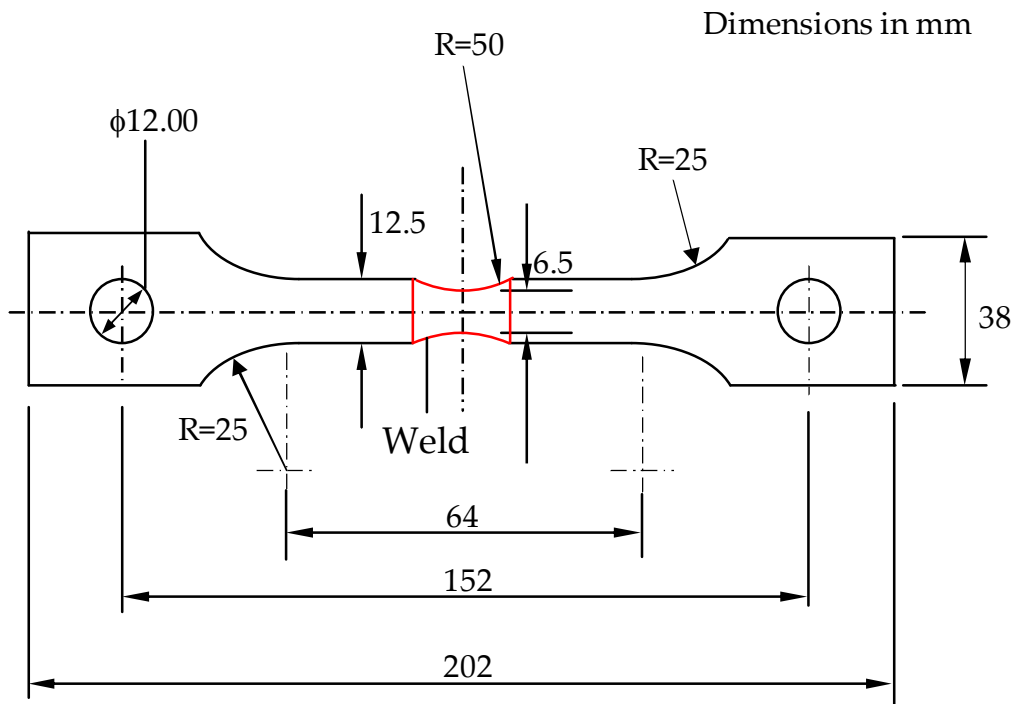


Figure 5.26: Fatigue test specimen

The fatigue specimen geometry is shown in Figure 5.26. Even though the width of the test section was reduced for these tests to try to avoid failures at the holes, the initial fatigue tests still failed at the specimen holes rather than in the necked test section due to the inadequate finish left by the hole drilling process (see Figure 5.27). To counter this problem, the holes of the fatigue specimens were thoroughly polished before testing using three different grades of wet and dry paper wrapped around a spindle in a bench drill. The test sections were finished by hand using a polishing stone and three different grades of wet and dry paper.



Figure 5.27: Fatigue specimen hole failure

5.7.2 High temperature fatigue test results

The results of the fatigue testing at 620°C are presented in Table 5-4 and Figure 5.28. The welded specimens were not able to withstand the same nominal stresses as the non-welded specimens and the corresponding failure lives are lower for the welded specimens for any given nominal stress.

Table 5-4: Fatigue test results at 620°C

	Specimen	Stress (MPa)	No. cycles to failure
Non-welded	F1	1050	29339*
	F2	1100	2495*
	F3	1100	13494
	F5	1050	35560*
	F4	1050	91360
	F7	1150	2650
	F6	1200	46
	F8	1175	3373
	F9	1200	6
	F10	1025	72662
Welded	W10	950	430
	W14	900	785
	W19	850	18541
	X2	800	169998
	W21	875	9996
	W11	825	14863
	W39	825	143709
	W7	825	8714
	X6	890	14814
	W1	925	304

*F1 failed at top hole

*F2 failed at a large machining mark

*F5 failed at bottom hole

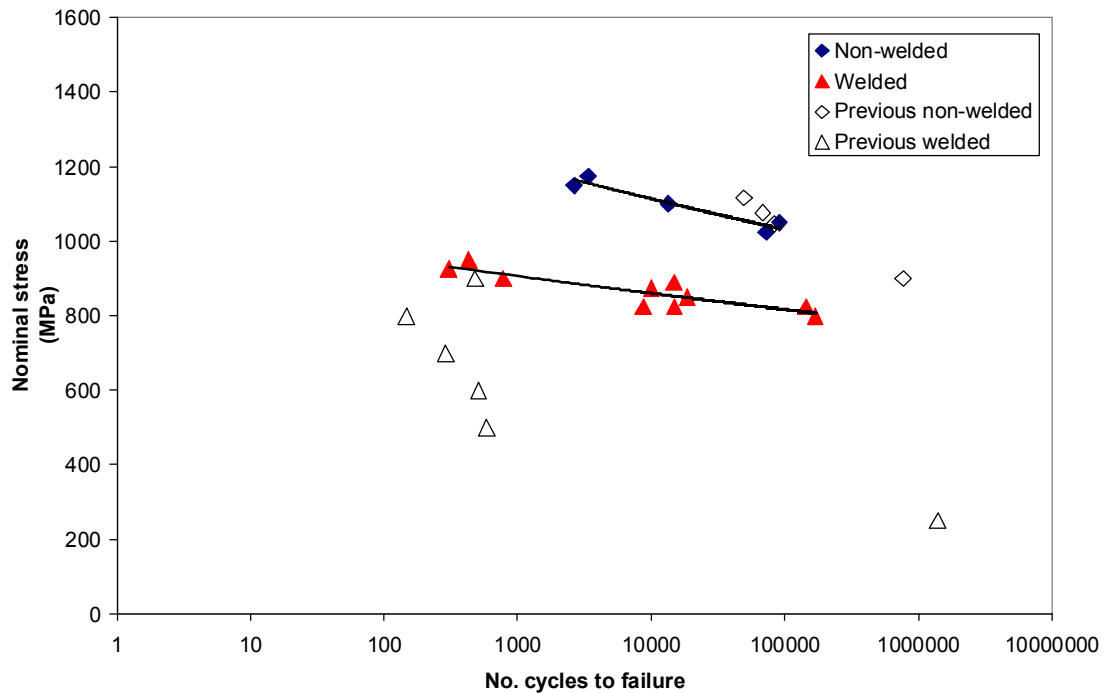


Figure 5.28: Fatigue test cycles to failure for maximum nominal stress, at 620°C (compared with similar previous testing where weld bead excess was not removed and the welded specimens were distorted)

Figure 5.28 also shows the comparison between the results of the current testing programme and those from a similar programme previously carried out at the University of Nottingham. The results from the previous study were compromised since weld bead excess was not removed and the welding process caused significant out-of-plane distortion.

It is clear that the fatigue results obtained during the work for this thesis are more applicable for life assessment and prediction purposes than those obtained previously; the new results presented here can be used for life prediction with a fair degree of accuracy and lower uncertainty than before.

The welded specimen fatigue lives have been improved by finishing weld bead excess and mitigating weld-induced distortion. However, the weld region and the heat-affected zone (HAZ) still exhibit lower tensile strength

and ductility than the base material, and the failure lives for the welded specimens remain lower than the corresponding non-welded values for any given nominal stress.

All fatigue specimen failures occurred in the waist section, with the welded specimens failing in the weld region. Fatigue cracks propagated perpendicular to the loading direction, followed by tensile overload fracture along a 45° plane to the specimen surface, which indicates shear failure. Optical microscopy was performed on some of the failed, welded and non-welded fatigue specimens, the results of which are discussed and compared with those of the creep and tensile specimens in section 5.8. Some low magnification photographs of the common fatigue failures observed are shown in Figures 5.29-5.32.

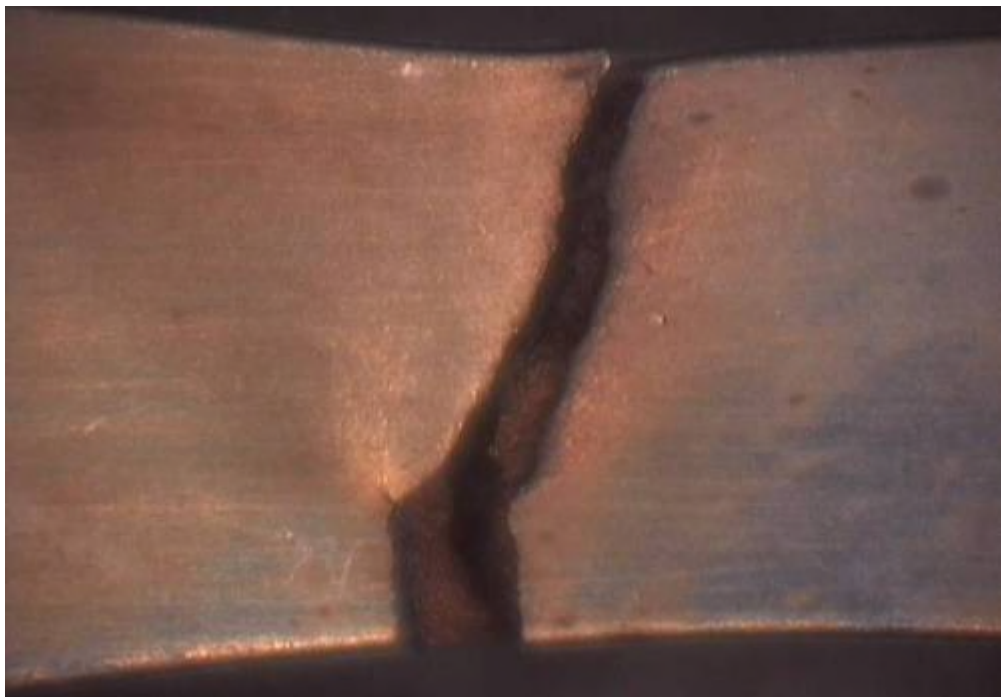


Figure 5.29: Failed non-welded fatigue specimen F3 –photograph (top view)



Figure 5.30: Failed non-welded fatigue specimen F3 –photograph (end view)



Figure 5.31: Failed welded fatigue specimen W14 –photograph (top view)

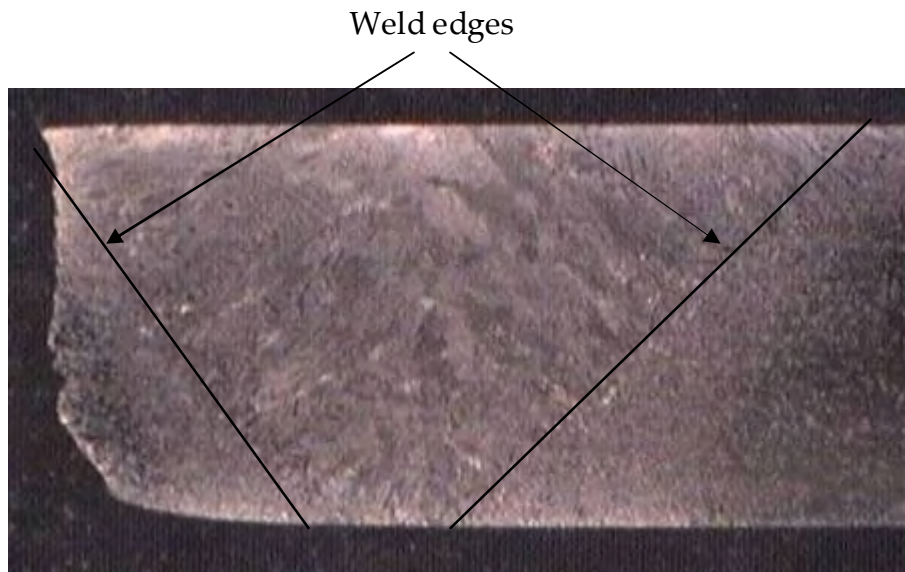


Figure 5.32: Failed welded fatigue specimen W39 –photograph (side view)

Figure 5.33 shows load-extension data logged after different numbers of cycles (i.e. different times) during a 620°C non-welded 1025MPa maximum ‘on-load’ nominal stress fatigue test. There is very little hysteresis during the cycles. Creep strain is identified by the increase in both maximum and minimum extension readings for the same load levels, as time increases.

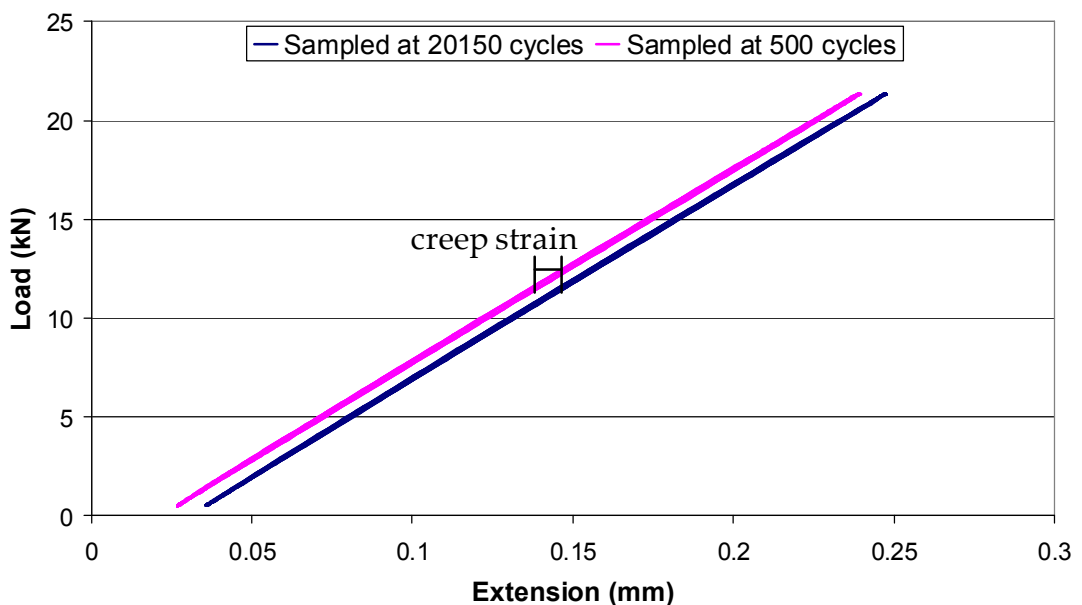


Figure 5.33: Load-extension plot for different cycles during non-welded 1025MPa fatigue test

5.8 Optical microscopy/fractography

Welded joints that are subject to high loads should ideally contain no obvious nucleation sites for cracks, such as microfissures in the HAZ. However, in common with other nickel superalloys, welded IN718 exhibits varied and complex microstructures in the fusion zone (FZ) and in the HAZ [89], while the parent (base) material only consists of fine equiaxed grains.

Optical microscopy was performed on some of the failed, welded and non-welded specimens, in order to identify the failure mechanisms and the different microstructures present. The reasons behind the lower creep and high temperature fatigue performance of the welded material may then be identified. The crack initiation sites were distinguishable by discolouration due to differing amounts of exposure to the hot atmosphere during the test (e.g. Figure 5.34).



Figure 5.34: Discolouration around the crack initiation site

5.8.1 Procedure

The specimens were cross-sectioned using a large and then a small cut off wheel (with lubricant). The samples were mounted using *conducto* Phenolic mounting resin and polished to 1 μ m using rotary grinding machines.

The chemical etchant used was “Kalling’s No. 2” (waterless Kalling’s):

2g Cu Cl₂

40ml HCl

40-80ml ethanol

This etchant is especially suited to both nickel-base superalloys and stainless steels.

The following two types of microscope were used:

Nikon Binocular stereoscopic microscope (for low magnification)

Nikon Optiphot microscope (for higher magnification)

5.8.2 Tensile tests

The welded and non-welded tensile test failures occurred in the centre of the specimens by tensile overload, causing shear transgranular fracture. All welded specimen failures occurred in the weld FZ, which consists of large columnar dendritic grains (e.g. Figure 5.35).

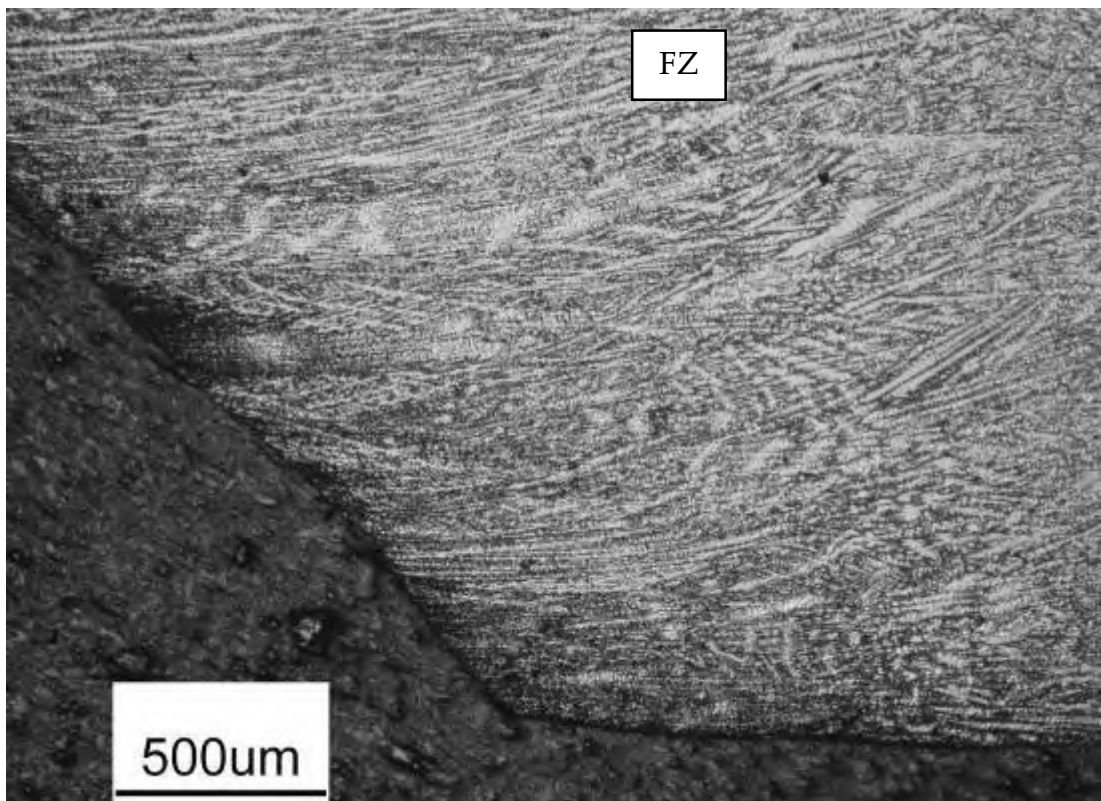


Figure 5.35: Failed welded tensile specimen W8 –micrograph (side view)

5.8.3 Creep tests

The welded and non-welded creep tests showed small intergranular creep cracks at the edges of the specimens (Figure 5.36) and significant final tensile overload shear transgranular fractures (Figure 5.37). The welded specimen creep cracks initiated in a coarse equiaxed grain HAZ. Here the large grains were unable to accommodate large straining by grain boundary sliding (Figure 5.38 and Figure 5.39). The final failure occurred by shearing through the weaker weld FZ (Figure 5.40 and Figure 5.41). Figure 5.42 shows the microstructure away from the fractured edge, the weld FZ and coarse and fine equiaxed grain HAZ are labelled.

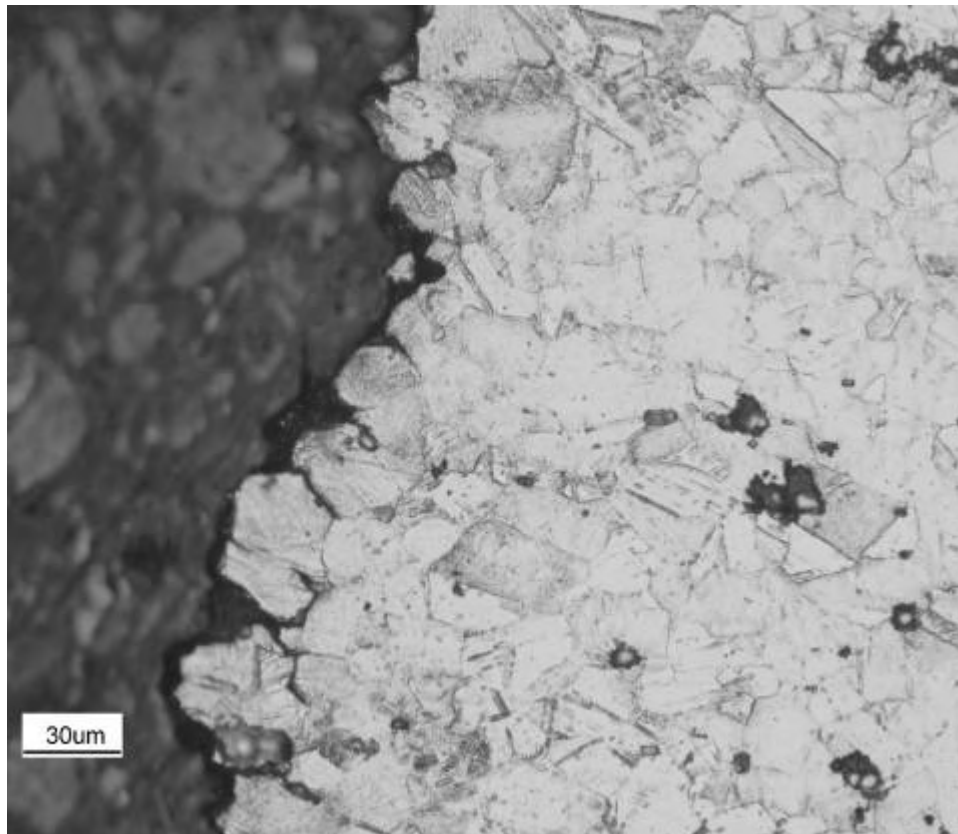


Figure 5.36: Non-welded specimen C5 creep crack –micrograph (side view)

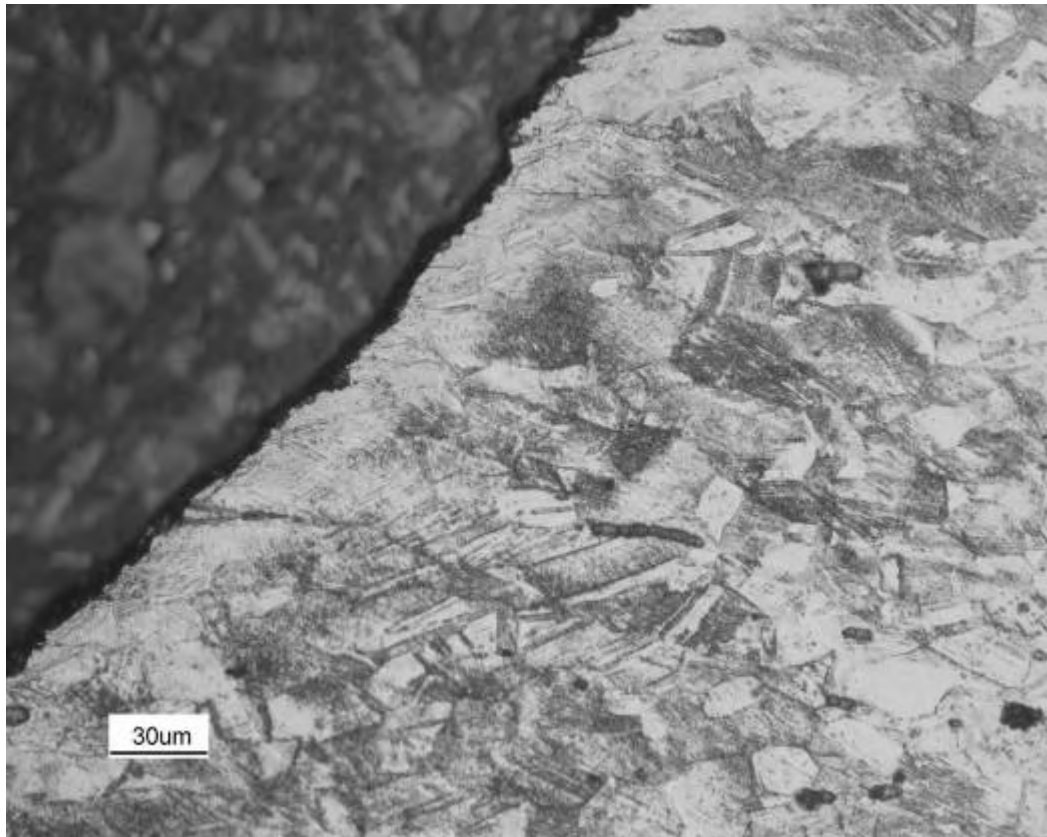


Figure 5.37: Non-welded specimen C5 shear failure –micrograph (side view)

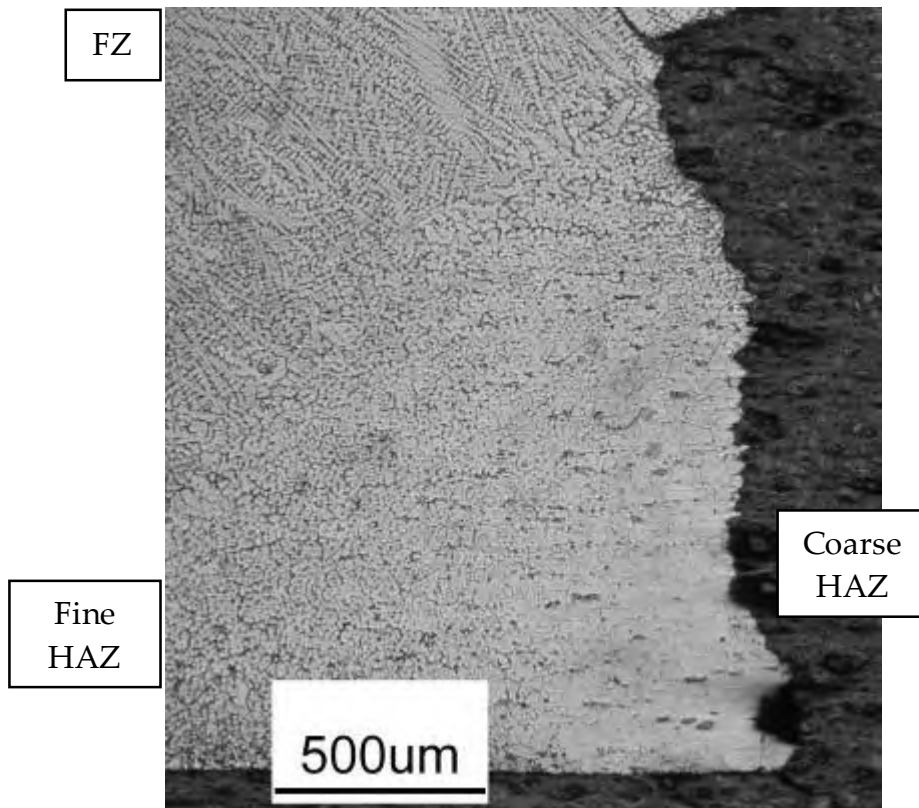


Figure 5.38: Welded specimen W12 creep crack –micrograph (side view)

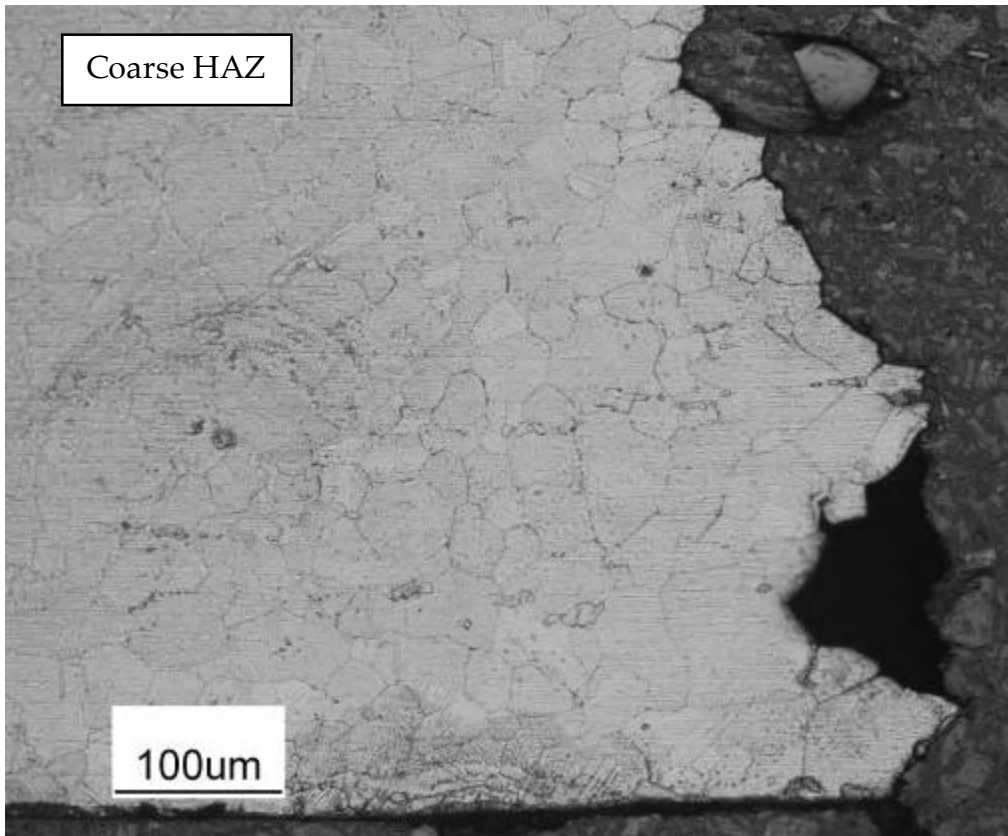


Figure 5.39: Welded specimen W12 creep crack (higher magnification)

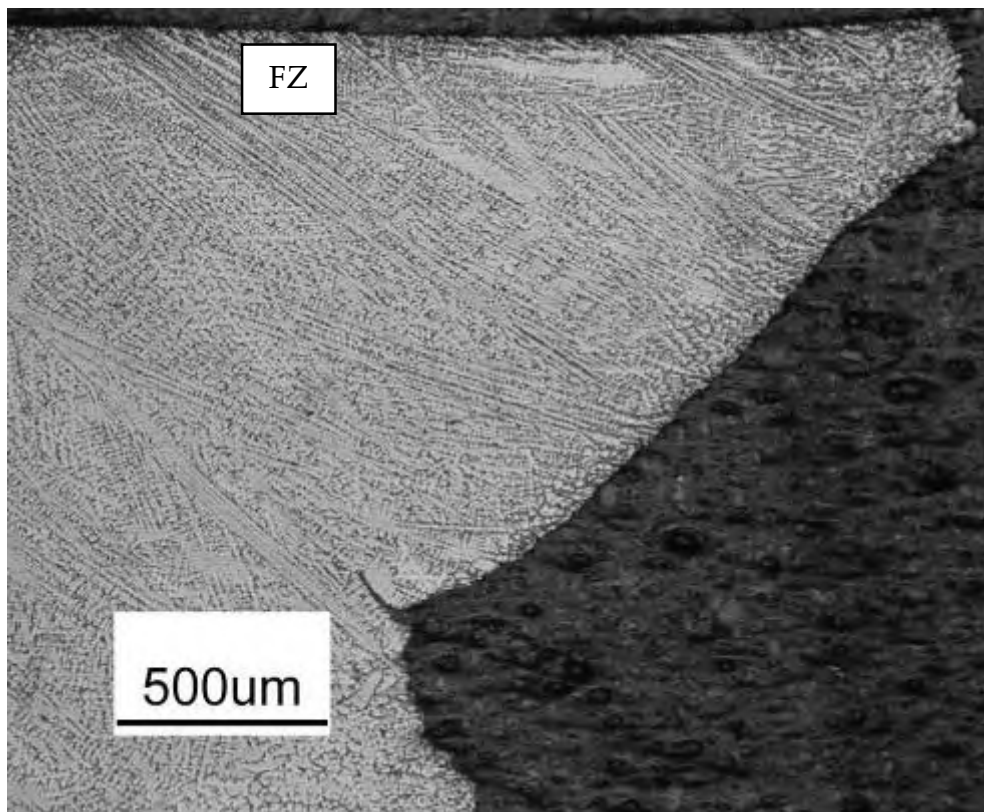


Figure 5.40: Welded specimen W12 shear failure –micrograph (side view)

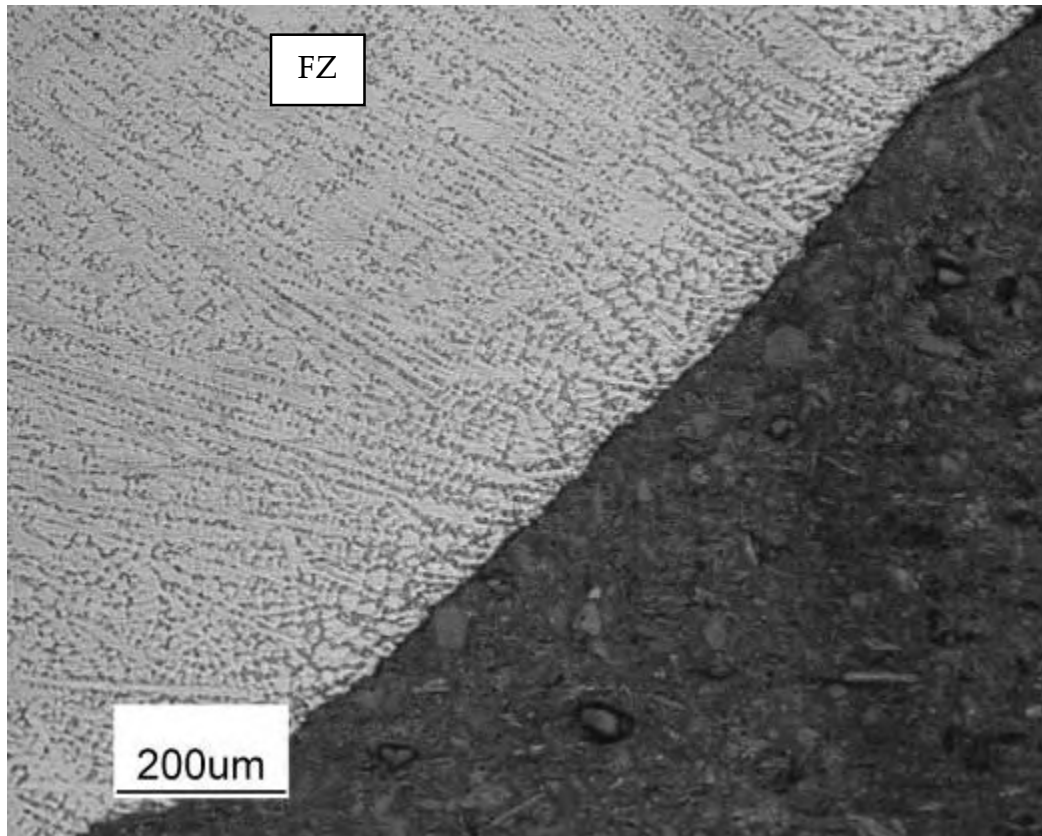


Figure 5.41: Welded specimen W12 shear failure (higher magnification)

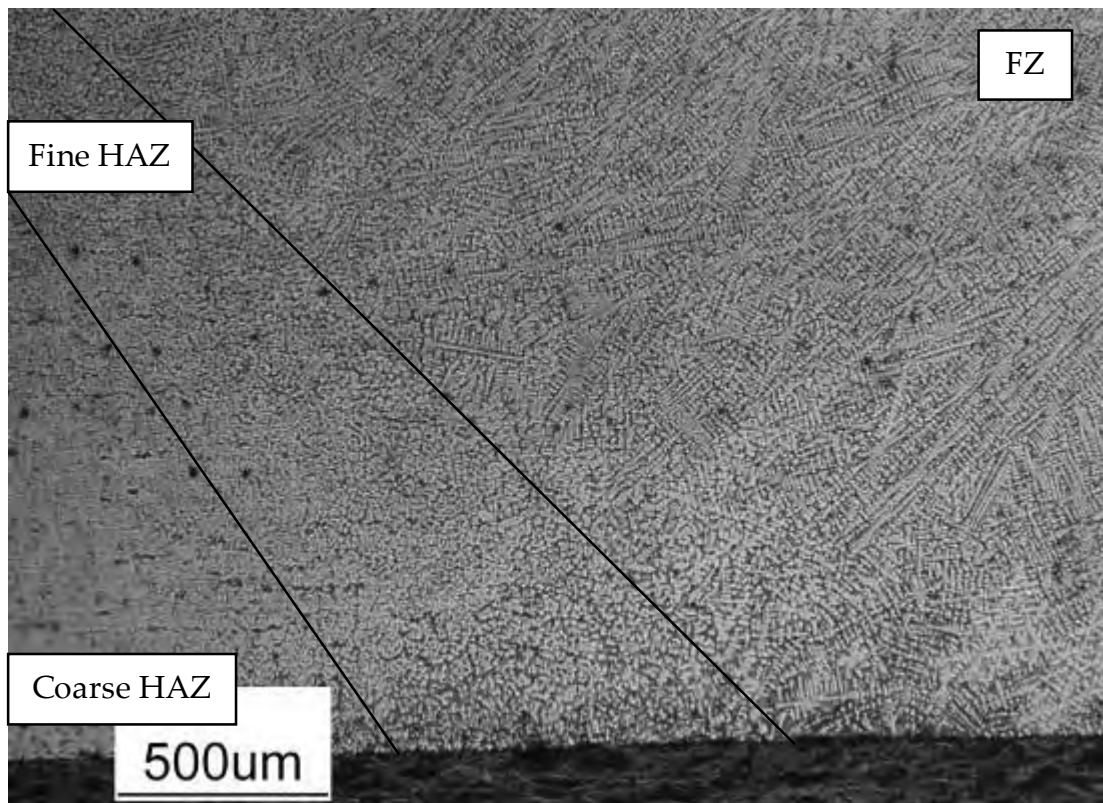


Figure 5.42: Welded creep specimen W12 away from fractured edge

5.8.4 High temperature fatigue tests

The non-welded high temperature fatigue tests showed small mixed intergranular/transgranular fatigue cracks at the edges of the specimens (Figure 5.43) and significant final tensile overload shear transgranular fractures (Figure 5.44). The welded specimen fatigue cracks were much larger and initiated in a fine-grained HAZ (Figures 5.45-5.49), where grain boundary segregation was prominent. The final failure of the welded specimens occurred by shearing through either the FZ (Figure 5.50) or the coarse-grained HAZ (Figure 5.51), depending on the exact position of the initial crack.

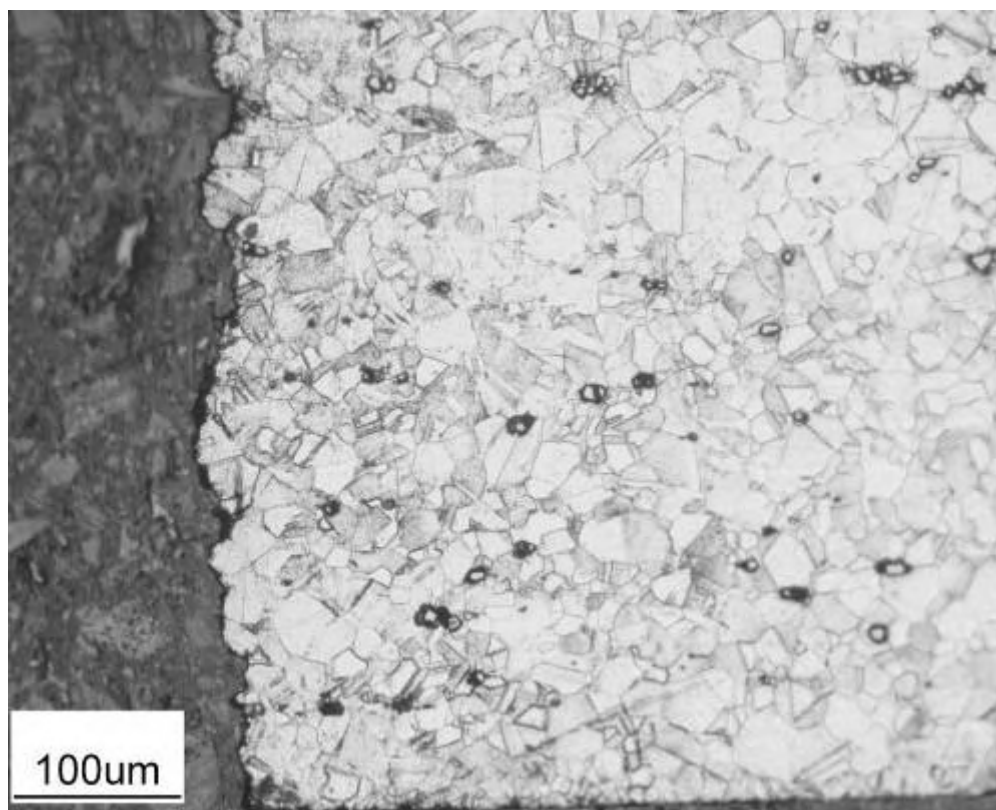


Figure 5.43: Non-welded specimen F3 fatigue crack –micrograph (side view)

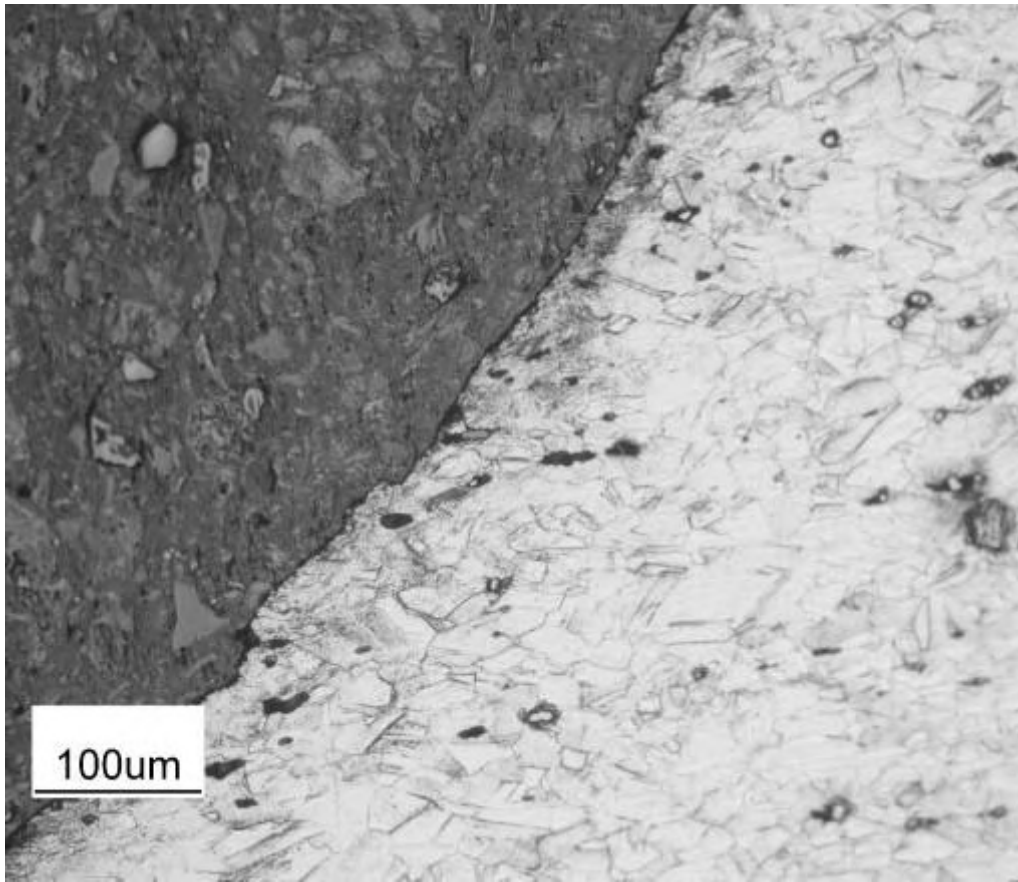


Figure 5.44: Non-welded specimen F3 shear failure –micrograph (side view)

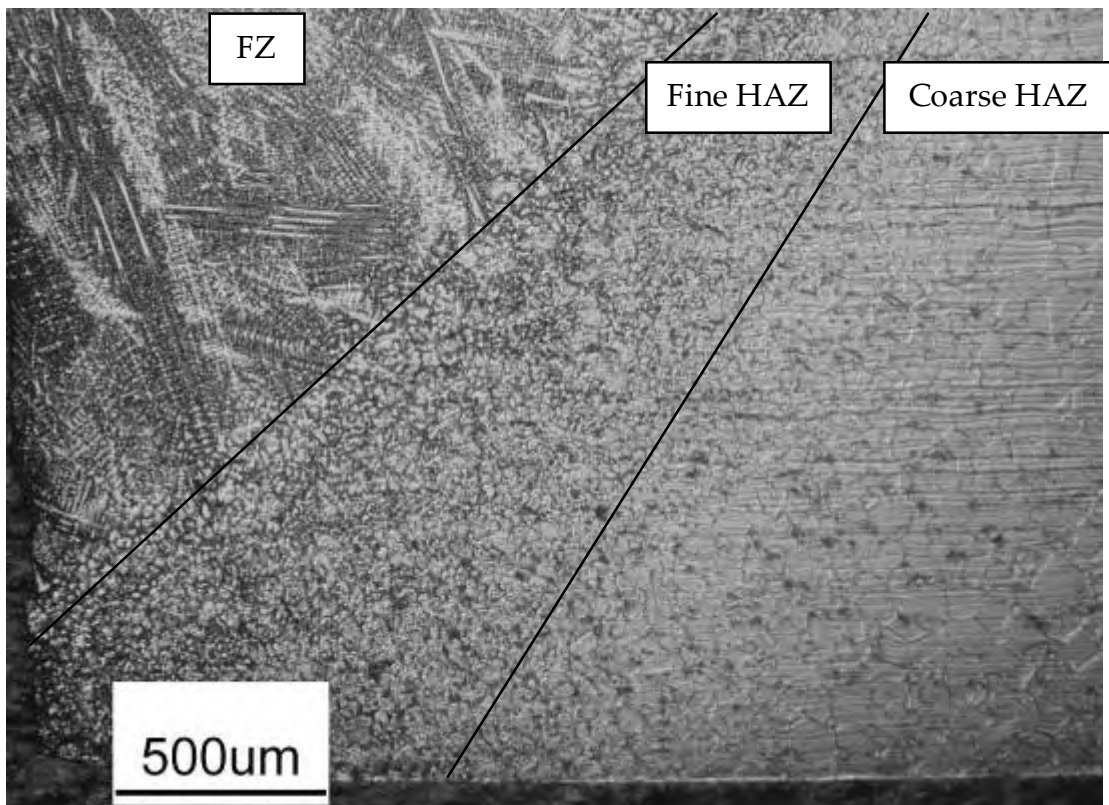


Figure 5.45: Welded specimen W11 fatigue crack –micrograph (side view)

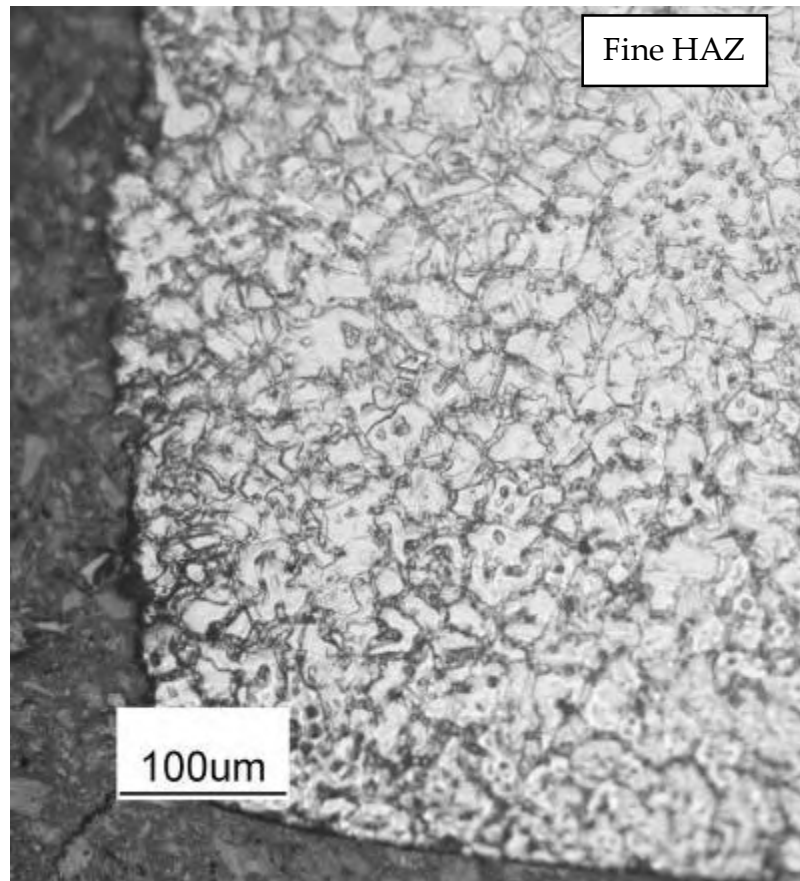


Figure 5.46: Welded specimen W11 fatigue crack (higher magnification)

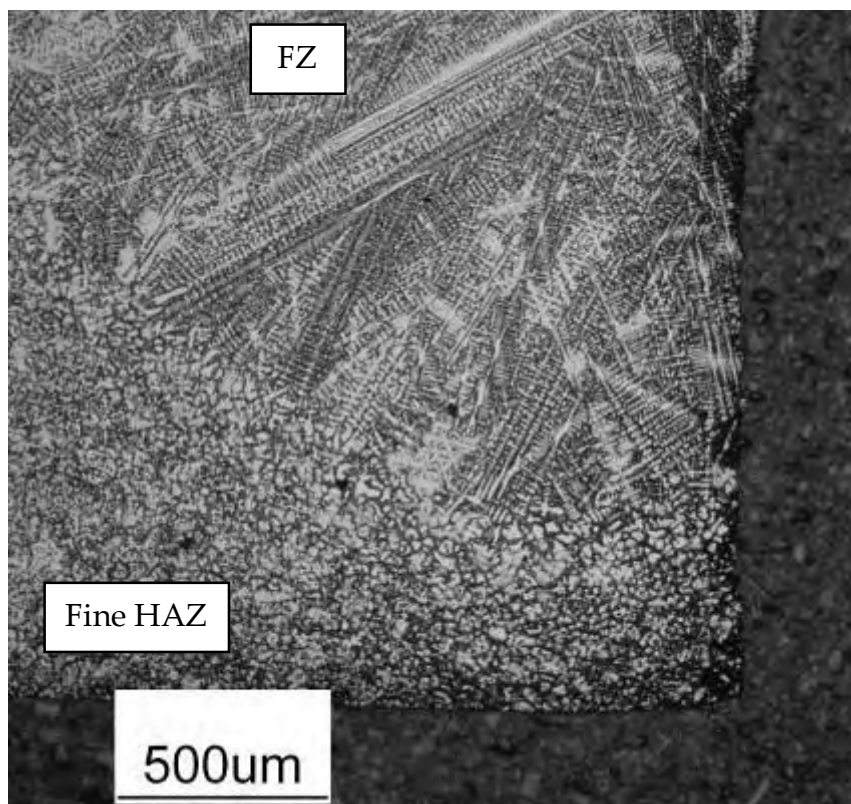


Figure 5.47: Welded specimen W11 fatigue crack (other section)

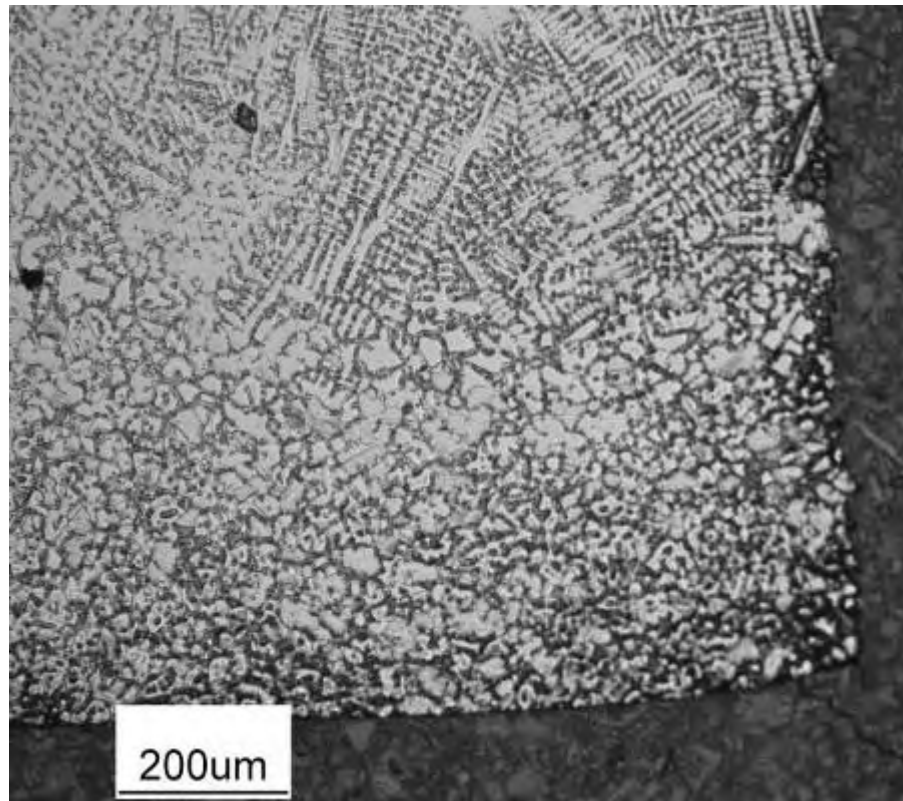


Figure 5.48: Welded specimen W11 fatigue crack (other section, higher magnification)

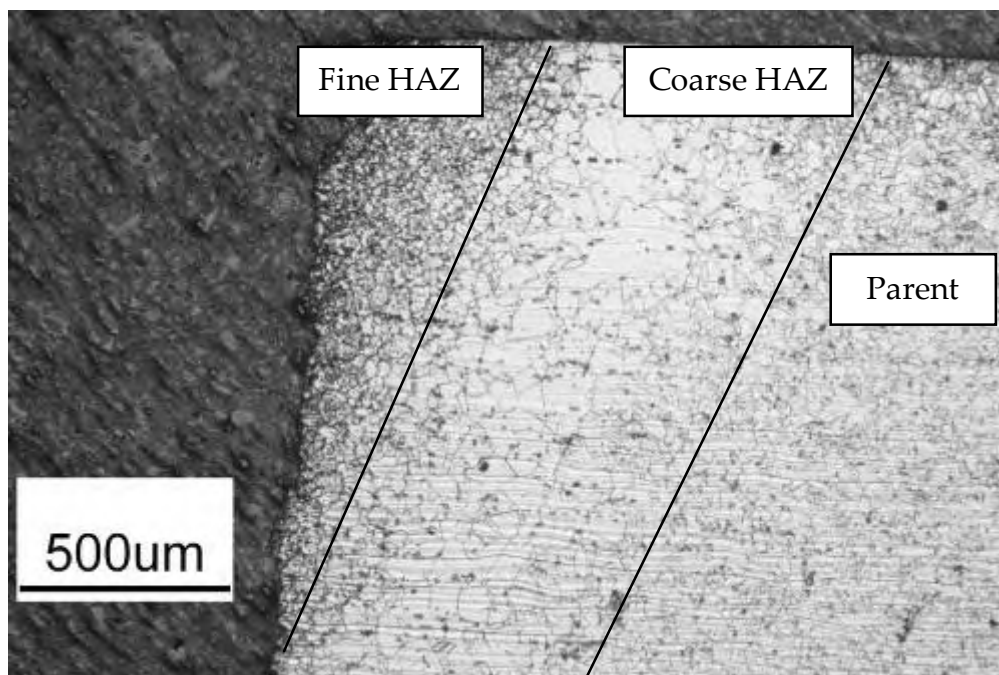


Figure 5.49: Welded specimen W39 fatigue crack –micrograph (side view)

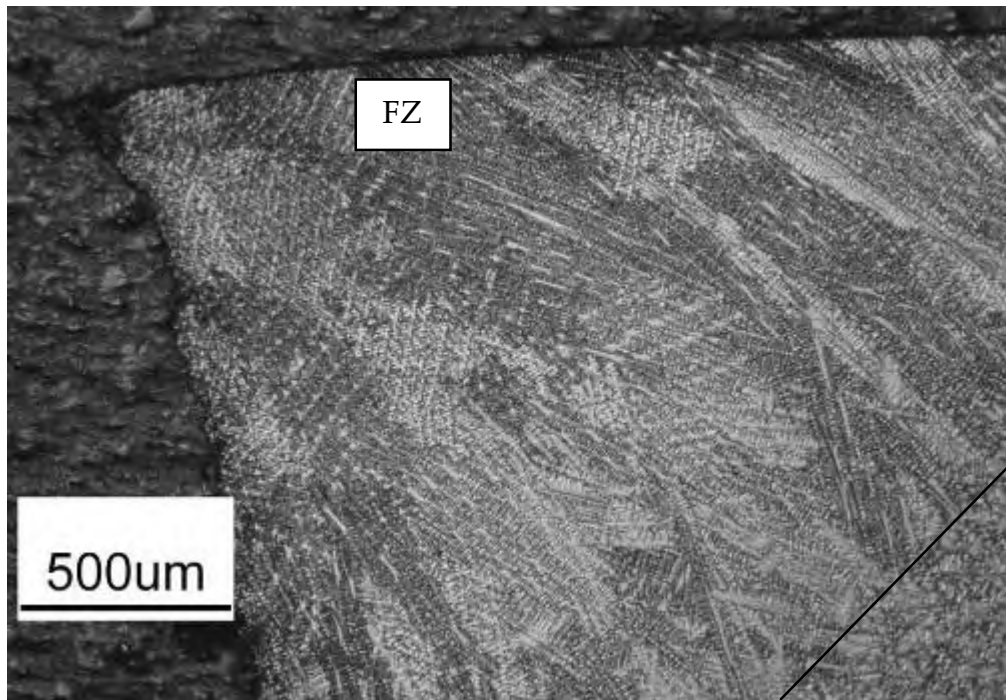


Figure 5.50: Welded specimen W11 shear failure –micrograph (side view)

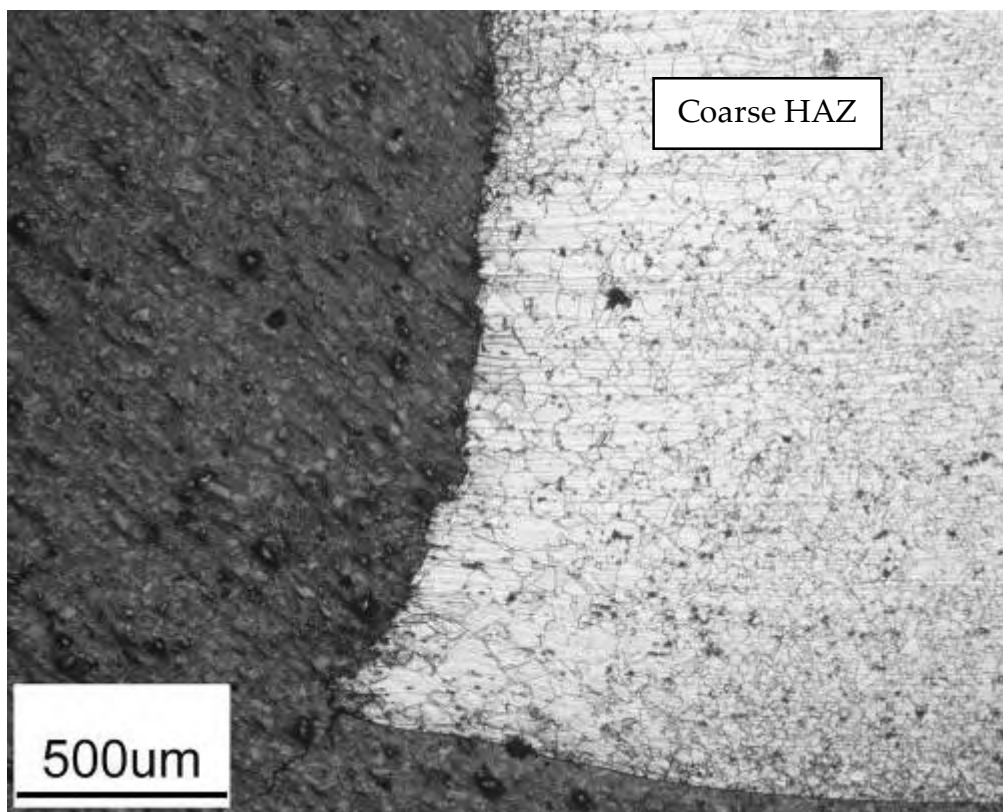


Figure 5.51: Welded specimen W39 shear failure –micrograph (side view)

5.9 Discussion and conclusions

IN718 welds exhibit slightly lower tensile strength and significantly lower ductility than the parent material. Although the welds show comparatively little loss of tensile strength, the creep and high temperature fatigue properties are severely compromised.

A prominent intermetallic phase that forms as a result of welding IN718 is Laves [(Ni,Cr,Fe)₂(Nb,Mo,Ti)]. This interdendritic and intergranular phase is observed in IN718 weld FZs and at grain boundaries in the fine-grain HAZ. Laves phase precipitates in the fine-grain HAZ due to extensive boundary liquation following segregation of melting point depressants such as boron, and consequent segregation of elements such as niobium into an enriched residual liquid film as the boundary solidifies inwards on cooling. In extreme cases, the boundary may be embrittled by formation of continuous Laves sheets. Likewise, microfissures, nucleated at liquated boundaries, may be healed by the influx of Nb-rich eutectic from the weld, which crystallises into thick Laves walls. These walls often merge into open fissures, and are also a potential long-term source of significant cracks [89]. Short intergranular HAZ liquation cracks (microfissures) are not easy to detect and can influence the early stages of fatigue crack growth [120]. Both the amount and nature of postweld heat treatment (PWHT) strengthening precipitation can be significantly affected due to niobium segregation. The presence of brittle Laves phase lowers ductility, aids excessive microvoid nucleation, and presents a low energy intergranular or interdendritic fracture path and early fatigue crack initiation site, resulting in lower tensile elongation and life [75, 88, 121]. Laves phase is not dissolved during conventional PWHT and can only be removed through solution/homogenisation treatment. Complete dissolution of Laves phase and homogenisation of niobium is difficult to

achieve, and high temperature solution treatments result in undesirable grain coarsening of the base/parent metal and can result in HAZ cracking [86].

The welded specimen fatigue cycles to failure have more scatter than the non-welded results. This can be attributed to microstructure inhomogeneity, differing amounts of Laves phase or more severely, the presence of microfissures [121].

The lower performance of the welded plates can be attributed to the microstructural differences when compared with the non-welded material. The large columnar dendritic grains in the weld FZ and the presence of brittle Laves phase here and at the fine-grain HAZ grain boundaries, along with the large grains in the coarse-grain HAZ, decreases ductility, and creep and fatigue life.

A summary of the tests completed is given in Table 5-5.

Table 5-5: Test programme summary

Test Type	Temp. (°C)	Nominal Stress (MPa)	Tests Performed			
			SHT	PWHT	Welded Material	
					SHT	PWHT
Tensile	20	N/A	√	√	√	√
	200	N/A	√	√	√	√
	400	N/A	√	√	√	√
	620	N/A	√	√	√	√
	700	N/A	√	√	√	√
	800	N/A	√	√	√	√
	1000	N/A	√	√	√	√
Constant Load Creep	620	800, 850, 900(N), 950(N), (925N)*	-	√	-	-
		600, 650, 700, 750(N), 800(N)	-	-	-	√
High Temperature Fatigue	620	1025, 1050, 1100, 1150, 1175	-	√	-	-
		800, 825, 850, 875, 890, 900, 925, 950	-	-	-	√

SHT – solution heat-treated (as received)

PWHT – postweld heat-treated (or equivalent ageing for non-welded material)

(N) – notched specimen also tested at the specified nominal stress

* – notched specimen only tested at the specified nominal stress

Material property determination – weld, creep and fatigue modelling

6.1 Summary

The results of the testing presented in Chapter 5 show that IN718 weld material exhibits noticeably depleted mechanical properties. In this chapter, the stress-strain relationships (and hence the mechanical properties) of the IN718 weld material were calculated using the test measurements and determining what the behaviour of the weld must have been in order to give the measured test results. Finite element (FE) verification of the material properties is conducted by modelling the uniaxial tensile and creep tests to check the accuracy of the material properties assigned to the weld region. A creep continuum damage mechanics approach is suggested in order to capture the significant tertiary creep that was observed during the testing programme, and obtain more accurate failure times. The determination of the necessary material constants required for the damage equations is discussed. The high temperature uniaxial fatigue tests are also accurately modelled using FE analysis for all the load cases used during the testing, for both the butt-welded and non-welded specimens. The modelling technique is validated by comparing the FE-calculated strain results with the measured test results. A Smith, Watson and Topper (SWT) strain range parameter is introduced and FE-calculated values compared with values determined using the test data, in order to validate the suitability of this life assessment method. The modelling technique, the material properties obtained and the SWT values can now be used for life assessment of structures with more complex geometry and loading conditions.

6.2 Introduction

As the discussion by Casavola and Pappalettere [122] makes clear: 'Fatigue behaviour of welded structures is a very complex phenomenon because it depends simultaneously on many quantities affecting the stress and strain fields right where the final fracture occurs. Such complexity (that makes it very cumbersome to estimate the stress field in the critical region) is principally due to: (i) structural geometry, (ii) nonhomogeneous material, and (iii) welding residual stress.' They state that therefore, it is apparent that fatigue of structures including welded junctions is a problem far more complicated than simply fatigue of materials.

In the work presented in this thesis, the geometry of the weld is simplified by finishing of the stress-raising weld bead excess, and weld distortions and misalignment were carefully avoided. For the purpose of life assessment, the welds are assumed to be free from any imperfections such as porosity. The generation of welding residual stress is discussed and modelled in Chapters 2 and 3, respectively. The effects of residual stress are neglected elsewhere throughout this thesis due to the use of stress-relieving heat treatment, the added complication of modelling the effects on the stress field of postweld machining and heat treatment, the difficulty in generating adequate three-dimensional stress fields through experimental measurements, and since any effects are included during the determination of the bulk material stress-strain data. Welding-induced residual stresses also relax and are therefore less significant, during testing at high temperature [123].

The argument that fatigue behaviour of real welded structures can hardly be described by formulae or theoretical arguments or be deduced by studying a complex assembly through its elementary components [122] is debatable and in many cases these may be the only practical approaches available. Testing

full-scale welded structures can be extremely expensive. Therefore, methods involving the use of FE analysis such as those presented in this chapter and demonstrated through a case study in Chapter 7, which can help to improve the understanding of the fatigue, and subsequently improve the design of welded structures, are not to be discarded.

It is true that any theoretical and/or numerical approach necessarily relies on a set of simplifying assumptions, which, because of the complexity of fatigue phenomena, could result in some important aspects involved in the real structure behaviour being neglected. It is therefore prudent to try to include as many of these phenomena as possible in any analysis.

One aspect that is often overlooked is that, after the welding cycle, unless a particular case warrants it, the joint should not be considered a homogeneous material. In fact, base/ parent metal, material in the heat-affected zone (HAZ), and melted/weld metal, may have completely different microstructures and/or grain sizes. This results in different yield limits and hence different load carrying and re-distribution capabilities, as well as different creep, fatigue and failure behaviours. Therefore, the strategy employed by many authors to model welded joints as homogeneous structures seems to be questionable [122]. The effects of differing material behaviour must be carefully considered when modelling a welded structure with finite elements. Different constitutive (stress-strain) equations should be used for each region as necessary, and care should be taken when meshing and analysing the model.

6.3 Weld material property determination

In this work, the stress-strain relationships (and hence the mechanical properties) of the IN718 welds were obtained using the difference in strain of non-welded and cross-welded specimen tests over the 50mm gauge length. The stress-strain behaviour of the weld material was calculated using the known ratio of weld to parent in the gauge length and presuming that the behaviour of the non-welded portion is known from the testing. The V-angle was neglected to simplify the weld geometry (Figure 6.1), which does not have a significant effect on strain [124]. In addition, the HAZ was not treated as one or more separate regions since its size is very small, which makes it difficult to obtain the properties. It has been shown that the properties (for IN718 TIG welds) vary fairly linearly across the HAZ from weld-parent [92], so the region can be approximately included globally by extending the weld zone slightly. Therefore, an average weld width of 8mm was assumed here, with the other 42mm of the gauge length consisting of non-welded (base) material (Figure 6.1), to give a weld to parent ratio of 0.16:0.84.

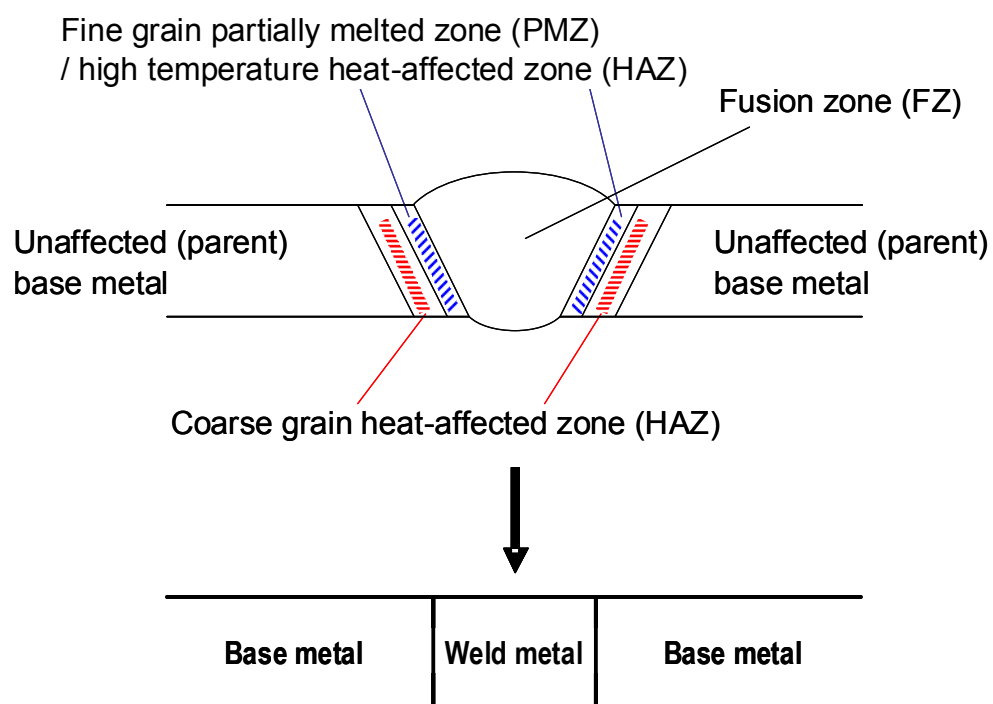


Figure 6.1 Weld geometry approximation

The weld properties at room temperature, calculated using the derived stress-strain curve from the test data presented in Chapter 5, compare well with electronic speckle pattern interferometry (ESPI)-obtained data in [92].

The calculated, heat-treated (HT) weld material, nominal stress-strain curve for 620°C is shown in Figure 6.2, along with that of the non-welded material test. The engineering uniaxial tensile properties are given in Table 6-1. The calculated weld material Young's moduli and yield (0.2% proof) stresses for all the test conditions are presented in Figure 6.3 and Figure 6.4 respectively, and tabulated in Table 6-2, alongside the non-welded (NW) and welded (W) test results. The values for non heat-treated material at 620, 700 and 800°C are excluded due to age-hardening of the material during these tests.

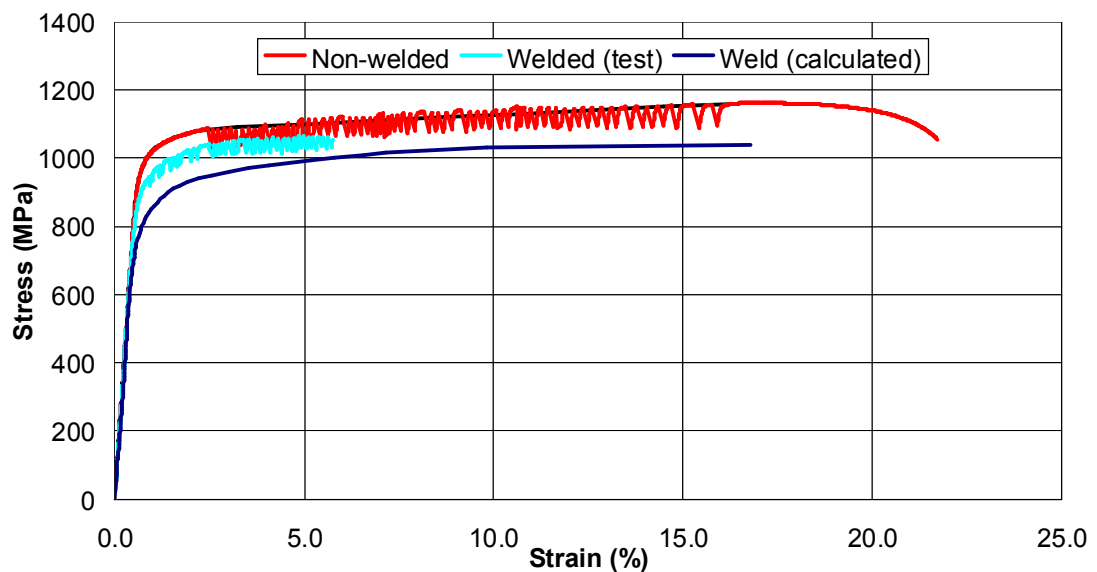


Figure 6.2: Nominal stress-strain curves for heat-treated IN718 at 620°C

Table 6-1: Uniaxial tensile properties of heat-treated IN718 at 620°C

	0.2% Proof stress (MPa)	Ultimate strength (MPa)	Young's modulus (GPa)	Failure strain (%)
Non-welded	992	1163	166	21.8
Welded (test)	920	1064	165	5.7
Weld (calculated)	808	-----	148	-----

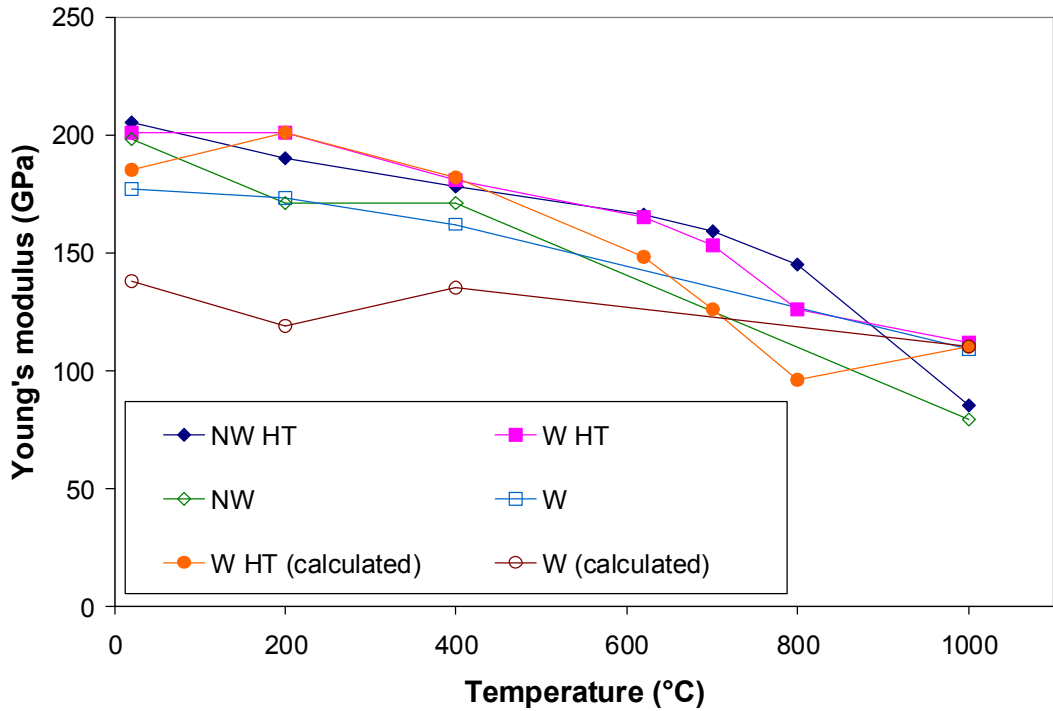


Figure 6.3: Calculated weld material Young's moduli against temperature, alongside non-welded and welded test results

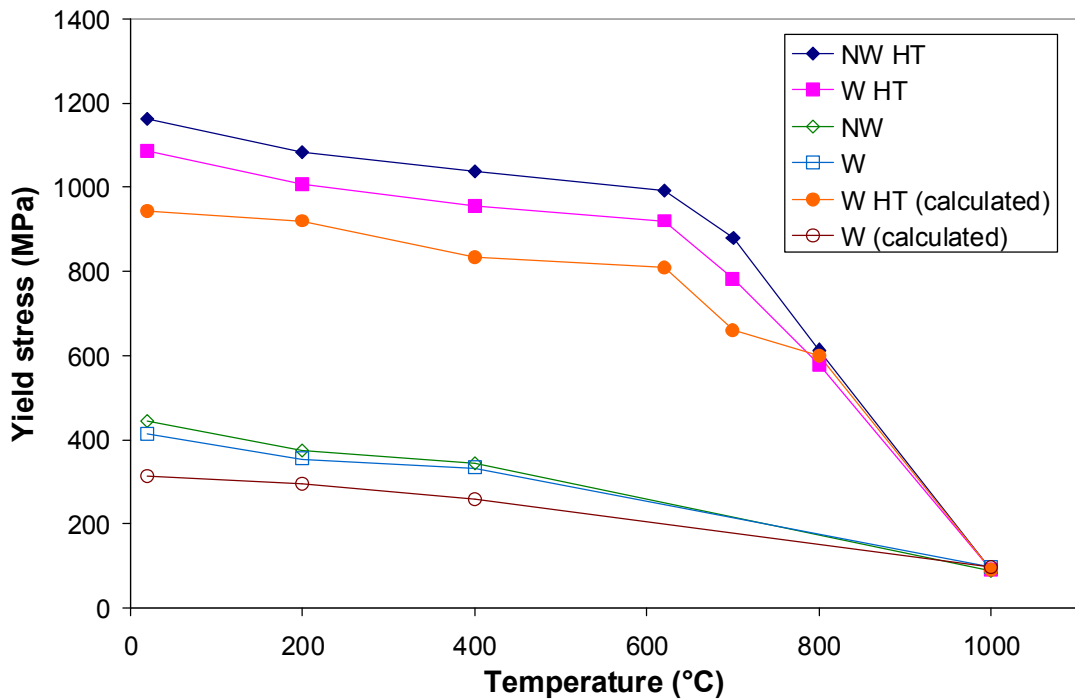


Figure 6.4: Calculated weld material yield stresses against temperature, alongside non-welded and welded test results

Table 6-2: Tested and calculated mechanical properties

	Temp. (°C)	Young's modulus (GPa)	Yield stress (MPa)
NW HT	20	205	1161
	200	190	1083
	400	178	1036
	620	166	992
	700	159	878
	800	145	613
	1000	85	91
NW	20	198	443
	200	171	373
	400	171	344
	620	166	474
	700	156	649
	800	130	619
	1000	79	87
W HT	20	201	1087
	200	201	1006
	400	181	956
	620	165	920
	700	153	781
	800	126	579
	1000	112	92
W (calculated) HT	20	185	944
	200	201	920
	400	182	834
	620	148	808
	700	126	659
	800	96	600
	1000	110	90
W	20	177	413
	200	173	354
	400	162	333
	620	151	428
	700	157	568
	800	137	584
	1000	109	96
W (calculated)	20	138	314
	200	119	296
	400	135	258
	620	104	350
	700	184	470
	800	162	499
	1000	110	96

Non-HT tests at 620, 700 and 800°C age-harden during the tests

The minimum (or steady-state) creep strain rates calculated for the welds (using the same approach mentioned above) are shown in Figure 6.5, and the calculated creep constants, A and n, required for the commonly employed Norton's uniaxial steady-state (secondary) creep power law, equation (6.1), in Table 6-3. The values determined for the non-welded material are also shown; extra tests were performed at 620MPa and 700MPa to avoid extrapolation of the non-welded results. These tests were not run to failure since this would have required a long duration.

$$\dot{\epsilon}_{\min}^c = A \sigma^n \quad (6.1)$$

where $\dot{\epsilon}_{\min}^c$ is the minimum creep strain rate and σ is the applied stress.

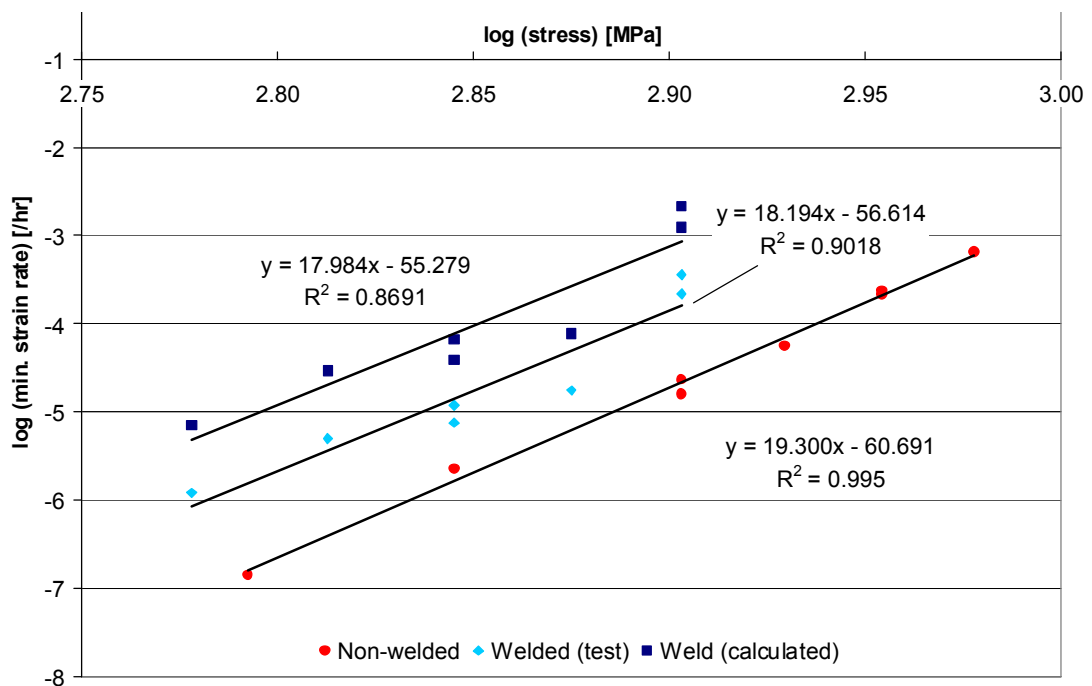


Figure 6.5: Minimum creep strain rates for heat-treated IN718 at 620°C

Table 6-3: Uniaxial creep constants of heat-treated IN718 at 620°C, based on units of stress in MPa and time in hours

	A	n
Non-welded	2.0370E-61	19.300
Welded (test)	2.4322E-57	18.194
Weld (calculated)	5.2602E-56	17.984

The creep stress index, n , is relatively high. However, it agrees well with those values found during the previous work at the University of Nottingham [93].

6.4 Finite element verification of material properties and validation of modelling

Simple, two-dimensional (2D) plane stress, elastic-plastic finite element (FE) models of the uniaxial tensile and creep tests were used to check the accuracy of the material properties assigned to the weld region. As throughout the rest of this thesis, the material properties are isotropic. The weld fusion lines were assumed to be vertical for simplicity as shown in Figure 6.1; good agreement between the test measurements and FE results measured over the same gauge length was obtained (Figure 6.6).

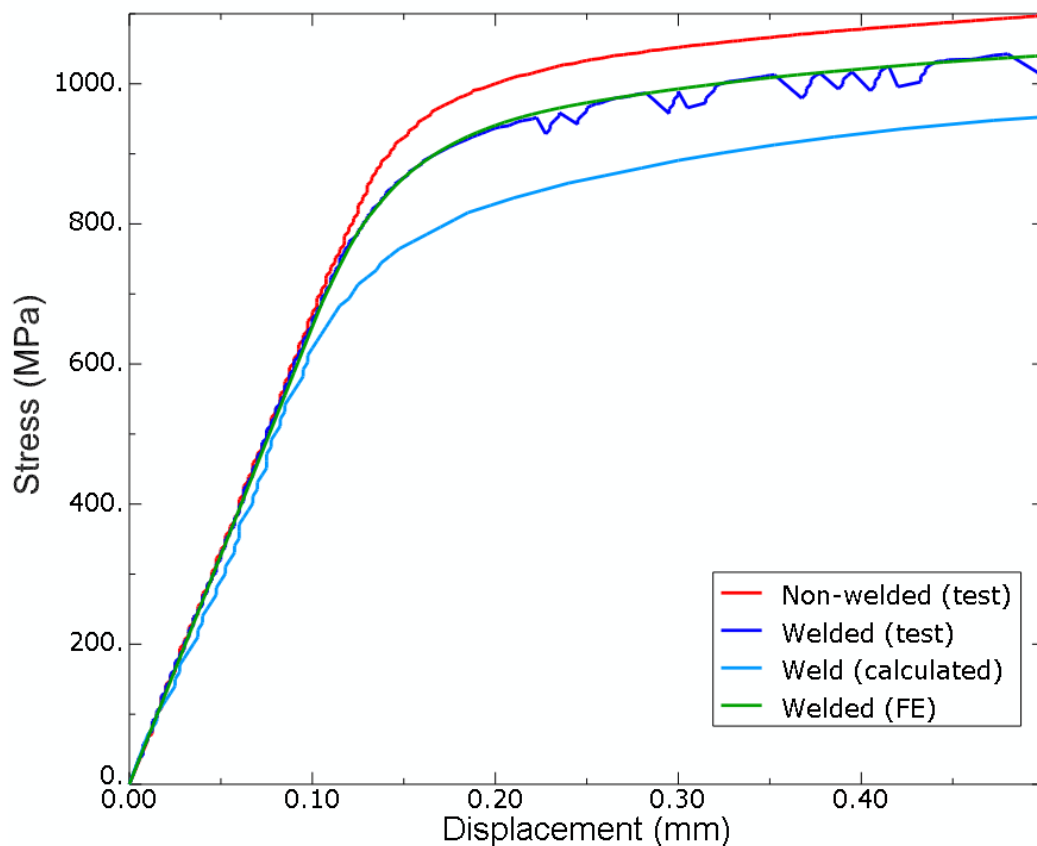


Figure 6.6: Comparison of example FE and experimental tensile test results

A complex triaxial stress state is generated in the welded specimens due to the differences in the material properties of the weld and parent (non-weld) metal, as illustrated in Figure 6.7. The necking of the weld that was observed during the tensile tests is replicated in the FE model due to the lower yield stress of the weld material. These results show how effective a tool FE analysis can be in evaluating the stress and strain distributions in a weldment.

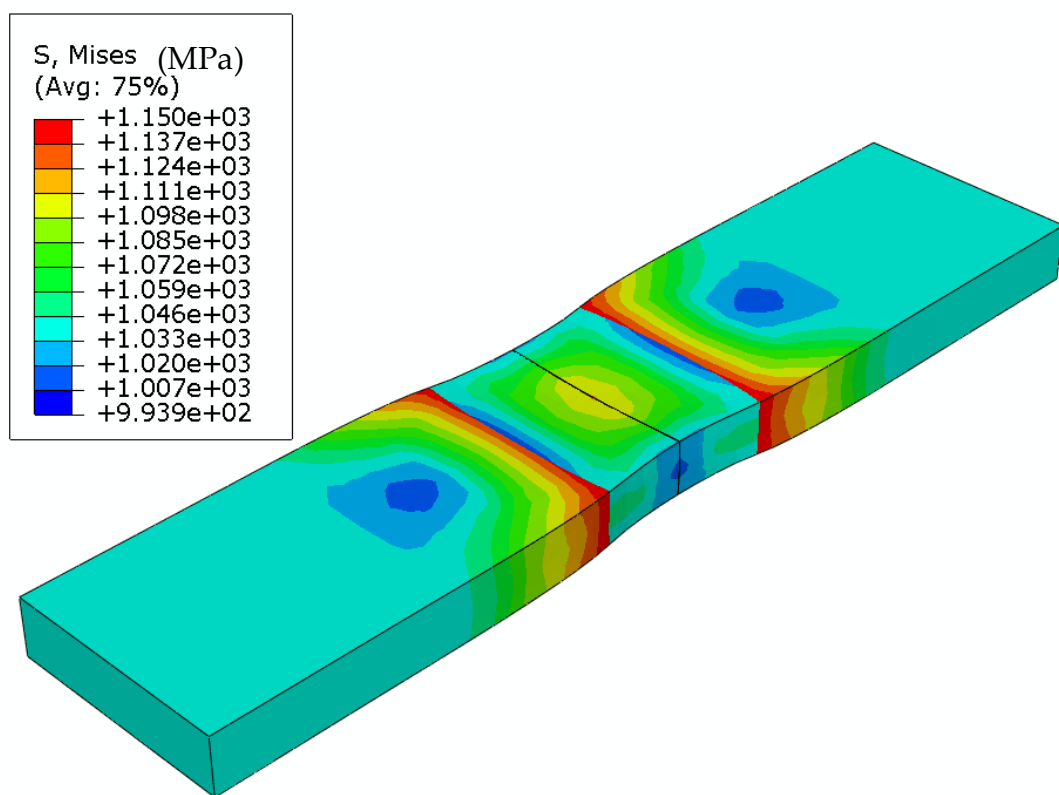


Figure 6.7: Welded tensile test 3D FE model
(5x deformation scale factor used for illustration purposes)

Some 2D plane stress, uniaxial creep FE-test comparisons are presented in Figure 6.8 (non-welded) and Figure 6.9 (welded). Norton's steady-state creep power law [equation (6.1)] was implemented in these analyses. A small amount of primary creep is observed in the test results but of more significance is the extensive amount of tertiary creep. The amount of tertiary

creep present suggests that a creep model using Norton's steady-state creep power law is not sufficient and a continuum damage mechanics approach may be more appropriate (see section 6.5). There are slight differences in the minimum creep strains between the test and the FE results; this is because the FE material parameters are derived from an average of all the test results. Despite this, the steady-state creep properties calculated for the weld material give very satisfactory results. Figure 6.10 shows the difference in minimum displacement (creep strain) rate obtained when using the calculated weld material properties instead of assuming that they are the same as the parent material.

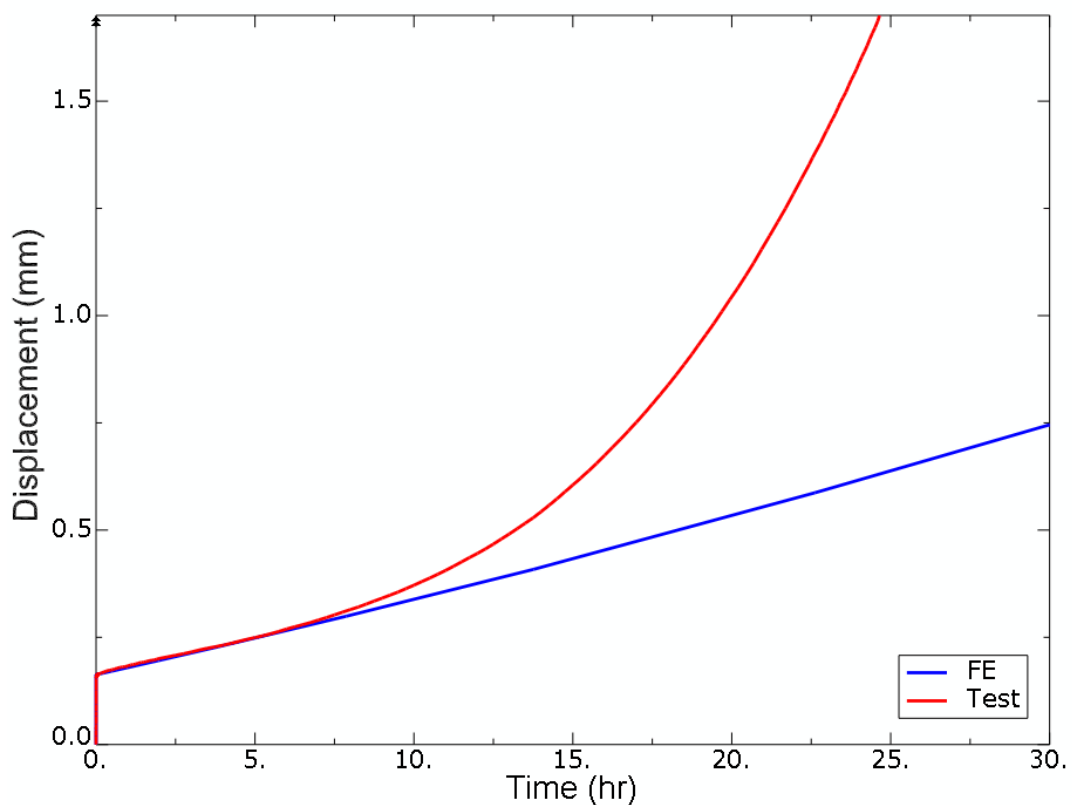


Figure 6.8: Non-welded creep FE-test comparison 950MPa

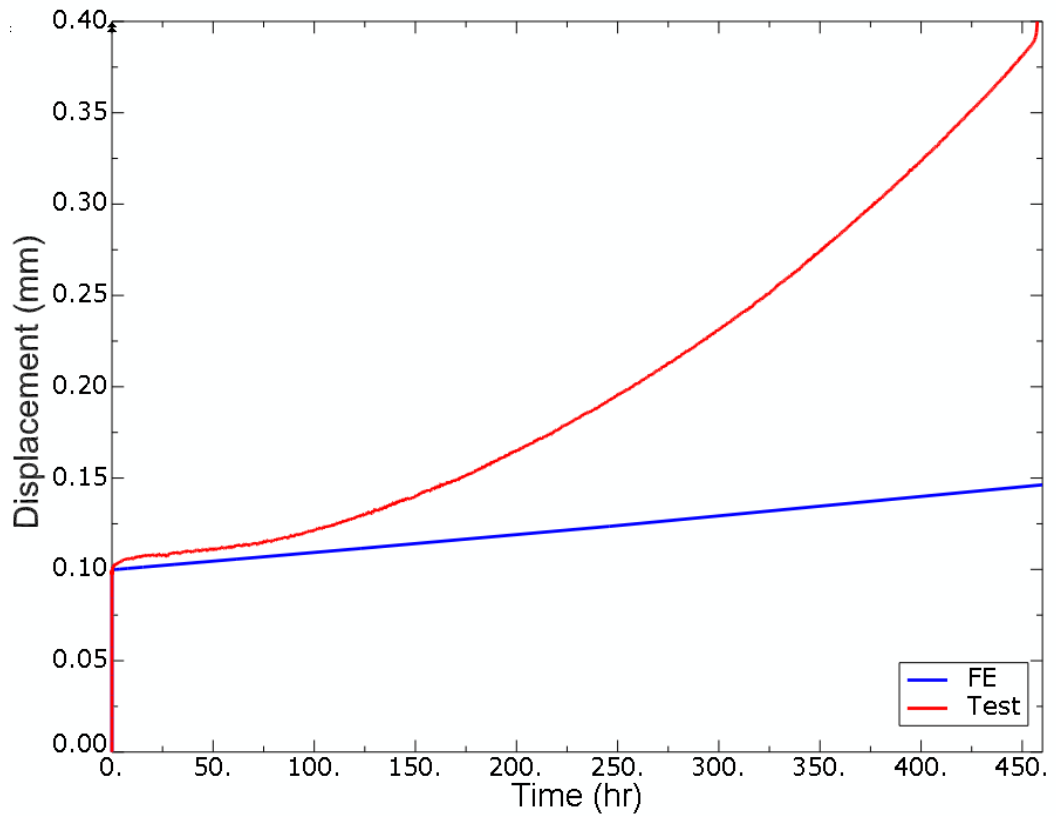


Figure 6.9: Welded creep FE-test comparison 650MPa

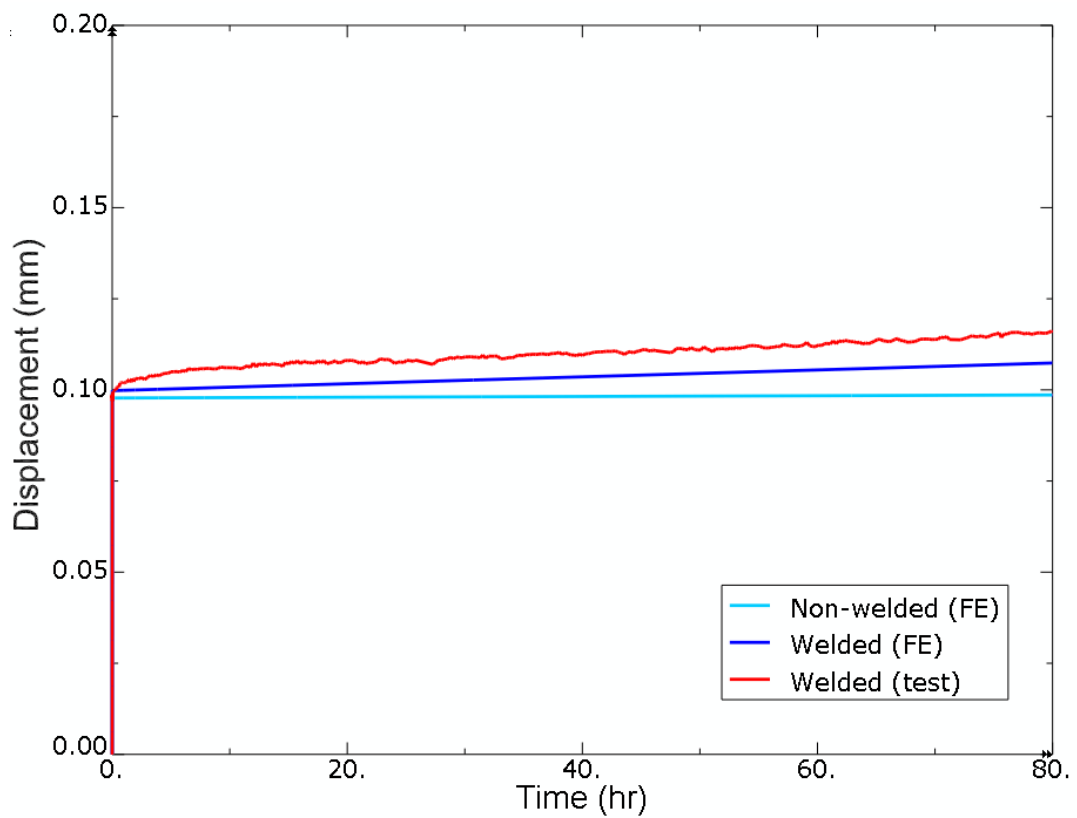


Figure 6.10: Steady-state (secondary) creep comparison at 650MPa

6.5 Finite element modelling of the creep tests

Creep damage localisation has been observed in weldments in both engineering practice and laboratory testing, and many component failures have arisen due to localised damage in welds [60]. This suggests that the implementation of creep continuum damage mechanics may be useful in determining the creep behaviour and life of welded structures (e.g. [125]).

A Kachanov-type damage mechanics approach is hence adopted for the FE creep law and life prediction, which is capable of capturing the significant tertiary creep that was observed during the testing programme (Chapter 5) [60]. A damage parameter ω is used to describe creep damage and varies from 0 (initially no damage) to 1 (failure). Its effect is to magnify the stress by a factor of $1/(1-\omega)$, accounting for the loss in load bearing cross section due to internal cavitation damage of the material. Thus, the uniaxial creep strain equation becomes:

$$\dot{\varepsilon}^c = A \left(\frac{\sigma}{1-\omega} \right)^n t^m \quad (6.2)$$

with the rate of damage given by:

$$\dot{\omega} = \frac{B\sigma^\lambda}{(1-\omega)^\phi} t^m \quad (6.3)$$

where m , B , λ , and ϕ are material constants determined from the creep tests as discussed below.

$m = 0$ since primary creep was not found to be significant during the testing.

Failure time t_f can be obtained by integrating equation (6.3) and substituting $\omega = 1$ at failure, to give:

$$t_f = \frac{1}{B(1 + \phi)\sigma^\chi} \quad (6.4)$$

χ can then be obtained from a plot of the creep rupture data (Figure 5.19 and Figure 5.20), and then ϕ (and therefore B) can be obtained by fitting the predicted creep strain from the creep damage equation to the uniaxial test creep strain history curves using:

$$\varepsilon^c = \frac{A\sigma^{(n-\chi)}}{B(n-\phi-1)} \left(\left[1 - \frac{B(1+\phi)\sigma^\chi t^{(1+m)}}{1+m} \right]^{\frac{\phi+1-n}{\phi+1}} - 1 \right) \quad (6.5)$$

The above equation is derived by integrating equation (6.2) with respect to time, and integrating equation (6.3) with respect to time to substitute for ω , using $\omega = 0$ and $\varepsilon^c = 0$ at $t = 0$.

The ϕ value obtained for the parent (non-weld) material was 12.0 (Figure 6.11), this was then used to calculate the weld material value, 4.0 (Figure 6.12), through:

$$\varepsilon_{\text{Welded}}^c = K_1 \varepsilon_{\text{Parent}}^c + K_2 \varepsilon_{\text{Weld}}^c \quad (6.6)$$

where K_1 (=0.84) and K_2 (=0.16) are the ratios of parent and weld material respectively, that form the welded specimen gauge length.

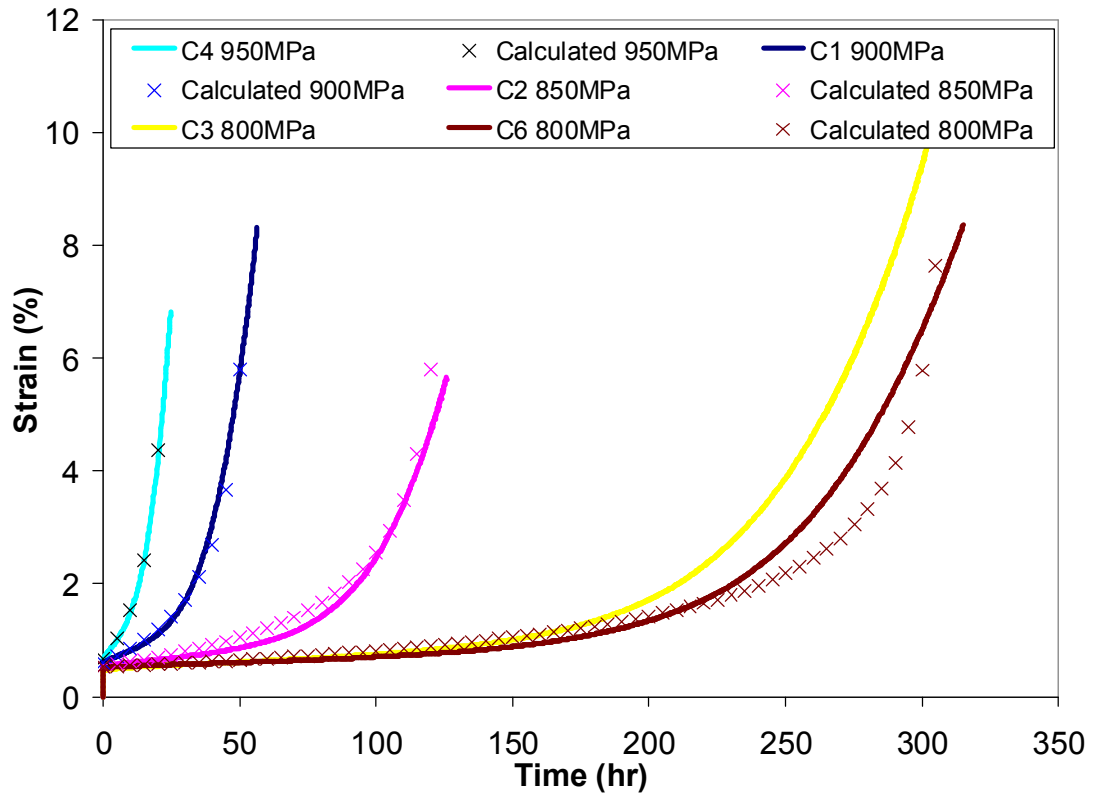


Figure 6.11: Non-welded creep curve comparison ($\phi = 12.0$)

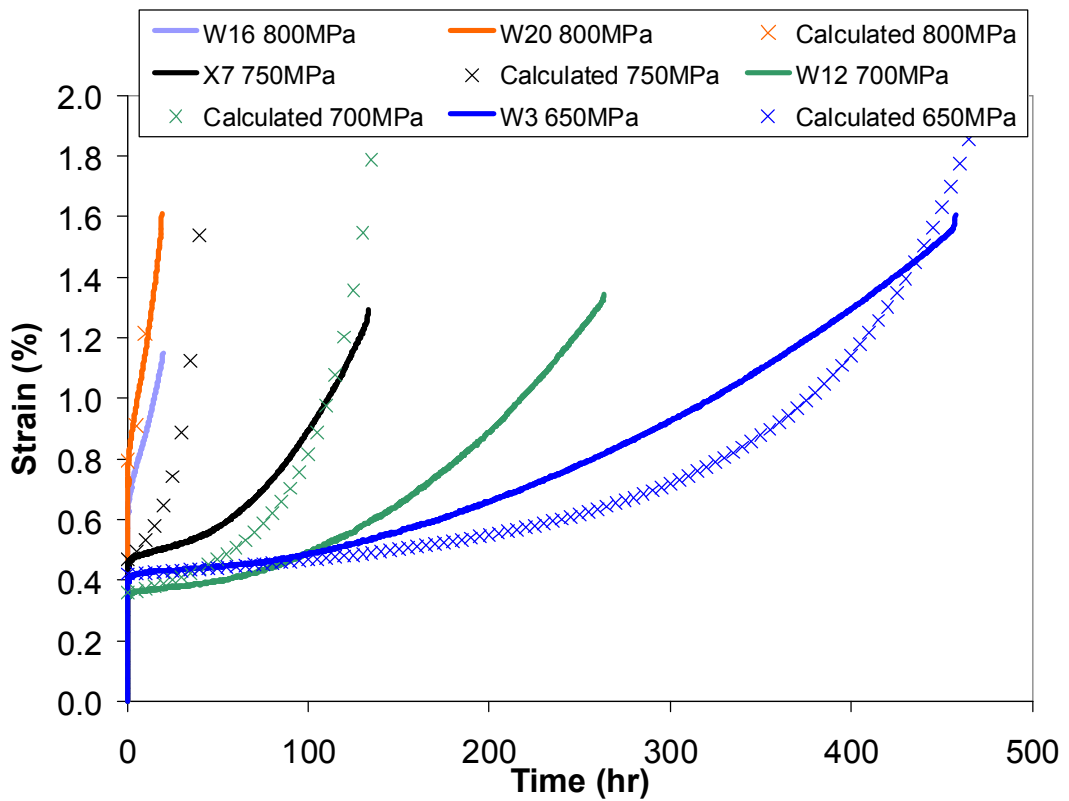


Figure 6.12: Welded creep curve comparison ($\phi = 4.0$)

It is apparent from Figure 6.12, that fitting one value of ϕ to all of the welded creep test data is difficult. This is because the logarithmic creep rupture times did not have a linear fit (as discussed in Chapter 5). Using $\phi = 4.0$ is adequate for the tests at 600MPa and 800MPa but a better fit can be obtained for the tests at 650MPa, 700MPa and 750MPa using parameters from this dataset only, with $\phi = 3.0$ (Figure 6.13).

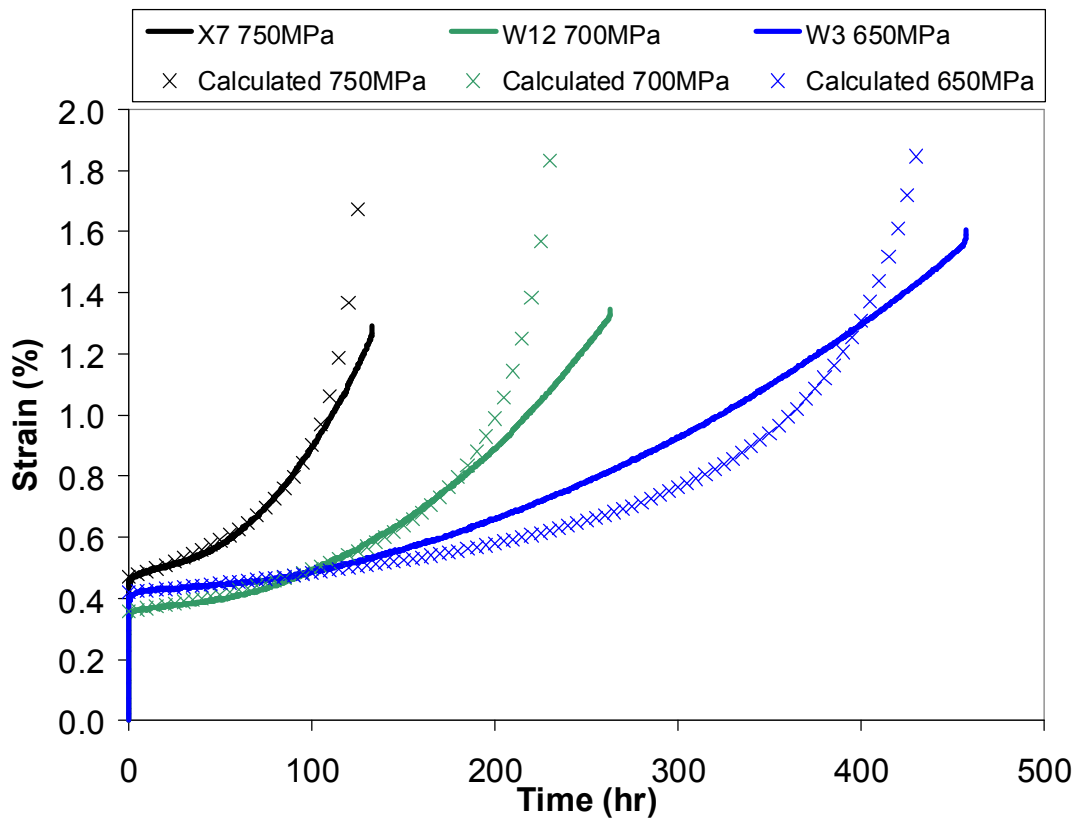


Figure 6.13: Welded creep curve comparison ($\phi = 3.0$)

For multiaxial creep, the implementation of which is important for welded material since it exhibits a complex multiaxial stress state when loaded (see Figure 6.7 for example), and for structures that are not stressed uniaxially, the following constitutive equations can be used [126]:

$$\dot{\varepsilon}_{ij}^c = \frac{3}{2} A \left(\frac{\sigma_{\text{eq}}}{1 - \omega} \right)^n \frac{S_{ij}}{\sigma_{\text{eq}}} t^m$$

$$\sigma_r = \alpha_r \sigma_1 + (1 - \alpha_r) \sigma_{\text{eq}} \quad (6.7)$$

$$\dot{\omega} = \frac{B \sigma_r^\lambda}{(1 - \omega)^\phi} t^m$$

where σ_{eq} , σ_1 , and σ_r are the equivalent, maximum principal and rupture stresses, respectively. S_{ij} are the deviatoric stress components. At time, $t = 0$, $\omega = 0$ and creep strain, $\varepsilon_{ij}^c = 0$. Here the “rupture stress” is assumed to be a function of the maximum principal stress and the equivalent stress with α_r , a multiaxial rupture parameter, determined using notched specimen creep testing and FE damage modelling. α_r ranges from 1 (maximum principal stress dominant) to 0 (equivalent stress dominant). These equations have been shown to be capable of accurately representing the stress dependence of the creep strain-rate components, over a wide range of stress levels and temperature for a number of metals and metallic alloys [127].

It is necessary to input equations (6.7) into ABAQUS using a FORTRAN user subroutine. In the FE analysis, failure is determined at a particular point when $\omega \rightarrow 1$. It is common to choose a distinct ω value for failure (e.g. 0.9) to avoid numerical difficulties (damage accumulates relatively quickly as ω approaches 1 so there is little loss in accuracy).

The value of α_r is determined using FE damage models of notched creep tests by testing different values until the calculated rupture times are consistent with the tested rupture times (Figure 6.14). Here, $\alpha_r = 0.1$ for the IN718 parent material (NW – Figure 6.15) and $\alpha_r = 0.2$ for the weld material (W – Figure 6.16).

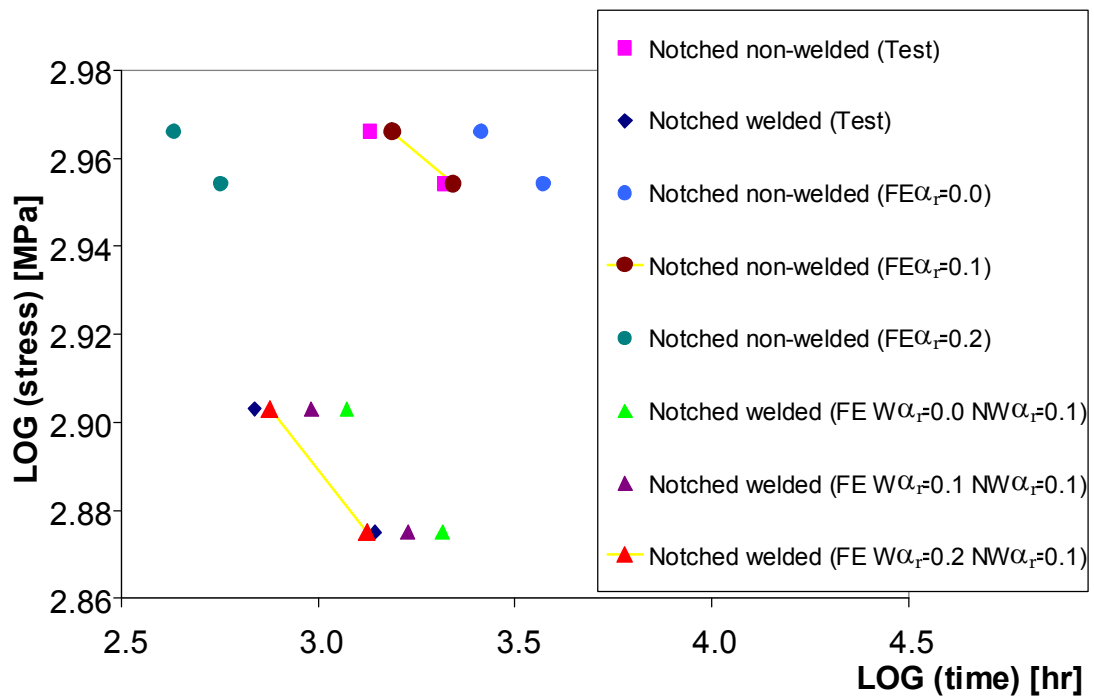


Figure 6.14: Rupture time comparison for different α_r

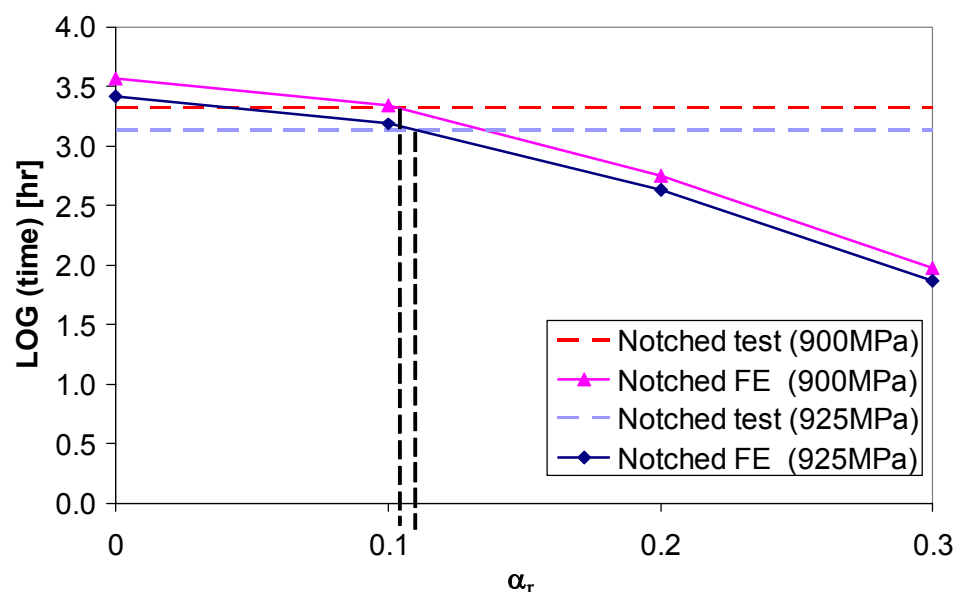


Figure 6.15: Non-welded notched FE rupture times for different α_r

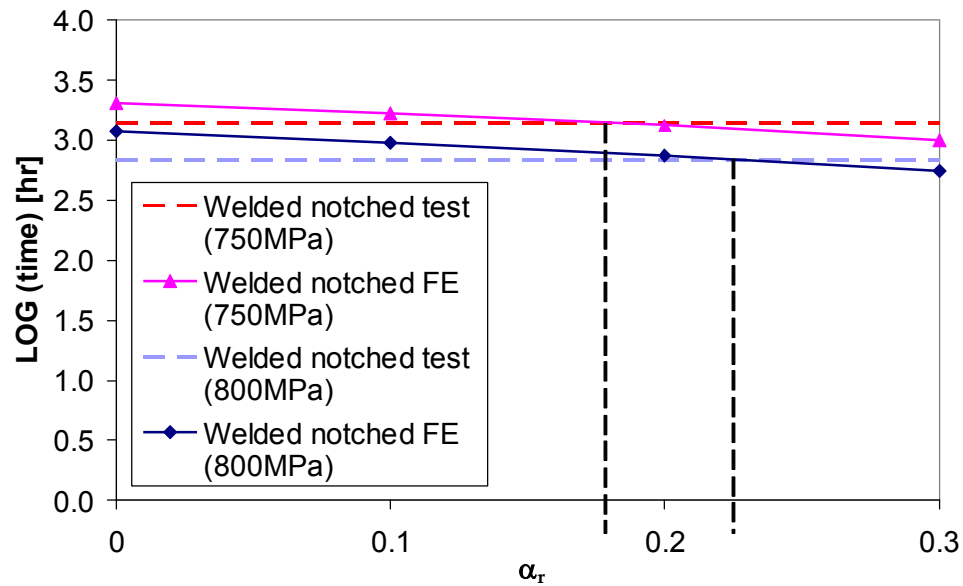


Figure 6.16: Welded notched FE rupture times for different α_r

The complete set of material constants for both IN718 parent (non-weld) and weld material at 620°C, determined for the creep continuum damage mechanics model, are presented in Table 6-4.

Table 6-4: Creep damage constants for IN718 at 620°C, based on units of stress in MPa and time in hours

	A	n	m	B	χ	ϕ	α_r
Parent (non-weld)	2.037E-61	19.300	0.0	4.322E-47	14.728	12.0	0.1
Weld	5.260E-56	17.984	0.0	2.623E-50	16.367	4.0	0.2

The improvement in creep strain history calculated by the damage mechanics approach over the steady-state (secondary creep) approach can be seen in Figure 6.17. A comparison for all test stresses, between FE-damage predicted and test rupture times, is presented in Figure 6.18. It is clear that for values of stress of 650MPa, 700MPa and 750MPa, better predictions are obtained for the welded material by excluding the other test results when fitting the material constants (welded dataset FE -B).

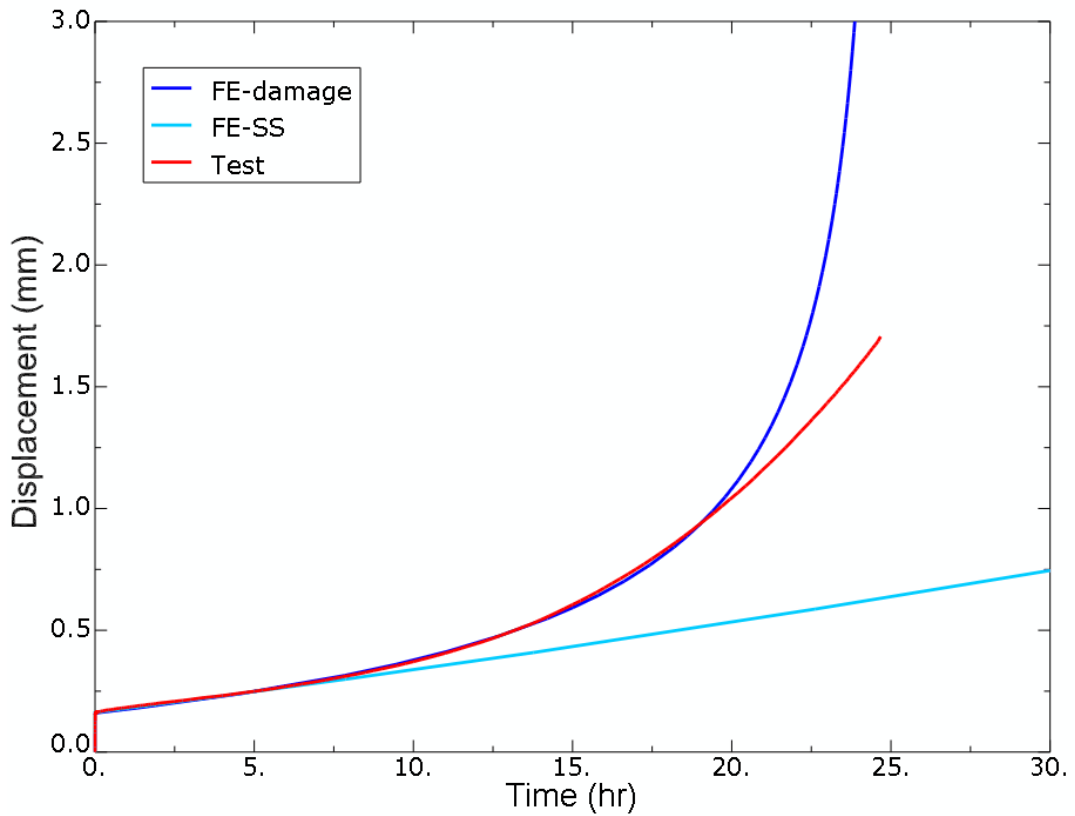


Figure 6.17: FE-SS (steady-state), FE-damage and test displacement-time curves for non-welded specimen at 950MPa

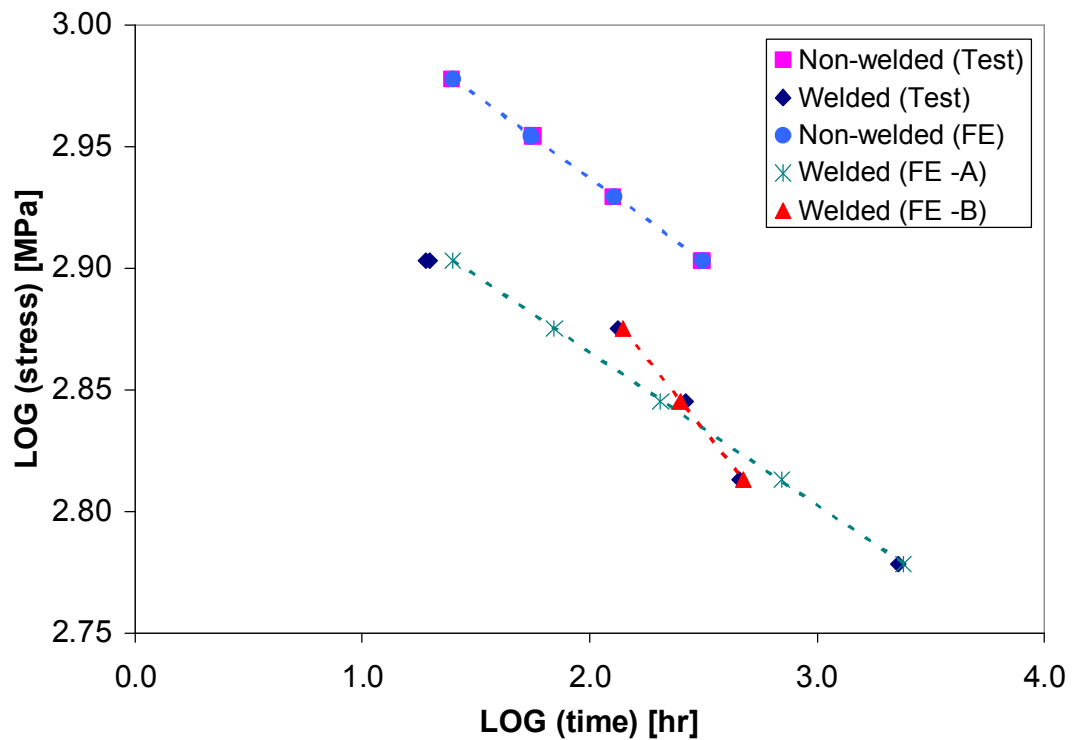


Figure 6.18: Comparison between FE-damage predicted and test rupture times (A – all data used for determining properties, B – high and low stress points omitted)

6.6 Finite element modelling of the high temperature fatigue tests

Fatigue life can generally be divided into two distinct phases: time to crack initiation, and then time for subsequent crack propagation until failure. In the analyses performed here, the lifing method used is based on the time to crack initiation and this is considered to be the same as the life until complete failure. Crack propagation modelling using fracture mechanics techniques is not covered since for the thin-sections considered, any small crack will quickly propagate and cause failure.

In this section, the high temperature uniaxial fatigue tests described in Chapter 5 are modelled using FE analysis, in order to develop a lifing methodology by determining failure criteria, which can later be applied to more complex geometries and loading conditions (such as the case study in Chapter 7 for example).

The fatigue cycles had a trapezoidal (1-1-1-1) form with a load frequency of 0.25Hz and a stress ratio of (approximately) zero (see section 5.7.1). Since the loading amplitude is constant during a test, damage summation using, for example Miner's rule, is not required.

Again, the material properties used in these analyses were obtained from the uniaxial tensile and creep tests of both welded and non-welded heat-treated IN718 at 620°C, outlined in Chapter 5. The properties have been previously presented in this chapter (see section 6.3). The weld material true stress-strain curve used in all of the FE analyses is shown in Figure 6.19.

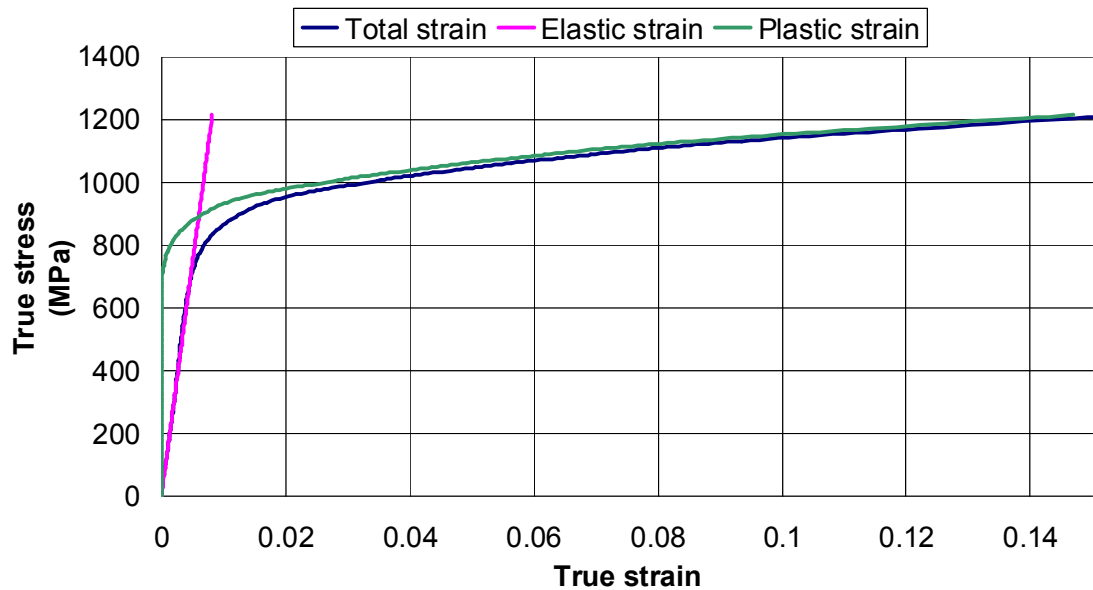


Figure 6.19: Weld material true stress-strain curve used in the FE analyses

Since creep effects were found to be small due to the low amount of hold time during each fatigue cycle, the creep damage mechanics approach employed when modelling the creep tests (section 6.5) is not necessary for the fatigue tests. Instead, only steady-state (secondary) creep strain accumulation is accounted for during the fatigue cycles using Norton's creep law [equation (6.1)].

The fatigue tests were modelled using a two-dimensional quarter-symmetry, plane stress, elastic-plastic FE model with the mesh shown in Figure 6.20. The mesh refinement was found to be acceptable in giving adequate results in reasonable computation time for the range of loads applied. 299, 8-node biquadratic, plane stress, quadrilateral continuum elements with reduced integration were employed. The material properties were assigned to the appropriate regions as shown in Figure 6.20.

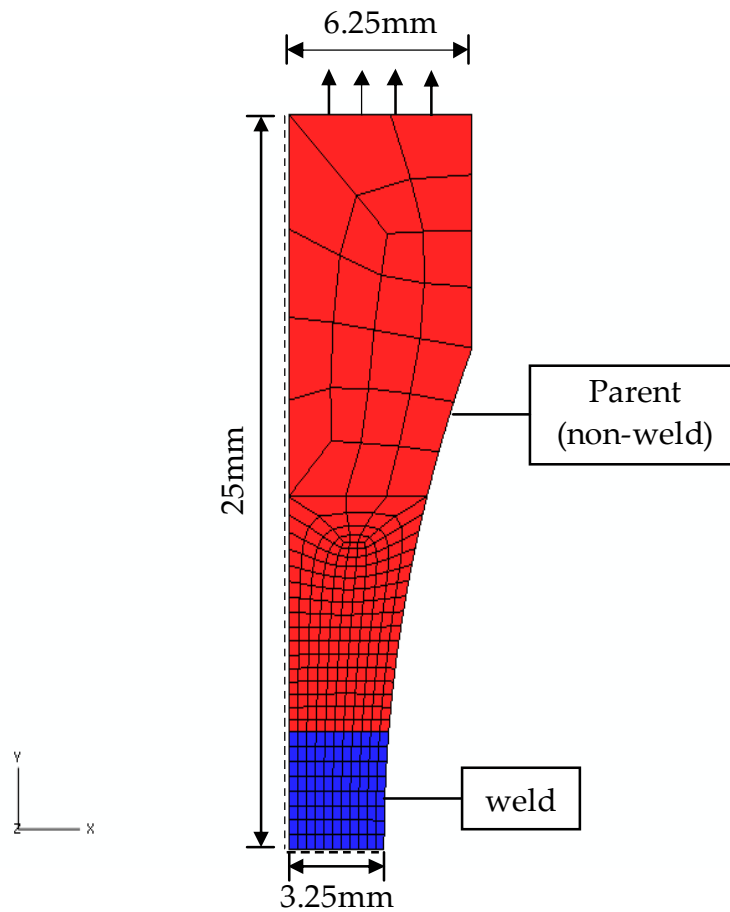


Figure 6.20: 2D FE fatigue model mesh

The necessary symmetry boundary conditions were imposed and the fatigue load was applied through a uniformly distributed, normal tensile surface traction, acting on the original area of the top surface (as shown in Figure 6.20). Results were obtained for all of the loads used in the high temperature fatigue testing (section 5.7.2).

Nonlinear quasi-static analyses were performed to include the effect of creep (*VISCO in ABAQUS). Two steps were performed, each equivalent to one cycle; all results were taken from the second step, which is a more stable representation of subsequent cycles than the initial loading cycle. The large-displacement (geometric nonlinearity) formulation was used and fairly small time increments were required to satisfactorily model the loading waveform.

A strain-based parameter lifing method that accounts for mean stress was chosen since this is the common approach used when lifing aero engine structures, see [128] for example. The Walker strain parameter (based on the original work by Walker [129]) takes the form:

$$\varepsilon_w = \frac{\sigma_{\max}}{E} \left\{ \frac{\Delta\varepsilon E}{\sigma_{\max}} \right\}^w \quad (6.8)$$

where σ_{\max} is the maximum von Mises equivalent stress, $\Delta\varepsilon$ is the total strain range within a cycle, E is Young's modulus and w is a fitting exponent (material constant) that varies between 0 and 1 [130]. If w is not known for the material or given temperature, w is often set to 0.5 to yield:

$$\varepsilon_w = \sqrt{\left(\frac{\sigma_{\max} \Delta\varepsilon}{E} \right)} \quad (6.9)$$

The one-one relationship between maximum stress and strain range in this equation is a strain formulation equivalent to the Smith, Watson and Topper (SWT) stress-strain function, which has units of stress and ε_a is the strain amplitude [131]:

$$\sqrt{\sigma_{\max} \varepsilon_a E} \quad (6.10)$$

The more general, Walker strain parameter will be used here, but with $w = 0.5$ as in equation (6.9), and this will be referred to as the SWT 'strain range' parameter, or just SWT. The parameter can be correlated with test cycles to failure and used for life assessment. The correlation between SWT and number of cycles to failure using the nominal maximum on-load stress and measured strain range from the fatigue tests is shown in Figure 6.21. The similarity between the results for nominal stress and corresponding SWT and the clear trend lines indicate that the SWT parameter can be used to predict the fatigue life of both welded and non-welded IN718 at 620°C.

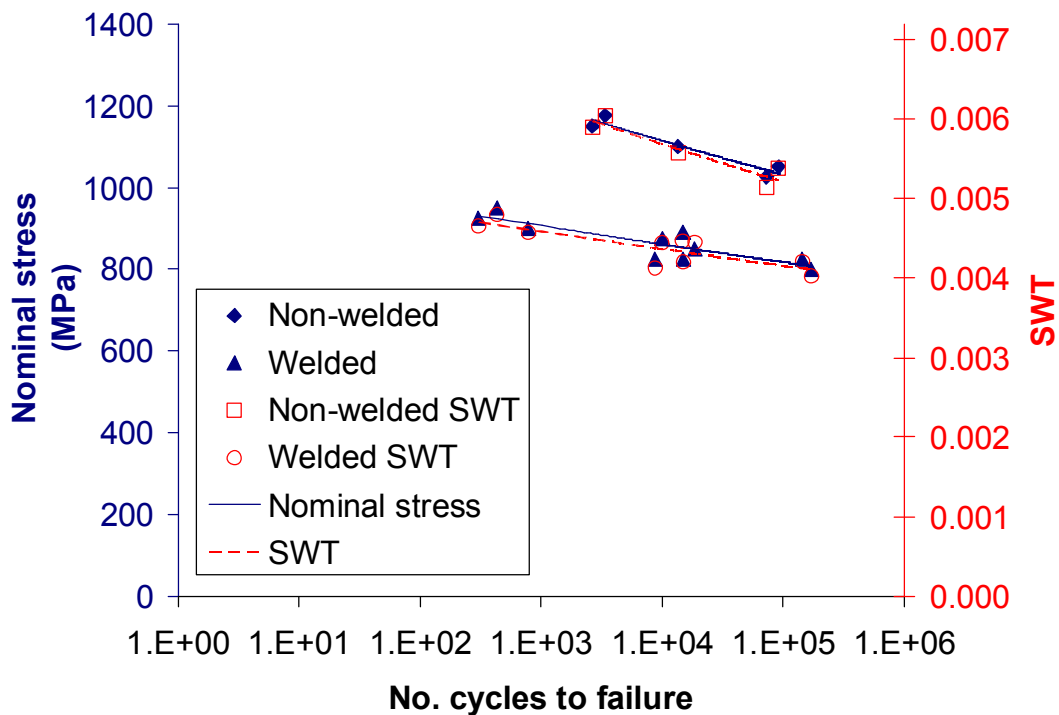


Figure 6.21: Comparison between SWT strain range parameter and nominal stress against cycles to failure for the test data at 620°C

The Smith, Watson and Topper (SWT) strain range parameter was calculated for each point during the FE fatigue analysis using equation (6.9).

Figures 6.22-6.27 show typical FE results (for a 925MPa welded specimen). Plastic yielding is present during the first cycle and then this stabilizes due to material strain-hardening (Figure 6.22 and Figure 6.25). Since there is only a short period of hold during each fatigue cycle, little creep (Figure 6.24 and Figure 6.25) and no noticeable subsequent stress relaxation occurs (Figure 6.23). A complex stress state is produced with the maximum von Mises stress at the interface between the weld and parent (on the parent side), where the heat-affected zone (HAZ) would be found (Figure 6.26). The peak SWT occurs in the weld, in the middle of the specimen (Figure 6.27).

Table 6-5 and Table 6-6 list the SWT strain range parameter values for all non-welded and welded load cases, respectively. The SWT results are also plotted in Figure 6.28. The FE results compare well with those obtained using the test specimen measurements, by averaging over the same gauge length. Peak FE results are also given in Tables 6-5 and 6-6, and plotted in Figure 6.29. Using these results, an FE analysis of a structure could be performed to calculate the peak SWT value, and the corresponding life could be predicted by correlating with the peak SWT and the fatigue test cycles to failure data, as in the case study presented in Chapter 7.

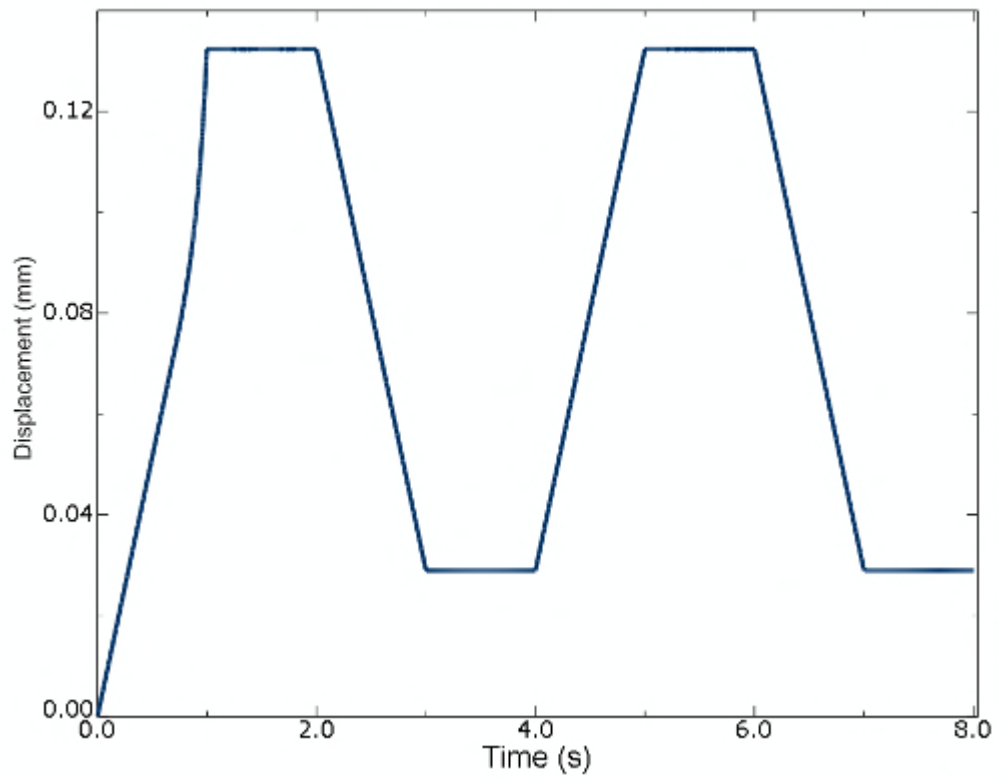


Figure 6.22: FE displacement-time plot for one half of the specimen (925MPa welded fatigue)

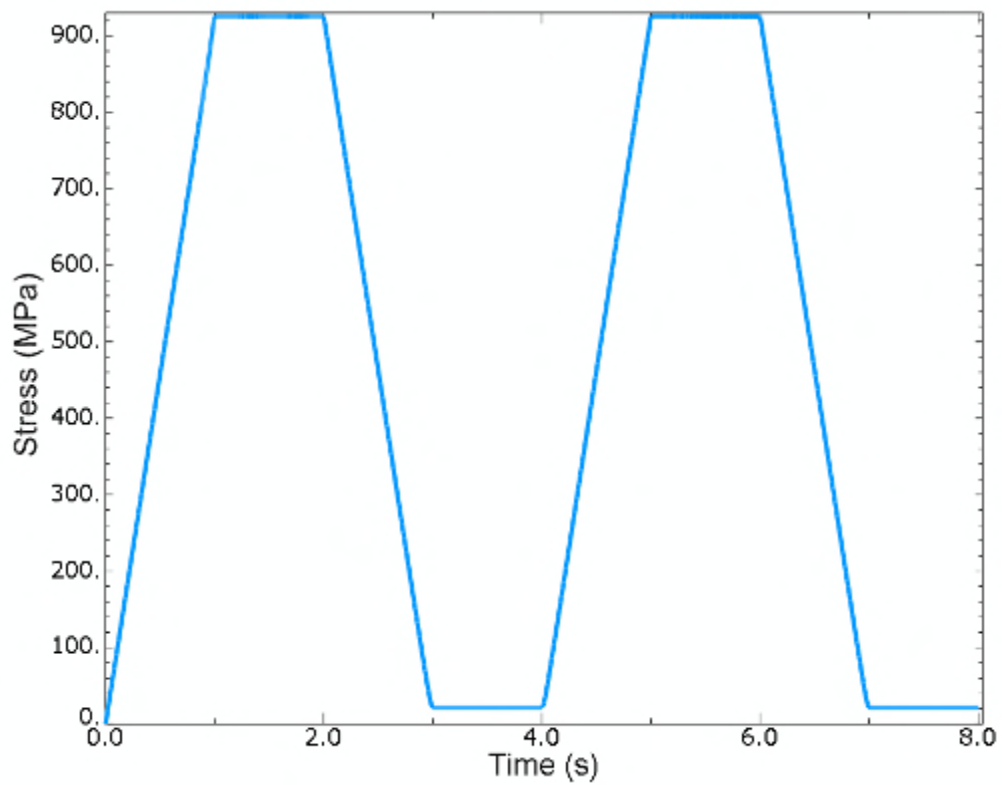


Figure 6.23: FE fatigue loading (stress) history (925MPa)

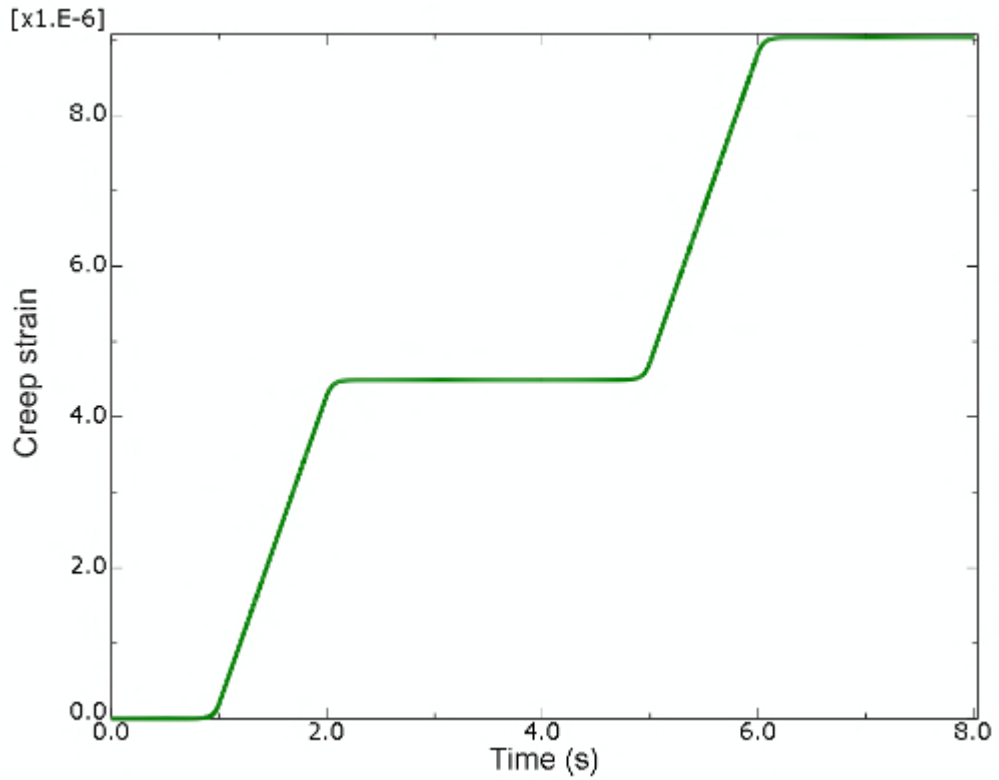


Figure 6.24: FE creep strain history at peak position (in the weld). Relatively little creep strain occurs (925MPa welded fatigue)

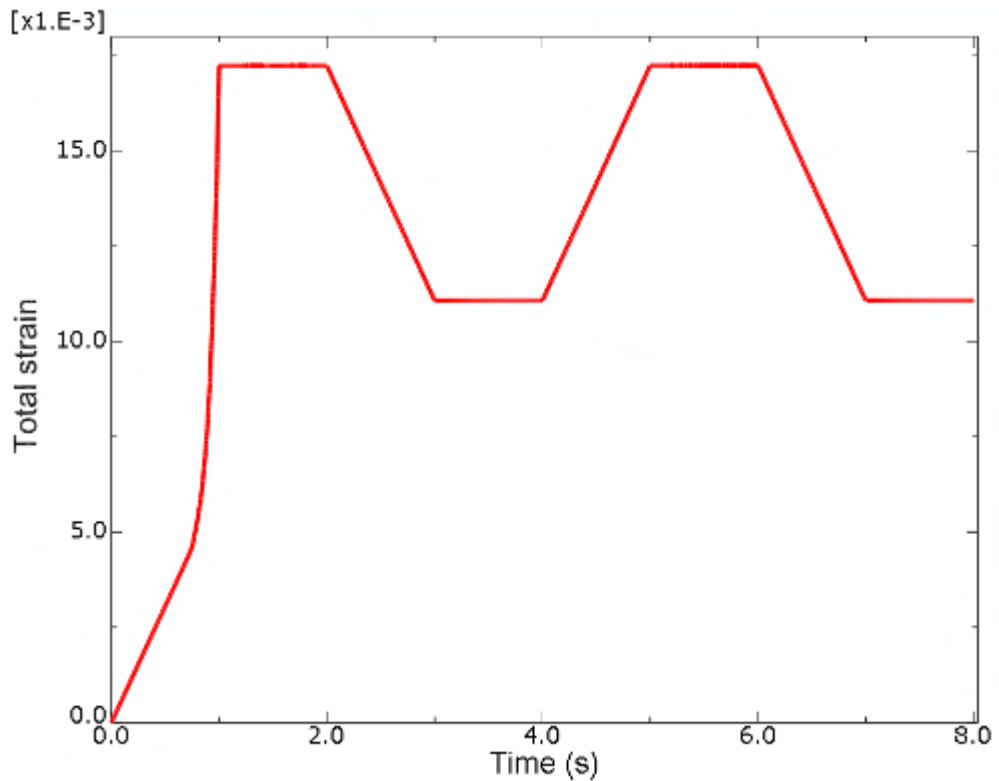


Figure 6.25: FE total strain history at peak position (in the weld) (925MPa welded fatigue)

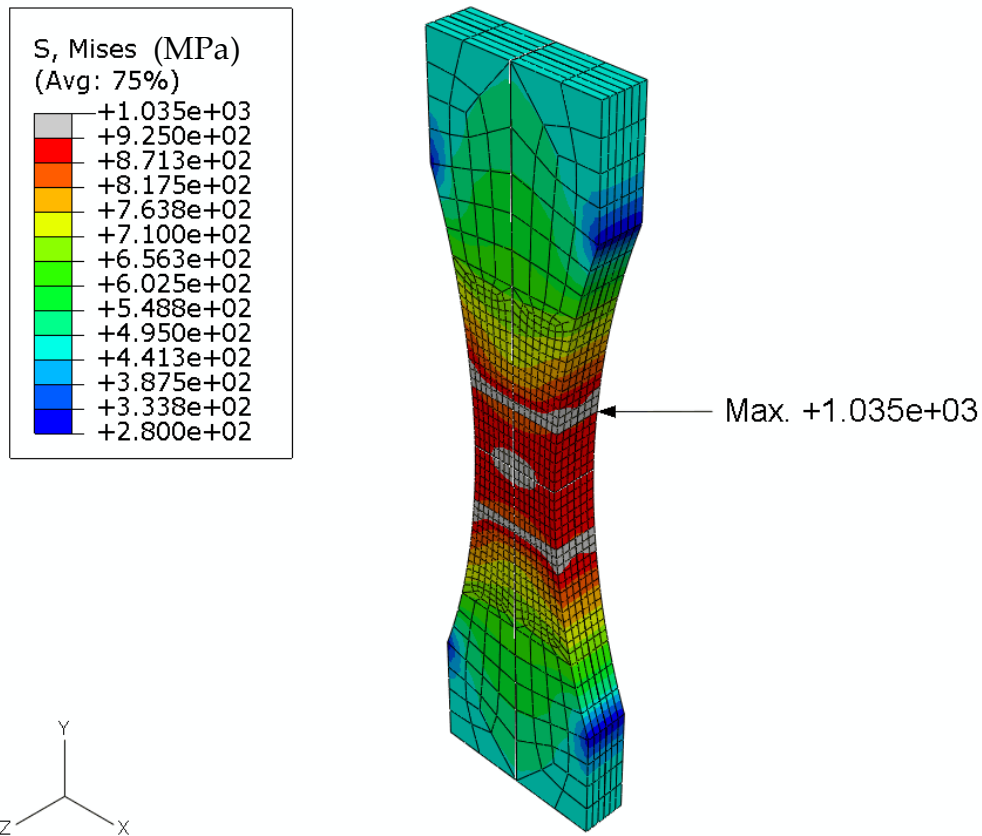


Figure 6.26: Maximum von Mises stress. Mirrored 3D model shown for illustration purposes (925MPa welded fatigue)

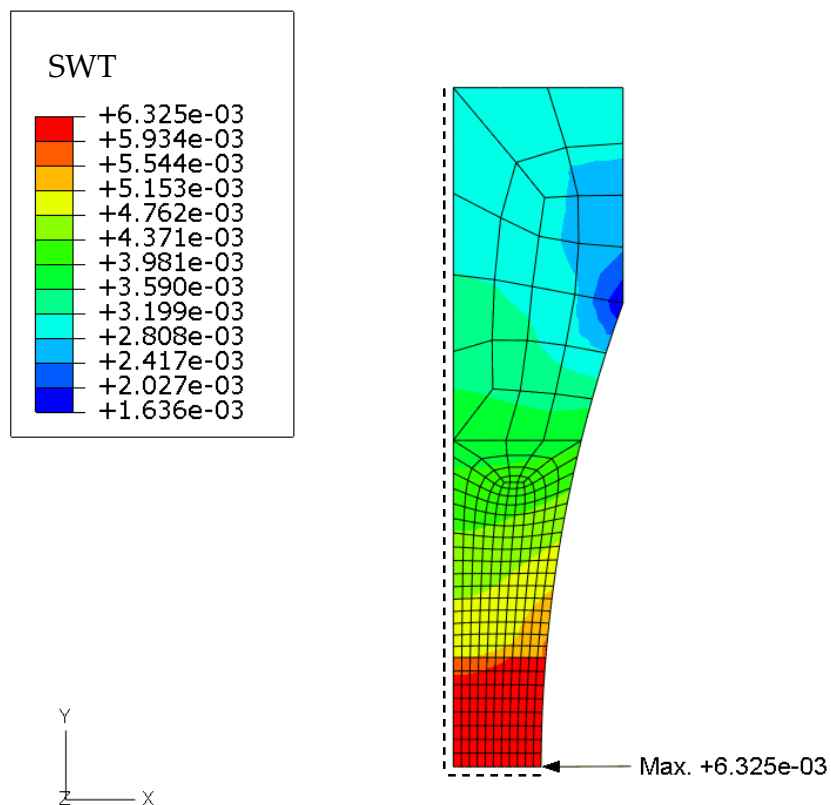


Figure 6.27: FE SWT parameter distribution (925MPa welded fatigue)

Table 6-5: SWT strain range parameter for all non-welded fatigue load cases

<u>Non-welded</u>				FE			
Nominal stress (MPa)	Test cycles to failure	Test		Over gauge length		Peak	
		strain range	SWT	strain range	SWT	strain range	SWT
1025	72662	4.27E-03	5.13E-03	4.37E-03	5.19E-03	5.87E-03	6.21E-03
1050	91360	4.59E-03	5.39E-03	4.48E-03	5.32E-03	6.04E-03	6.37E-03
1100	13494	4.68E-03	5.57E-03	4.72E-03	5.59E-03	6.42E-03	6.76E-03
1150	2650	5.03E-03	5.90E-03	5.11E-03	5.95E-03	7.30E-03	7.76E-03
1175	3373	5.17E-03	6.05E-03	5.37E-03	6.17E-03	8.10E-03	8.35E-03

For tests (where measurements use gauge length):

$$\begin{aligned}
 E \text{ non-welded} &= 1.66E+11 \text{ Pa} \\
 E \text{ welded} &= 1.65E+11 \text{ Pa}
 \end{aligned}$$

Table 6-6: SWT strain range parameter for all welded fatigue load cases

<u>Welded</u>				FE			
Nominal stress (MPa)	Test cycles to failure	Test		Over gauge length		Peak	
		strain range	SWT	strain range	SWT	strain range	SWT
800	169998	3.34E-03	4.02E-03	3.47E-03	4.09E-03	5.17E-03	5.44E-03
825	14863	3.52E-03	4.20E-03	3.58E-03	4.22E-03	5.32E-03	5.61E-03
825	143709	3.54E-03	4.21E-03	3.58E-03	4.22E-03	5.32E-03	5.61E-03
825	8714	3.42E-03	4.13E-03	3.58E-03	4.22E-03	5.32E-03	5.61E-03
850	18541	3.85E-03	4.45E-03	3.70E-03	4.35E-03	5.49E-03	5.78E-03
875	9996	3.73E-03	4.45E-03	3.81E-03	4.48E-03	5.67E-03	5.95E-03
890	14814	3.71E-03	4.47E-03	3.88E-03	4.56E-03	5.77E-03	6.06E-03
900	785	3.83E-03	4.57E-03	3.93E-03	4.62E-03	5.85E-03	6.13E-03
925	304	3.86E-03	4.65E-03	4.05E-03	4.75E-03	6.03E-03	6.33E-03
950	430	4.00E-03	4.80E-03	4.17E-03	4.88E-03	6.24E-03	6.54E-03

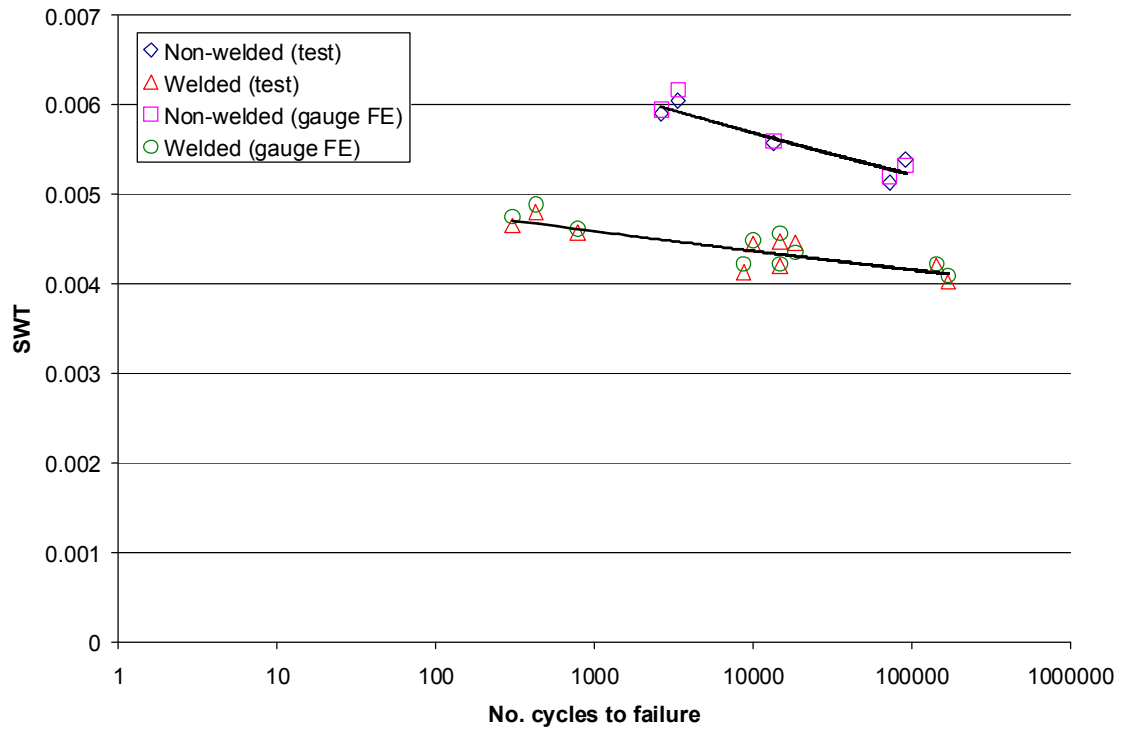


Figure 6.28: SWT strain range parameter against number of cycles to failure (FE results averaged over specimen gauge length)

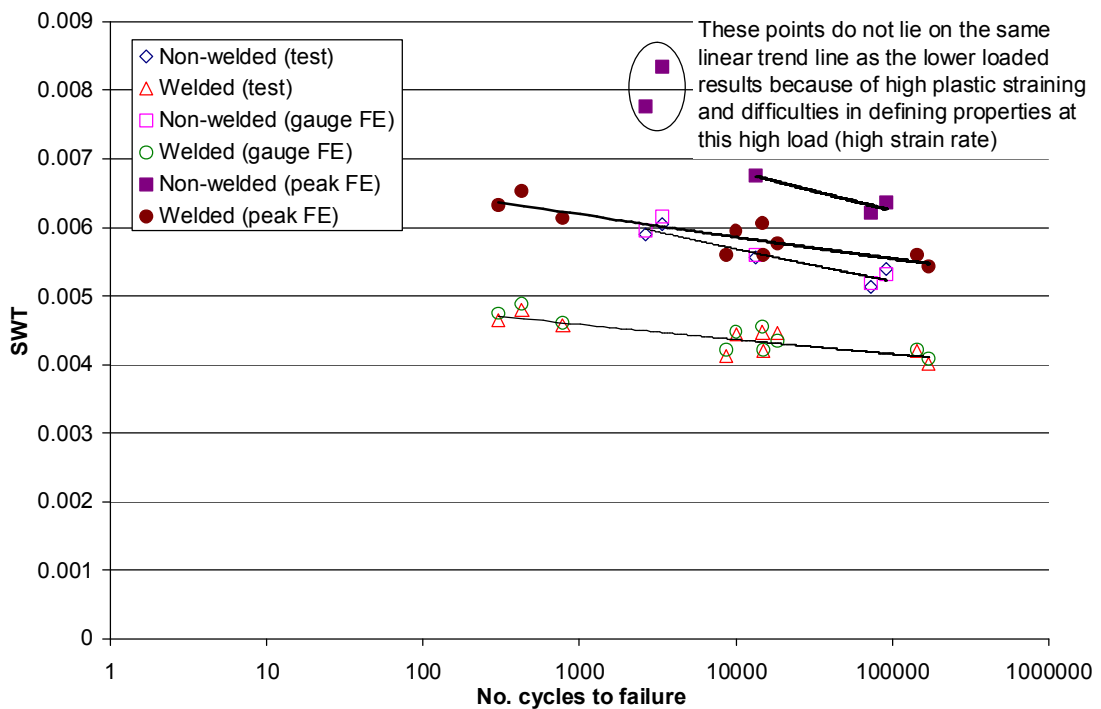


Figure 6.29: Peak FE SWT compared with test and FE results averaged over specimen gauge length
Care should be taken if $SWT > 0.007$ since these results show that a linear trend is not valid here.

6.7 Conclusion

In this chapter, the stress-strain relationships (and hence the mechanical properties) of the IN718 weld material were calculated using the test measurements and determining what the behaviour of the weld must have been in order to give the measured test results. FE verification of the material properties was conducted by modelling the uniaxial tensile and creep tests to check the accuracy of the material properties assigned to the weld region, very good agreement was obtained. A creep continuum damage mechanics approach was suggested in order to capture the significant tertiary creep that was observed during the testing programme, and obtain more accurate failure times. Determination of the necessary material constants required for the damage equations was presented. The high temperature uniaxial fatigue tests were also accurately modelled using FE analysis for all the load cases used during the testing, for both the butt-welded and non-welded specimens. The modelling technique was validated by comparing the FE-calculated strain results with the measured test results. A Smith, Watson and Topper (SWT) strain range parameter was introduced and the FE-calculated values were found to compare well with values determined using the test data, validating the suitability of this life assessment method.

Creep and high temperature fatigue life assessment case study

7.1 Summary

In this chapter, a life assessment case study of a welded feature in a generic spoke structure is conducted using three-dimensional, quasi-static elastic-plastic and creep finite element analyses. The complete structure consists of multiple IN718 TIG-welded features so a multi-material analysis is necessary for accurate life predictions. The effect of including a weld (i.e. welded material) in a critical region is investigated for both constant (creep) and cyclic loading (creep-fatigue) conditions at 620°C. Creep damage and Smith, Watson and Topper (SWT) strain range parameter lifing methods are used, based upon the material properties and lifing validation discussed in Chapter 6. It is shown that the lower fatigue strength of the welded IN718 material at high temperature has a negative effect on the fatigue life⁵ of the structure (reducing the life by two orders of magnitude). The effect of the weld on the creep life⁶ is found to be more difficult to evaluate due to significant stress relaxation, and the predicted failure location is affected by the weld in the constant load case (due to stress relaxation) but not in the fatigue load case.

⁵ The number of cycles before fatigue failure occurs

⁶ The time under constant loading at high temperature before failure occurs

7.2 Introduction

Allowable static design stresses are usually related to the yield strength of the material used, introducing a factor of safety. In practice, few structures are subject to purely static loading. Fluctuations in loading may range from simple cyclic fluctuations, such as those that will be covered here, to a completely random variation. The temperature may also fluctuate as in the case of thermal or thermomechanical fatigue, or be high enough for time-dependent creep to be significant. Only isothermal conditions are considered throughout this work, but the temperature of 620°C is high enough to cause significant creep and eventually, creep failure in IN718. Although the loading may remain within the limit of the allowable static stress, a structure subjected to variations in loading and/or high temperatures can no longer be regarded as safe without considering the effects of fatigue and/or creep. While the word 'fatigue' implies an exhaustion of some kind such as a loss of properties, this is not necessarily the case, instead the term refers to failure under fluctuating loading at a load less than that required to cause static failure [132]. Fatigue failure is cycle-dependent whereas creep failure is time-dependent since it occurs when a load less than that required to cause immediate static failure is sustained over time. Ideally, the stress would remain below the fatigue endurance limit of the material so that the fatigue problem could be avoided. Likewise, the stress and temperature would ideally remain low so that creep would not be significant. However, it is rarely economic to design structures to give infinite life because the allowable stress (and/or temperature) would be relatively low. Therefore, predicting the life of components subjected to cyclic loading or high temperatures (or both) are important disciplines.

The expected fatigue life of a component subjected to a particular cyclic stress can be obtained from a Wöhler (after the work by August Wöhler in the 19th century) or S-N (stress against number of fatigue cycles to failure) curve for the geometry of the particular component. In the absence of S-N curves for a particular component geometry, it is common to use S-N curves from simple test specimen geometries that are most representative of the component geometry, tested under the same loading conditions that regions in the component experience. Finite element models can then be used to calculate the stress at positions within the component and fatigue life can be predicted by comparing with the corresponding simple test specimen results. For example, the fatigue strengths of aligned and misaligned joints agree if the latter is expressed in terms of the resulting total stress range. Thus, the appropriate S-N curve for the aligned joint can still be applied as long as the stress concentration due to misalignment is taken into consideration when calculating the stress range [132]. Multiaxial stress states can also be considered by using appropriate equivalent measures such as von Mises stress criterion [133].

Creep life estimates can be obtained in a similar fashion to that mentioned above for fatigue life estimation by using stress rupture time curves instead of S-N curves (see [98] for example).

The environment, temperature, and frequency and waveform of loading can all significantly affect the life of structures, which is why the service conditions were replicated as practically as possible in the work presented in this thesis. Of course, time-dependent effects such as creep and corrosion are difficult to replicate in accelerated tests, since even the time taken to perform these tests can still be considerable.

The creep and fatigue strength of welded structures is often dramatically reduced by stress concentrations arising from the change in geometry at the weld bead, misalignment and distortions, and high tensile residual stresses.

In this work, the stress-raising weld bead excess was removed, the careful selection of welding process avoided misalignment and distortion, and the residual stresses have been relieved somewhat by postweld heat treatment (PWHT). The effects of residual stress are also included implicitly in the testing programme since applied nominal stresses are quoted and the effects of residual stress would have consistently modified the actual stress experienced by the welded specimens. Therefore, the stress-strain and creep behaviour determined in Chapter 6 includes the effects of residual stress. It has also been suggested that for tensile-only fatigue cycles, tensile residual stresses have little effect on fatigue life, depending on the material's crack growth sensitivity to mean stress [132].

It is worth noting that if the welds contained crack-like discontinuity defects such as weld toe intrusions or incomplete penetration, then the creep and fatigue crack initiation periods would be significantly reduced. The factors that govern the crack initiation processes, which may occupy most of the life in a non-welded component, can have quite different effects on crack propagation, which occupies most of the life of a welded joint. As a result, there are important contrasts between the creep and fatigue behaviour of welded and non-welded material and conclusions based on the behaviour of the non-welded material alone can be quite misleading when applied to welded material [132]. Changes in the microstructure of the material due to the welding process can also severely alter the overall behaviour of the material.

7.3 Model definition

Structures that are subjected to high service temperatures where creep (and possibly creep-fatigue interaction) is significant require well-defined material behaviour, and for all integral structural components, the lifetime requires assessment. For this case study, a generic hollow spoke structure formed from 5mm sheets was analysed using the finite element (FE) method, to demonstrate the application of high temperature lifing methodologies to a complicated geometry including a weld with differing material properties. Comparisons are then made to identify how the inclusion of the weld affects the life of the structure.

The material used throughout this study was IN718; determination of the material properties for both the parent and the weld region is discussed in Chapter 6. The temperature chosen for the life assessment analyses was 620°C since this is the temperature limit permitted for many critical applications of the material [4], and is the temperature at which the material properties were obtained. An example of the application of IN718 in this particular environment is in the aerospace industry, where IN718 is used in shell structures such as the combustor in a gas turbine engine [2].

7.4 Finite element model setup

A one-spoke (30°) section of the generic spoke structure was modelled, with a fully-penetrating 5mm-wide weld (i.e. welded material) positioned in the blend between the hollow spoke and the inner ring, in order to demonstrate the lifing methodology (Figure 7.1 and Figure 7.2).

A three-dimensional solid ABAQUS FE mesh consisting of 20804 quadratic tetrahedron (C3D10 in ABAQUS) elements and 40587 nodes was generated.

The mesh was refined in the regions of high stress that were identified after an initial analysis had been run. The same mesh (Figure 7.2 and Figure 7.3) was used for all analyses.

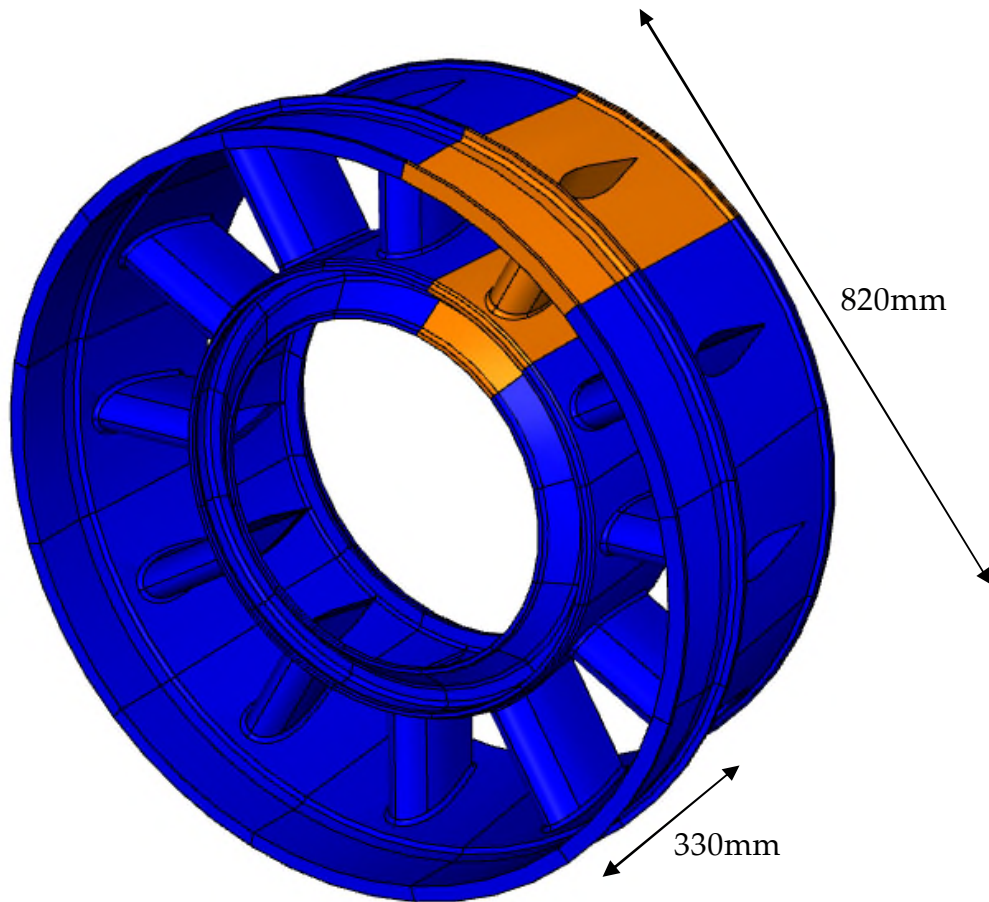


Figure 7.1: Complete structure with one-spoke section highlighted in orange

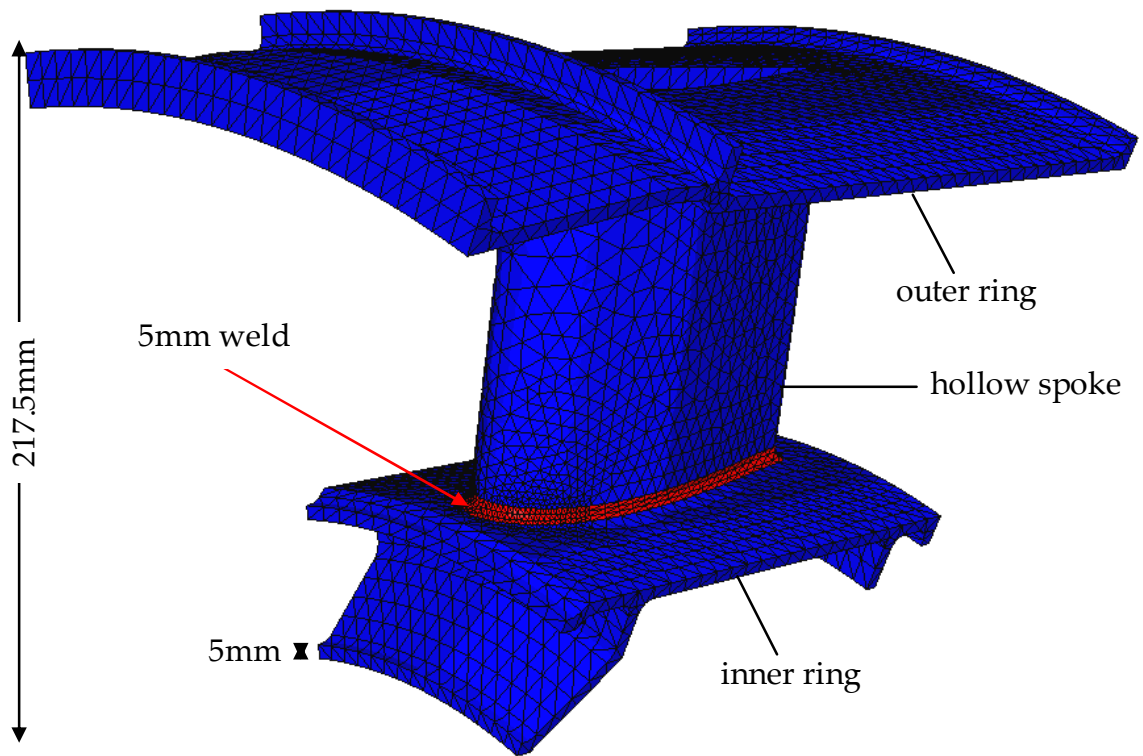


Figure 7.2: FE mesh of one-spoke section with the weld highlighted in red

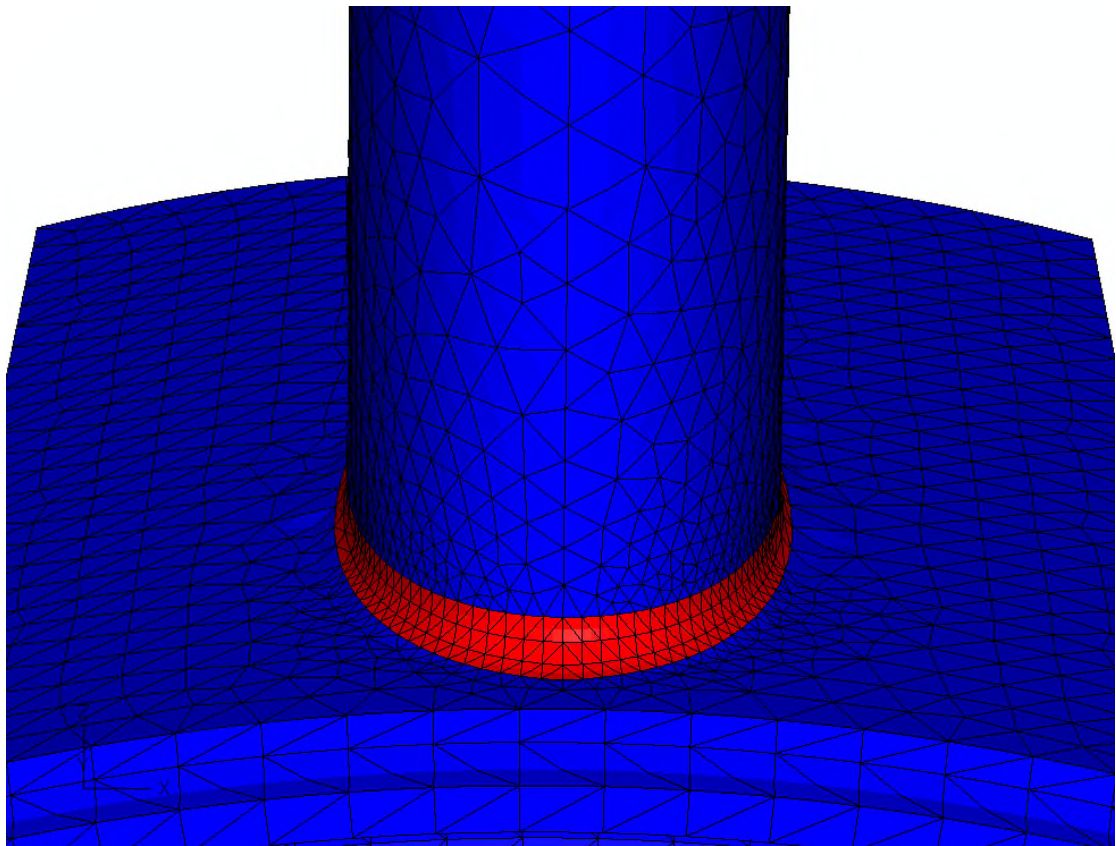


Figure 7.3: Refined FE mesh in the critical area around the weld on the front (loaded) side of the spoke

The boundary and loading conditions are described below and shown in Figure 7.4. A cylindrical coordinate system with the origin at the centre of the complete structure was employed in order to conveniently define the cyclic symmetry along the edge surfaces of the one-spoke section. These surfaces (in dark blue) were constrained in the circumferential (T) direction. The front-facing surfaces (in light blue/green) were constrained in all directions to reflect the realistic boundary conditions for this type of structure. Load was applied as equal nodal force in the negative direction of the axis of rotation of the cylindrical coordinate system (-Z), to the nodes on the front surface of the spoke (in red).

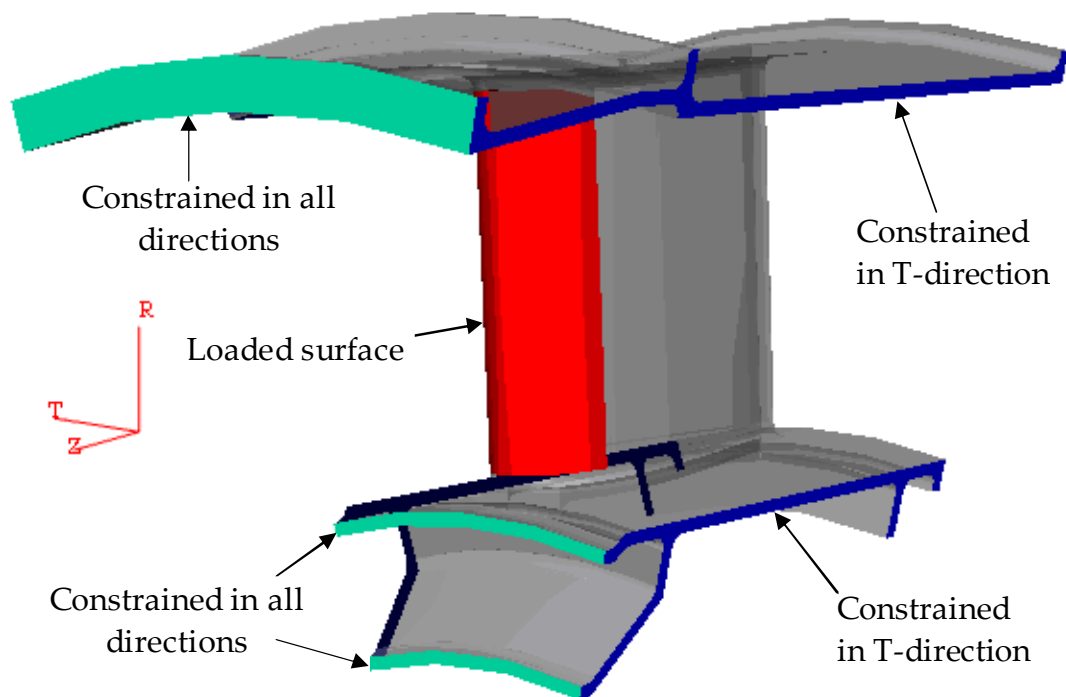


Figure 7.4: FE boundary and loading conditions

Two types of FE analyses were performed. A constant load creep analysis at 620°C and a fatigue analysis at 620°C. The results of which are presented below.

7.5 Finite element creep analysis

The creep FE analysis was conducted in two steps. Firstly, the load was applied gradually during a nonlinear elastic-plastic static step. A nonlinear visco (transient, quasi-static) plastic step followed the loading step, for which the load was held constant. A Kachanov-type damage mechanics approach was used for the creep law and life prediction as described in Chapter 6. The multiaxial formulation was used [equations (6.7)]. Failure was determined when the damage parameter, $\omega = 0.8$ at any location in the model.

Below are the results from creep FE analyses with and without a weld for a total applied load of 870kN. It should be noted that the results obtained at the relevant failure positions are compared in some of the figures. Position A refers to the failure location of the welded feature, which is on the parent side (inner ring) of the weld-parent interface (see Figure 7.18). Position B refers to the failure location of the feature without a weld, this location is on the blend of the spoke-inner ring, where the weld would have been (see Figure 7.17).

The highest stress occurred in and around the blend between the spoke and the inner ring (Figure 7.5 and Figure 7.6). This is also the site of the weld. A large amount of stress relaxation occurred during the creep step (Figures 7.7-7.9). The welded material was unable to support as high a stress as the non-welded material (Figure 7.8) and relaxed at a quicker rate initially before steadying at a lower rate (Figure 7.9). The peak creep strain, which generally occurred around the bottom of the front of the spoke (Figure 7.10), was greater in the weld (Figure 7.12 and welded position B, Figure 7.11) but lower in the region of failure of the welded case (welded position A, Figure 7.11), where the highest stresses caused the most creep damage (Figure 7.18).

The peak damage generally occurred around the bottom of the front of the spoke (Figure 7.13); its evolution at positions A and B is plotted in Figure 7.16. A comparison of damage magnitude and distribution after 100hrs, and distribution at failure, between the welded and non-welded cases, is shown in Figure 7.14 and Figure 7.15, respectively.

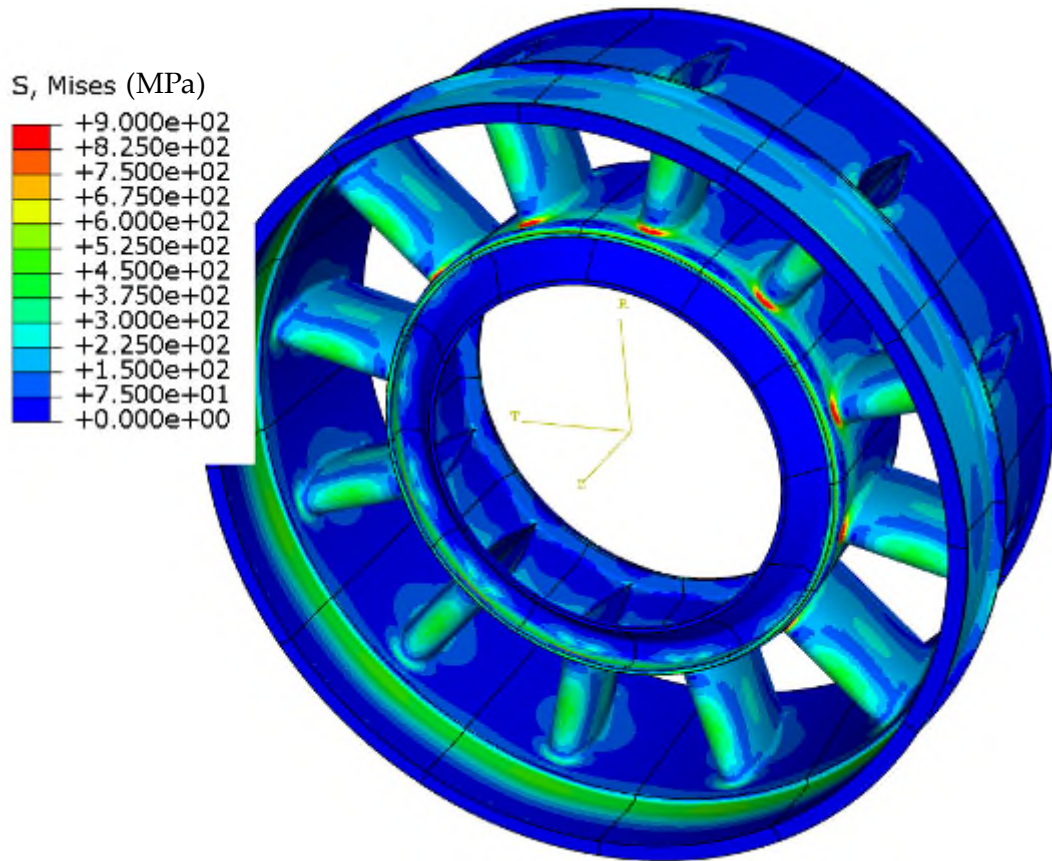


Figure 7.5: von Mises stress distribution during loading (non-welded case) (mirrored around z-axis for illustration purposes)

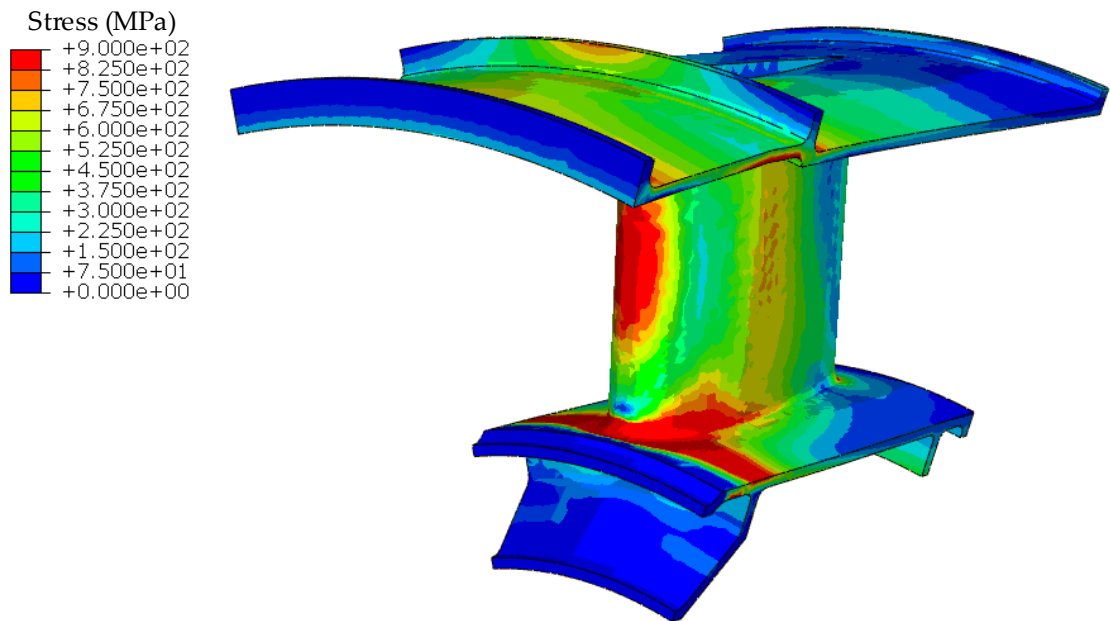


Figure 7.6: Rupture stress [as defined in equations (6.7)] immediately after loading (non-welded case)

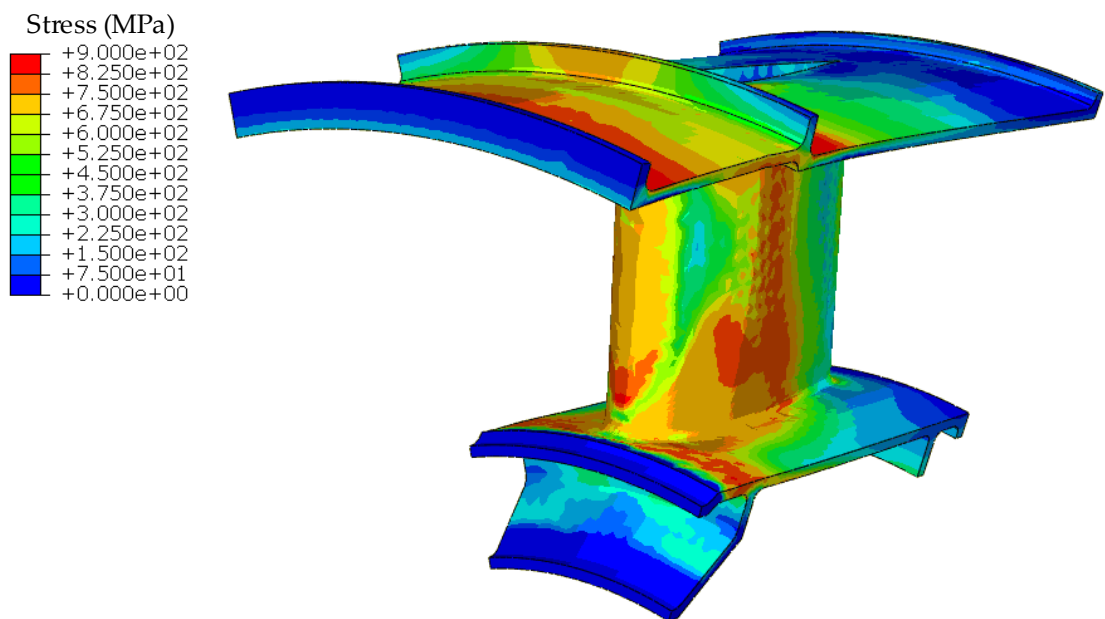


Figure 7.7: Final (relaxed) rupture stress (non-welded case)

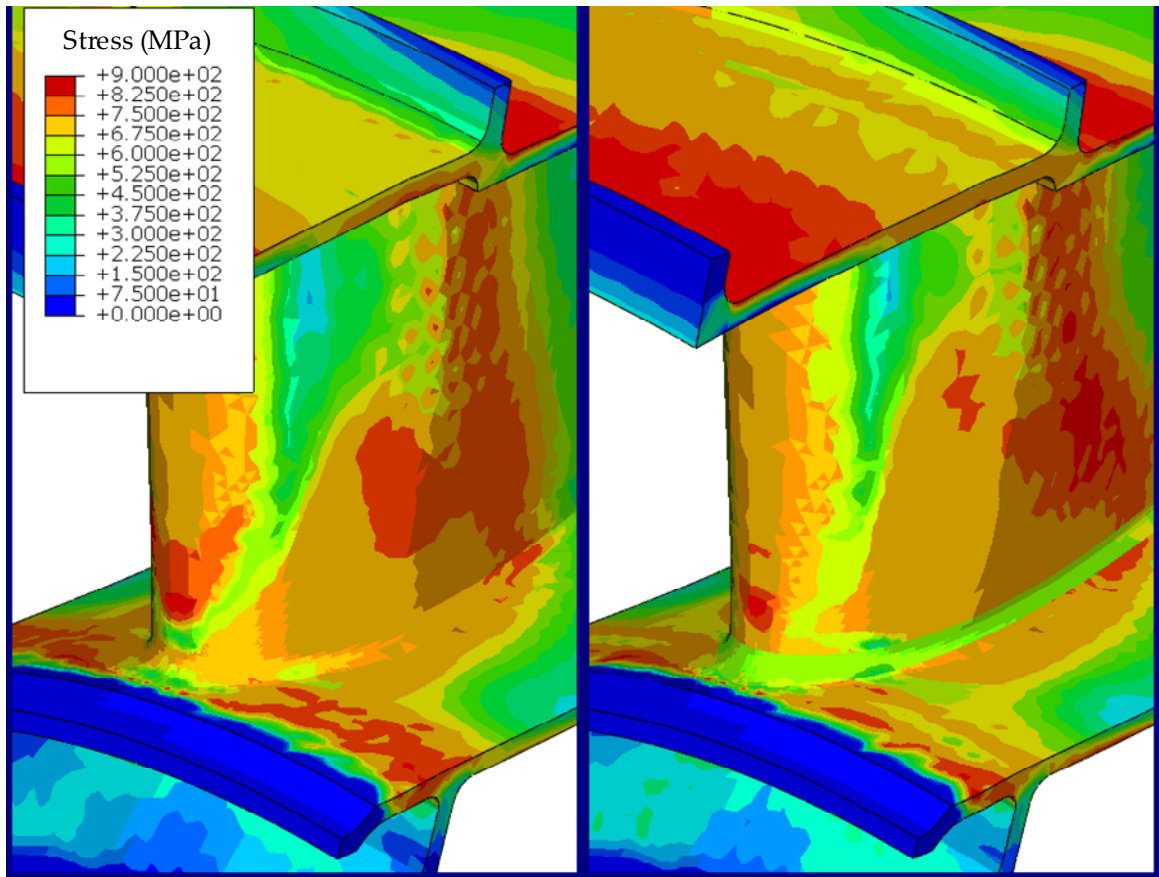


Figure 7.8: Greater (rupture) stress relaxation in weld (right)

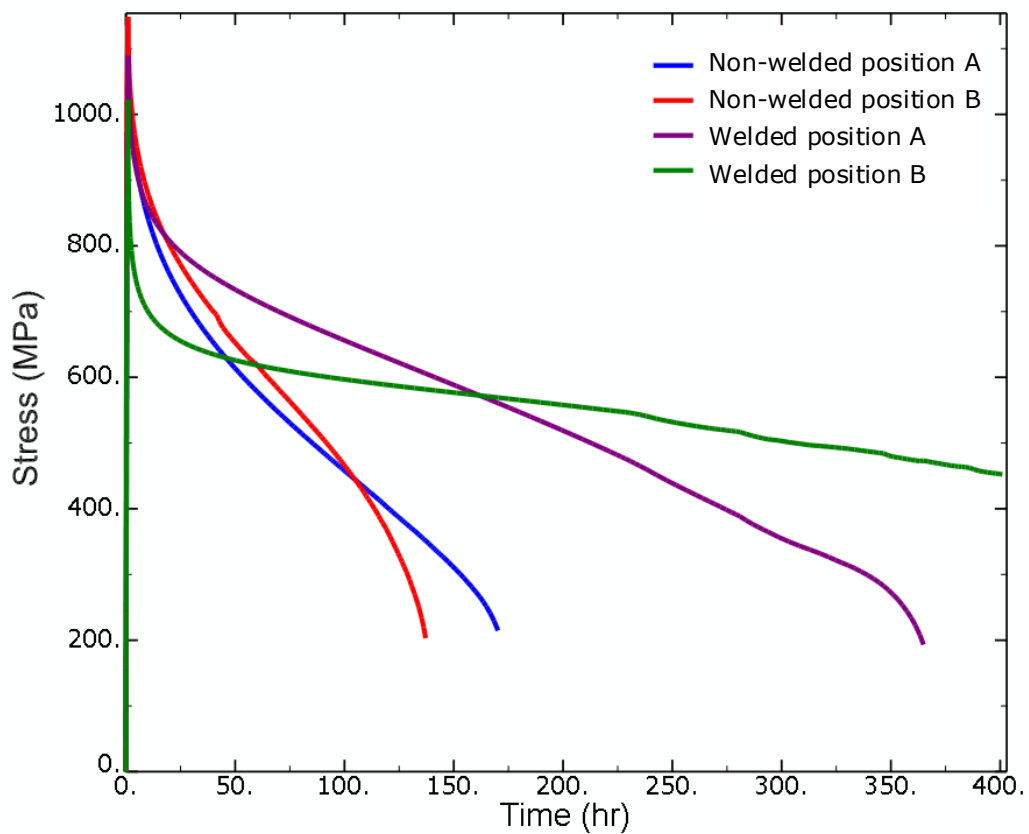


Figure 7.9: von Mises stress history at positions A and B

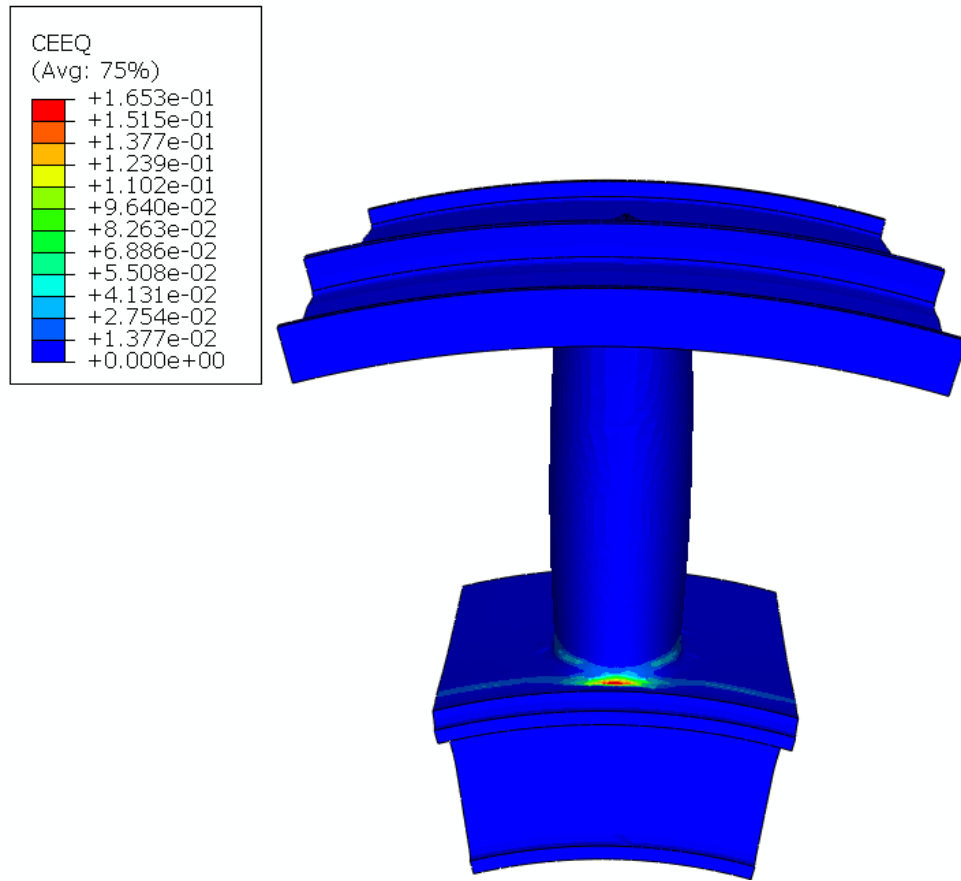


Figure 7.10: Peak creep strain around the bottom of the front of the spoke

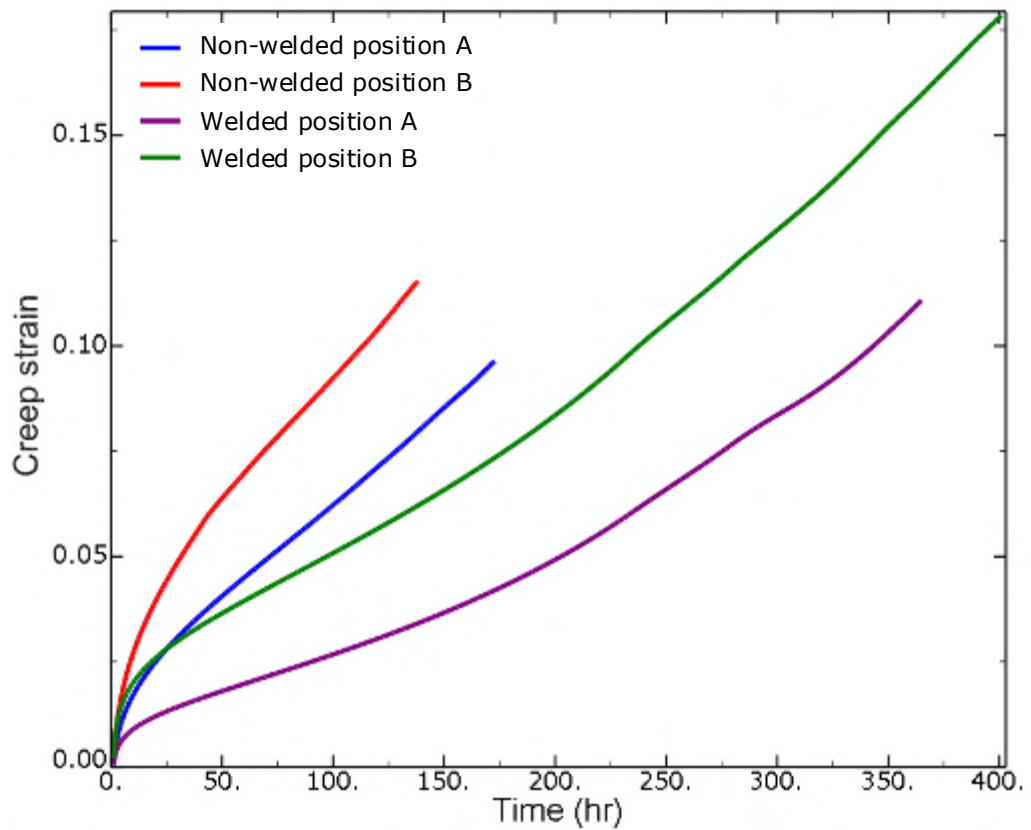


Figure 7.11: Creep strain history at positions A and B

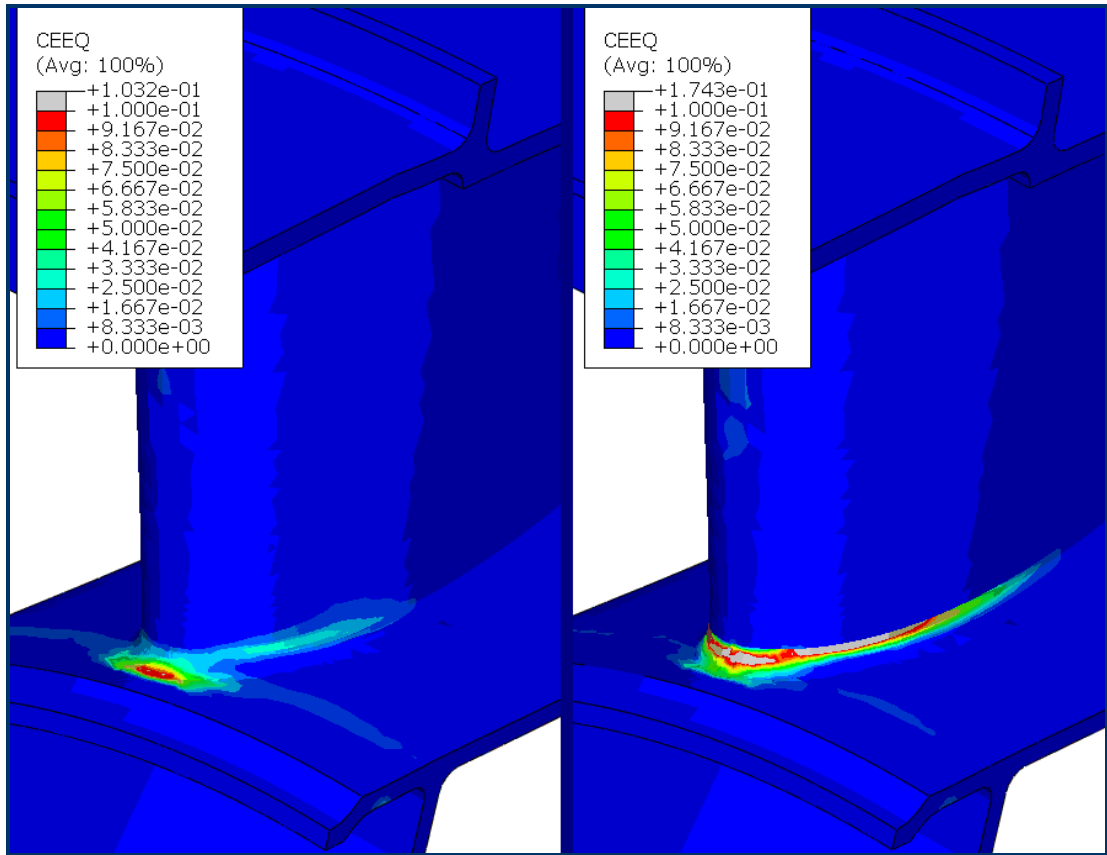


Figure 7.12: Creep strain after 100hrs, greater for welded (right)

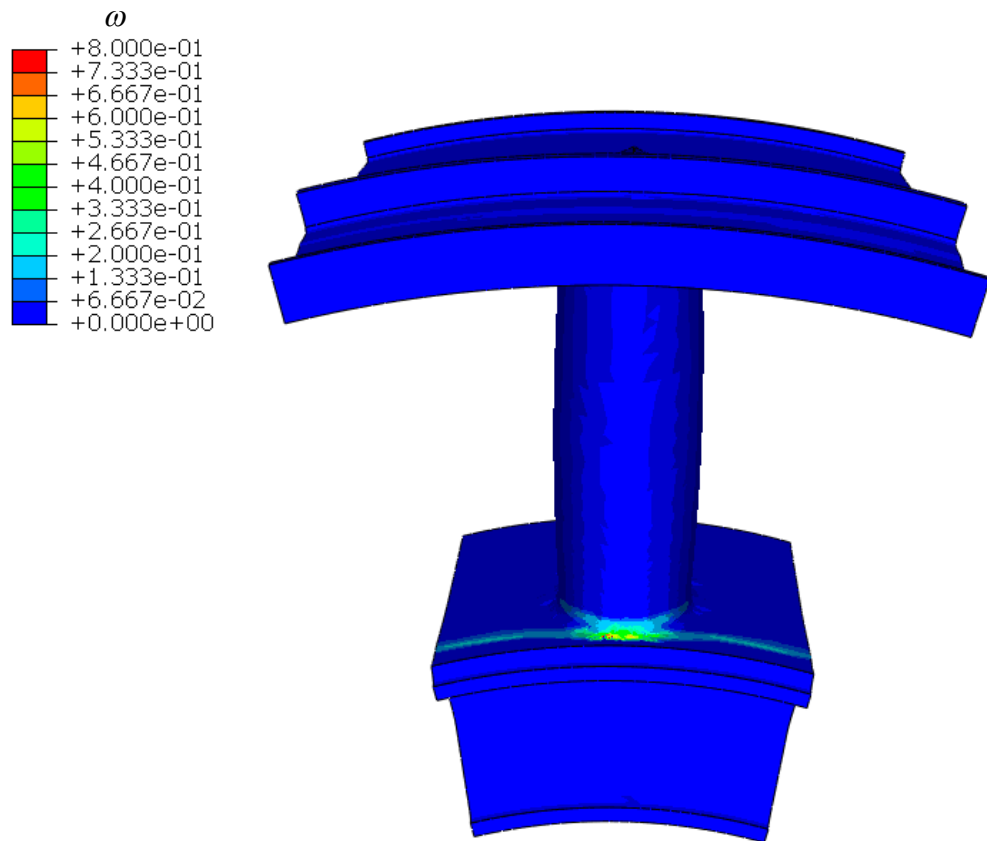


Figure 7.13: Peak damage (ω) around the bottom of the front of the spoke

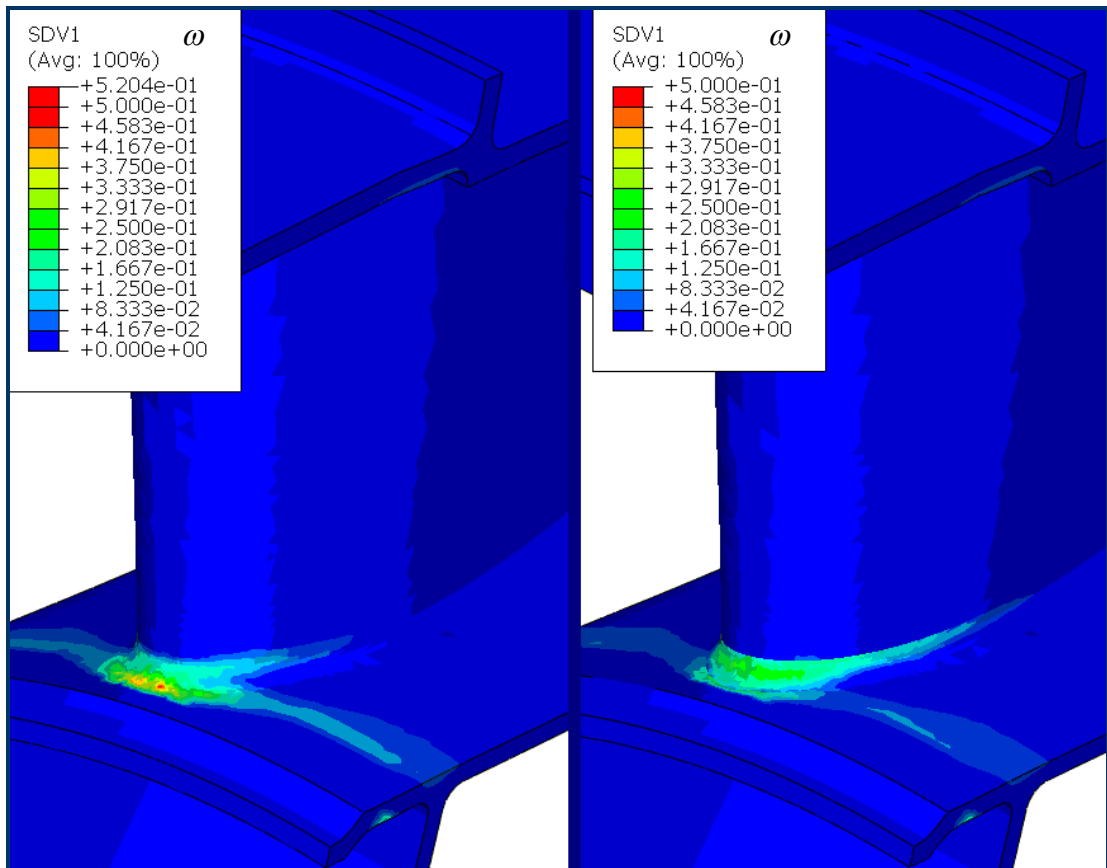


Figure 7.14: Creep damage after 100hrs, greater for non-welded (left)

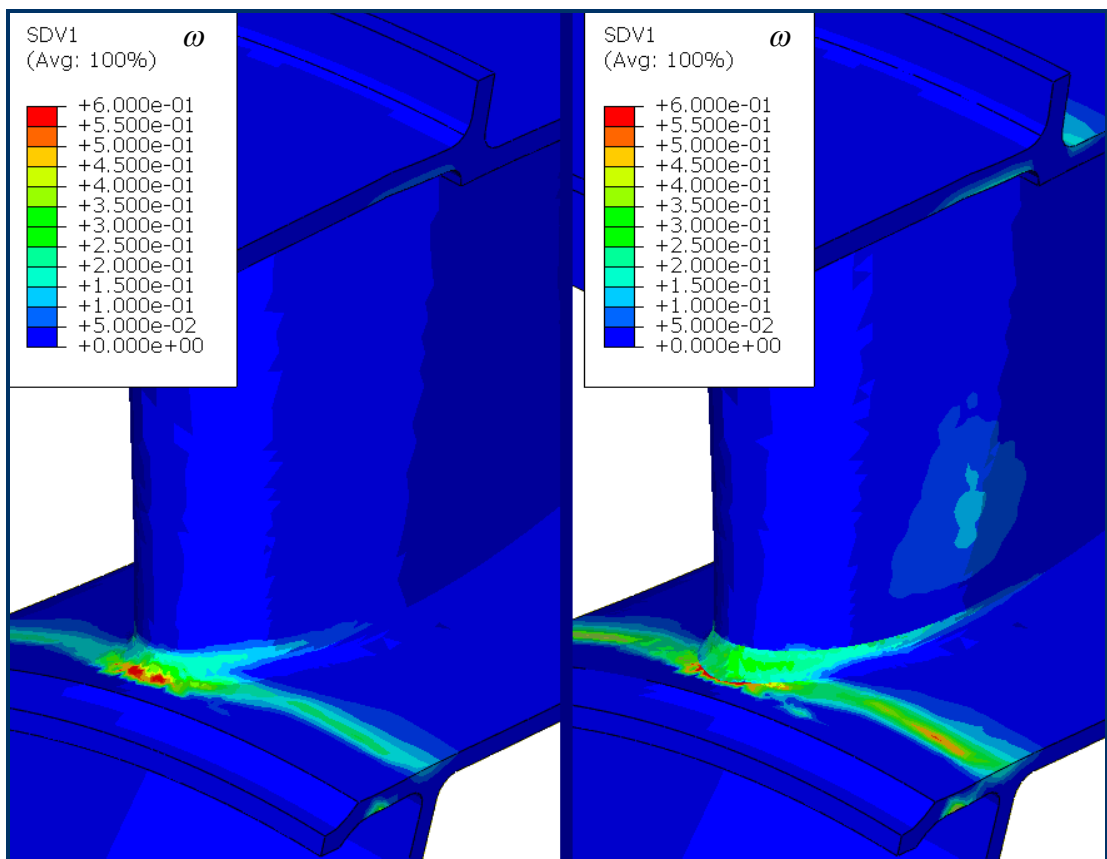


Figure 7.15: Creep damage at failure (welded case – right)

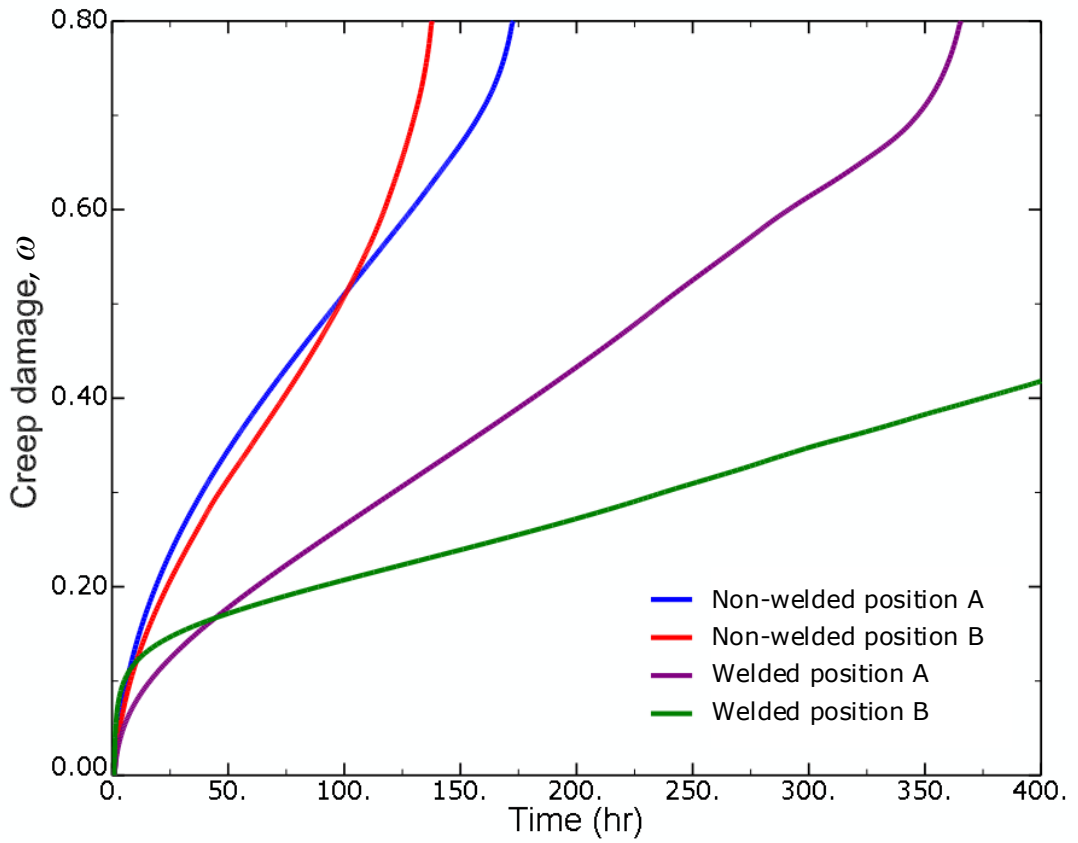


Figure 7.16: Creep damage evolution at positions A and B

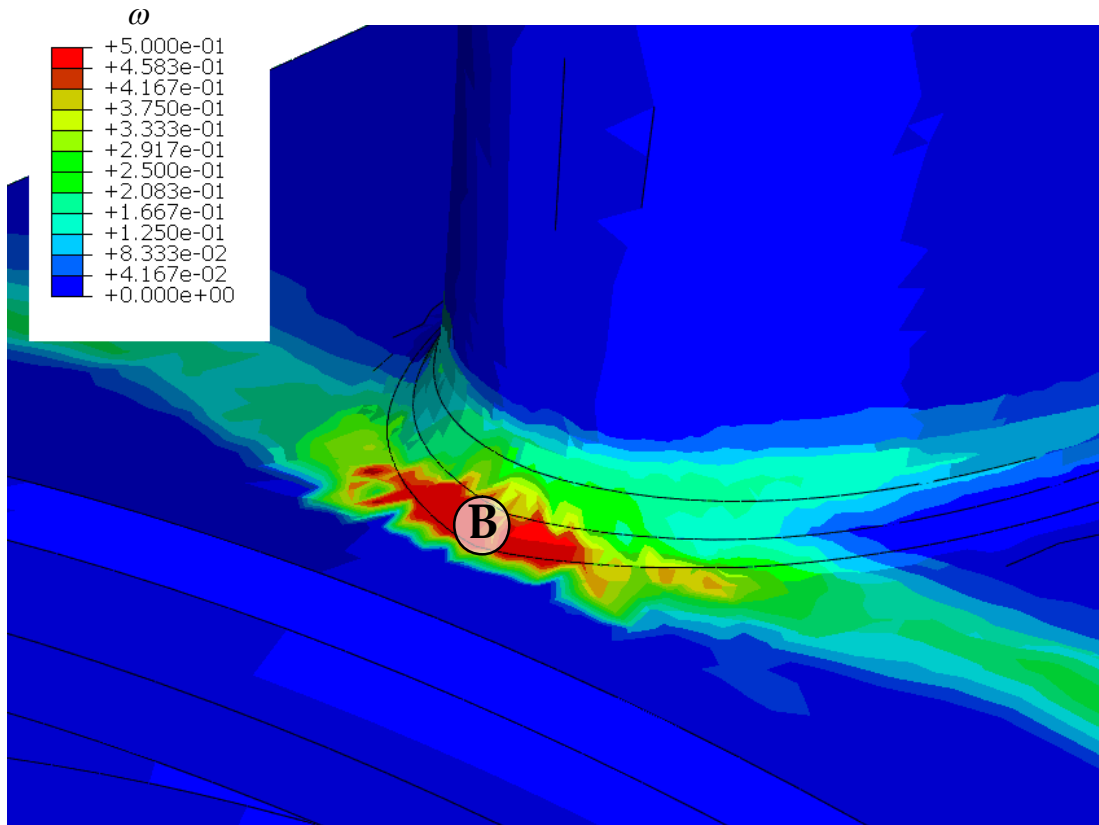


Figure 7.17: Damage, close-up of non-welded failure position (Position B)

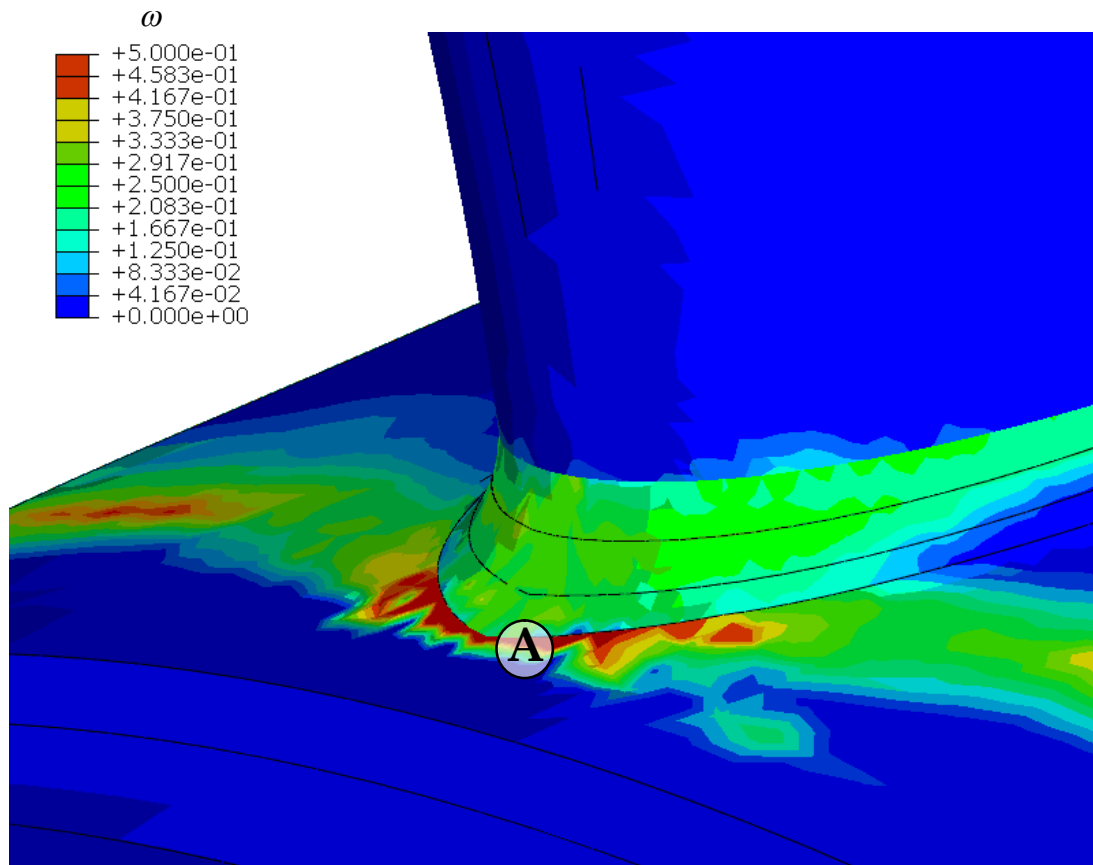


Figure 7.18: Damage, close-up of welded failure position (Position A)

Failure of the non-welded case was deemed to have occurred after 137hrs in the blend of the spoke-inner ring, where the weld would have been (Position B, Figure 7.17). Failure of the welded case occurred after 365hrs on the parent side (inner ring) of the weld-parent interface (Position A, Figure 7.18). The life of the welded case was increased due to the greater stress relaxation of the weld, which causes the failure location to shift into an area of non-welded material that experiences lower stress than the failure location of the non-welded case. However, it should be noted that the non-welded case uses properties obtained from wrought material, but this geometry cannot be manufactured without casting or welding. In addition, the peak creep strain is very high in the weld (Figure 7.12) and this may cause failure before the creep damage parameter indicates. Failure time determined by the time taken for maximum principal strain to reach 0.1 would give a non-welded

life of 53hrs and a welded life of 17hrs. The failure locations for this criterion are in the lower part of the blend for the non-welded case and in the upper part of the side of the blend (in the weld) for the welded case (Figure 7.19).

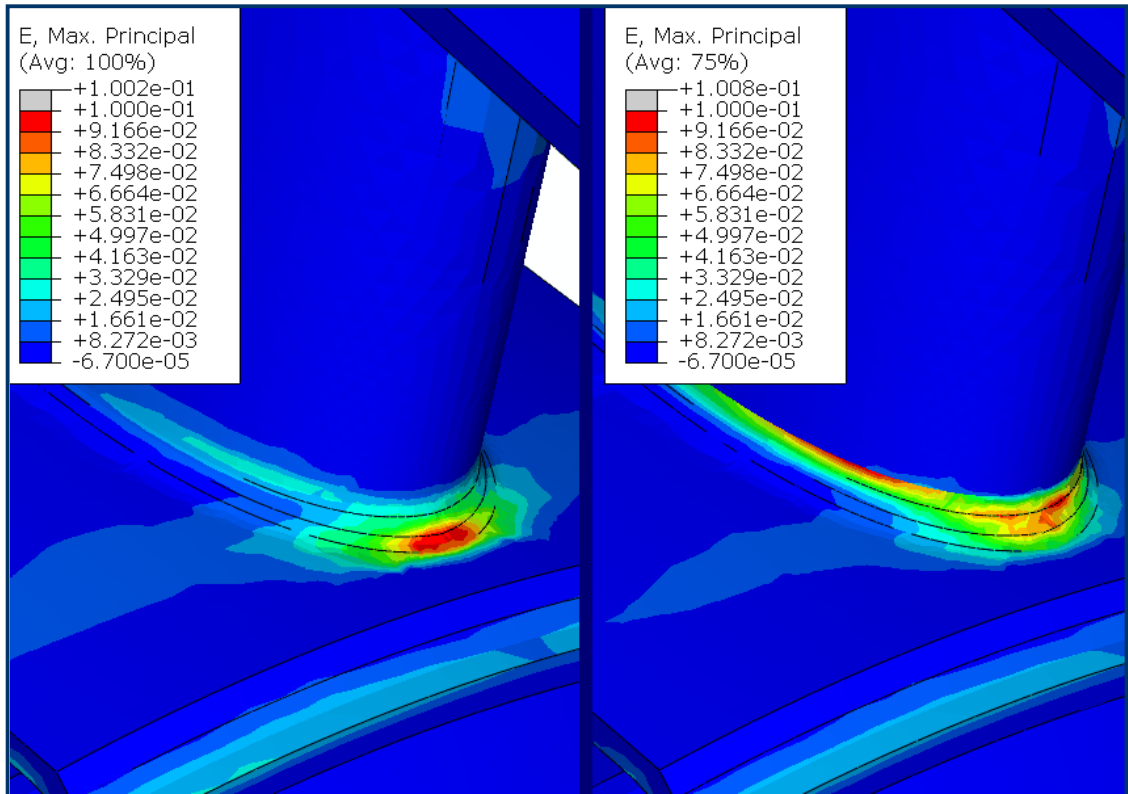


Figure 7.19: 0.1 maximum principal strain after 53hrs non-welded (left), 17hrs welded (right)

7.6 Finite element fatigue analysis

The FE mesh, weld position, boundary conditions, loading position and direction were the same as those used in the creep analysis described above. The fatigue cycles have a trapezoidal (1-1-1-1) form with a load frequency of 0.25Hz and a stress ratio of (approximately) zero, the same used during the material testing presented in Chapter 5 and the modelling of the fatigue tests in Chapter 6. This loading is used to replicate high temperature, fluctuating on-off load service conditions that are typically experienced by many structures of the type modelled here.

The fatigue FE analysis was nonlinear visco (transient, quasi-static) plastic so as to include the effect of creep, the accumulation of which was accounted for during the fatigue cycles using Norton's steady-state creep power law as used when modelling the fatigue tests in Chapter 6 [equation (6.1)]. Two steps were performed, each equivalent to one cycle; all results were taken from the second step, which is a more stable representation of subsequent cycles than the initial loading cycle.

The Smith, Watson and Topper (SWT) strain range parameter was used for predicting the fatigue life, as introduced in Chapter 6 [equation (6.9)]. The values of maximum stress, strain range and Young's modulus, taken from the FE models, were converted to SWT strain range and read into the lifing curve (Figure 6.29).

Below are the results from fatigue FE analyses with and without a weld for a maximum (on-load) applied load of 250kN.

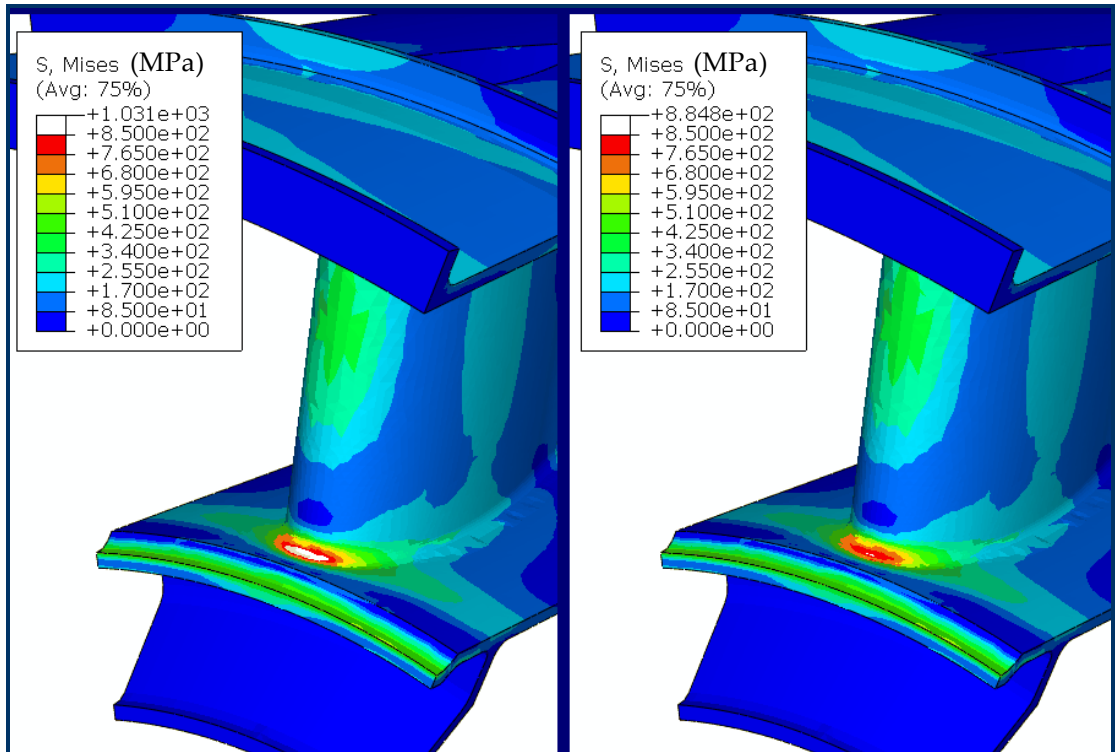


Figure 7.20: von Mises stress distribution at maximum load (welded case – right)

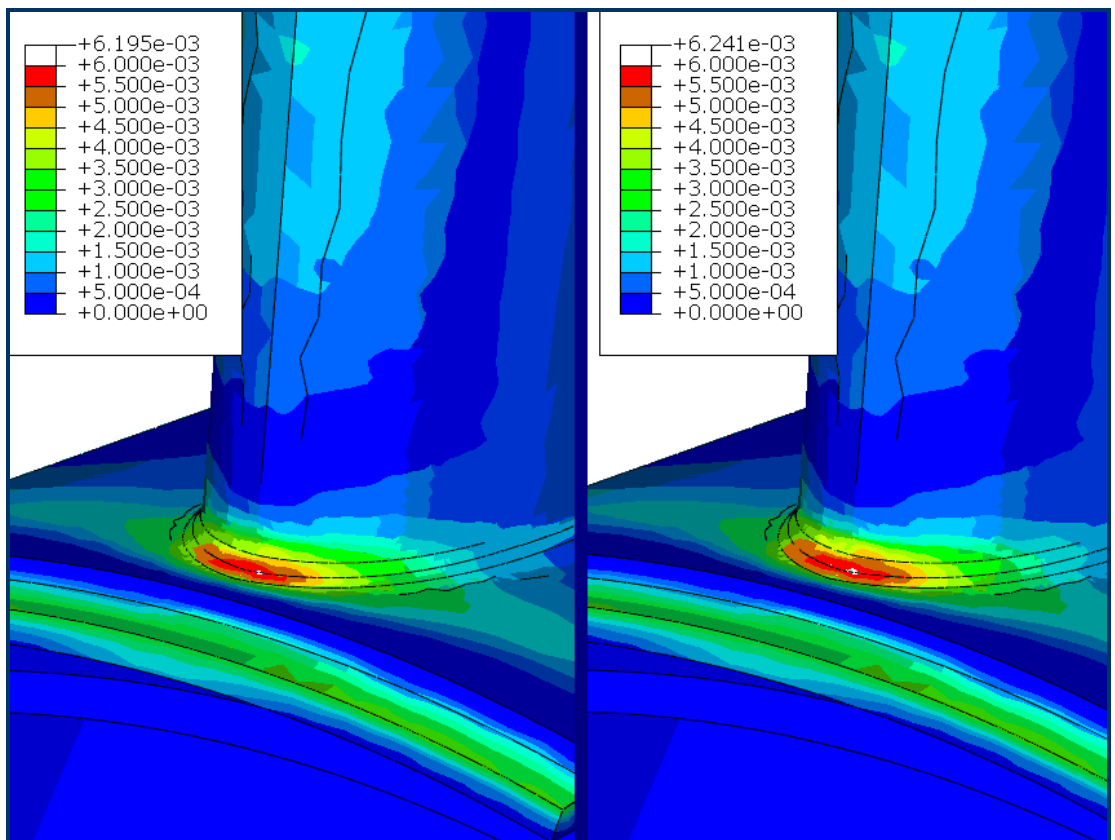


Figure 7.21: SWT distribution (welded case – right)

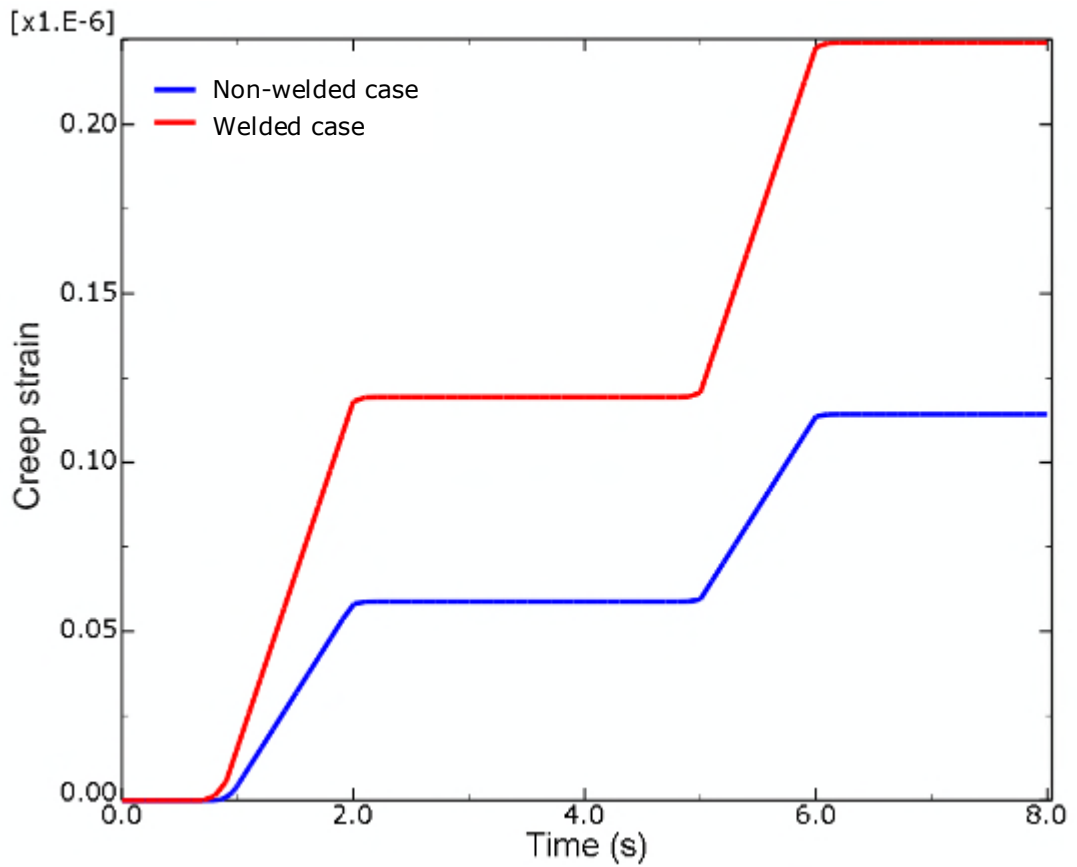


Figure 7.22: Creep strain history at peak position

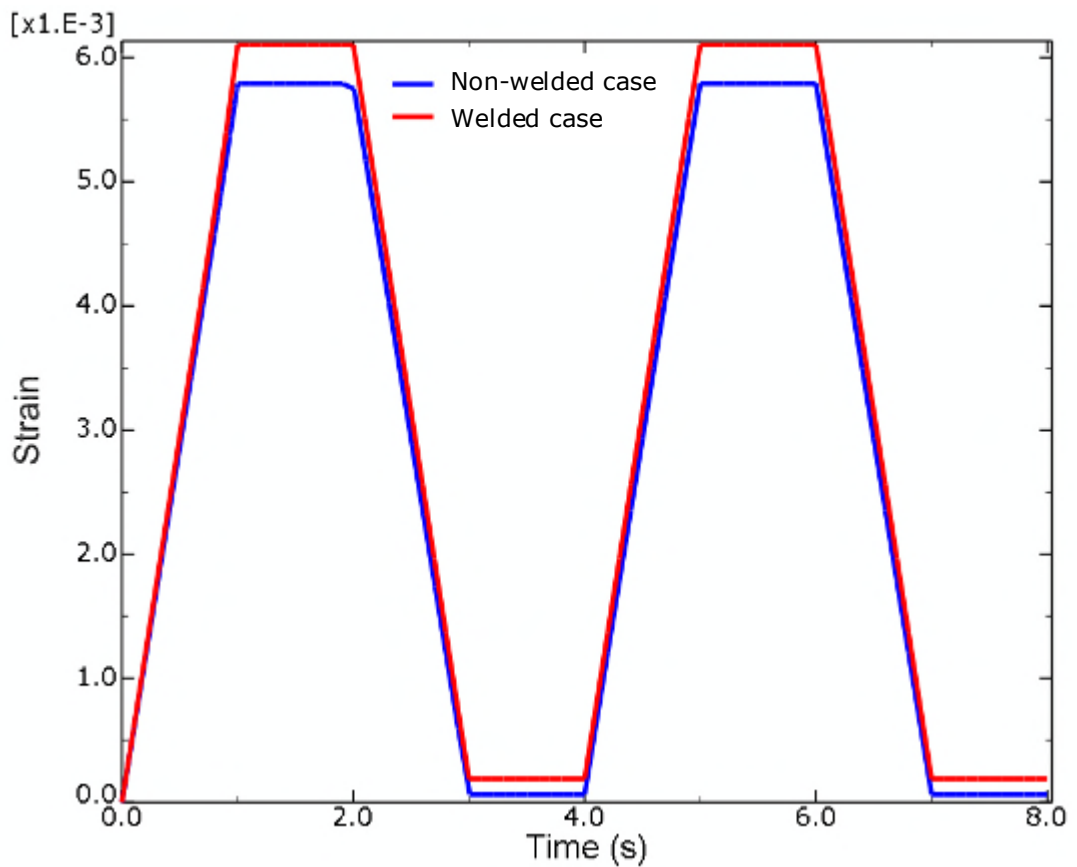


Figure 7.23: Maximum principal strain history at peak position

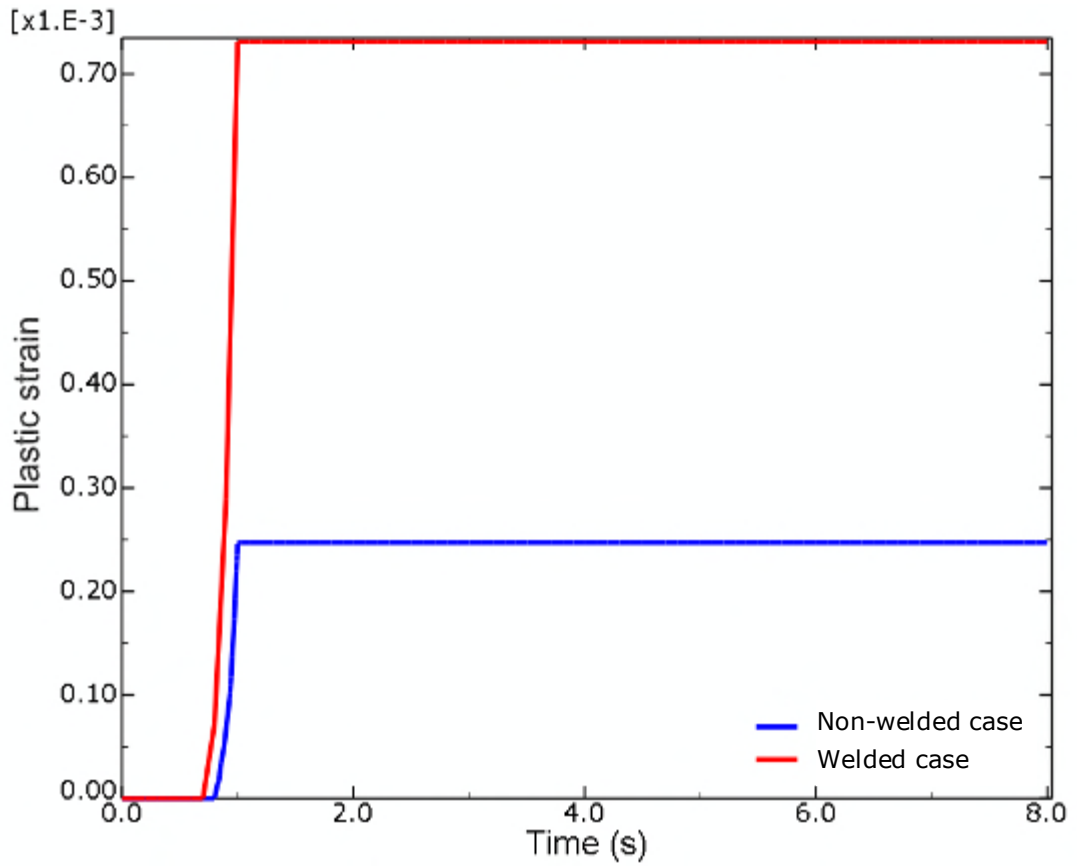


Figure 7.24: Equivalent plastic strain history at peak position

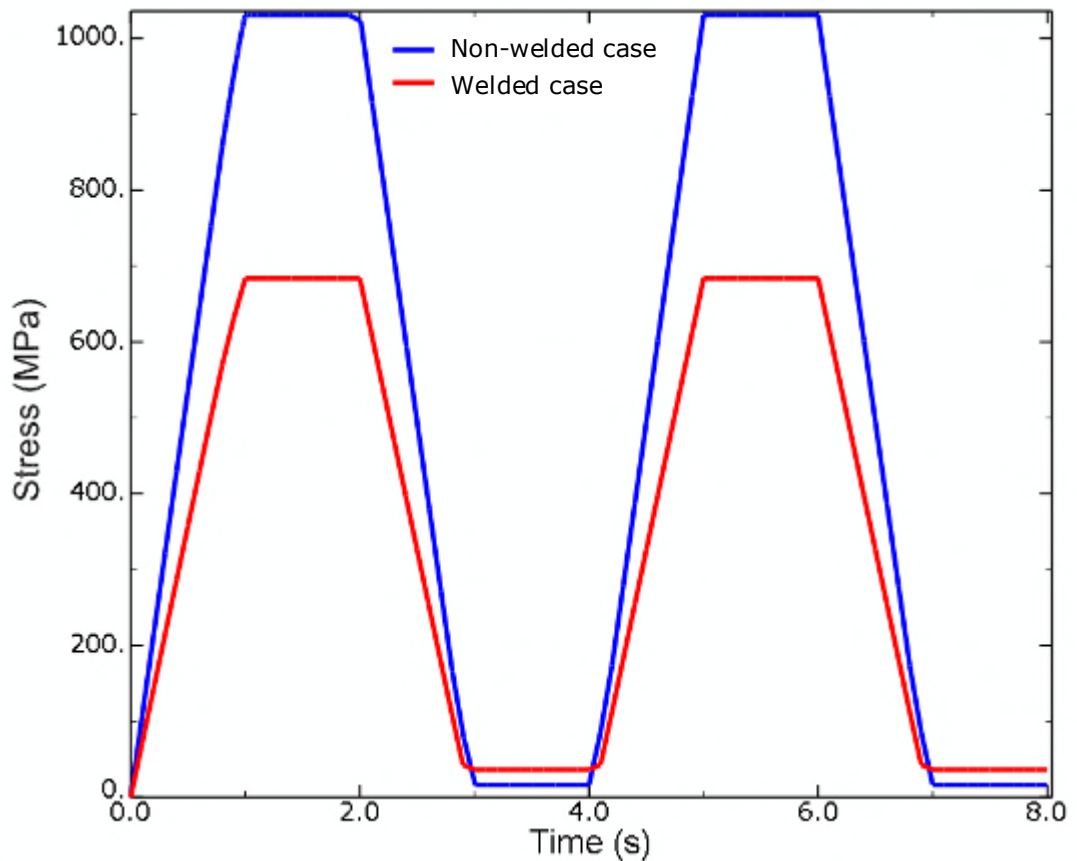


Figure 7.25: von Mises stress history at peak position

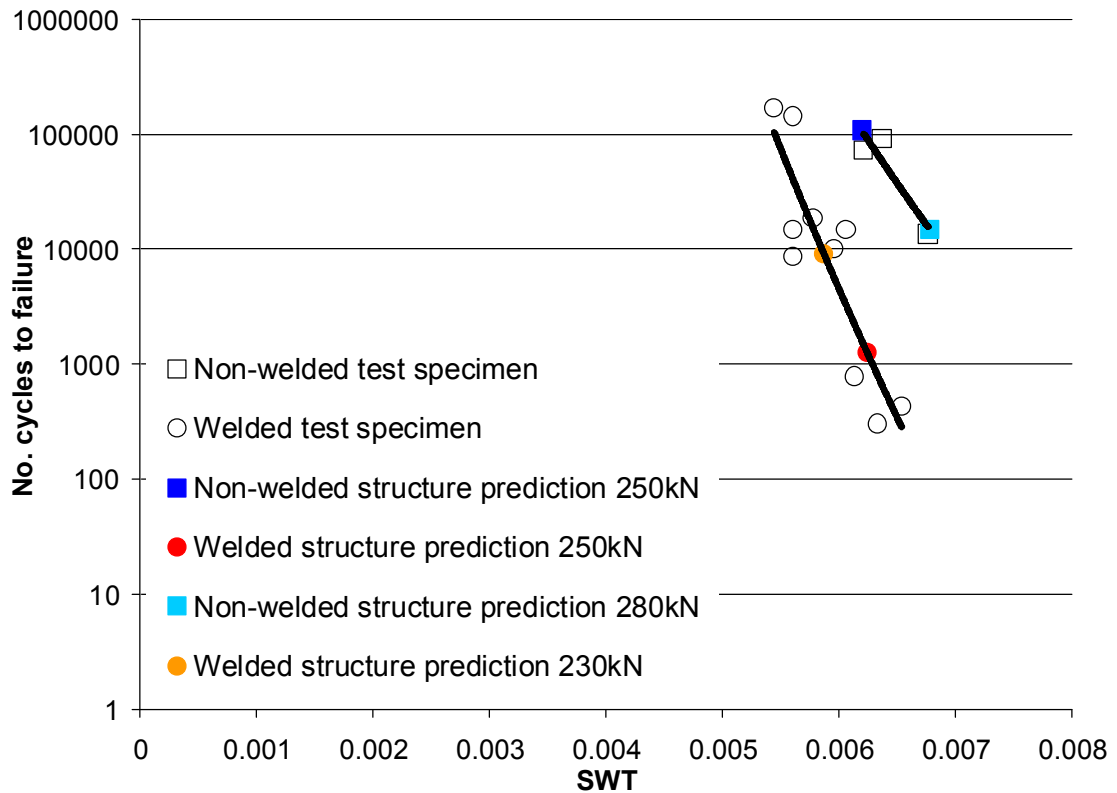


Figure 7.26: Predicted number of cycles to failure for FE-calculated SWT

Since there is only a short period of hold during each fatigue cycle, little creep and subsequent stress relaxation occurs in either the welded or the non-welded case, however the welded material does creep at a higher rate (see Figures 7.22-7.25). Plastic yielding is present during the first cycle and then this stabilises due to material hardening (Figure 7.24). The welded material yields more and is unable to support as high a stress as the non-welded material due to its lower yield stress (Figures 7.20 and 7.24-7.25), therefore it also strains more (Figure 7.23 and Figure 7.24). The welded material also has a higher residual stress upon the release of the load (Figure 7.25).

The predicted location of failure occurs in the blend region between the spoke and the inner ring in both cases, shown by the highest value of SWT in Figure 7.21. This is also the site of the weld. The value of SWT is only

slightly higher (<1% increase) for the welded case since the slightly higher strain range is countered by the lower peak stress reached and the lower Young's modulus of the welded material. When the FE-calculated values of SWT are compared with those obtained from the test specimens, a life prediction of 108300 cycles is obtained for the non-welded case, and just 1260 cycles for the welded case (Figure 7.26). This marked reduction in life is expected due to the lower fatigue properties of the welded material at high temperature, as discussed in Chapter 5. To give an expected life of approximately 10000 cycles for the welded case, the applied load would need to be reduced by 8% to 230kN. To give a similar life for the non-welded case (using wrought material properties as discussed in section 7.5), a load of 280kN could be applied, which is an increase of 12% from the original load and over 20% higher than the load for the equivalent welded case (Figure 7.26).

7.7 Conclusion

The material properties determined in Chapter 6 were applied to a more complicated generic spoke structure, and established lifing techniques were used along with FE analyses, to demonstrate how to evaluate the effects of a weld on the life of a structure.

The depleted high temperature fatigue properties of the welded IN718 material had a negative effect on the high temperature fatigue life of the structure (reducing the life by two orders of magnitude). The effect of welding on the life of the structure under constant loading at high temperature was found to be more difficult to evaluate due to significant stress relaxation. The predicted failure location was affected by the weld in the constant load case but not in the fatigue load case. Failure would

normally be expected to occur in the region of greatest stress but due to significant stress relaxation in the constant load welded case, the failure location shifted out of this region and into the stronger surrounding non-welded material.

Conclusions and future work

The overall aim behind the work presented in this thesis was to gain and apply an understanding of the mechanical effects of welding, in order to mitigate distortions that had previously hampered uniaxial testing of TIG butt-welded, thin rectangular section, nickel-base superalloy INCONEL 718. With this aim achieved, better test data could be obtained, leading to more reliable material data for IN718 welds, which can be used for more accurate life assessments for shell structures and components, with a particular emphasis on those operating at high temperature.

8.1 Conclusions

Life assessment covering creep and high temperature fatigue has been reported for non-welded IN718, but assessment for welded thin-section structures is more complex due to the residual stresses, deformations and material microstructural changes caused by the welding process. In particular, out-of-plane weld distortions compromise uniaxial testing and complicate life assessment. Therefore, finite element (FE) simulations of the arc welding process were performed (Chapter 3) using user subroutines in ABAQUS with the purpose of trying to understand the development of weld-induced distortions and reduce their prevalence. The models developed are capable of calculating the evolution of stress and deformation, and predicting the residual stresses and distortions that occur as a result of the welding process. Sequentially-coupled nonlinear thermal and elastic-plastic analyses were employed and successfully validated using experimental and numerical results from literature. The heat input from the welding torch was modelled using a simplified heat source approach.

The simulations have added complexity, particularly since the effects of restraint are considered, and the addition of filler is included, along with the formation of the typical weld underbead that forms during the welding of thin plates. The need for a three-dimensional model was justified since a plane strain assumption is often unsuitable and inaccurate for modelling transient welding with multiple distortions modes occurring simultaneously. The importance of including the effects of plastic strain relaxation was also highlighted in terms of residual stress and distortion. For a simple two-dimensional case, it was found that the residual stress in the molten region was significantly reduced and the direction of angular distortion was reversed when plastic strain relaxation was accounted for. The FE welding simulations were used to determine the effects of some distortion mitigation techniques. The complications of presetting and the effects of using different types of clamping, and the possible heat loss to a welding jig or backing plate were analysed. Presetting did not reduce the amount of distortion predicted but clamping was more successful.

By using the FE welding simulations (from Chapter 3), it was decided that an efficient way of reducing weld-induced distortions was to only weld small plates that were just large enough to form one tensile test specimen. The small size increases the relative stiffness of the plates, and reduces the welding time and therefore the total time for which nonuniform thermal contraction exists, which is the driving force of the distortions. Unlike other methods of distortion prevention, such as those involving trailing heat sources or sinks, this solution does not modify the effects of the welding process on the thermal history of the material and so is ideal for test specimens designed to compare welded and non-welded material. Since the plates remained flat after welding, the stress-concentrating weld bead excess could be removed by a finishing process. This step is important since the

sharp fillet radii of the weld beads result in high stress concentrations at the weld bead and parent interface. This theoretical welding procedure was put into practice during the welding and specimen manufacture covered in Chapter 4 and resulted in TIG butt-welds free of distortion as predicted by the numerical models.

In Chapter 5, the results of uniaxial tensile, creep and high temperature fatigue tests on both welded and non-welded IN718 specimens are presented. The main objectives of the testing were to determine the effect the welds have on life, analyse any differences in their failure behaviour, and obtain material properties for input into more advanced FE analyses for welding simulation (Chapter 3) and life prediction purposes (Chapter 6 and Chapter 7).

Tensile tests at temperatures from 20°C to 1000°C resulted in both the 0.2% proof stress and the ultimate strength of most of the welded specimens exceeding 90% of the values of the non-welded specimens. However, the strains to failure for the welded specimens were significantly less than those of the non-welded specimens.

Constant load creep tests at 620°C also showed noticeably lower total strains to failure for the welded specimens than the non-welded specimens. The time to failure for a given load was also markedly less for the welded specimens. The welded specimen creep failures occurred in a coarse-grained heat-affected zone (HAZ) where large grains were unable to accommodate large straining by grain boundary sliding, leading to premature fracture.

Low cycle fatigue tests at 620°C, with a trapezoidal (1-1-1-1) form, load frequency of 0.25 Hz and zero stress ratio, resulted in lower failure times for

the welded specimens than the corresponding non-welded values for any given nominal stress. This was attributed to the presence of brittle Laves phase at fine-grained HAZ boundaries, which is known to decrease ductility and life.

The lower performance of the welded plates was attributed to the microstructural differences when compared with the non-welded material. Large columnar dendritic grains in the weld fusion zone (FZ) and the presence of brittle Laves phase here and at fine-grain HAZ grain boundaries, along with large grains in an adjacent coarse-grain HAZ, decrease ductility, and creep and fatigue life.

In conclusion, it was found that IN718 welds exhibit significantly lower ductility than the parent material and although welded IN718 shows comparatively little loss of tensile strength, its creep and high temperature fatigue properties are severely compromised.

The results of the testing presented in Chapter 5 showed that IN718 weld material exhibits noticeably depleted mechanical properties. In Chapter 6, the stress-strain relationships and mechanical properties of the IN718 weld material were calculated using the test measurements and determining what the behaviour of the weld must have been in order to give the measured test results. FE verification of the material properties was conducted by modelling the uniaxial tensile and creep tests to check the accuracy of the material properties assigned to the weld region, and very good agreement was obtained. A creep continuum damage mechanics approach was suggested in order to capture the significant tertiary creep that was observed during the testing programme, and obtain more accurate failure times. Determination of the necessary material constants required for the damage

equations was presented. The high temperature uniaxial fatigue tests were also accurately modelled using FE analysis for all the load cases used during the testing, for both the butt-welded and non-welded specimens. The modelling technique was validated by comparing the FE-calculated strain results with the measured test results. A Smith, Watson and Topper (SWT) strain range parameter was introduced and the FE-calculated values were found to compare well with values determined using the test data, validating the suitability of this life assessment method. The modelling technique, the material properties obtained and the SWT values calculated in Chapter 6 can be used to estimate the life of structures with more complex geometry and loading conditions, such as the case study presented in Chapter 7.

In Chapter 7, a life assessment case study of a welded feature in an IN718 generic spoke structure was conducted using three-dimensional, quasi-static elastic-plastic and creep FE analyses. The effect of including a weld (i.e. welded material) in a critical region was investigated for both constant (creep) and cyclic (creep-fatigue) loading conditions at 620°C. Creep damage and SWT strain parameter lifing methods were used, based upon the material properties and lifing validation discussed in Chapter 6. The depleted high temperature fatigue properties of the welded IN718 material had a negative effect on the high temperature fatigue life of the structure (reducing the life by two orders of magnitude). The effect of welding on the life of the structure under constant loading at high temperature was found to be more difficult to evaluate due to significant stress relaxation. The predicted failure location was affected by the weld in the constant load case but not in the fatigue load case. Failure would normally be expected to occur in the region of greatest stress but due to significant stress relaxation in the constant load welded case, the failure location shifted out of this region and into the surrounding stronger non-welded material.

8.2 Future work

In the work presented in this thesis, the welded specimens were modelled using two materials, parent (non-weld) and weld. However, it was observed that IN718 welds have two types of HAZ (one coarse grain and one fine grain) along with the FZ. The two-region approximation of the welded specimens was deemed appropriate but an investigation into the determination of the properties of all of the distinct regions should be carried out to assess their influence in detail. For example, nanoindentation [134] or small punch testing techniques may be used for this purpose [135]. Any interaction effects between these additional regions should also be investigated to help improve the models if necessary. In addition, the weld material properties were assumed to be isotropic and the nature of the weld solidification suggests an element of anisotropy. If the above topics were investigated and the results implemented then more reliable life assessments of real welded components could be made. It is also necessary to validate the life assessments using component tests.

The modelling and life assessment of component repair welds or 'green welds' (welds that are not postweld heat-treated and the substrate is welded in the precipitation heat-treated condition) is another area of work that is also of interest to the engineering industry.

The creep and high temperature fatigue material testing could be expanded to different temperatures and loading conditions, or into the high-cycle regime. Many components are also subject to multiaxial loading and testing of this nature is therefore important. Crack growth tests and their modelling could be performed in order to assess the effects of oxidation and/or creep-fatigue interaction, and to include crack propagation time into life predictions. Microstructure evolution/degradation could also be included.

Full-scale weld modelling of components is another topic that is currently receiving the attention of researchers. With the ever-increasing computer capability available, the weld models may also be expanded to include weld pool phenomena and microstructure evolution (such as grain growth, for example). The weld model results can also be fed into heat treatment models, where the material properties evolve and the residual stresses relax and redistribute. Machining processes can also be modelled and the final results, covering the entire manufacturing process, may be used as input into life assessment analyses.

References

- [1] **Y. Song, A.A. Becker, T.H. Hyde, P. Andrews, and P. Spiller**, Mechanical Properties of INCO718 Superalloy at High Temperatures, in *Proceedings of the International Conference on Metal Fabrication and Welding Technology (METFAB)*, Edited by A. A. Becker, Nottingham, UK, pp. 233-244, 2003.
- [2] **D. Dye**, *Mechanical effects arising from the welding of superalloys*, PhD Thesis, University of Cambridge, UK, pp. 154, 2000.
- [3] **T. Sanders, R. Frishmuth, and G. Embley**, Temperature Dependent Deformation Mechanisms of Alloy 718 in Low Cycle Fatigue, *Metallurgical and Materials Transactions A*, vol. 12, pp. 1003-1010, 1981.
- [4] **Y. Song, A.A. Becker, T.H. Hyde, and W. Sun**, Effects of welding distortion and bead geometry on the stress concentration of TIG-butt welded Inco718 sheets subjected to creep, in *Proceedings of the International Conference on Metal Fabrication and Welding Technology (METFAB)*, Edited by A. A. Becker, Nottingham, UK, pp. 95-106, 2003.
- [5] **H.D. Hibbitt and P.V. Marcal**, A Numerical, Thermo-mechanical Model for the Welding and Subsequent Loading of a Fabricated Structure, *Computers & Structures*, vol. 3, pp. 1145-1174, 1973.
- [6] *Welding Handbook*, vol. 2: Welding Processes, 8th ed. Miami, FL, USA: American Welding Society (AWS), 1991.
- [7] **K. Masubuchi**, *Analysis of welded structures: residual stresses, distortion, and their consequences* 1ed. Oxford: Pergamon Press, 1980.
- [8] **S. Sahin, M. Toparli, I. Ozdemir, and S. Sasaki**, Modelled and measured residual stresses in a bimaterial joint, *Journal of Materials Processing Technology*, vol. 132, pp. 235-241(7), 2003.
- [9] **B. Taljat, B. Radhakrishnan, and T. Zacharia**, Numerical analysis of GTA welding process with emphasis on post-solidification phase transformation effects on residual stresses, *Materials Science and Engineering A*, vol. 246, pp. 45-54, 1998.
- [10] **B. Brickstad and B.L. Josefson**, A parametric study of residual stresses in multi-pass butt-welded stainless steel pipes, *International Journal of Pressure Vessels and Piping*, vol. 75, pp. 11-25, 1998.

- [11] **J.R. Dydo, H.R. Castner, and K. Koppenhoefer**, Guidelines for Control of Distortion in Thin Ship Structures, Edison Welding Institute (Report 42372GDE/R/99 for Navy Joining Center), Ohio 1999.
- [12] **E. Bendek, I. Lira, M. Francois, and C. Vial**, Uncertainty of residual stresses measurement by layer removal, *International Journal of Mechanical Sciences*, vol. 48, pp. 1429-1438, 2006.
- [13] **P. Pasquale, W. Pfeiffer, and W. Burget**, Numerical and experimental investigation on residual stresses in multi-run heavy section high strength welded joints, in *Mathematical Modelling of Weld Phenomena 4*, Edited by H. Cerjak, Graz, Austria: The Institute of Materials, pp. 620-630, 1998.
- [14] **D.E. Rodgers and P.R. Fletcher**, The Determination of Internal Stresses from the Temperature History of a Butt Welded Pipe, *Welding Journal Research Supplement*, pp. 4-7, 1938.
- [15] **Y.V.L.N. Murthy, G.V. Rao, and P.K. Iyer**, Numerical simulation of welding and quenching processes using transient thermal and thermo-elasto-plastic formulations, *Computers & Structures*, vol. 60, pp. 131-154, 1996.
- [16] **D. Dye, O. Hunziker, and R.C. Reed**, Numerical analysis of the weldability of superalloys, *Acta Materialia*, vol. 49, pp. 683-697, 2001.
- [17] **R.H. Leggatt**, Residual stresses in welded structures, *International Journal of Pressure Vessels and Piping*, vol. 85, pp. 144-151, 2008.
- [18] **D. Deng, Y. Luo, H. Serizawa, M. Shibahara, and H. Murakawa**, Numerical simulation of residual stress and deformation considering phase transformation effect, *Transactions of the JWRI*, vol. 32, pp. 325-333, 2003.
- [19] **P. Dong and F.W. Brust**, Welding Residual Stresses and Effects on Fracture in Pressure Vessel and Piping Components: A Millennium Review and Beyond, *Journal of Pressure Vessel Technology*, vol. 122, pp. 329-338, 2000.
- [20] **A. Pilipenko**, *Computer Simulation of Residual Stress and Distortion of Thick Plates in Multielectrode Submerged Arc Welding: Their Mitigation Techniques*, PhD Thesis, Norwegian University of Science and Technology, Trondheim, Norway, pp. 222, 2001.

- [21] **E. Friedman**, Thermomechanical analysis of the welding process using the finite element method, *ASME Journal of Pressure Vessel Technology*, vol. 97, pp. 206-213, 1975.
- [22] **Y. Ueda and T. Yamakawa**, Analysis of Thermal Elastic-plastic Stress and Strain During Welding by Finite Element Method, *Transactions of the Japan Welding Society*, vol. 2, pp. 186-196, 1971.
- [23] **L.E. Lindgren**, Numerical modelling of welding, *Computer Methods in Applied Mechanics and Engineering*, vol. 195, pp. 6710-6736, 2006.
- [24] **A. Bachorski, M.J. Painter, A.J. Smailes, and M.A. Wahab**, Finite-element prediction of distortion during gas metal arc welding using the shrinkage volume approach, *Journal of Materials Processing Technology*, vol. 92-93, pp. 405-409, 1999.
- [25] **D. Camilleri, T. Comlekci, and T.G.F. Gray**, Computational prediction of out-of-plane welding distortion and experimental investigation, *The Journal of Strain Analysis for Engineering Design*, vol. 40, pp. 161-176, 2005.
- [26] **P. Mollicone, D. Camilleri, T.G.F. Gray, and T. Comlekci**, Simple thermo-elastic-plastic models for welding distortion simulation, *Journal of Materials Processing Technology*, vol. 176, pp. 77-86, 2006.
- [27] **C.L. Tsai, S.C. Park, and W.T. Cheng**, Welding Distortion of a Thin-Plate Panel Structure, *A.W.S. Welding Journal, Research Supplement*, vol. 78, pp. 156-165, 1999.
- [28] **H. Murakawa, Y. Luo, and Y. Ueda**, Inherent strain as an interface between computational welding mechanics and its industrial application, in *Mathematical Modelling of Weld Phenomena 4*, Edited by H. Cerjak: Institute of Materials, pp. 597-619, 1998.
- [29] **H. Nishikawa, H. Serizawa, and H. Murakawa**, Actual application of FEM to analysis of large scale mechanical problems in welding, *Science and Technology of Welding and Joining (UK)*, vol. 12, pp. 147-152, 2007.
- [30] **D. Camilleri, P. Mollicone, and T. Gray**, Computational methods and experimental validation of welding distortion models, *Proceedings of the Institution of Mechanical Engineers, Part L: Journal of Materials: Design and Applications*, vol. 221, pp. 235-249, 2007.

- [31] **D. Deng, H. Murakawa, and W. Liang**, Numerical simulation of welding distortion in large structures, *Computer Methods in Applied Mechanics and Engineering*, vol. 196, pp. 4613-4627, 2007.
- [32] **P. Durantou, J. Devaux, V. Robin, P. Gilles, and J.M. Bergheau**, 3D modelling of multipass welding of a 316L stainless steel pipe, *Journal of Materials Processing Technology*, vol. 153-154, pp. 457-463, 2004.
- [33] **M. Hamide and M. Bellet**, Adaptive Anisotropic Mesh Technique For Coupled Problems: Application To Welding Simulation, *AIP Conference Proceedings*, vol. 908, pp. 1561-1566, 2007.
- [34] **T.W. Greene and A.A. Holzbaur**, Controlled low-temperature stress relieving, *Welding Journal Research Supplement*, vol. 11, pp. 171-185, 1946.
- [35] **T.D. Huang, P. Dong, L.A. DeCan, and D.D. Harwig**, Residual Stresses and Distortions in Lightweight Ship Panel Structures, *Technology Review Journal*, vol. 11, pp. 1-26, 2003.
- [36] **F.W. Brust and E.F. Rybicki**, A computational model of backlay welding for controlling residual stresses in welded pipes, *ASME Journal of Pressure Vessel Technology*, vol. 103, pp. 226-232, 1981.
- [37] **Q. Guan, D.L. Guo, C.Q. Li, and R.H. Leggatt**, Low stress non-distortion (LSND) welding -a new technique for thin materials, *Welding in the World (UK)*, vol. 33, pp. 160-167, 1994.
- [38] **E.M. van der Aa, M.J.M. Hermans, and I.M. Richardson**, Conceptual model for stress and strain development during welding with trailing heat sink, *Science and Technology of Welding and Joining (UK)*, vol. 11, pp. 488-495, 2006.
- [39] **D.A. Price, S.W. Williams, A. Wescott, C.J.C. Harrison, A. Rezai, A. Steuwer, M. Peel, P. Staron, and M. Kocak**, Distortion control in welding by mechanical tensioning, *Science and Technology of Welding and Joining (UK)*, vol. 12, pp. 620-633, 2007.
- [40] **P. Michaleris and X. Sun**, Finite element analysis of thermal tensioning techniques mitigating weld buckling distortion, *Welding Journal (USA)*, vol. 76, pp. 451-457, 1997.
- [41] **Y.P. Yang, P. Dong, J. Zhang, and X. Tian**, A hot cracking mitigation technique for TIG welding of high strength aluminum alloys, *Welding journal research supplement*, vol. 79, pp. 9-17, 2000.

- [42] **G.A. Taylor, M. Hughes, N. Strusevich, and K. Pericleous**, Finite volume methods applied to the computational modelling of welding phenomena, *Applied Mathematical Modelling*, vol. 26, pp. 311-322(12), 2002.
- [43] **M. Do-Quang and G. Amberg**, Modeling of Time-Dependent 3D Weld Pool Due to a Moving Arc, in *Modeling, Simulation and Optimization of Complex Processes*, Edited by H. G. Bock, E. A. Kostina, H. X. Phu, and R. Rannacher, Berlin: Springer, pp. 127-138, 2005.
- [44] **D. Dye, O. Hunziker, S.M. Roberts, and R.C. Reed**, Modeling of the mechanical effects induced by the tungsten inert-gas welding of the IN718 superalloy, *Metallurgical and Materials Transactions A - Physical Metallurgy and Materials Science*, vol. 32A, pp. 1713-1725, 2001.
- [45] **W. Jiang, K. Yahiaoui, F.R. Hall, and T. Laoui**, Finite element simulation of multipass welding: full three-dimensional versus generalized plane strain or axisymmetric models, *The Journal of Strain Analysis for Engineering Design*, vol. 40, pp. 587-598(12), 2005.
- [46] **J. Goldak, A. Chakravarti, and M. Bibby**, A New Finite Element Model for Welding Heat Sources, *Metallurgical Transactions B*, vol. 15B, pp. 299-305, 1984.
- [47] **D. Rosenthal**, Mathematical theory of heat distribution during welding and cutting, *Welding Journal Research Supplement*, vol. 20, pp. 220-234, 1941.
- [48] **D. Rosenthal**, The Theory of Moving Sources of Heat and Its Application to Metal Treatments, *Transactions of the ASME*, vol. 68, pp. 849-866, 1946.
- [49] **V. Pavelic, R. Tanbakuchi, O.A. Uyehara, and P.S. Myers**, Experimental and Computed Temperature Histories in Gas Tungsten-Arc Welding of Thin Plates *Welding Journal Research Supplement*, vol. 48, pp. 295-305, 1969.
- [50] **A. Lundbäck**, *Finite Element Modelling and Simulation of Welding of Aerospace Components*, Licentiate Thesis, Luleå University of Technology, Sweden, 2003.
- [51] **L.-E. Lindgren, H. Runnemalm, and M.O. Näsström**, Simulation of multipass welding of a thick plate, *International Journal for Numerical Methods in Engineering*, vol. 44, pp. 1301-1316, 1999.

- [52] **P.J. Bouchard**, Validated residual stress profiles for fracture assessments of stainless steel pipe girth welds, *International Journal of Pressure Vessels and Piping*, vol. 84, pp. 195-222, 2007.
- [53] **W. Cheng**, *In-Plane shrinkage strains and their effects on welding distortion in thin-Wall structures*, PhD Thesis, Ohio State University, USA, pp. 268, 2005.
- [54] **N.R. Mandal**, *Welding and Distortion Control*. New Dehli: Narosa Publishing House, 2004.
- [55] **P. Michaleris and A. DeBiccari**, Prediction of welding distortion, *Welding Journal (USA)*, vol. 76, pp. 172-181, 1997.
- [56] *ASM Handbook*, vol. 6: Welding, Brazing, and Soldering. Materials Park, Ohio, USA: ASM International, 1993.
- [57] **M. Ericsson**, *Simulation of robotic TIG-welding*, Licentiate Thesis, University of Trollhättan, Sweden, 2003.
- [58] **K.Y. Benyounis and A.G. Olabi**, Optimization of different welding processes using statistical and numerical approaches - A reference guide, *Advances in Engineering Software*, vol. 39, pp. 483-496, 2008.
- [59] **M. Kartal, R. Molak, M.Turski, S. Gungor, M.E. Fitzpatrick, and L. Edwards**, Determination of Weld Metal Mechanical Properties Utilising Novel Tensile Testing Methods, *Applied Mechanics and Materials*, vol. 7-8, pp. 127-132, 2007.
- [60] **W. Sun**, *Creep of service-aged welds*, PhD Thesis, University of Nottingham, UK, pp. 411, 1996.
- [61] **S. Kou**, *Welding Metallurgy*, 2nd ed. Hoboken, New Jersey, USA: John Wiley and Sons, 2003.
- [62] **O. Grong**, *Metallurgical Modelling of Welding*. London, UK: The Institute of Materials, 1997.
- [63] **S. Kou**, Solidification and liquation cracking issues in welding, *JOM Journal of the Minerals, Metals and Materials Society*, vol. 55, pp. 37-42, 2003.
- [64] **H. Yoshimura and K. Winterton**, Solidification mode of weld metal in inconel 718, *Welding Journal Research Supplement*, vol. 51, pp. 132-137, 1972.

- [65] **K. Easterling**, *Introduction to the physical metallurgy of welding*, 2nd ed: Butterworth-Heinemann, 1992.
- [66] **S. Lampman**, *Weld Integrity and Performance*. Materials Park, Ohio, USA: ASM International, 1997.
- [67] **S. Ghosh, S. Yadav, and G. Das**, Study of standard heat treatment on mechanical properties of Inconel 718 using ball indentation technique, *Materials Letters*, vol. 62, pp. 2619-2622, 2008.
- [68] **K.-M. Chang**, Metallurgical Control of Fatigue Crack Propagation in Alloy 718, in *Superalloys 718, 625 and Various Derivatives*, Edited by E.A.Loria: The Minerals, Metals & Materials Society, pp. 447-456, 1991.
- [69] **L. Xiao, D.L. Chen, and M.C. Chaturvedi**, Effect of boron on fatigue crack growth behavior in superalloy IN 718 at RT and 650°C, *Materials Science and Engineering: A*, vol. 428, pp. 1-11, 2006.
- [70] **A. Thomas, M. El-Wahabi, J.M. Cabrera, and J.M. Prado**, High temperature deformation of Inconel 718, *Journal of Materials Processing Technology*, vol. 177, pp. 469-472, 2006.
- [71] **J.Y. Guedou, G. Simon, and J.M. Rongvaux**, Development of Damage Tolerant INCO 718 for High Temperature Usage, in *Superalloys 718, 625, 706 and Various Derivatives*, Edited by E.A.Loria: The Minerals, Metals & Materials Society, pp. 509-522, 1994.
- [72] **M. Clavel and A. Pineau**, Frequency and wave-form effects on the fatigue crack growth behavior of alloy 718 at 298 K and 823 K, *Metallurgical and Materials Transactions A*, vol. 9, pp. 471-480, 1978.
- [73] **R.W. Hayes**, Creep Deformation of Inconel Alloy 718 in the 650°C to 760°C Temperature Regime, in *Superalloys 718, 625 and Various Derivatives*, Edited by E.A.Loria: The Minerals, Metals & Materials Society, pp. 549-561, 1991.
- [74] **J.P. Collier, A.O. Selius, and J.K. Tien**, On Developing a Microstructurally and Thermally Stable Iron-Nickel Base Superalloy, in *Superalloys 1988; Champion, Pennsylvania; USA*, Edited by S. Reichman, D. N. Duhl, G. Maurer, S. Antolovich, and C. Lund: The Metallurgical Society, pp. 43-52, 1988.
- [75] **C. Radhakrishna and K. Prasad Rao**, Studies on creep/stress rupture behaviour of superalloy 718 weldments used in gas turbine applications, *Materials at High Temperatures*, vol. 12, pp. 323-327, 1994.

- [76] **R.P. Jewett and J.A. Halchak**, The use of Alloy 718 in the Space Shuttle main engine, in *Superalloys 718, 625 and Various Derivatives*, Edited by E.A.Loria: The Minerals, Metals & Materials Society, 1991.
- [77] **S. Kalluri, K. Rao, G. Halford, and M. McGaw**, Deformation and Damage Mechanisms in Inconel 718 Superalloy, in *Superalloys 718, 625, 706 and Various Derivatives*, Edited by E.A.Loria: The Minerals, Metals & Materials Society, pp. 593-605, 1994.
- [78] **R.W. Swindeman and M.J. Swindeman**, A comparison of creep models for nickel base alloys for advanced energy systems, *International Journal of Pressure Vessels and Piping*, vol. 85, pp. 72-79, 2008.
- [79] **Y.N. Gornostyrev, O.Y. Kontsevoi, K.Y. Khromov, M.I. Katsnelson, and A.J. Freeman**, The role of thermal expansion and composition changes in the temperature dependence of the lattice misfit in two-phase g/g' superalloys, *Scripta Materialia*, vol. 56, pp. 81-84, 2007.
- [80] **J.F. Radavich**, The physical metallurgy of cast and wrought alloy 718, in *Superalloy 718: Metallurgy and Applications*, Edited by E.A.Loria: The Minerals, Metals & Materials Society, pp. 229-240, 1989.
- [81] **M. Gao, D. Harlow, R. Wei, and S. Chen**, Preferential coarsening of γ'' precipitates in INCONEL 718 during creep, *Metallurgical and Materials Transactions A*, vol. 27, pp. 3391-3398, 1996.
- [82] **J. Gordine**, Welding of Inconel 718, *Welding Journal, Research Supplement*, vol. 49, pp. 531-537, 1970.
- [83] **M.J. Lucas and C.E. Jackson**, The Welded Heat-Affected Zone in Nickel Base Alloy 718, *Welding Journal, Research Supplement*, vol. 49, pp. 46-54, 1970.
- [84] **D.S. Duvall and W.A. Owczarski**, Studies of Postweld Heat-Treatment Cracking in Nickel-Base Alloys, *Welding journal research supplement*, vol. 48, pp. 10-22, 1969.
- [85] **A. Lingenfelter**, Welding of Inconel Alloy 718: a Historical Overview, in *Superalloy 718: Metallurgy and Applications*, Edited by E.A.Loria: The Minerals, Metals & Materials Society, pp. 673-683, 1989.
- [86] **C. Radhakrishna and K. Prasad Rao**, The formation and control of Laves phase in superalloy 718 welds, *Journal of Materials Science*, vol. 32, pp. 1977-1984, 1997.

- [87] **J.S. Ogborn, D.L. Olson, and M.J. Cieslak**, Influence of solidification on the microstructural evolution of nickel base weld metal, *Materials Science and Engineering A*, vol. 203, pp. 134-139, 1995.
- [88] **G.D.J. Ram, A.V. Reddy, K.P. Rao, and G.M. Reddy**, Microstructure and mechanical properties of Inconel 718 electron beam welds, *Materials Science and Technology*, vol. 21, pp. 1132-1138, 2005.
- [89] **R. Vincent**, Precipitation around welds in the nickel-base superalloy, Inconel 718, *Acta Metallurgica*, vol. 33, pp. 1205-1216, 1985.
- [90] **X. Huang, M.C. Chaturvedi, and N.L. Richards**, Effect of homogenization heat treatment on the microstructure and heat-affected zone microfissuring in welded cast alloy 718, *Metallurgical Transactions A*, vol. 27, pp. 785-790, 1996.
- [91] **R.A. Mayor**, Selected mechanical properties of Inconel 718 and 706 weldments *Welding Journal, Research Supplement*, vol. 55, pp. 269-275, 1976.
- [92] **Y. Kyriakoglou, M. Preuss, and P. Bowen**, Tensile properties and HAZ definition for TIG and EB welds using electronic speckle pattern interferometry (ESPI), *Applied Mechanics and Materials*, vol. 7-8, pp. 119-125, 2007.
- [93] **T.H. Hyde, A.A. Becker, Y. Song, and W. Sun**, Failure estimation of TIG butt-welded Inco718 sheets at 620°C under creep and plasticity conditions, *Computational Materials Science*, vol. 35, pp. 35-41, 2006.
- [94] **C.A. Huang, T.H. Wang, Y.Z. Chang, W.C. Han, and C.H. Lee**, Tensile behaviour of different pretreated alloy 718 sheets welded with electron beam welding (EBW), *Science and Technology of Welding & Joining*, vol. 13, pp. 646-655, 2008.
- [95] **G. Ram, A. Reddy, K. Rao, and G. Reddy**, Improvement in stress rupture properties of inconel 718 gas tungsten arc welds using current pulsing, *Journal of Materials Science*, vol. 40, pp. 1497-1500, 2005.
- [96] **L.A. James and W.J. Mills**, Effect of Heat-Treatment Upon the Fatigue-Crack Growth Behaviour of Alloy 718 Weldments -Part I: Macroscopic behaviour, *Transactions of the ASME. Journal of Engineering Materials and Technology*, vol. 107, pp. 34-40, 1985.

- [97] **W.J. Mills and L.A. James**, Effect of Heat-Treatment Upon the Fatigue-Crack Growth Behaviour of Alloy 718 Weldments -Part II: Microscopic behaviour, *Transactions of the ASME. Journal of Engineering Materials and Technology*, vol. 107, pp. 41-47, 1985.
- [98] **Y. Song, A.A. Becker, T.H. Hyde, and W. Sun**, Creep Testing and Finite Element Modelling of TIG Butt-Welded Inco718 Sheets at 620°C, *Materials Science Forum*, vol. 440-441, pp. 439-446, 2003.
- [99] **R.G. Andrews, A.K. Koul, and P. Au**, Fatigue Crack Initiation in Alloy 718 at 650°C, in *Superalloys 718, 625 and Various Derivatives*, Edited by E.A.Loria: The Minerals, Metals & Materials Society, pp. 943-954, 1991.
- [100] **S. Li, J. Zhuang, J. Yang, Q. Deng, J. Du, X. Xie, B. Li, Z. Xu, Z. Cao, Z. Su, and C. Jiang**, The Effect of δ -phase on Crack Propagation Under Creep and Fatigue Conditions in Alloy 718, in *Superalloys 718, 625, 706 and Various Derivatives*, Edited by E.A.Loria: The Minerals, Metals & Materials Society, pp. 545-555, 1994.
- [101] **J.Z. Xie**, Low Cycle Fatigue and Fatigue Crack Growth Behaviors of Alloy IN718, in *Superalloys 718, 625 and Various Derivatives*, Edited by E.A.Loria: The Minerals, Metals & Materials Society, pp. 491-500, 1991.
- [102] **S.-i. Komazaki, Y. Watanabe, and T. Shoji**, Nondestructive evaluation of high temperature low-cycle fatigue damage accumulation in Inconel 718 by chemical method, in *Superalloys 718, 625, 706 and Various Derivatives*, Edited by E.A.Loria: The Minerals, Metals & Materials Society, pp. 617-628, 1997.
- [103] **D. Fournier and A. Pineau**, Low cycle fatigue behavior of inconel 718 at 298 K and 823 K, *Metallurgical and Materials Transactions A*, vol. 8, pp. 1095-1105, 1977.
- [104] **M. Clavel and A. Pineau**, Fatigue Behavior of Two Nickel-Base Alloys. I.--Experimental Results on Low-Cycle Fatigue, Fatigue Crack Propagation and Substructures, *Materials Science and Engineering*, vol. 55, pp. 157-171, 1982.
- [105] **M. Andersson, C. Persson, and S. Melin**, High-temperature fatigue crack growth in Inconel 718 subjected to high strain amplitudes, *Fatigue & Fracture of Engineering Materials & Structures*, vol. 29, pp. 863-875, 2006.

- [106] **B. Pieraggi and J.F. Uginet**, Fatigue and Creep Properties in Relation With Alloy 718 Microstructure, in *Superalloys 718, 625, 706 and Various Derivatives*, Edited by E.A.Loria: The Minerals, Metals & Materials Society, pp. 535-544, 1994.
- [107] **J. Pedron and A. Pineau**, The effect of microstructure and environment on the crack growth behavior of Inconel 718 alloy at 650°C under fatigue, creep and combined loading, *Materials Science and Engineering*, vol. 56, pp. 143-156, 1982.
- [108] **C.R. Brinkman, M.K. Booker, and J.L. Ding**, Creep and creep-rupture behavior of Alloy 718, in *Superalloys 718, 625 and various derivatives*, Edited by E.A.Loria: The Minerals, Metals & Materials Society, pp. 519-536, 1991.
- [109] *ABAQUS Analysis User's Manual, Version 6.5*: ABAQUS Inc., 2004.
- [110] **D. Deng and H. Murakawa**, Numerical simulation of temperature field and residual stress in multi-pass welds in stainless steel pipe and comparison with experimental measurements, *Computational Materials Science*, vol. 37, pp. 269-277, 2006.
- [111] **S.A. Tsirkas, P. Papanikos, and T. Kermanidis**, Numerical simulation of the laser welding process in butt-joint specimens, *Journal of Materials Processing Technology*, vol. 134, pp. 59-69, 2003.
- [112] **D. Gery, H. Long, and P. Maropoulos**, Effects of welding speed, energy input and heat source distribution on temperature variations in butt joint welding, *Journal of Materials Processing Technology*, vol. 167, pp. 393-401, 2005.
- [113] **G.D. Janaki Ram, A. Venugopal Reddy, K. Prasad Rao, G.M. Reddy, and J.K. Sarin Sundar**, Microstructure and tensile properties of Inconel 718 pulsed Nd-YAG laser welds, *Journal of Materials Processing Technology*, vol. 167, pp. 73-82, 2005.
- [114] **N. Saunders, Z. Guo, X. Li, A.P. Miodownik, and J.-P. Schillé**, Modelling the material properties and behaviour of Ni-based superalloys, in *Superalloys 2004*, Edited by K.A.Green, T. M. Pollock, H. Harada, T. E. Howson, R. C. Reed, J. J. Schirra, and S. Walston: The Minerals, Metals & Materials Society (TMS), pp. 849-858, 2004.

- [115] **G.D. Janaki Ram, A. Venugopal Reddy, K. Prasad Rao, and G. Madhusudhan Reddy**, Improvement in stress rupture properties of inconel 718 gas tungsten arc welds using current pulsing, *Journal of Materials Science*, vol. V40, pp. 1497-1500, 2005.
- [116] British Standard 3500 : Part 3 : 1969 *Methods for creep and rupture testing of metals - Part 3. Tensile creep testing*.
- [117] **Miller Electric Mfg Co.** *TIG Handbook*
<http://www.millerwelds.com/resources/TIGhandbook/>
 Accessed 19/12/2008.
- [118] AMS 5596K: Nickel Alloy, Corrosion and Heat-Resistant, Sheet, Strip, Foil and Plate; 52.5Ni - 19Cr - 3.0Mo - 5.1 Cb (Nb) - 0.90Ti - 0.50Al - 18Fe; Consumable Electrode Remelted or Vacuum Induction Melted; 1775°F (968°C) Solution Heat Treated, Society of Automotive Engineers (SAE) 2007.
- [119] **V. Garat, J.M. Cloue, D. Poquillon, and E. Andrieu**, Influence of Portevin-Le Chatelier effect on rupture mode of alloy 718 specimens, *Journal of Nuclear Materials*, vol. 375, pp. 95-101, 2008.
- [120] **N.L. Richards and M.C. Chaturvedi**, Effect of minor elements on weldability of nickel base superalloys, *International Materials Reviews*, vol. 45, pp. 109-129, 2000.
- [121] **J.J. Schirra, R.H. Caless, and R.W. Hatala**, The Effect of Laves Phase on the Mechanical Properties of Wrought and Cast + HIP Inconel 718, in *Superalloys 718, 625 and Various Derivatives*, Edited by E. A. Loria: The Minerals, Metals & Materials Society, pp. 375-388, 1991.
- [122] **C. Casavola and C. Pappalettere**, Discussion on local approaches for the fatigue design of welded joints, *International Journal of Fatigue*, vol. 31, pp. 41-49, 2009.
- [123] **G.A. Webster and A.N. Ezeilo**, Residual stress distributions and their influence on fatigue lifetimes, *International Journal of Fatigue*, vol. 23, pp. 375-383, 2001.
- [124] **A.A. Tang**, *The creep behaviour of cross-weld specimens and welded pipes*, PhD Thesis, University of Nottingham, UK, pp. 462, 2000.

- [125] **T.H. Hyde, W. Sun, A.A. Becker, and J.A. Williams**, Creep Continuum Damage Constitutive Equations for the Base, Weld and Heat-Affected Zone Materials of a Service-Aged 1/2Cr1/2Mo1/4V:2 1/4Cr1Mo Multipass Weld at 640°C, *The Journal of Strain Analysis for Engineering Design*, vol. 32, pp. 273-287, 1997.
- [126] **D.R. Hayhurst**, Creep rupture under multi-axial states of stress, *Journal of the Mechanics and Physics of Solids*, vol. 20, pp. 381-390, 1972.
- [127] **T.H. Hyde, W. Sun, and A.A. Becker**, Failure prediction for multi-material creep test specimens using a steady-state creep rupture stress, *International Journal of Mechanical Sciences*, vol. 42, pp. 401-423, 2000.
- [128] **R.S.J. Corran and S.J. Williams**, Lifting methods and safety criteria in aero gas turbines, *Engineering Failure Analysis*, vol. 14, pp. 518-528, 2007.
- [129] **K. Walker**, The Effect of Stress Ratio During Crack Propagation and Fatigue for 2024-T3 and 7075-T6 Aluminum, in *Effects of Environment and Complex Load History on Fatigue Life*, ASTM STP 462, Edited by: American Society for Testing and Materials, pp. 1-14, 1970.
- [130] **P.J. Hurley, M.T. Whittaker, S.J. Williams, and W.J. Evans**, Prediction of fatigue initiation lives in notched Ti 6246 specimens, *International Journal of Fatigue*, vol. 30, pp. 623-634, 2008.
- [131] **K.N. Smith, P. Watson, and T.H. Topper**, A stress-strain function for the fatigue of metals, *Journal of Materials*, vol. 5, pp. 767-778, 1970.
- [132] **S.J. Maddox**, *Fatigue strength of welded structures*, 2nd ed. Cambridge, England: Abington Publishing, 1991.
- [133] **A. Carpinteri, A. Spagnoli, and S. Vantadori**, Multiaxial fatigue life estimation in welded joints using the critical plane approach, *International Journal of Fatigue*, vol. 31, pp. 188-196, 2009.
- [134] **N.K. Mukhopadhyay and P. Paufler**, Micro- and nanoindentation techniques for mechanical characterisation of materials, *International Materials Reviews*, vol. 51, pp. 209-245, 2006.
- [135] **T.H. Hyde, W. Sun, and J.A. Williams**, Requirements for and use of miniature test specimens to provide mechanical and creep properties of materials: a review, *International Materials Reviews*, vol. 52, pp. 213-255, 2007.